

Dissertation  
submitted to the  
Combined Faculty of Mathematics, Engineering and Natural Sciences  
of Heidelberg University, Germany  
for the degree of  
Doctor of Natural Sciences

Put forward by  
*Giovanni Leidi*  
*Born in: Bergamo, Italy*  
*Oral examination: 15.07.2024*





# Simulating magnetohydrodynamic phenomena in the interior of stars

Referees: Prof. Dr. Friedrich K. Röpke  
Prof. Dr. Ralf Klessen



## Zusammenfassung

In dieser Arbeit werden mehrdimensionale Simulationen von magnetohydrodynamischen Phänomenen im Inneren von Sternen vorgestellt. Das Verständnis dieser Phänomene ist für die Verbesserung der aktuellen Theorien zur Sternentwicklung von wesentlicher Bedeutung. Die hochgradig subsonischen Strömungsregime, die in den Regionen tief im Inneren von Sternen zu finden sind, stellen herkömmliche Methoden der numerischen Magnetohydrodynamik (MHD) vor große Herausforderungen. Daher konzentriert sich der erste Teil dieser Arbeit auf die Entwicklung eines geeigneten numerischen Lösers, der für magnetisierte, stellare Strömungen bei niedrigen Machzahlen optimiert ist. Der vorgeschlagene MHD-Löser wird in den Seven-League Hydro (SLH) Code implementiert und dann verwendet, um neuartige Simulationen der turbulenten Dynamowirkung in einer sauerstoffbrennenden Schale eines massereichen Sterns durchzuführen. Es wird gezeigt, dass starke, dynamisch erzeugte Magnetfelder einen erheblichen Einfluss auf die Entwicklung der konvektiven Schicht haben und möglicherweise den Explosionsmechanismus von Kernkollaps-Supernovae beeinflussen. Die neuen MHD-Fähigkeiten von SLH ebnen den Weg für die nächste Generation von Sternmodellen und helfen bei der Untersuchung verschiedener stellarer MHD-Prozesse in Strömungsregimen, die bisher unzugänglich waren.

## Abstract

This thesis presents multidimensional simulations of magnetohydrodynamic phenomena occurring in the interior of stars. Understanding these phenomena is essential for improving current theories of stellar evolution. The highly subsonic flow regimes found in the regions deep inside stars pose severe challenges to conventional methods of computational magnetohydrodynamics (MHD). Therefore, the first part of this thesis focuses on the development of a suitable numerical solver optimized for magnetized, low-Mach-number stellar flows. The proposed MHD solver is implemented in the Seven-League Hydro (SLH) code and then used to perform unprecedented simulations of turbulent dynamo action in an oxygen-burning shell of a massive star. It is demonstrated that strong, dynamically generated magnetic fields have a significant impact on the evolution of the convective shell and potentially influence the explosion mechanism of core-collapse supernovae. The new MHD capabilities of SLH pave the way for the next generation of stellar models and will aid in the study of various stellar MHD processes in flow regimes that were previously inaccessible.



---

# Contents

---

<b>1</b>	<b>Introduction</b>	<b>1</b>
1.1	Stellar evolution modeling approaches . . . . .	1
1.1.1	Stellar evolution in one dimension . . . . .	1
1.1.2	Shortcomings of 1D stellar modeling . . . . .	2
1.1.3	Calibrating 1D prescriptions against observations . . . . .	3
1.1.4	Multidimensional modeling of stars . . . . .	4
1.2	Going one step further: stellar magnetohydrodynamics . . . . .	5
1.2.1	Modeling MHD flows in the interior of stars: numerical challenges . . . . .	6
1.2.2	Existing approaches to model stellar MHD flows . . . . .	8
1.3	Goal of the thesis: developing a fully compressible MHD solver for low-Mach-number stellar flows . . . . .	9
1.3.1	Methodology . . . . .	10
1.3.2	Implementation and testing . . . . .	11
1.3.3	An astrophysical application: simulations of turbulent dynamo action in an oxygen-burning shell . . . . .	12
1.3.4	Thesis outline . . . . .	13
<b>2</b>	<b>Numerical methods for stellar MHD</b>	<b>15</b>
2.1	The equations of stellar MHD . . . . .	15
2.1.1	Physical considerations . . . . .	15
2.1.2	The model equations . . . . .	16
2.1.3	Linear MHD waves . . . . .	17
2.2	Finite volume discretization . . . . .	19
2.2.1	The Godunov algorithm . . . . .	20
2.3	Higher-order Godunov methods for MHD . . . . .	22
2.3.1	Higher-order spatial reconstruction methods . . . . .	23
2.3.2	Approximate Riemann solvers . . . . .	25
2.3.3	Higher-order time integration . . . . .	26
2.4	The $\nabla \cdot \mathbf{B} = 0$ constraint in Godunov-type schemes . . . . .	29
2.4.1	Projection methods . . . . .	30
2.4.2	Powell’s eight-wave method . . . . .	30
2.4.3	Hyperbolic divergence cleaning . . . . .	31
2.4.4	Constrained transport . . . . .	32
<b>3</b>	<b>Results</b>	<b>35</b>
3.1	Publication I: A numerical scheme for modeling low-Mach-number magnetohydrodynamic flows in stars . . . . .	36
3.2	Publication II: Comparison of different Godunov-like methods in simulations of astrophysical subsonic flows . . . . .	67
3.3	Publication III: Turbulent dynamo action in an oxygen-burning shell . . . . .	111
<b>4</b>	<b>Conclusions</b>	<b>127</b>
4.1	Summary of the individual publications . . . . .	127

## CONTENTS

---

4.1.1	Implementation of a low-Mach scheme optimized for stellar MHD flows [Section 3.1] . . . . .	127
4.1.2	Comparison of higher-order Godunov-type methods in simulations of astrophysical subsonic flows [Section 3.2] . . . . .	128
4.1.3	Simulations of turbulent dynamo action in an oxygen-burning shell [Section 3.3] . . . . .	129
4.2	Discussion and outlook . . . . .	129
4.2.1	Low-Mach-number modeling of stellar MHD flows . . . . .	129
4.2.2	MHD simulations of late burning shells of massive stars . . . . .	133
	<b>List of abbreviations</b>	<b>135</b>
	<b>List of publications by Giovanni Leidi</b>	<b>137</b>
	<b>Bibliography</b>	<b>139</b>

# CHAPTER 1

---

## Introduction

---

### 1.1 Stellar evolution modeling approaches

Stars are the building blocks of the visible Universe. They are the main contributors to the chemical evolution of galaxies and act as tracers of the evolution of the cosmos as a whole. In light of these facts, understanding the physical mechanisms that drive stellar evolution is one of the most important tasks in astrophysics.

In its simplest form, a star can be described as a gaseous sphere held together by its own gravity. The temperatures reached in its innermost regions are high enough to ignite nuclear reactions and generate thermal energy at the expense of the rest mass of the star (e.g., [Prialnik, 2000](#); [Salaris and Cassisi, 2005](#); [Iliadis, 2007](#)). This excess thermal energy is transported to cooler regions and eventually reaches the stellar surface, making it shine.

Several physical processes are responsible for transporting the energy deposited by nuclear reactions in the core to the surface of the star, including convection, radiative diffusion, and thermal conduction (e.g., [Maeder, 2008](#); [Kippenhahn et al., 2012](#)). These processes can be modeled self-consistently by solving the equations of fluid dynamics in three spatial dimensions (3D), along with source terms such as gravity, nuclear energy generation, neutrino cooling, and thermal diffusion ([Kupka and Muthsam, 2017](#)). The model equations must be supplemented by an equation of state, thermal opacities, and nuclear reaction rates, which describe the microscopic properties of the stellar plasma. Ideally, by solving this set of equations (together with a suitable treatment of the energy transport through the stellar atmosphere) it is possible to determine the evolution of stars with any given initial mass and composition.

#### 1.1.1 Stellar evolution in one dimension

Although analytic solutions to the fluid-dynamic equations can be found for some idealized problems (e.g., [Lamb, 1932](#); [Landau et al., 1959](#)), one generally needs to rely on numerical simulations to model more complicated systems such as stars. However, the vast range of spatial and temporal scales that characterizes these astronomical objects makes it extremely difficult (if not impossible) to follow their entire evolution by solving the model equations numerically. For instance, in our Sun, the dynamical response of the gas to small perturbations in the solar structure occurs in about 20 minutes, while the nuclear burning time scale is on the order of 10 billion years; the typical size of the convective cells in the solar photosphere is approximately  $10^3$  km, while the radius of the Sun is  $7 \times 10^5$  km (e.g., [Kippenhahn et al., 2012](#)). Even with the help of massively parallelized simulations, such wide ranges of spatial and temporal scales cannot yet be tackled by 3D models of stellar evolution.

Therefore, in order to evolve a star over most of its lifetime in a computer, drastic assumptions must be made on the model equations. A common approach is to treat stars as spherically symmetric objects, in which the physical quantities that character-

ize their structure depend only on the radial distance from the center of the star (e.g., [Maeder, 2008](#)). Moreover, since the dynamical time scale is much shorter than the nuclear time scale in most evolutionary stages, 1D codes assume that the star evolves through sequences in which its structure is in hydrostatic equilibrium. These simplifications drastically reduce the computational effort required to solve the model equations and enable us to provide a qualitative description of stellar evolution.

### 1.1.2 Shortcomings of 1D stellar modeling

The simplicity and computational inexpensiveness of 1D calculations are achieved at the cost of crudely parameterizing the rich variety of inherently multidimensional hydrodynamic processes that occur in stellar interiors, which cannot be treated self-consistently by approximating stars as hydrostatic spheres. One such process is convective energy transport, which is modeled in most 1D codes by means of the mixing-length theory (MLT, [Prandtl, 1925](#); [Böhm-Vitense, 1958](#)). Although MLT provides good estimates of the convective energy flux, the choice of the free parameters that enter this prescription for convection has a significant impact on the evolution of a star, thus introducing large uncertainties into the stellar models ([Joyce and Tayar, 2023](#)).

One-dimensional prescriptions also fail to provide insight into the physical mechanisms behind stellar hydrodynamic processes. In the MLT, for example, the criterion for convective instability is derived from the linearization of the fluid-dynamic equations with a gravitational source term. In reality, convective flows in stars are highly turbulent (i.e., nonlinear) due to the fact that the particle mean free path in the stellar plasma is many orders of magnitude shorter than the characteristic length scale of the convective flows (in other words, the Reynolds number of the stellar flows is very high<sup>1</sup>, see also [Jermyn et al., 2022](#)). Turbulent flows are extremely efficient at mixing chemical elements in a burning region of a star over the relatively short revolution time scale of the turbulent eddies, thus affecting the nuclear energy generation rate (e.g., [Meakin and Arnett, 2007](#); [Ritter et al., 2018](#); [Andrassy et al., 2020](#); [Yadav et al., 2020](#); [Rizzuti et al., 2023](#)).

Convective flows also scrape material from neighboring convectively stable layers and bring fresh fuel into burning regions, ultimately prolonging the lifetime of the star. The conglomeration of the mixing processes that occur at convective boundaries, such as shear instabilities, surface wave breaking, or convective overshooting, is referred to in the literature as “convective boundary mixing” (CBM, e.g., [Cristini et al., 2019](#); [Andrassy et al., 2022](#); [Anders and Pedersen, 2023](#)). CBM increases the size of convective regions over time (see [Fig. 1.1](#)) and is crucial in explaining a large number of observations, including the distribution of galactic massive stars in the Hertzsprung-Russell diagram ([Castro et al., 2014](#)), the properties of double-lined eclipsing binaries ([Claret and Torres, 2016](#); [Valle et al., 2016](#)), or the rate of period change of classical Cepheids ([Miller et al., 2020](#)). Despite its importance, the mixing that occurs at stellar convective boundaries is not modeled by most parameterized theories of convection. To be able to study the effects of CBM on stellar evolution, 1D codes must therefore use additional prescriptions (e.g., diffusive overshooting or convective penetration models; see also [Anders and Pedersen, 2023](#), for a recent review) where the ignorance about

---

<sup>1</sup>In fluid dynamics, the Reynolds number is a dimensionless quantity defined as  $Re := uL/\nu$ , where  $u$  is the flow speed,  $L$  is the characteristic length scale of the flow, and  $\nu$  is the kinematic viscosity of the fluid. Thus,  $Re$  measures the ratio of inertial to viscous forces in the fluid.



the physics of turbulent mixing processes is put into additional parameters<sup>2</sup>.

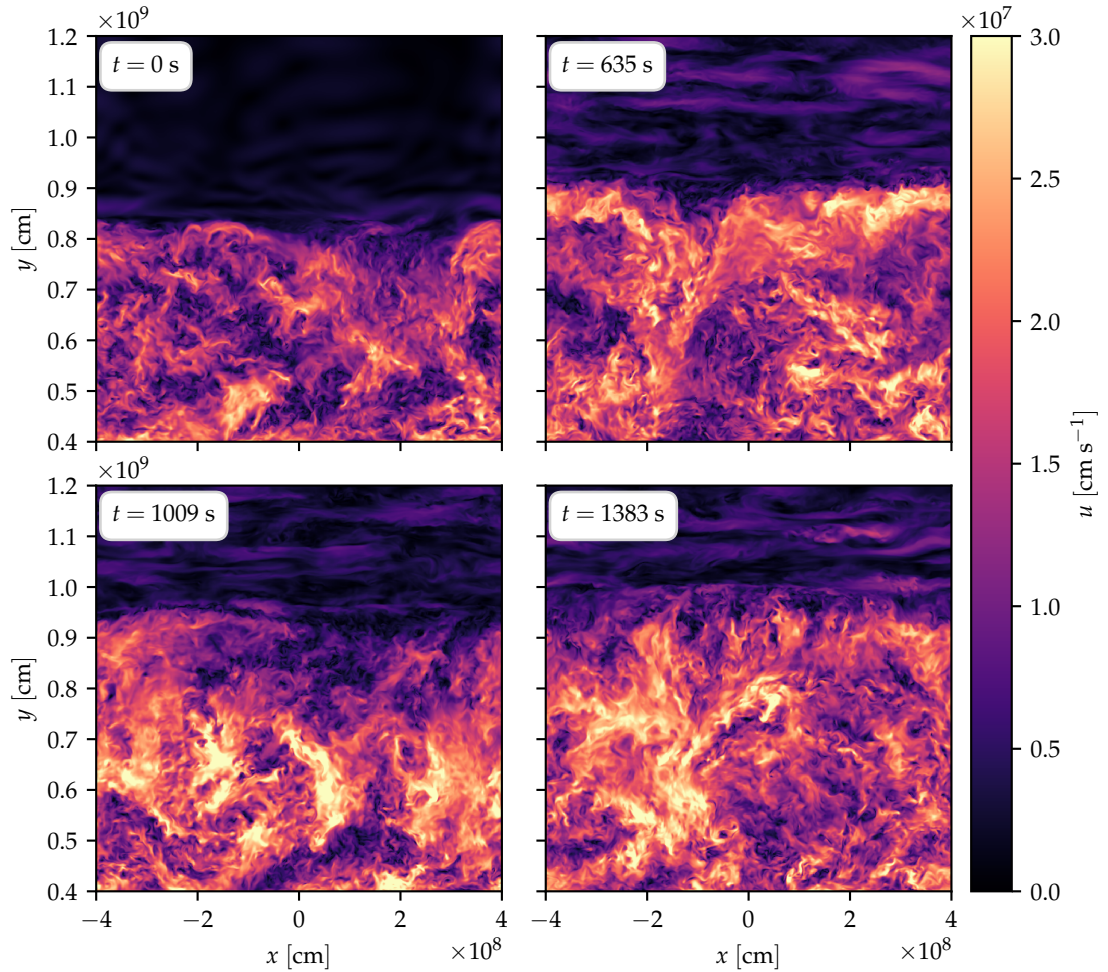


Figure 1.1: 3D simulations of turbulent convection and convective boundary mixing in an oxygen-burning shell of a massive star. The panels are adapted from [Leidi et al. \(2023\)](#) and show the absolute value of the fluid velocity in the  $z = 0$  plane at different times during the evolution of the shell, as indicated by the insets. In this setup, the turbulent convective region grows over time due to the convective boundary mixing processes operating at its boundary that entrain material from the stable layer above.

### 1.1.3 Calibrating 1D prescriptions against observations

The crude treatment of convective energy transport, CBM, and other complex hydrodynamic phenomena in 1D codes has far-reaching consequences for our understanding of supernova explosion mechanisms (e.g., [Davis et al., 2019](#); [Temaj et al., 2024](#)), the chemical evolution of galaxies (e.g., [Romano et al., 2010](#)), and the evolution of stellar populations (e.g., [Willson, 2000](#)). It is therefore imperative that 1D prescriptions of

<sup>2</sup>There have been several attempts to develop nonlocal theories of convection (e.g., [Kuhfuss, 1986](#); [Canuto, 1997](#); [Garaud et al., 2010](#)), but their use in stellar evolution codes is still limited.

multidimensional hydrodynamic processes are properly calibrated to produce reliable models of stars.

An effective way to calibrate the free parameters that are incorporated into 1D prescriptions is to fit theoretical models against observations. This can be done using different methods, including the fitting of stellar isochrones to the color-magnitude diagram of stellar clusters (VandenBerg et al., 2006), the analysis of asteroseismic data (Guenther et al., 2014; Aerts, 2021), or by reproducing the main observational properties of double-lined eclipsing binaries (Stancliffe et al., 2015; Claret and Torres, 2016). Ideally, in order to build a comprehensive grid of stellar models, the values of the free parameters should be constrained as functions of the stellar mass, age, and composition. In practice, this approach is challenged by the scarcity of suitable stellar samples and by the observational uncertainties that inevitably propagate into the stellar models. Furthermore, the degeneracy between the parameters makes it difficult to disentangle the role of different hydrodynamic processes in the stellar evolution.

#### 1.1.4 Multidimensional modeling of stars

A complementary approach to calibrating 1D prescriptions against observations is the direct study of hydrodynamic processes in the stellar interior using multidimensional simulations. Multidimensional stellar modeling has become increasingly more attractive in recent years due to the continuous advancements in high-performance computing, which have made it possible to study a variety of stellar hydrodynamic processes with high spatial resolution, even in 3D. In particular, much effort has been devoted to the study of turbulent convection, convective boundary mixing, time-dependent burning, and excitation mechanisms of internal waves during the main sequence (e.g., Gilet et al., 2013; Pratt et al., 2016; Käpylä, 2019; Horst et al., 2020; Baraffe et al., 2023; Lecoanet and Edelman, 2023) and later evolutionary stages (e.g., Meakin and Arnett, 2007; Jones et al., 2017; Cristini et al., 2017; Andrassy et al., 2020; Blouin et al., 2023).

A drawback of multidimensional hydrodynamic simulations is that they can only evolve the flows of interest on their characteristic time scales (e.g., the revolution time scale of the convective plumes, see also Kupka and Muthsam, 2017), which are much shorter than the evolution time scale of the star. However, in contrast to 1D calculations, they allow the main physical processes occurring in the stellar interior to be disentangled and modeled self-consistently. Thus, multidimensional simulations can be used as testbeds for parameterized theories of, e.g., stellar convection and convective boundary mixing when calibration against observations is not feasible (e.g., Trampedach et al., 2014; Cristini et al., 2019; Sonoi et al., 2019; Higl et al., 2021; Horst et al., 2021; Rizzuti et al., 2023). Multidimensional stellar modeling is also required to explore the violent burning stages prior to the collapse of the iron core in supernova progenitors (e.g., Powell and Müller, 2020; Yadav et al., 2020; Varma and Müller, 2021). In fact, in such evolutionary stages, the assumptions of hydrostatic equilibrium and spherical symmetry made by 1D codes are inadequate even for describing the background stellar stratification (Müller, 2020) and observational constraints on the flow properties are difficult to obtain (Van Dyk, 2017).

## 1.2 Going one step further: stellar magnetohydrodynamics

Despite the recent encouraging successes in multidimensional stellar modeling, our understanding of stellar hydrodynamic processes and how they relate to stellar evolution is far from being complete. An additional layer of complexity is provided by the presence of magnetic fields, which have been observed in many different types of stars (Reiners, 2012; Brun and Browning, 2017; Keszthelyi, 2023).

Like gravity, magnetic fields exert long-range forces that can affect the star as a whole. Under certain conditions, magnetohydrodynamic (MHD) effects on the stellar structure can be quite dramatic. For example, magnetic fields play a crucial role in spinning down newly formed stars and getting rid of most of their angular momentum through disk locking and protostellar outflows (e.g., Mestel, 1999; Pudritz and Ray, 2019). Fully convective, low-mass stars are highly active with average surface magnetic fields on the order of a few kG (Reiners, 2012). Such strong magnetic activity gives rise to violent transient events (e.g., flares and coronal mass ejections) during which the star loses mass at a rate hundreds of times higher than the current solar wind rate (Crosley and Osten, 2018). In the convective layers deep inside the star, magnetic fields can be amplified by the action of a turbulent dynamo (e.g., Brun et al., 2005; Augustson et al., 2011), thus affecting the convective energy transport and the mixing at convective boundaries (Hotta, 2017). Magnetic fields can also change the stratification of core-collapse supernova progenitors (Varma and Müller, 2021) and are thought to power some of the most energetic events in the Universe, i.e., hypernovae (e.g., Powell et al., 2023; Müller, 2024).

The field of stellar magnetohydrodynamics has been driven mainly by the study of our Sun, whose surface magnetism is constrained by a large number of observations (e.g., Brun and Browning, 2017, and references therein). In particular, many works have attempted to infer the generation mechanism for the observed 22-year solar cycle, which has puzzled researchers for decades (e.g., Brun et al., 2004; Ghizaru et al., 2010; Passos and Charbonneau, 2014; Fan and Fang, 2014; Augustson et al., 2015; Käpylä et al., 2023). Although the interplay between the solar differential rotation and the convection in the solar envelope has been recognized as crucial for exciting a large-scale dynamo and driving a cyclic activity (e.g., Charbonneau, 2020, and references therein), no simulation has yet been able to fully reproduce the global properties of the solar cycle.

Even more uncertain are the implications for stellar evolution of potential MHD processes operating in deep stellar interiors. Some efforts have been made to infer the magnetic field generation mechanism in fully convective (e.g., Browning, 2008; Käpylä, 2021) and upper-main-sequence stars (e.g., Brun et al., 2004; Augustson et al., 2016), but very little has been done so far to explore the effects of magnetic fields on the evolution of stellar flows in post-main-sequence burning phases. Only very recently, a few pioneering studies revealed that small-scale dynamos operating in late convective shells of massive stars can build up relatively strong magnetic fields and affect the dynamics of the shells to some extent (Varma and Müller, 2021; Canivete Cuissa and Teyssier, 2022). However, even the state-of-the-art numerical methods used in these studies suffer from major flaws when applied to model MHD flows at the conditions found in stellar interiors, severely limiting their applicability (see Sect. 1.2.1). Further investigation of multidimensional MHD processes in stellar interiors, which is crucial for improving current theories of stellar evolution, requires

specialized numerical techniques that have not yet been implemented.

### 1.2.1 Modeling MHD flows in the interior of stars: numerical challenges

Due to the high conductivity of the stellar plasma (e.g., [Mestel, 1999](#); [Spruit, 2013](#)), the evolution of the magnetic field and its effects on the dynamics of stellar flows can be modeled to a good approximation by the set of 3D, fully compressible MHD equations (see [Chapter 2](#)). Like the fluid-dynamic equations, solutions to the MHD equations can in most cases only be found numerically.

The need for robust numerical methods capable of tackling supersonic and highly magnetized flows, which occur in many different astrophysical environments and confined laboratory plasma experiments, has led to a flourishing development of conservative, shock-capturing MHD schemes in the last thirty years (e.g., [Powell, 1994](#); [Tóth, 2000](#); [Dedner et al., 2002](#); [Balsara, 2004](#); [Miyoshi and Kusano, 2005](#); [Stone and Gardiner, 2009](#); [Martí and Müller, 2015](#); [Mignone and Del Zanna, 2021](#)). Most of these schemes are based on higher-order extensions of the Godunov algorithm ([Godunov, 1959](#)), where the MHD variables are represented by piecewise polynomial functions over the computational grid. Discontinuities in the state quantities at the grid cell boundaries define a Riemann problem (e.g., [LeVeque, 2002](#); [Toro, 2009](#)), which can be easily solved to obtain the MHD fluxes and update the quantities in each grid cell. The popularity of this method derives from the fact that the solution to the Riemann problem is naturally upwind, i.e., it is biased toward the incoming direction of the flow, which is an essential property for building stable and accurate numerical schemes for hyperbolic conservation laws such as the MHD equations ([LeVeque, 1990](#)).

In the field of computational astrophysics, Godunov-type methods for MHD have found fertile ground in simulations of star-forming regions (e.g., [Federrath and Klessen, 2012](#); [Teyssier and Commerçon, 2019](#)), accretion disks (e.g., [Zanni et al., 2007](#); [Flock et al., 2010](#)), binary interactions (e.g., [Schneider et al., 2019](#); [Röpke and De Marco, 2023](#)), supernova explosions (e.g., [Mösta et al., 2014](#); [Müller, 2024](#); [Morán-Fraile et al., 2024](#)), and outer layers of stars (e.g., [Freytag et al., 2012](#); [Feng et al., 2021](#)). In contrast to such astrophysical environments, the flows in the deep interior of stars have characteristic speeds  $u$  that are much lower than the speed of sound  $a$ , i.e., they are highly subsonic. Their typical Mach number ( $\mathcal{M} := u/a$ ) ranges between  $10^{-4}$  and 0.1 (e.g., [Kupka and Muthsam, 2017](#); [Jermyn et al., 2022](#)). Most Godunov-type, shock-capturing methods for MHD are optimized for the treatment of supersonic flows ( $\mathcal{M} \gtrsim 1$ ) and face several numerical challenges when modeling low-Mach-number flows. These challenges are briefly summarized in the following sections.

#### 1.2.1.1 Strict constraint on the time step

First, shock-capturing MHD schemes based on time-explicit discretizations can retain numerical stability only if the time step used for the numerical integration satisfies the Courant-Friedrichs-Lewy (CFL) condition ([Courant et al., 1928](#)). This condition states that the fastest wave generated in the system cannot cross more than one cell per time step. For MHD, the fastest signals are the fast-magnetosonic waves (see [Chapter 2](#)), whose speed is orders of magnitude higher than that of the fluid in highly subsonic flow regimes. Because in stellar interiors these fast waves carry very little energy as



compared to convective motions<sup>3</sup>, they play a marginal role in shaping the dynamics of stellar flows. Still, fast-magnetosonic waves impose an overly strict constraint on the time step when simulating low-Mach flows, so that they become parasitic in the simulations (Dumbser et al., 2019). Simply advecting the convective flows by a single cell on the computational grid would require an enormous number of integration steps, making the simulation exceedingly expensive.

### 1.2.1.2 Large numerical dissipation

Second, conventional MHD schemes introduce an excessive amount of numerical dissipation when modeling slow flows (Minoshima and Miyoshi, 2021). The reason for this flawed behavior is that Godunov-type schemes always introduce discontinuities in the MHD variables at every grid cell boundary by construction. While such a representation for the numerical solution is suitable for supersonic flows and shocks, which are naturally discontinuous, it gives rise to artificial nonlinear waves when the flow is highly subsonic. These waves are dissipated within the sound crossing time scale over the grid cell, which in the long run converts a large fraction of the kinetic energy content of the flow into internal energy of the gas. Although increasing the grid resolution helps reduce the size of the discontinuities at grid cell boundaries and the effects of the artificial waves, this approach can be particularly expensive for grid-based MHD simulations<sup>4</sup>.

By evaluating the Rankine–Hugoniot jump conditions across the nonlinear, fast-magnetosonic waves arising from the Riemann discontinuity (see Chapter 2), one can compute the value of the gas pressure fluctuation  $\delta p = p - p_0$  around the mean state  $p_0$  at the grid cell interface. In the limit  $\mathcal{M} \rightarrow 0$ , the solution to the Riemann problem for the gas pressure fluctuation is

$$\delta p \approx \frac{1}{2}(\delta p_L + \delta p_R) - \frac{\bar{\rho} \bar{a}}{2}(V_{n,R} - V_{n,L}), \quad (1.1)$$

where  $\bar{\rho}$  and  $\bar{a}$  are appropriate averages of the left and right Riemann states of the gas density and sound speed, respectively. The  $V_{n,L,R}$  are the left (L) and right (R) Riemann states in the component of the velocity vector normal to the grid cell boundary. Equation (1.1) is inconsistent with the solution to the MHD equations in the asymptotic limit  $\mathcal{M} \rightarrow 0$ , where the flow approaches the incompressible regime (Matthaeus and Brown, 1988) and

$$\delta p = \mathcal{O}(\mathcal{M}^2). \quad (1.2)$$

In fact, while the physical term  $(\delta p_L + \delta p_R)/2$  in Eq. (1.1) has the correct Mach number scaling,

$$\frac{1}{2}(\delta p_L + \delta p_R) = \mathcal{O}(\mathcal{M}^2), \quad (1.3)$$

the upwind dissipative term, which is crucial to retain numerical stability, is

$$-\frac{\bar{\rho} \bar{a}}{2}(V_{n,R} - V_{n,L}) = \mathcal{O}(\mathcal{M}), \quad (1.4)$$

---

<sup>3</sup>The ratio of the acoustic energy flux  $P_{ac}$  radiated by a turbulent flow to the turbulent kinetic energy flux is  $P_{ac}/\rho u^3 \approx \mathcal{M}^5$ , where  $\rho$  is the density of the gas,  $u$  is the mean velocity of the flow, and  $\mathcal{M}$  is the turbulent Mach number (e.g., Lighthill, 1952). Therefore, the energy transported by acoustic waves is negligibly small compared to the kinetic energy content of the flow in subsonic velocity regimes.

<sup>4</sup>The complexity of a 3D, Godunov-type algorithm for MHD is  $\mathcal{O}(N^4)$ , where  $N$  is the number of grid cells given along a certain spatial axis. Therefore, doubling the grid resolution in each spatial dimension makes the numerical simulation 16 times more expensive.

so that it eventually overwhelms the physical flux at low Mach numbers.

### 1.2.1.3 Spurious flows from unbalanced stratifications

Lastly, standard Godunov-type schemes for MHD cannot preserve hydrostatic solutions owing to the different ways pressure gradients and gravitational forces are discretized on the computational grid (e.g., Käppeli, 2022). Such discretization errors affect the evolution of stellar flows, which can be viewed as small disturbances of the mean hydrostatic stellar stratification. If the Mach number of the flow is very low or if the medium is strongly stratified (i.e., the grid spans several pressure scale heights), the spurious flows arising from an unbalanced background stratification can even dominate the dynamics of the simulated system, leading to unreliable results (Edelmann et al., 2021).

## 1.2.2 Existing approaches to model stellar MHD flows

The dynamical conditions found in the deep interior of stars are extremely challenging to tackle with fully compressible MHD codes. To circumvent such numerical difficulties, three fundamentally different approaches have been proposed so far in the literature that allow MHD processes in stellar interiors to be modeled with a certain degree of accuracy.

### 1.2.2.1 The anelastic approximation

One of these approaches consists in filtering out the fast-magnetosonic waves to overcome the strict CFL stability criterion on the time step, which is then determined only by the much slower Alfvén and entropy waves. In order to discard the fast-magnetosonic waves from the numerical solution, the original set of partial differential equations is often modified in the anelastic approximation (e.g., Glatzmaier, 1984; Lantz and Fan, 1999). In this approximation, the gas pressure is not given by the equation of state of the stellar plasma, but rather its value is constrained by the velocity field (similar to the incompressible limit of the fluid-dynamic equations) and the mean density stratification. This constraint leads to an elliptic equation that can be solved efficiently with spectral or multigrid-based methods. After computing the distribution of the gas pressure on the computational grid, the other MHD quantities are advanced over the Alfvén or advective time step using simple time-explicit marching schemes. Anelastic codes have been used quite extensively to study the solar dynamo (e.g., Brun et al., 2004; Ghizaru et al., 2010; Cameron et al., 2017) and other turbulent dynamo mechanisms operating in the convective cores of massive main-sequence stars (e.g., Brun et al., 2005; Augustson et al., 2016).

Despite being efficient, these codes suffer from two major shortcomings. First, they produce highly inaccurate solutions if the Mach number of the flow is higher than  $\sim 10^{-2}$ . Such velocity regimes are often found, for instance, in simulations of late burning shells of massive stars (e.g., Jones et al., 2017; Varma and Müller, 2021) or subsurface convective layers (e.g., Bhatia et al., 2022). Second, because they filter out fast-magnetosonic waves by design, anelastic codes cannot be used to simulate the excitation of compressible, pressure ( $p$ ) modes of oscillations. Such oscillation modes have been detected in many classes of stellar objects and can be used to probe the stellar stratification (Michielsen et al., 2019; Mathis et al., 2021; Aerts, 2021). Retaining

$p$ -modes in the numerical solution is therefore highly desirable because it allows us to compare simulation results to observations and better constrain the role of different wave excitation mechanisms and theories of convective boundary mixing in the stellar interior.

### 1.2.2.2 The luminosity enhancement method

The second approach retains the fully compressible nature of the original MHD equations at the cost of artificially driving convection at much higher Mach numbers ( $\mathcal{M} \approx 0.1 - 0.3$ ), where conventional MHD methods are reasonably efficient and accurate (e.g., Käpylä et al., 2023, and references therein). Faster convective flows are obtained in the numerical simulations by boosting the nuclear energy generation rate or the radiative energy flux, thereby increasing the luminosity of the star. This method has been used to study the solar dynamo (e.g., Käpylä et al., 2013; Warnecke et al., 2016) and low-mass stars (e.g., Dobler et al., 2006; Käpylä, 2021). Although fast-magnetosonic waves are part of the numerical solution in this approach, driving faster convective flows significantly increases the amplitude of fluctuations around the hydrostatic equilibrium, enhances the convective energy flux, and modifies the spectrum of internal waves.

### 1.2.2.3 The reduced speed of sound technique

The third method makes it possible to model fully compressible stellar MHD flows at their nominal speeds by artificially reducing the speed of sound (or the fast-magnetosonic speed) to diminish the gap between the acoustic and advective time scales. This so-called “reduced speed of sound technique” (RSST, Rempel, 2005; Hotta et al., 2012; Iijima et al., 2019) has mostly been used to study turbulent dynamos in the solar convection zone (Hotta et al., 2015; Hotta, 2017). Although RSST can efficiently model convection and internal gravity waves without increasing the luminosity of the star, it greatly overestimates the effects of fluid compressibility by construction. Highly compressible flows can significantly alter the mixing processes that occur at stiff convective boundaries and the mechanisms of magnetic field generation.

## 1.3 Goal of the thesis: developing a fully compressible MHD solver for low-Mach-number stellar flows

All of the numerical approaches used to date to model MHD processes in the interior of stars suffer from serious shortcomings that severely limit their applicability. Due to the complex nature of the numerical problem, no Godunov-type scheme capable of modeling fully compressible stellar MHD flows at low Mach numbers has yet been presented in the literature. The goal of this thesis is to fill this gap and provide a reliable method that is both accurate and efficient for such flows. The new numerical scheme should have good scalability properties, thus allowing it to exploit modern high-performance computing resources in unprecedented multidimensional simulations of stellar MHD.

### 1.3.1 Methodology

In order to develop an optimized numerical scheme for MHD flows in stellar interiors, the main numerical challenges listed in Sect. 1.2.1 need to be approached and solved separately.

#### 1.3.1.1 Semi-implicit time discretization

One way to relax the strict CFL criterion on the time step while preserving the fully compressible character of the MHD equations is to use time-implicit discretization techniques (e.g., [Aydemir and Barnes, 1985](#); [Chacón, 2008](#); [Lütjens and Luciani, 2010](#)). Owing to their unconditional stability, fully implicit time steppers promise to deliver a considerable performance improvement over explicit time steppers, provided that the time step is chosen to be long enough to overcome the overhead cost of the implicit solver. However, fully implicit methods for MHD require finding the roots of a large system of highly nonlinear equations, which is ill-conditioned for low-Mach-number flows<sup>5</sup> and may yield nonconverged solutions ([Dumbser et al., 2019](#); [Fambri, 2021](#)). Moreover, most of the fully implicit solvers for MHD presented in the literature have been developed to model tokamak plasmas, where the magnetic pressure is usually larger than the gas pressure ([Boyd and Sanderson, 2003](#)). In contrast to such plasma regimes, stellar interiors are weakly magnetized and equipartition is achieved only between the magnetic and kinetic energy reservoirs of the flow ([Mestel, 1999](#)). Therefore, it is generally unnecessary to treat Alfvén waves implicitly in MHD simulations of subsonic stellar flows.

In this thesis, a hybrid (semi-implicit) method is used instead. In particular, the magnetic field is marched in time by solving the induction equation with an explicit Runge–Kutta integrator, while the rest of the MHD system is solved using implicit time discretization. The advantage of the proposed approach over fully implicit methods is that the subset of equations that is solved implicitly is better conditioned than the full system of MHD equations, making the numerical solution easier to compute. The two subsets of equations are then coupled together using a staggered-in-time approach (i.e., Strang splitting, [Strang, 1968](#)) to achieve second-order temporal accuracy. Unlike fully implicit time discretization techniques, the proposed implicit-explicit Strang splitting (IESS) method is conditionally stable, but the time step is limited only by the speed of the fastest Alfvén and entropy waves on the grid. In highly subsonic flow regimes, these waves are much slower than the fast-magnetosonic waves that determine the CFL time step, so IESS is expected to be significantly more performant than conventional methods for computational MHD.

#### 1.3.1.2 Low-dissipation Riemann solvers

The second shortcoming of conventional Godunov-based methods (i.e., the large amount of numerical dissipation introduced at low Mach numbers) is addressed by a low-dissipation 5-wave Riemann solver for MHD ([Minoshima and Miyoshi, 2021](#)). This special solver corrects for the flawed Mach number scaling of the numerical

---

<sup>5</sup>The condition number of the fully compressible system of MHD equations is approximately given by the ratio of the highest fast-magnetosonic wave speed to the lowest entropy wave speed in the spatial domain of interest. Therefore, in highly subsonic flows, the condition number is typically much larger than one, i.e., the system of MHD equations is ill-conditioned.



viscosity generated by shock-capturing methods (see Eq. (1.4)), which considerably reduces the amount of spurious dissipation introduced during the evolution of the flow. We note that this low-dissipation method is optimized only for high plasma- $\beta$  environments<sup>6</sup>. The solver would still be excessively dissipative in simulations of highly magnetized plasmas at low Mach numbers. However, such regimes are far from the applications of interest of this dissertation.

### 1.3.1.3 Well balancing

The Deviation well-balancing method (Berberich et al., 2021; Edelmann et al., 2021) is used to preserve hydrostatic solutions on the computational grid and to suppress the spurious flows that arise in simulations of stratified low-Mach-number flows. The method works by splitting the MHD quantities into a time-independent, hydrostatic state and a fully nonlinear fluctuation. The MHD equations are then solved by subtracting the contribution of the equilibrium state from the spatial residuals (i.e., the difference between the discretized flux divergence and source terms). This guarantees that hydrostatic solutions are maintained even in the discrete sense except for deviations due to the finite precision of the floating-point representation. This approach is justified by the fact that, at the level of the partial differential equations, the spatial residuals associated with hydrostatic solutions are zero by definition. Therefore, the chosen numerical discretization is consistent with the model equations.

## 1.3.2 Implementation and testing

The proposed MHD scheme has been implemented into the Seven-League Hydro code (SLH, Miczek, 2013; Edelmann, 2014; Miczek et al., 2015). SLH is a finite-volume, time-implicit, Godunov-like code that was originally developed in the context of Fabian Miczek's Ph.D. thesis (Miczek, 2013) and it has since been used to study turbulent convection, mixing processes (Edelmann et al., 2017; Horst et al., 2021; Andrassy et al., 2022, 2023), and the spectrum of internal waves (Horst et al., 2020) in stellar interiors. SLH works with arbitrarily curvilinear, but logically rectangular, Eulerian grids. The code is parallelized with the message passing interface (MPI) using domain decomposition and it has been shown to scale up to several hundred thousand processes (Edelmann and Röpke, 2016). The MHD implementation uses the same parallelization strategy.

The performance and accuracy of the new MHD scheme can only be assessed through a series of verification benchmarks. Such tests should include i) a linear wave analysis to infer the actual convergence rate of the code; ii) shear instabilities, which are fundamental to trigger the energy cascade in a turbulent flow field; and iii) magnetoconvection under dynamic conditions similar to those found in the interior of stars. A detailed description of the newly developed numerical algorithm, together with results from numerical tests and a thorough analysis of the main shortcomings of conventional methods for stellar MHD is given in Sect. 3.1.

The use of a low-dissipation Riemann solver is crucial for the development of an asymptotic-preserving scheme capable of simulating highly subsonic flow regimes. However, it is unclear how the choice of the polynomial used to reconstruct the Riemann states affects the quality of the numerical solution. Simply increasing the degree

---

<sup>6</sup>In plasma physics,  $\beta$  is the ratio of gas pressure to magnetic pressure.

of the polynomial does not always lead to more accurate solutions, especially when the flow is characterized by discontinuities, large gradients, or unresolved features (e.g., [Greenough and Rider, 2003](#)). If the numerical problem admits convergent solutions, then theoretically any method should produce the same results on sufficiently fine grids. Unfortunately, this approach is not feasible for astrophysical simulations due to their high computational cost, which makes it impractical to use an excessively fine grid. Therefore, it is fundamental to determine which method achieves the lowest computational cost per fixed accuracy. The answer to this question is given in Sect. 3.2, where a comparison of different combinations of reconstruction methods and Riemann solvers is carried out with a special focus on subsonic flow regimes. To be meaningful, the chosen benchmark should be close to the application of interest. In particular, the comparison is performed over a test problem involving turbulent convection, convective boundary mixing, and internal wave excitation, all of which processes occur in the interior of stars.

### 1.3.3 An astrophysical application: simulations of turbulent dynamo action in an oxygen-burning shell

After the first phase of development, implementation, and tests, the new low-Mach MHD scheme of SLH is used for the first time to answer some specific physical questions. In particular, the second part of this thesis focuses on the study of an oxygen-burning shell in a non-rotating massive star that features turbulent dynamo action. The initial conditions of the chosen setup are taken from the work of [Andrassy et al. \(2022\)](#), who performed a comparison of five hydrodynamic codes in simulations of turbulent convection and convective boundary mixing without the inclusion of magnetic fields. Here, a weak magnetic seed field is added to the system and allowed to evolve under the influence of the convective motions occurring inside the shell.

In the absence of rotation, the magnetic field is mostly amplified at scales smaller than those at which the turbulent convective flows are driven, that is a small-scale turbulent dynamo (SSD, e.g., [Meneguzzi et al., 1981](#); [Schekochihin et al., 2004](#); [Brandenburg and Subramanian, 2005](#)). SSDs can only be excited if the magnetic Reynolds number<sup>7</sup> of the turbulent flows exceeds a certain threshold value, usually on the order of 100 (e.g., [Schober et al., 2012](#); [Warnecke et al., 2023](#)). In Godunov-like codes such as SLH, the resistivity of the plasma is not explicitly modeled, but rather some degree of numerical resistivity is introduced by the methods used to simulate the evolution of the magnetic field. Numerical methods that are too dissipative would not be able to excite the SSD or would significantly underestimate the magnetic field strength in the saturated stage of the dynamo (e.g., [Schekochihin et al., 2004](#)). By using low-dissipation solvers, SLH can successfully excite SSDs even on coarse grids. This is a significant advantage over conventional methods, which can only reduce the effects of numerical dissipation by considerably increasing the grid resolution (see Sect. 3.1 for a performance comparison between a conventional and a low-dissipation MHD Riemann solver).

The SSD can convert a significant fraction of the kinetic energy of the turbulent flows into magnetic energy, thereby influencing convective energy transport and the mixing at the boundaries of the convective oxygen shell. The efficiency of both these processes is directly proportional to the mean velocity of the convective flows. The implications of strong dynamo action within the oxygen shell for later evolutionary stages can be

---

<sup>7</sup>The magnetic Reynolds number is defined as  $Re_M := uL/\eta$ , where  $\eta$  is the magnetic diffusivity.

important. Inefficient convective boundary mixing processes would result in a lower rate of mass entrainment into the burning shell and could ultimately prevent shell mergers (e.g., Ritter et al., 2018; Mocák et al., 2018; Yadav et al., 2020; Andrassy et al., 2020). In addition, strong magnetic fields generated in the convective oxygen shell can alter the spatial structure of convective motions and the magnitude of the density fluctuations around the mean background state. The stratification of the core-collapse supernova progenitor and the dynamical conditions found in its innermost convective shells are fundamental parameters that determine the efficacy of the perturbation-aided explosion mechanism (e.g., Müller et al., 2017; Couch et al., 2020). Therefore, this work aims to answer the following questions: What is the saturation strength of the magnetic field in the oxygen shell? What is the topology of the magnetic field? How do strong fields affect the dynamics of the convective shell? The results of this study are presented in Sect. 3.3.

### 1.3.4 Thesis outline

Chapter 2 introduces the equations of stellar magnetohydrodynamics and gives a brief overview of conventional Godunov-type methods for computational MHD. Chapter 3 presents the main results of this thesis, including the development of a new MHD scheme optimized for low-Mach-number stellar flows (Sect. 3.1), the evaluation of the performance of different Godunov-type methods in simulations of subsonic flows (Sect. 3.2), and the study of turbulent dynamo action and its effects on the dynamics of an oxygen-burning shell (Sect. 3.3). A short summary and conclusions are given in Chapter 4.



# CHAPTER 2

---

## Numerical methods for stellar MHD

---

This Chapter introduces some of the most commonly used methods for simulating stellar MHD flows. It is not intended to be a comprehensive review of numerical schemes in computational MHD, which can be found elsewhere (e.g., [Tóth, 2000](#); [Bal-sara, 2004](#); [Mignone and Del Zanna, 2021](#)), but serves only to put into context the results presented in this thesis.

As discussed in Chapter 1, conventional schemes for fully compressible MHD suffer from major shortcomings when used to model flows at the dynamical conditions found in the regions deep inside stars. The wealth of methods listed in this Chapter must therefore be modified and extended in order to accurately and efficiently simulate MHD processes in stellar interiors. The development and application of a novel MHD scheme suitable for low-Mach stellar MHD flows is presented in Chapter 3.

### 2.1 The equations of stellar MHD

#### 2.1.1 Physical considerations

The plasma in stars can be described as an interacting mixture of negatively and positively charged particles, with each species behaving as a charged, ideal gas. The constituents of the stellar plasma are strongly collisionally coupled, such that as one species evolves, the other reacts instantaneously. Under these conditions, the two sets of model equations for the charged species can be reduced to a single set of fluid-dynamic equations that models the evolution of the plasma only in terms of its density, momentum, and energy.

To account for the influence of electromagnetic fields on the stellar plasma, the fluid-dynamic equations must be coupled to Maxwell's equations. Since the flows in the stellar interior are highly subluminal, Maxwell's equations can be greatly simplified. In particular, the displacement current can be excluded from Ampère's law, resulting in

$$\nabla \times \mathbf{b} = \frac{4\pi\mathbf{j}}{c}. \quad (2.1)$$

In Eq. (2.1),  $\mathbf{b} = (b_x, b_y, b_z)$  is the magnetic field,  $\mathbf{j} = (j_x, j_y, j_z)$  the electric current, and  $c$  the speed of light. Also, in the non-relativistic limit, Ohm's law is

$$\mathbf{j} = \sigma \left( \mathbf{E} + \frac{\mathbf{V}}{c} \times \mathbf{b} \right), \quad (2.2)$$

where  $\sigma$  is the electrical conductivity of the plasma,  $\mathbf{E} = (E_x, E_y, E_z)$  is the electric field, and  $\mathbf{V} = (V_x, V_y, V_z)$  is the velocity field. Equation (2.2) can be inserted into Eq. (2.1) to obtain

$$\mathbf{E} = \frac{c}{4\pi\sigma} \nabla \times \mathbf{b} - \frac{\mathbf{V}}{c} \times \mathbf{b}. \quad (2.3)$$

Then, after inserting Eq. (2.3) into Faraday's law of induction and some algebraic manipulation, one obtains the induction equation for an electrically resistive fluid,

$$\frac{\partial \mathbf{b}}{\partial t} = \eta \nabla^2 \mathbf{b} + \nabla \times (\mathbf{V} \times \mathbf{b}), \quad (2.4)$$

where

$$\eta = \frac{c^2}{4\pi\sigma} \quad (2.5)$$

is the magnetic diffusivity.

The ratio of induction to magnetic diffusion,

$$\frac{|\nabla \times (\mathbf{V} \times \mathbf{b})|}{|\eta \nabla^2 \mathbf{b}|} \approx \frac{Lu}{\eta}, \quad (2.6)$$

is very high in stellar interiors. In fact, the right-hand side of Eq. (2.6) is the magnetic Reynolds number, which in stars is typically higher than  $10^6$  (e.g., [Spruit, 2013](#); [Jermyn et al., 2022](#)). Thus, the stellar plasma can be assumed to be a perfect conductor to a very good approximation.

The magnetic field exerts the Lorentz force on the fluid,

$$\mathbf{f}_L = \frac{1}{4\pi} (\nabla \times \mathbf{b}) \times \mathbf{b}, \quad (2.7)$$

which does work on the system according to

$$W_L = -\nabla \cdot \left[ \frac{1}{8\pi} |\mathbf{b}|^2 \mathbf{V} - \frac{1}{4\pi} \mathbf{b} (\mathbf{b} \cdot \mathbf{V}) \right]. \quad (2.8)$$

Equations (2.7) and (2.8) must be supplemented in the equations modeling the evolution of the the momentum and energy density of the fluid, respectively.

Additionally, that effects of viscosity can be neglected on the typical spatial scales of convection in the stellar interior. This statement becomes clear after estimating the ratio of advective to viscous forces,

$$\frac{|\nabla(\rho \mathbf{V} \otimes \mathbf{V})|}{|\rho \nu \nabla^2 \mathbf{V}|} \approx \frac{Lu}{\nu}, \quad (2.9)$$

for typical values of the kinematic viscosity  $\nu$  of the stellar plasma and the length scale  $L$  and velocity  $u$  of the convective flows. Here,  $\rho$  denotes the gas density. The right-hand side of Eq. (2.9) is the fluid Reynolds number, which in the interior of stars is usually much higher than  $10^{10}$  (e.g., [Kupka and Muthsam, 2017](#); [Jermyn et al., 2022](#); [Lecoanet and Edelmann, 2023](#)).

### 2.1.2 The model equations

In the limit of zero viscosity and electrical resistance, the dynamical evolution of the flows and the magnetic field in the interior of stars is described by the equations of ideal MHD, together with the advection of chemical species and source terms such as gravity, radiative diffusion, and energy generation. In conservation form, these

equations read<sup>1</sup> (e.g., Mestel, 1999)

$$\frac{\partial \rho}{\partial t} + \nabla \cdot (\rho \mathbf{V}) = 0, \quad (2.10)$$

$$\frac{\partial(\rho \mathbf{V})}{\partial t} + \nabla \cdot [\rho \mathbf{V} \otimes \mathbf{V} + (p + p_B)\mathbb{I} - \mathbf{B} \otimes \mathbf{B}] = \rho \mathbf{g}, \quad (2.11)$$

$$\frac{\partial(\rho e)}{\partial t} + \nabla \cdot [(\rho e + p + p_B)\mathbf{V} - \mathbf{B}(\mathbf{B} \cdot \mathbf{V})] = \rho \mathbf{g} \cdot \mathbf{V} + \nabla \cdot (K \nabla T) + \rho \dot{e}, \quad (2.12)$$

$$\frac{\partial \mathbf{B}}{\partial t} + \nabla \cdot (\mathbf{V} \otimes \mathbf{B} - \mathbf{B} \otimes \mathbf{V}) = \mathbf{0}, \quad (2.13)$$

$$\frac{\partial(\rho X_l)}{\partial t} + \nabla \cdot (\rho X_l \mathbf{V}) = \rho \dot{X}_l. \quad (2.14)$$

Here,  $p_B = |\mathbf{B}|^2/2$  denotes the magnetic pressure,  $\mathbb{I}$  the unit tensor,  $\otimes$  the tensor product,  $\mathbf{g} = (g_x, g_y, g_z)$  the gravitational field,  $e$  the specific energy of the gas, and  $X_l$  the mass fractional abundance of the species  $l$ . The system in Eqs. (2.10)–(2.14) is closed by an equation of state (EoS), which gives the gas pressure ( $p$ ) and temperature ( $T$ ) as a function of density ( $\rho$ ), internal energy ( $e_{\text{int}}$ ), and composition,

$$p = p(\rho, e_{\text{int}}, \{X_l\}), \quad (2.15)$$

$$T = T(\rho, e_{\text{int}}, \{X_l\}), \quad (2.16)$$

where

$$e_{\text{int}} = e - \frac{1}{2}|\mathbf{V}|^2 - \frac{1}{2\rho}|\mathbf{B}|^2. \quad (2.17)$$

Furthermore, Eqs. (2.10)–(2.14) must be provided with the thermal conductivity of the gas ( $K$ ), the production rate of the species  $l$  ( $\dot{X}_l$ ), and the rate of energy generation per unit mass ( $\dot{e}$ ),

$$K = K(\rho, e_{\text{int}}, \{X_l\}), \quad (2.18)$$

$$\dot{X}_l = \dot{X}_l(\rho, e_{\text{int}}, \{X_l\}), \quad (2.19)$$

$$\dot{e} = \dot{e}(\rho, e_{\text{int}}, \{X_l\}). \quad (2.20)$$

Equations (2.10)–(2.14) can be cast into a system of conservation laws,

$$\frac{\partial \mathbf{U}}{\partial t} + \nabla \cdot \mathbf{F}(\mathbf{U}) = \mathbf{S}(\mathbf{U}), \quad (2.21)$$

where  $\mathbf{U} = (\rho, \rho \mathbf{V}, \rho e, \mathbf{B}, \rho X_l)$  is the set of conservative variables,  $\mathbf{F}$  is the tensor of MHD fluxes, and  $\mathbf{S}$  is a source term.

### 2.1.3 Linear MHD waves

In the absence of gravity and other source terms, an ideal MHD flow supports 4 types of linear waves: fast- and slow-magnetosonic, Alfvén, and entropy waves. Their wave speeds,  $\lambda_v$ , correspond to the eigenvalues of the flux-Jacobian  $\mathbf{A}_x$  in the following 1D, quasi-linear form of the homogeneous MHD system (left-hand side of Eqs. (2.10)–(2.13)),

$$\frac{\partial \mathbf{U}}{\partial t} + \mathbf{A}_x(\mathbf{U}) \frac{\partial \mathbf{U}}{\partial x} = \mathbf{0}, \quad (2.22)$$

<sup>1</sup>Here, the Lorentz-Heaviside units are used, i.e.,  $\mathbf{B} = \mathbf{b}/\sqrt{4\pi}$ .

where

$$\mathbf{A}_x(\mathbf{U}) = \frac{\partial \mathbf{F}_x(\mathbf{U})}{\partial \mathbf{U}} \quad (2.23)$$

and

$$\mathbf{F}_x(\mathbf{U}) = (1, 0, 0) \cdot \mathbf{F}(\mathbf{U}). \quad (2.24)$$

The eigenstructure of  $\mathbf{A}_x$  comprises 7 waves: two fast-magnetosonic waves,

$$\lambda_{1,7} = V_x \mp c_{f,x}, \quad (2.25)$$

two Alfvén waves,

$$\lambda_{2,6} = V_x \mp c_{a,x}, \quad (2.26)$$

two slow-magnetosonic waves,

$$\lambda_{3,5} = V_x \mp c_{s,x}, \quad (2.27)$$

and one entropy wave,

$$\lambda_4 = V_x. \quad (2.28)$$

The complete set of MHD waves is ordered as

$$\lambda_1 \leq \lambda_2 \leq \lambda_3 \leq \lambda_4 \leq \lambda_5 \leq \lambda_6 \leq \lambda_7, \quad (2.29)$$

where

$$c_{f,s,x} = \left[ \frac{1}{2} \left( a^2 + \frac{|\mathbf{B}|^2}{\rho} \pm \sqrt{\left( a^2 + \frac{|\mathbf{B}|^2}{\rho} \right)^2 - 4a^2 c_{a,x}^2} \right) \right]^{\frac{1}{2}} \quad (2.30)$$

are the fast- and slow-magnetosonic speeds,

$$c_{a,x} = |B_x| / \sqrt{\rho} \quad (2.31)$$

is the Alfvén speed, and

$$a = \left( \frac{\partial p}{\partial \rho} + \frac{p}{\rho^2} \frac{\partial p}{\partial e_{\text{int}}} \right)^{\frac{1}{2}} \quad (2.32)$$

is the adiabatic sound speed.

The fast- and slow-magnetosonic waves are compressible modes of propagation, in which oscillations in the gas pressure and the magnetic field are in phase and anti-phase, respectively. Alfvén waves, on the other hand, are incompressible and transport only perturbations in the components of the velocity and the magnetic field transverse to the wave vector. The entropy wave is advected with the fluid and carries density and entropy perturbations. The knowledge of the wave-structure arising from Eq. (2.22) is crucial in building accurate numerical methods for MHD with proper up-winding to ensure numerical stability (see Sect. 2.3.2).

The system of ideal MHD equations is hyperbolic, meaning  $\mathbf{A}_x$  has a complete set of linearly independent eigenvectors and the corresponding eigenvalues are all real. However, unlike the system of fluid-dynamic equations, the MHD system is not strictly hyperbolic because the eigenvalues are not all distinct under all circumstances (see Eq. (2.29)). Wave degeneracy occurs, e.g., when  $B_x = 0$ , in which case the slow-magnetosonic and Alfvén waves collapse onto the entropy wave, or when  $|B_x| / \sqrt{\rho} > a$  and  $B_y = B_z = 0$ , in which case the Alfvén waves collapse onto the fast-magnetosonic



waves. Other degenerate cases can also occur (e.g., Mestel, 1999). In the nonlinear regime of the MHD equations, the loss of strict hyperbolicity at one point does not guarantee the uniqueness of the solution, can lead to compound solutions where shocks and rarefaction waves travel together, and gives rise to other non-regular waves that may be unphysical (e.g., Torrilhon and Balsara, 2004). Fortunately, wave degeneracy is unlikely to occur under the dynamic conditions found in stellar interiors. In fact, the sonic Mach number inside stars is very low and the Alfvén Mach number

$$\mathcal{M}_{\text{Alf}} = \sqrt{\rho} \frac{|\mathbf{V}|}{|\mathbf{B}|} \quad (2.33)$$

is usually on the order of unity, so the MHD wave speeds are well separated. Moreover, the only weak (i.e., discontinuous) solutions to the MHD equations that may characterize stellar interiors are in the form of genuinely linear waves (e.g., contact or rotational discontinuities), which are physical and easy to treat numerically.

## 2.2 Finite volume discretization

The finite-volume method is a powerful tool for finding numerical solutions to Eq. (2.21). This approach divides the spatial domain of interest into a number of grid cells (finite volumes) and performs time updates on cell-volume averages rather than on point values. Each cell in the computational grid is denoted by a set of indices such as  $\{i, j, k\}$ , which is also associated with any quantity located at the center of the cell. Quantities located at cell boundaries are denoted by half-integers, e.g.,  $\{i + 1/2, j, k\}$ , which represents the interface between cell  $\{i, j, k\}$  and cell  $\{i + 1, j, k\}$ . The model equation for the cell-volume averages in cell  $\{i, j, k\}$  is derived by integrating Eq. (2.21) over the volume of cell  $V_{i,j,k}$ ,

$$V_{i,j,k} \left( \frac{\partial \mathbf{u}_{i,j,k}}{\partial t} \right) + \sum_s \mathcal{F}_s \cdot \hat{\xi}_s A_s = V_{i,j,k} \mathcal{S}_{i,j,k}. \quad (2.34)$$

Here,  $\mathbf{u}_{i,j,k}$  denotes the cell-volume averaged vector of conservative quantities,

$$\mathbf{u}_{i,j,k} = \frac{1}{V_{i,j,k}} \int_{V_{i,j,k}} \mathbf{U} \, dV, \quad (2.35)$$

$\mathcal{F}_s$  the surface-averaged fluxes across the cell boundary  $s$ ,

$$\mathcal{F}_s = \frac{1}{A_s} \int_{A_s} \mathbf{F} \, dA, \quad (2.36)$$

$\hat{\xi}_s$  the outward normal vector to the surface  $A_s$ , and  $\mathcal{S}_{i,j,k}$  the cell-volume averaged source term,

$$\mathcal{S}_{i,j,k} = \frac{1}{V_{i,j,k}} \int_{V_{i,j,k}} \mathbf{S} \, dV. \quad (2.37)$$

If the values of the cell-volume averaged conservative quantities are known at the initial time  $t = 0$ , the solution to Eq. (2.34) at an arbitrary time  $t$  is then given by

$$\mathbf{u}_{i,j,k}(t) = \mathbf{u}_{i,j,k}(0) - \int_0^t \left( \frac{1}{V_{i,j,k}} \sum_s \mathcal{F}_s(t) \cdot \hat{\xi}_s A_s - \mathcal{S}_{i,j,k}(t) \right) dt. \quad (2.38)$$

Usually, it is not possible to find analytic solutions to the system of stellar MHD equations. Therefore, Eq. (2.38) must be discretized both in space and time to approximate the solution numerically. If suitable discretizations of  $\mathcal{F}_s(t)$  and  $\mathcal{S}_{i,j,k}(t)$  are provided,

$$\mathcal{F}_s(t) \approx \tilde{\mathcal{F}}_s, \quad (2.39)$$

$$\mathcal{S}_{i,j,k}(t) \approx \tilde{\mathcal{S}}_{i,j,k}, \quad (2.40)$$

the cell-volume averaged conservative quantities can be updated from time  $t^n$  to time  $t^{n+1} = t^n + \Delta t$  using a simple, first-order accurate Forward Euler method,

$$\mathbf{u}_{i,j,k}^{n+1} = \mathbf{u}_{i,j,k}^n - \left( \frac{1}{V_{i,j,k}} \sum_s \tilde{\mathcal{F}}_s^n \cdot \hat{\xi}_s A_s - \tilde{\mathcal{S}}_{i,j,k}^n \right) \Delta t, \quad (2.41)$$

or higher-order time integration methods (see Sect. 2.3.3). For the numerical scheme to be stable, the time step  $\Delta t$  must satisfy the Courant-Friedrichs-Lewy (CFL) condition (Courant et al., 1928). On a uniform Cartesian grid, the CFL condition is formulated as

$$\Delta t \leq C \min_{i,j,k,d} \left[ \frac{\Delta x}{|V_d|_{i,j,k} + c_{f,d,i,j,k}} \right], \quad (2.42)$$

where  $\Delta x$  is the width of the grid cell,  $d$  represents the three spatial directions, and  $C$  is a parameter whose value depends on the time integration method, typically of the order of unity.

The advantage of the finite-volume method over other discretization techniques (e.g., finite differences) is that it preserves the conservation properties of Eq. (2.21). Therefore, for an isolated system in the absence of source terms, this method allows the total mass, momentum, energy, and magnetic field to be conserved at the level of machine precision. Since the finite-volume method is conservative by construction, the Lax-Wendroff theorem (Lax and Wendroff, 1960) guarantees that if the scheme is numerically stable, the numerical solution will converge to a weak solution of Eq. (2.34). This property is crucial in simulations of supersonic flows, as it ensures that shock fronts are propagated at the correct speed. In subsonic flow regimes, it ensures accurate treatment of contact and rotational discontinuities.

In order to advance the numerical solution over time, it is necessary to first compute the discretized source terms and fluxes in Eq. (2.41). To second-order approximation, the cell-volume averaged source terms can simply be estimated from cell-centered point values as

$$\mathcal{S}_{i,j,k}(t^n) \approx \tilde{\mathcal{S}}_{i,j,k}^n = \mathbf{S}_{i,j,k}^n + \mathcal{O}(\Delta x^2). \quad (2.43)$$

Although it may be tempting to compute the surface-averaged fluxes  $\tilde{\mathcal{F}}_s^n$  by interpolating corresponding cell-centered values to the cell boundary  $s$ , this approach lacks proper upwinding and is known to generate numerically unstable solutions (e.g., LeVeque, 2002).

## 2.2.1 The Godunov algorithm

A better flux discretization is provided by the Godunov algorithm (Godunov, 1959). In this method, the time update from  $t^n$  to  $t^{n+1} = t^n + \Delta t$  is performed in four successive steps:

1. The time step  $\Delta t$  is computed using Eq. (2.42).
2. A pair of Riemann states  $U_{s,L,R}^n$  is reconstructed at each grid cell boundary through 1D sweeps by assuming that the distribution of the conservative quantities is piecewise constant across the grid. For example, at the interface  $s = \{i + 1/2, j, k\}$ , the Riemann states are given by

$$U_{i+1/2,j,k,L}^n = \mathbf{U}_{i,j,k}^n \quad (2.44)$$

$$U_{i+1/2,j,k,R}^n = \mathbf{U}_{i+1,j,k}^n. \quad (2.45)$$

At domain boundaries, a layer of “ghost cells” is utilized to obtain a pair of Riemann states at the outermost grid cell interfaces and to enforce boundary conditions.

3. The Riemann states  $U_{i+1/2,j,k,L,R}^n$  define the following 1D Riemann problem of ideal MHD (see, e.g., Toro, 2009),

$$\frac{\partial \mathbf{U}}{\partial t} + \frac{\partial \mathbf{F}_x(\mathbf{U})}{\partial x} = \mathbf{0}, \quad (2.46)$$

$$\mathbf{U}(x, t_n) = \begin{cases} \mathbf{U}_{i+1/2,j,k,L}^n & x < x_{i+1/2,j,k} \\ \mathbf{U}_{i+1/2,j,k,R}^n & x > x_{i+1/2,j,k} \end{cases} \quad (2.47)$$

After finding the solution to the Riemann problem,  $U^*(x, t)$ , the discretized surface-averaged fluxes are computed as

$$\tilde{\mathcal{F}}_{i+1/2,j,k}^n = \mathbf{F}_x(U^*(x_{i+1/2,j,k}, t^n)). \quad (2.48)$$

This operation is performed at every cell boundary on the grid.

4. The newly computed fluxes, together with discretized cell-volume averaged source terms, are used to update the cell-volume averaged conservative quantities according to Eq. (2.41).

These steps are repeated until the desired maximum time is reached. The solution to the Riemann problem defined by Eqs. (2.46) and (2.47) is computed by taking into account the wave structure resulting from the initial Riemann discontinuity (see Fig. 2.1). Therefore, the numerical solution is naturally upwind, allowing the numerical scheme to remain stable.

Despite its robustness and stability properties, the original method of Godunov (1959) has two major shortcomings. First, the assumption that the conservative quantities are distributed on the grid according to piecewise constant functions leads to a poor, first-order accurate estimation of the surface-averaged fluxes<sup>2</sup>,

$$\mathcal{F}_s(t^n) = \tilde{\mathcal{F}}_s^n + \mathcal{O}(\Delta x). \quad (2.49)$$

<sup>2</sup> This result follows from i) the assumption that the distribution of the conservative quantities is constant in space within the grid cells; ii) the consistency property of the numerical flux, i.e.,  $\tilde{\mathcal{F}}_s(\bar{\mathbf{U}}, \bar{\mathbf{U}}) = \mathcal{F}_s(\bar{\mathbf{U}})$ ; and iii) the Lipschitz continuity property of the numerical flux. The last two properties are fundamental to guarantee convergence of the numerical scheme. Thus, in the limit  $\mathbf{U}_i, \mathbf{U}_{i+1} \rightarrow \bar{\mathbf{U}}$ , there exists a constant  $C$  so that  $|\tilde{\mathcal{F}}_{i+1/2}(\mathbf{U}_i, \mathbf{U}_{i+1}) - \mathcal{F}_{i+1/2}(\bar{\mathbf{U}})| \leq C \max(|\mathbf{U}_i - \bar{\mathbf{U}}|, |\mathbf{U}_{i+1} - \bar{\mathbf{U}}|)$  (see also LeVeque, 2002). Because  $\max(|\mathbf{U}_i - \bar{\mathbf{U}}|, |\mathbf{U}_{i+1} - \bar{\mathbf{U}}|) = \mathcal{O}(\Delta x)$ , then  $\mathcal{F}_{i+1/2} = \tilde{\mathcal{F}}_{i+1/2}(\mathbf{U}_i, \mathbf{U}_{i+1}) + \mathcal{O}(\Delta x)$ .

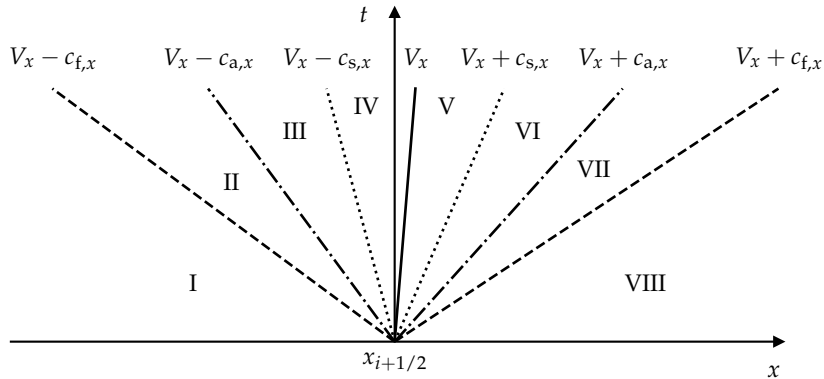


Figure 2.1: Space-time structure of a 1D Riemann problem of MHD. The Riemann fan is comprised of 8 states separated by 7 waves: two fast-magnetosonic waves ( $V_x \pm c_{f,x}$ , dashed lines), two Alfvén waves ( $V_x \pm c_{a,x}$ , dashed-dotted lines), two slow-magnetosonic waves ( $V_x \pm c_{s,x}$ , dotted lines), and one entropy wave ( $V_x$ , solid line).

Thus, numerical solutions computed with the Godunov algorithm tend to be much more dissipative than those produced by second-order accurate methods such as Lax-Wendroff or MacCormack (e.g., [LeVeque, 2007](#)). Second, solving a Riemann problem of MHD exactly requires finding the roots of a highly nonlinear equation, which is typically accomplished using iterative methods such as Raphson–Newton (e.g., [Takahashi et al., 2014](#)). The solution to the nonlinear equation can only be computed at the level of machine accuracy by performing multiple iterations within the root-finding algorithm. This operation can be relatively expensive, especially if a tabulated EoS has to be evaluated in each iteration. Since the Riemann problem must be solved at each grid cell boundary on the computational grid, using an exact Riemann solver can make the computational cost of the simulation excessively high.

### 2.3 Higher-order Godunov methods for MHD

Numerous attempts have been made to improve both the accuracy and the performance of the original algorithm of [Godunov \(1959\)](#) for solving the system of ideal MHD equations. These attempts led to the development of high-resolution shock-capturing methods (e.g., [Brio and Wu, 1988](#); [Powell, 1994](#); [Dai and Woodward, 1998](#); [Balsara, 2004](#); [Fromang et al., 2006](#); [Stone and Gardiner, 2009](#)), which are now routinely used in simulations of astrophysical magnetized flows. These methods are based on higher-order extensions of the Godunov algorithm. Their peculiarity is that they achieve at least second-order accuracy in smooth regions of the flow while at the same time they are able to robustly capture discontinuous solutions without sacrificing stability. These properties result from suitable modifications of the main steps of the Godunov algorithm, i.e., the spatial reconstruction procedure, the solution strategy of the Riemann problem, and the time integration method. Such modifications are discussed in the following sections. For the sake of simplicity, it is assumed that the MHD equations are solved on a 1D, uniform, Cartesian grid.

### 2.3.1 Higher-order spatial reconstruction methods

To achieve higher-order spatial accuracy in the numerical solution, one can represent the distribution of the MHD variables within each grid cell using higher-order polynomials. The price to pay for this increased accuracy is that the reconstruction stencil is now wider than a single cell. In fact, the coefficients of the polynomial expressions can only be determined if information about the values of the MHD variables in neighboring cells is provided. The more accurate the method the wider the stencil must be. Second-order spatial accuracy is achieved for smooth solutions by means of piecewise first-order polynomials, i.e., straight lines,

$$U_i(x; x_i) = a_i + b_i(x - x_i) + \mathcal{O}(\Delta x^2), \quad (2.50)$$

where  $U_i$  is the variable being reconstructed inside cell  $i$ . From the constraint

$$\frac{1}{\Delta x} \int_{x_i - \Delta x/2}^{x_i + \Delta x/2} U_i(x; x_i) dx = \mathcal{U}_i, \quad (2.51)$$

follows  $a_i = \mathcal{U}_i$ , while the slope  $b_i$  can be estimated using, e.g., the Fromm method,

$$b_i = \frac{\mathcal{U}_{i+1} - \mathcal{U}_{i-1}}{2\Delta x}. \quad (2.52)$$

which requires a stencil that is three-cell wide,  $\{i-1, i, i+1\}$ . However, other choices for approximating  $b$  are possible (e.g., [LeVeque, 2002](#)). The Riemann states at the sides of the cell  $i$  are then reconstructed as

$$U_{i+1/2,L} = U_i(x_i + \Delta x/2; x_i) = a_i + b_i \frac{\Delta x}{2}, \quad (2.53)$$

$$U_{i-1/2,R} = U_i(x_i - \Delta x/2; x_i) = a_i - b_i \frac{\Delta x}{2}. \quad (2.54)$$

Analogous formulas can be derived for third- or even higher-order polynomials (e.g., [Toro, 2009](#), and Sect. 3.2).

Despite their high accuracy in representing smooth solutions, higher-order reconstruction polynomials suffer from a serious flaw. According to Godunov's theorem ([Godunov, 1959](#)), linear methods (i.e., those in which the value of the reconstructed state depends linearly on the quantities across the reconstruction stencil) that are more accurate than first-order cannot be monotonicity preserving. Therefore, the simple use of higher order polynomials in Godunov-type schemes leads to spurious oscillations in the MHD quantities in the vicinity of large gradients or discontinuities. Strong undershoots generated at shock fronts are particularly disastrous, as they can lead to unphysical negative densities and pressures and cause severe stability problems. In simulations of subsonic flows, which are free of strongly nonlinear waves, these oscillations generate unphysical mass fractional abundances and alter the properties of material and rotational discontinuities.

For higher-order reconstruction methods to be monotonicity preserving, they must be nonlinear. Nonlinear reconstruction can be achieved by means of slope limiters, such as the one proposed by [van Leer \(1974\)](#). The van-Leer reconstruction method computes the slope  $b_i$  used in Eqs. (2.53) and (2.54) according to

$$b_i = \begin{cases} \frac{2\delta_{i-1/2}\delta_{i+1/2}}{\delta_{i-1/2} + \delta_{i+1/2}} & \text{if } \delta_{i-1/2}\delta_{i+1/2} > 0, \\ 0 & \text{otherwise,} \end{cases} \quad (2.55)$$

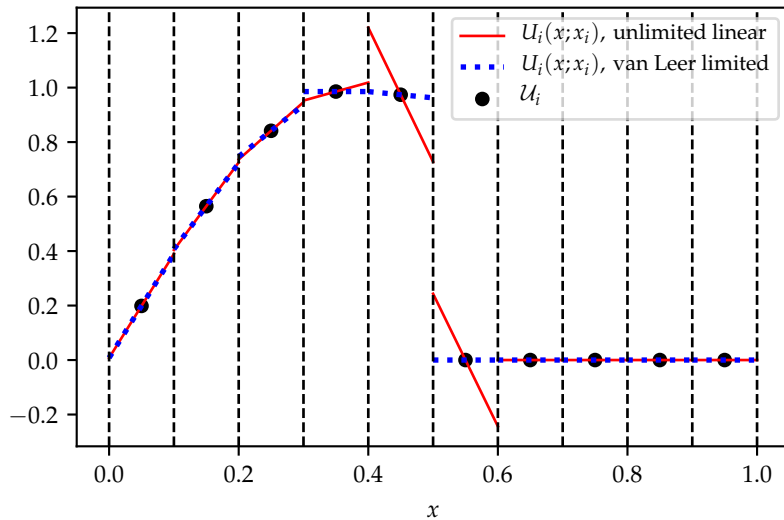


Figure 2.2: Cell-volume averaged values,  $\mathcal{U}_i$ , and their piecewise-linear reconstruction,  $U_i(x; x_i)$ , obtained using an unlimited linear reconstruction method (red solid line) and the van-Leer slope limiter (blue dotted line). The vertical dashed lines represent the boundaries of the cells. Here, the cell-volume averages are given by a sinusoidal function truncated at  $x = 0.5$ . Although the two methods reconstruct smooth solutions in a similar way, the unlimited reconstruction method introduces large undershoots and overshoots near the discontinuity, which are absent when using the slope limiter.

where

$$\delta_{i-1/2} = \frac{\mathcal{U}_i - \mathcal{U}_{i-1}}{\Delta x}, \quad (2.56)$$

$$\delta_{i+1/2} = \frac{\mathcal{U}_{i+1} - \mathcal{U}_i}{\Delta x}. \quad (2.57)$$

are second-order accurate, interface-centered slopes. This method is total-variation-diminishing (TVD), which implies that it is monotonicity-preserving (e.g. [LeVeque, 2002](#)). It is second-order accurate for smooth flows and avoids oscillations by reducing or flattening the slope  $b_i$  near large gradients or discontinuities. The result of using a slope limiter versus an unlimited method in the reconstruction of the Riemann states in a problem characterized by a discontinuous solution is shown in [Fig. 2.2](#).

Other TVD methods are, e.g., the minmod, superbee, and monotized central limiters (see [LeVeque, 2002](#), for an overview of slope limiters). Higher than second-order, nonlinear (limited) reconstruction schemes have also been presented in the literature, such as the piecewise-parabolic-method (PPM) of [Colella and Woodward \(1984\)](#), an extension of PPM that preserves extrema ([Colella and Sekora, 2008](#)), essentially nonoscillatory (ENO), or weighted-ENO (WENO) schemes (e.g., [Liu et al., 1994](#); [Jiang and Shu, 1996](#); [Shu, 2009](#)).

### 2.3.2 Approximate Riemann solvers

Computing the exact solution to the Riemann problem of MHD can be particularly expensive. In most applications, it is sufficient to use approximate Riemann solvers that can roughly capture the main properties of the solution without having to use an iterative method. Although this approach may sound very crude, the discretization errors resulting from the reconstruction of the Riemann states at the grid cell interfaces are often larger than the errors made in approximating the solution of the Riemann problem. Nevertheless, some approximate Riemann solvers may be better suited than others for accurately modeling the physical properties of the flow in question.

The simplest method is the Rusanov flux function (Rusanov, 1962, also known as the “local Lax-Friedrichs solver”), which estimates the flux at the cell interface as

$$\tilde{\mathcal{F}}(\mathbf{U}_L, \mathbf{U}_R) = \frac{1}{2} [\mathbf{F}_x(\mathbf{U}_L) + \mathbf{F}_x(\mathbf{U}_R)] - \frac{1}{2} S_{\max}(\mathbf{U}_R - \mathbf{U}_L). \quad (2.58)$$

Here, the complex upwinding resulting from the exact Riemann solver is approximated by a simple dissipative term that is proportional to the maximum wave speed at the cell interface,

$$S_{\max} = \max(|V_{x,L}| + c_{f,L,x}, |V_{x,R}| + c_{f,R,x}). \quad (2.59)$$

This dissipative term allows numerical stability to be retained in the simulation by smoothening out any discontinuity that may arise in the system within a few time steps. The Rusanov flux is computationally inexpensive and robust when simulating fast-magnetosonic shocks. However, its simplicity and efficiency come at the cost of disregarding the complex structure of the Riemann fan (see also Fig. 2.1). Thus, this method is usually too dissipative for practical use.

A better way to describe the structure of the solution to the Riemann problem without sacrificing performance is to retain only a subset of the original 7 MHD waves and provide appropriate parameterizations of the Rankine–Hugoniot jump conditions across each of the considered waves,

$$\mathbf{F}_x^{**} - \mathbf{F}_x^* = \lambda_v(\mathbf{U}^{**} - \mathbf{U}^*). \quad (2.60)$$

In Eq. (2.60),  $\lambda_v$  is the speed of the wave separating the states  $\mathbf{U}^{**}$  and  $\mathbf{U}^*$ , while  $\mathbf{F}_x^{**}$  and  $\mathbf{F}_x^*$  are the fluxes in the \*\* and \* regions, respectively. If suitable estimates of the wave speeds  $\{\lambda_v\}$  are provided beforehand, the system of Rankine–Hugoniot jump conditions can be solved to obtain the fluxes in each region of the Riemann fan without using an iterative method. Then, the flux at the cell interface is chosen according to the direction of propagation of the waves, so the solution is upwind. This is the Harten-Lax-van Leer-family (HLL) of approximate Riemann solvers. In particular, the two-wave HLL solver of Einfeldt et al. (1991) retains only the outermost fast-magnetosonic waves in the Riemann fan, similar to the Rusanov flux<sup>3</sup>. Thus, HLL is accurate and robust for modeling fast-magnetosonic waves, but it strongly dissipates the intermediate states. Improvements over HLL can be made by restoring the contact wave back to the structure of the solution to the Riemann problem, such as in the three-wave HLL-Contact (HLLC) solver of Li (2005). HLLC is accurate for fast-magnetosonic and contact waves, but it still introduces excessive dissipation for the

<sup>3</sup>Rusanov is a special case of HLL with  $\lambda_1 = \lambda_7 = S_{\max}$ .



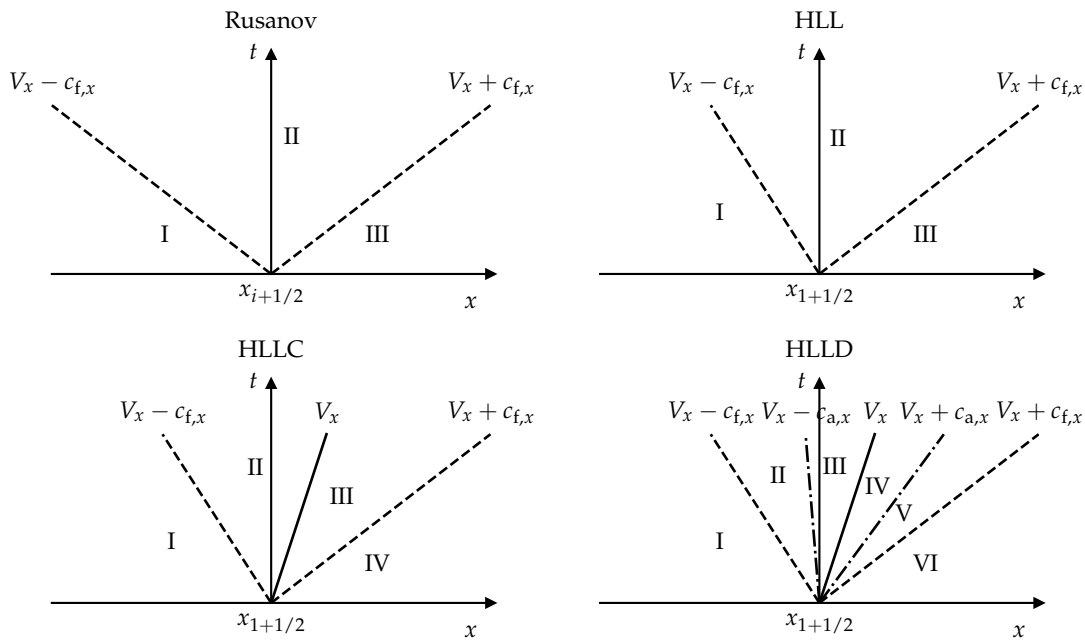


Figure 2.3: Structure of the solution to a Riemann problem of MHD in four approximate Riemann solvers: Rusanov (upper left), HLL (upper right), HLLC (lower left), and HLLD (lower right).

slow-magnetosonic and Alfvén waves. Even more complex is the five-wave HLL-Discontinuities (HLLD) solver of [Miyoshi and Kusano \(2005\)](#), which restores both the contact and the rotational discontinuities into the Riemann fan, but it still excludes slow-magnetosonic waves (see Fig. 2.3 for a visualization of the wave structure of the Rusanov, HLL, HLLC, and HLLD solvers). All the members of the HLL-family are positivity preserving, i.e., they guarantee that density and pressure always remain positive (at least in 1D flows), which is a highly desirable property for any numerical scheme.

Besides Rusanov and the HLL-family, a wide variety of approximate Riemann solvers for MHD have been presented in the literature. These include solvers based on a linearization of the MHD equations around some average state, for which even exact solutions can be computed easily (e.g., [Cargo and Gallice, 1997](#)), relaxation approaches (e.g., [Waagan et al., 2011](#)), or flux splittings (e.g., [Balsara et al., 2016](#)).

### 2.3.3 Higher-order time integration

Globally second-order accurate methods require that both the spatial and time discretizations are at least second-order accurate, i.e., the global error must be equal to or better than  $\mathcal{O}(\Delta x^2, \Delta t^2)$ . There are two main ways to achieve higher-order temporal accuracy in Godunov-type methods. The first family is that of fully discrete schemes, in which the spatial and temporal discretizations are performed at the same time. These schemes include the monotonic upstream-centered scheme for conservation laws (MUSCL) of [van Leer \(1974\)](#) and the corner transport upwind (CTU) method of [Colella \(1990\)](#). In both MUSCL and CTU, the key idea is to advance the numerical



solution in a single step as

$$\mathbf{u}_i^{n+1} = \mathbf{u}_i^n + \Delta t \mathcal{R}_i^{n+1/2}. \quad (2.61)$$

Here,  $\mathcal{R}_i^{n+1/2}$  approximates the time derivative of the cell-volume averaged state quantities at half time step, so

$$\mathcal{R}_i^{n+1/2} = \tilde{\mathcal{S}}_i^{n+1/2} - \frac{\tilde{\mathcal{F}}_{i+1/2}^{n+1/2} - \tilde{\mathcal{F}}_{i-1/2}^{n+1/2}}{\Delta x}. \quad (2.62)$$

The right-hand side of Eq. (2.62) can only be computed if the conservative quantities at  $t^{n+1/2}$  are known. These can be obtained by the second-order Taylor expansion

$$\mathbf{U}_i^{n+1/2} = \mathbf{u}_i^n - \frac{\Delta t}{2} \left( \mathbf{A}_{i,x}^n \frac{\Delta \mathbf{U}_i^n}{\Delta x} - \tilde{\mathcal{S}}_i^n \right), \quad (2.63)$$

$$\mathbf{U}_{i\pm 1/2}^{n+1/2} = \mathbf{u}_i^n \pm \frac{1}{2} \left( \mathbb{I} - \frac{\Delta t}{\Delta x} \mathbf{A}_{i,x}^n \right) \Delta \mathbf{U}_i^n + \frac{\Delta t}{2} \tilde{\mathcal{S}}_i^n. \quad (2.64)$$

In Eqs. (2.63) and (2.64),  $\mathbf{A}_{i,x}^n$  is the flux-Jacobian of the MHD system (see Eq. (2.23)) computed in  $\mathbf{u}_i^n$  and

$$\Delta \mathbf{U}_i^n = \mathbf{U}_{i+1/2,L}^n - \mathbf{U}_{i-1/2,R}^n. \quad (2.65)$$

Unlike MUSCL, CTU performs the spatial reconstruction in Eq. (2.65) by discarding the waves (characteristics) that do not reach the cell boundaries within  $\Delta t/2$  starting from the cell center. This operation generally increases the accuracy of the numerical solution but requires previous knowledge about the eigenstructure of the flux-Jacobian  $\mathbf{A}_x$  and makes the method somewhat more complicated to implement than MUSCL.

Semi-discrete schemes represent the second class of time steppers. Here the idea is to first discretize Eq. (2.34) in space while leaving the problem continuous in time according to the method of lines (e.g., [LeVeque, 2007](#)), thus giving rise to a system of ordinary differential equations (ODEs),

$$\frac{\partial \mathbf{u}_i}{\partial t} + \mathcal{R}_i^* = \mathbf{0}. \quad (2.66)$$

In Eq. (2.66),

$$\mathcal{R}_i^* = \frac{\tilde{\mathcal{F}}_{i+1/2}^* - \tilde{\mathcal{F}}_{i-1/2}^*}{\Delta x} - \tilde{\mathcal{S}}_i^*, \quad (2.67)$$

are the so-called ‘‘spatial residuals’’. Equation (2.66) can then be solved using any standard method for systems of ODEs, such as multi-stage Runge–Kutta methods. The strong-stability-preserving method of [Shu and Osher \(1988\)](#) is a popular choice for achieving second-order temporal accuracy in the numerical solution. In this method, the time update from time  $t^n$  to time  $t^{n+1} = t^n + \Delta t$  is performed in two steps,

$$\mathbf{u}_i^{(1)} = \mathbf{u}_i^n - \Delta t \mathcal{R}_i^n, \quad (2.68)$$

$$\mathbf{u}_i^{n+1} = \frac{1}{2} \left( \mathbf{u}_i^n + \mathbf{u}_i^{(1)} - \Delta t \mathcal{R}_i^{(1)} \right). \quad (2.69)$$

Unlike the MUSCL or CTU schemes, semi-discrete methods must integrate the model equations using at least two substeps to achieve second-order temporal accuracy, so

they are typically more expensive than fully discrete time-marching schemes. In addition, semi-discrete methods have a more restrictive time step constraint than fully discrete methods in more than one dimension. However, semi-discrete schemes can achieve arbitrarily high temporal accuracy by simply increasing the number of integration substeps without having to modify the algorithm for computing the spatial residuals. This is not true for fully discrete methods, which can only achieve higher than second-order temporal accuracy by adding extra terms to the Taylor expansion in Eqs. (2.63) and (2.64). In addition to increasing the implementation effort, retaining higher-order terms in the Taylor expansion makes the overall scheme less robust for discontinuous solutions (e.g., [LeVeque, 2002](#)).

### 2.3.3.1 Implicit time discretization

The MUSCL, CTU, and Runge–Kutta methods presented in the previous section belong to the family of explicit time steppers, where the time update of the state quantities from  $t^n$  to  $t^{n+1}$  is performed based uniquely on the knowledge of the numerical solution at time  $t^n$ . Explicit time marching schemes are conditionally stable, i.e., the time step  $\Delta t$  used to integrate the model equations must be constrained to retain numerical stability. For the system of fully compressible MHD equations, the time step must be limited by the CFL condition given by Eq. (2.42), which states that the fastest magnetoacoustic wave present on the grid cannot cross more than one cell per time step. Given this constraint, the number of time steps required to advect an entropy wave traveling at speed  $u = \mathcal{M}a$  through one grid cell is

$$N_{\text{exp}} = \frac{\Delta t_{\text{adv}}}{\Delta t_{\text{CFL}}} \approx \mathcal{M}^{-1}, \quad (2.70)$$

where  $\Delta t_{\text{adv}}$  is the crossing time scale of the entropy wave over a grid cell,

$$\Delta t_{\text{adv}} \approx \frac{\Delta x}{u}, \quad (2.71)$$

and  $\mathcal{M}$  and  $a$  are the Mach number of the wave and the local sound speed, respectively. When entropy waves are highly subsonic, following their propagation over the entire grid requires a large number of steps, making the simulation excessively expensive. In such situations, significant performance improvements can be obtained by using implicit time steppers, which are unconditionally stable and therefore allow the model equations to be integrated over a much longer time step than that imposed by the CFL condition. The simplest implicit time stepper is the first-order accurate backward Euler method<sup>4</sup>, in which Eq. (2.66) is discretized as

$$\frac{\mathbf{u}_i^{n+1} - \mathbf{u}_i^n}{\Delta t} + \mathcal{R}_i^{n+1} = \mathbf{0}. \quad (2.72)$$

Unlike explicit time steppers, here the numerical solution is not given in closed form, but rather it must be found using iterative, root-finding algorithms such as Raphson–Newton. In each iteration step of the root-finding algorithm, a large linear system of equations must be solved to improve the estimate of the root. This can be accomplished using, e.g., relaxation methods or Krylov subspace linear solvers (e.g., [LeVeque, 2007](#)). The iteration is eventually halted when the correction on the numerical solution is smaller than the prescribed tolerance.

---

<sup>4</sup>Higher than first-order accurate implicit time steppers are, e.g. the Crank–Nicolson method ([Crank et al., 1947](#)) or ESDIRK schemes ([Hosea and Shampine, 1996](#)).

The use of an iterative scheme for obtaining the numerical solution at time  $t^{n+1}$  significantly increases the computational cost per time step of implicit time steppers compared to conventional time-explicit methods. However, if the time step is chosen to be large enough to overcome the overhead cost of the root-finding algorithm, implicit time discretization can be significantly faster than explicit steppers. In practice, one should limit the time step to properly resolve the flow of interest in time and to produce accurate numerical solutions. For entropy waves, the time step should be limited by Eq. (2.71), which is about  $1/\mathcal{M}$  larger than  $\Delta t_{\text{CFL}}$ . Depending on the specific setup, the cost per time step of the implicit solver is 20 to 50 times higher than that of explicit time steppers, so implicit time discretization becomes convenient over explicit time steppers when  $\mathcal{M} \lesssim 0.05$  (e.g., [Miczek, 2013](#); [Edelmann, 2014](#)).

## 2.4 The $\nabla \cdot \mathbf{B} = 0$ constraint in Godunov-type schemes

One of Maxwell's equations states that magnetic monopoles do not exist,

$$\nabla \cdot \mathbf{B} = 0. \quad (2.73)$$

Analytic solutions to Eqs. (2.10)-(2.14) automatically satisfy the solenoidal property of the magnetic field. This property is also trivially satisfied in 1D simulations, where Eq. (2.73) implies  $B_x = \text{const}$ . However, in more than one dimension, Godunov-type schemes for MHD only satisfy the divergence-free condition for the magnetic field up to discretization errors,

$$\nabla \cdot \mathbf{B} = 0 + \mathcal{O}(\Delta x^p, \Delta t^q), \quad (2.74)$$

where  $p$  and  $q$  are the spatial and temporal orders of accuracy of the numerical scheme, respectively. Under the effects of a nonsolenoidal magnetic field, the fluid experiences a fictitious component of the Lorentz force parallel to the magnetic field lines,

$$f_{L\parallel} = \frac{\mathbf{f}_L \cdot \mathbf{B}}{|\mathbf{B}|} = -\mathbf{B}(\nabla \cdot \mathbf{B}), \quad (2.75)$$

which does work on the fluid according to

$$W_{L\parallel} = -\mathbf{B} \cdot \mathbf{V}(\nabla \cdot \mathbf{B}). \quad (2.76)$$

If left uncontrolled, these spurious terms can severely degrade the quality of the numerical solution (e.g., [Brackbill and Barnes, 1980](#)). Furthermore, most Godunov-type methods for multidimensional MHD rely on 1D Riemann solvers for computing the fluxes at each grid cell boundary (see Sect. 2.3.2). In 1D Riemann solvers, the condition  $\nabla \cdot \mathbf{B} = 0$  is implemented by assuming that the magnetic field component perpendicular to the cell boundary is continuous<sup>5</sup>. This representation is not suitable for multidimensional problems and can result in a lack of numerical dissipation, leading to numerical instabilities.

Several methods have been proposed to mitigate the effects caused by spurious magnetic monopoles on the evolution of the flow in multidimensional MHD simulations. Some of these techniques are described in the following sections.

---

<sup>5</sup>A typical way to ensure continuity in the magnetic field component perpendicular to the grid cell boundary is to compute the arithmetic mean of the two Riemann states, e.g.,  $B_x = (B_{x,L} + B_{x,R})/2$

### 2.4.1 Projection methods

Projection methods are based on the idea that the magnetic field solution produced by the base numerical scheme,  $\mathbf{B}_{i,j,k}^*$ , consists of a divergence-free and a divergent component. Therefore, the Hodge projection can be used to isolate the divergence-free part of the solution (e.g. [Brackbill and Barnes, 1980](#); [Balsara, 2004](#)),

$$\mathbf{B}^{n+1} = \mathbf{B}^* - \nabla\phi. \quad (2.77)$$

To find  $\phi$ , one computes the divergence of Eq. (2.77), which results in the Poisson equation

$$\nabla^2\phi = \nabla \cdot \mathbf{B}^*. \quad (2.78)$$

Equation (2.78) can be solved for  $\phi$  if suitable discretizations of the Laplacian and divergence operators are provided. Numerical solutions to Eq. (2.78) are then found, e.g., using fast-Fourier transform techniques, multigrid-based methods, or sparse linear solvers (e.g. [Ferziger and Perić, 2002](#); [LeVeque, 2007](#)). Once  $\phi$  is obtained, the corrected (divergence-free) magnetic field is computed using Eq. (2.77).

Projection methods are an effective way to enforce a particular discretization of  $\nabla \cdot \mathbf{B}$  to the level of machine accuracy. However, they require finding the solution of a large elliptic system of equations at each time step. In parallelized simulations, this operation involves all-to-all communication which can be particularly expensive compared to solving the hyperbolic system of MHD equations. Furthermore, the correction step in Eq. (2.77) can lead to negative pressures in strongly magnetized plasmas.

### 2.4.2 Powell's eight-wave method

Instead of numerically enforcing  $\nabla \cdot \mathbf{B} = 0$ , the method of [Powell \(1994\)](#) avoids the accumulation of errors at any given location by letting the fluid advect the magnetic monopoles away, i.e.,

$$\frac{\partial(\nabla \cdot \mathbf{B})}{\partial t} + \nabla \cdot (\mathbf{V}\nabla \cdot \mathbf{B}) = 0. \quad (2.79)$$

This result is achieved by retaining the source term proportional to the divergence of the magnetic field present in the more general form of the MHD equations (e.g., [Godunov, 1972](#); [Fuchs et al., 2011](#)),

$$\mathbf{S} \mapsto \mathbf{S} - \begin{bmatrix} 0 \\ \mathbf{B} \\ \mathbf{B} \cdot \mathbf{V} \\ \mathbf{V} \\ 0 \end{bmatrix} (\nabla \cdot \mathbf{B}). \quad (2.80)$$

The source term<sup>6</sup> in Eq. (2.80) is activated whenever  $\nabla \cdot \mathbf{B} \neq 0$  and adds an 8<sup>th</sup> wave to the eigenstructure of the MHD system (see Sect. 2.1.3) that travels with the fluid speed,  $\lambda_8 = V_x$ . The new wave transports fluctuations in the magnetic field component parallel to the wave vector, resulting in Eq. (2.79). Furthermore, the additional wave restores Galilean invariance and symmetrizes the system of ideal MHD equations ([Godunov, 1972](#)), thus increasing the stability of the numerical scheme at discontinuous solutions ([Powell et al., 1999](#)).

---

<sup>6</sup>Suitable upwind discretizations of the Powell source term can be found, e.g., in [Klingenberg and Waagan \(2010\)](#) or [Fuchs et al. \(2011\)](#).

The 8-wave formulation is inexpensive and in most applications is capable of keeping  $\nabla \cdot \mathbf{B}$  to relatively small values. However, this scheme does not conserve the total momentum, energy, and magnetic field, so it can yield wrong weak solutions (e.g., [Tóth, 2000](#)). Another drawback of Powell's method is that magnetic monopoles can accumulate at stagnation points and never leave the system unless outflow boundary conditions are used.

### 2.4.3 Hyperbolic divergence cleaning

Along the lines of Powell's 8-wave method is the hyperbolic divergence cleaning scheme of [Dedner et al. \(2002\)](#). In this method, the divergence-free constraint on the magnetic field is coupled to the induction equation by means of a generalized Lagrangian multiplier  $\psi$ ,

$$\frac{\partial \mathbf{B}}{\partial t} + \nabla \cdot (\mathbf{V} \otimes \mathbf{B} - \mathbf{B} \otimes \mathbf{V}) + \nabla \psi = \mathbf{0}, \quad (2.81)$$

$$\frac{\partial \psi}{\partial t} + c_h^2 \nabla \cdot \mathbf{B} = 0. \quad (2.82)$$

Equations (2.81) and (2.82) can be combined to obtain a wave equation for  $\nabla \cdot \mathbf{B}$ ,

$$\frac{\partial^2 (\nabla \cdot \mathbf{B})}{\partial t^2} = c_h^2 \nabla^2 (\nabla \cdot \mathbf{B}), \quad (2.83)$$

which implies that divergence errors generated at a given location are radiated away isotropically with constant speed  $c_h$ . In the case  $c_h = \infty$ , the divergence errors would be removed completely. However, such a case corresponds to the elliptic correction described in Sect. 2.4.1, which can be expensive to solve numerically. To maintain the hyperbolic character of the modified set of equations, the divergence waves can be assumed to propagate at the same speed of the fastest magnetosonic wave present on the grid, which yields

$$c_h = C \frac{\Delta x}{\Delta t}. \quad (2.84)$$

This choice allows divergence errors to be kept under control and the extended model equations to be solved numerically without having to modify the CFL criterion on the time step.

In order to use the hyperbolic correction in Godunov-type schemes, the conventional 1D Riemann solvers for MHD presented in Sect. 2.3.2 must be supplemented with the solution to the subset of equations

$$\frac{\partial B_x}{\partial t} + \frac{\partial \psi}{\partial x} = 0, \quad (2.85)$$

$$\frac{\partial \psi}{\partial t} + c_h^2 \frac{\partial B_x}{\partial x} = 0. \quad (2.86)$$

Equations (2.85) and (2.86) are decoupled from the rest of the system and they are linear in  $B_x$  and  $\psi$ . Therefore, their Riemann problem has an exact (upwind) solution that can be computed analytically,

$$B_x = \frac{1}{2}(B_{x,L} + B_{x,R}) - \frac{1}{2c_h}(\psi_R - \psi_L), \quad (2.87)$$

$$\psi = \frac{1}{2}(\psi_L + \psi_R) - \frac{c_h}{2}(B_{x,R} - B_{x,L}). \quad (2.88)$$

$B_x$  and  $\psi$  are then used to solve the Riemann problem of MHD and to compute the fluxes in Eqs. (2.85) and (2.86). To damp the magnetic monopoles over time, an extra parabolic term can be added to the right-hand side of Eq. (2.82),

$$\frac{\partial \psi}{\partial t} + c_h^2 \nabla \cdot \mathbf{B} = -\psi / \tau, \quad (2.89)$$

where  $\tau$  is a tunable parameter.

The main advantage of hyperbolic divergence cleaning over projection schemes is that it preserves the hyperbolic nature of the MHD equations and requires only a few minor modifications to the Godunov algorithm. Unlike Powell's 8-wave method, the fixed velocity  $c_h$  guarantees that magnetic monopoles are transported away under all circumstances. Even if the flow has stagnation points, magnetic monopoles cannot accumulate there. However, this method tends to introduce excessive dissipation for the magnetic field when the characteristic Alfvén and fluid speeds are much lower than  $c_h$ . Furthermore, the optimal value of the damping time scale  $\tau$  depends on the given problem and can sometimes be difficult to constrain.

#### 2.4.4 Constrained transport

Instead of solving the induction equation in its conservation form (see Eq. 2.13), constrained transport (CT) methods (e.g., [Evans and Hawley, 1988](#); [Dai and Woodward, 1998](#); [Balsara and Spicer, 1999](#)) aim to solve the equivalent form

$$\frac{\partial \mathbf{B}}{\partial t} + \nabla \times \mathbf{E} = \mathbf{0}, \quad (2.90)$$

where

$$\mathbf{E} = -\mathbf{V} \times \mathbf{B} \quad (2.91)$$

is the electromotive force. Using Stokes' theorem to perform the surface integral of Eq. (2.90) over the grid cell boundary  $\{i + 1/2, j, k\}$  gives<sup>7</sup>

$$\begin{aligned} \frac{\partial \mathcal{B}_{x,i+1/2,j,k}}{\partial t} = & -\frac{1}{\Delta y} (\mathcal{E}_{z,i+1/2,j+1/2,k} - \mathcal{E}_{z,i+1/2,j-1/2,k}) \\ & + \frac{1}{\Delta z} (\mathcal{E}_{y,i+1/2,j,k+1/2} - \mathcal{E}_{y,i+1/2,j,k-1/2}), \end{aligned} \quad (2.92)$$

where

$$\mathcal{B}_x = \frac{1}{A_{i+1/2,j,k}} \int_{A_{i+1/2,j,k}} B_x \, dA \quad (2.93)$$

is the surface-averaged magnetic field and, e.g.,

$$\mathcal{E}_{z,i+1/2,j+1/2,k} = \frac{1}{\Delta z_{i+1/2,j+1/2,k}} \int_{\Delta z_{i+1/2,j+1/2,k}} E_z \, dz \quad (2.94)$$

is the line-averaged z-component of the electromotive force. Analogous formulas can be derived for the other components of the electromotive force and the magnetic field.

---

<sup>7</sup>For simplicity, the following calculations assume that the grid is Cartesian.

When the surface-averaged magnetic field components are evolved according to equations such as Eq. (2.92), the update to the cell volume average of the magnetic field divergence,

$$\begin{aligned}
 (\nabla \cdot \mathbf{B})_{i,j,k} = & \frac{\mathcal{B}_{x,i+1/2,j,k} - \mathcal{B}_{x,i-1/2,j,k}}{\Delta x} + \\
 & \frac{\mathcal{B}_{y,i,j+1/2,k} - \mathcal{B}_{y,i,j-1/2,k}}{\Delta y} + \\
 & \frac{\mathcal{B}_{z,i,j,k+1/2} - \mathcal{B}_{z,i,j,k-1/2}}{\Delta z},
 \end{aligned} \tag{2.95}$$

vanishes up to rounding errors.

There are two caveats to this result. First, the magnetic field must be updated at cell boundaries and not at cell centers as in the original finite-volume method, which requires the use of a staggered grid. Second, the line-averaged electromotive forces used to update the magnetic field (see Eq. (2.92)) must be estimated somehow. The simple approach of averaging the electromotive force resulting from the Riemann problems at the four adjacent cell boundaries,

$$\begin{aligned}
 \mathcal{E}_{z,i+1/2,j+1/2,k} = & \frac{1}{4} \left( E_{z,i+1/2,j,k} + E_{z,i+1/2,j+1,k} \right. \\
 & \left. + E_{z,i,j+1/2,k} + E_{z,i+1,j+1/2,k} \right),
 \end{aligned} \tag{2.96}$$

lacks upwinding and gives rise to numerical instabilities. To produce upwind and robust solutions, dissipative terms can be added to Eq. (2.96) based on the sign of the contact wave at the grid cell boundaries, as described in [Gardiner and Stone \(2005\)](#). Another method is to solve a 2D Riemann problem for the induction equation at the grid cell edges as in the upwind constrained transport (UCT) method (e.g., [Londrillo and del Zanna, 2004](#); [Mignone and Del Zanna, 2021](#)).

CT has significant advantages over the methods discussed in the previous sections: i) it keeps a discretization of  $\nabla \cdot \mathbf{B}$  to zero (except for small errors due to the finite precision of floating-point arithmetic) while preserving the hyperbolic character of the MHD equations; ii) is a conservative scheme, so its numerical solution converges to the weak solution of the equations; and iii) it conserves the magnetic flux across the surface of each grid cell, which in numerical MHD is a more fundamental conservation property than preserving the volume integral of the magnetic field over the whole grid as in the cell-centered representation ([Gardiner and Stone, 2005](#)). However, the need for a staggered representation of the magnetic field makes CT difficult to use on arbitrarily curvilinear grids.





# CHAPTER 3

---

## Results

---

This Chapter presents the main results of the thesis. The content of each section consists of a peer-reviewed publication<sup>1</sup> preceded by a short introduction. The order of the sections does not necessarily correspond to the publication order of the papers, but rather reflects the interdependence of the content. The results are summarized and discussed further in Sect. 4.

---

<sup>1</sup>All the papers presented in this Chapter have been accepted for publication in the peer-reviewed journal "Astronomy & Astrophysics" (<https://www.aanda.org/>).

### 3.1 Publication I: A numerical scheme for modeling low-Mach-number magnetohydrodynamic flows in stars

Accurate treatment of MHD flows in the interior of stars requires special methods that can tackle highly subsonic flow regimes in strongly stratified media. Indeed, conventional methods of MHD are too dissipative and inefficient when used to model such dynamical conditions (see Sect. 1.2.1). This paper presents a novel scheme that is both accurate and efficient for flows in stellar interiors while preserving the fully compressible nature of the stellar MHD equations. The novel scheme comprises semi-implicit time discretization (IESS, see Sect. 1.3) to overcome the overly strict CFL condition on the time step, a low-dissipation Riemann solver to correct for the erroneous scaling of the numerical viscosity with the Mach number, and a well-balancing technique that maintains hydrostatic solutions on the computational grid. A staggered constrained transport method (see Sect. 2.4.4) is used to preserve one particular discretization of  $\nabla \cdot \mathbf{B}$ .

The paper first describes the major shortcomings of standard shock-capturing schemes in modeling stellar flows and provides implementation details of the proposed low-Mach-number MHD method in SLH. Then, the numerical properties of IESS are assessed through five verification benchmarks. These tests include i) a linear wave analysis; ii) a stable, magnetized vortex which allows the robustness of the scheme to be tested in a wide range of Mach numbers and regimes of magnetization; iii) simulations of a magnetized Kelvin–Helmholtz instability at various Mach numbers of the initial shear layers; iv) the rise of a buoyant bubble in a strongly stratified medium; and v) small-scale dynamo action in a stratification that resembles that of an oxygen-burning shell of a massive star. These tests are characterized by a progressively increasing level of difficulty and are designed to challenge the low-Mach capabilities of any numerical scheme.

### **Title**

A finite-volume scheme for modeling compressible magnetohydrodynamic flows at low Mach numbers in stellar interiors

### **Authors**

G. Leidi, C. Birke, R. Andrassy, J. Higl, P. V. F. Edelmann, G. Wiest, C. Klingenberg, and F. K. Röpké

### **Publication status**

The manuscript was published in December 2022.

### **DOI**

<https://doi.org/10.1051/0004-6361/202244665>






### **Author's contribution**

GL is the principal author of this paper. The project idea arose from an established collaboration between the astrophysics group of FR (Heidelberg University) and the mathematics group led by CK (Würzburg University). The presented IESS scheme was developed by GL and CB. The implementation of the new numerical method into the SLH code, followed by extensive testing and the analysis of the numerical results was carried out by GL. GL also produced all the figures and wrote the manuscript. All authors actively contributed to the project by discussing the results in various internal meetings.

### **Credit**

Leidi et al., A&A, 668, A143, 2022, reproduced with permission ©ESO.

# A finite-volume scheme for modeling compressible magnetohydrodynamic flows at low Mach numbers in stellar interiors

G. Leidi<sup>1,2</sup> , C. Birke<sup>3</sup>, R. Andrassy<sup>1</sup>, J. Higl<sup>1</sup> , P. V. F. Edelmann<sup>4</sup> , G. Wiest<sup>1</sup> ,  
C. Klingenberg<sup>3</sup>, and F. K. Röpke<sup>1,5</sup> 

<sup>1</sup> Heidelberger Institut für Theoretische Studien, Schloss-Wolfsbrunnenweg 35, 69118 Heidelberg, Germany  
e-mail: giovanni.leidi@h-its.org

<sup>2</sup> Zentrum für Astronomie der Universität Heidelberg, Astronomisches Rechen-Institut, Mönchhofstr. 12–14, 69120 Heidelberg, Germany

<sup>3</sup> Department of Mathematics, Würzburg University, Emil-Fischer-Str. 40, 97074 Würzburg, Germany

<sup>4</sup> Computer, Computational and Statistical Sciences (CCS) Division and Center for Theoretical Astrophysics (CTA), Los Alamos National Laboratory, Los Alamos, NM 87545, USA

<sup>5</sup> Zentrum für Astronomie der Universität Heidelberg, Institut für Theoretische Astrophysik, Philosophenweg 12, 69120 Heidelberg, Germany

Received 2 August 2022 / Accepted 18 September 2022

## ABSTRACT

Fully compressible magnetohydrodynamic (MHD) simulations are a fundamental tool for investigating the role of dynamo amplification in the generation of magnetic fields in deep convective layers of stars. The flows that arise in such environments are characterized by low (sonic) Mach numbers ( $\mathcal{M}_{\text{son}} \lesssim 10^{-2}$ ). In these regimes, conventional MHD codes typically show excessive dissipation and tend to be inefficient as the Courant–Friedrichs–Lewy (CFL) constraint on the time step becomes too strict. In this work we present a new method for efficiently simulating MHD flows at low Mach numbers in a space-dependent gravitational potential while still retaining all effects of compressibility. The proposed scheme is implemented in the finite-volume SEVEN-LEAGUE HYDRO (SLH) code, and it makes use of a low-Mach version of the five-wave Harten–Lax–van Leer discontinuities (HLLD) solver to reduce numerical dissipation, an implicit–explicit time discretization technique based on Strang splitting to overcome the overly strict CFL constraint, and a well-balancing method that dramatically reduces the magnitude of spatial discretization errors in strongly stratified setups. The solenoidal constraint on the magnetic field is enforced by using a constrained transport method on a staggered grid. We carry out five verification tests, including the simulation of a small-scale dynamo in a star-like environment at  $\mathcal{M}_{\text{son}} \sim 10^{-3}$ . We demonstrate that the proposed scheme can be used to accurately simulate compressible MHD flows in regimes of low Mach numbers and strongly stratified setups even with moderately coarse grids.

**Key words.** magnetohydrodynamics (MHD) – methods: numerical

## 1. Introduction

The interplay between turbulent convection and shear is fundamental in understanding the role of small- and large-scale dynamo mechanisms in the generation of strong magnetic fields in stellar interiors. These processes can only be modeled self-consistently with multidimensional magnetohydrodynamic (MHD) simulations (Brun et al. 2004; Browning et al. 2006; Browning 2008; Brown et al. 2010; Ghizaru et al. 2010; Käpylä et al. 2012; Masada et al. 2013; Karak et al. 2015; Hotta et al. 2015; Yadav et al. 2016; Augustson et al. 2016; Brun & Browning 2017; Rempel 2018; Käpylä 2021). Nowadays, many codes used for astrophysical MHD rely on finite-volume discretization and Godunov-like methods to retain the conservative property of the MHD equations. This method is particularly suited for simulating flows in the transonic and supersonic regimes, which characterize many astrophysical systems. However, stars are objects in nearly magnetohydrostatic equilibrium (MHSE), and the flows arising from such stratifications have a very low sonic Mach number, typically  $\mathcal{M}_{\text{son}} = |V|/a \lesssim 10^{-2}$  (Kupka & Muthsam 2017), where  $V$  is the flow speed and

$a$  is the adiabatic sound speed. It is well known that conventional finite-volume schemes are not designed to work in such regimes (Viallet et al. 2011; Miczek et al. 2015; Dumbser et al. 2019; Minoshima et al. 2020). First, the approximate Riemann solvers used in many astrophysical MHD codes, such as the Harten–Lax–van Leer (HLLC; Einfeldt et al. 1991), Roe (Cargo & Gallice 1997), and Harten–Lax–van Leer discontinuities (HLLD; Miyoshi & Kusano 2005) solvers, show excessive numerical dissipation when the typical Mach number of the flow is below  $10^{-2}$ . Second, explicit time-steppers have to satisfy the Courant–Friedrichs–Lewy (CFL) stability criterion (Courant et al. 1928) so that the propagation of fast magnetosonic waves is resolved in time. This poses a severe limitation when simulating low-Mach-number flows. In this regime, the fast magnetosonic waves become parasitic since they transport very little energy and drastically reduce the time step. This makes convectional schemes exceedingly expensive for simulating the evolution of fluid motions and Alfvén waves, which are orders of magnitude slower than fast magnetosonic waves in deep layers of stars (Brun et al. 2005; Browning 2008; Käpylä 2011; Augustson et al. 2016). Lastly, standard Godunov-type schemes, by

construction, cannot preserve stratifications in MHSE. This happens because hyperbolic fluxes and gravitational source terms are separately discretized and do not balance exactly in hydrostatic setups, which inevitably leads to the generation of spurious flows even in pure hydrodynamic simulations (Edelmann et al. 2021). This problem becomes even more critical in steep stratifications, where the spatial reconstruction from cell centers results in large jumps in the pressure at the cell interfaces, considerably accelerating the fluid along the gravity vector. Such numerical artifacts can dominate over the physical convective motions, leading to unreliable results.

Difficulties in modeling low-Mach-number MHD flows in stellar interiors are usually overcome by using alternative approaches based on a different formulation of the physical problem. One of them consists in artificially boosting the energy flux (or energy generation) to drive faster convective motions, such that the typical Mach number of the resulting flows falls above the low-Mach regime ( $M_{\text{son}} \gtrsim 10^{-2}$ ), where explicit time-steppers can be used efficiently (Käpylä et al. 2011, 2012, 2013; Viviani et al. 2019; Käpylä 2021). However, this approach significantly enhances the relative fluctuations of thermodynamic quantities (Warnecke et al. 2016; Käpylä et al. 2020), alters the mixing at convective boundaries (Hotta 2017; Käpylä 2019), and modifies the spectrum of internal waves in radiative regions of stars (Rogers et al. 2013; Edelmann et al. 2019; Horst et al. 2020; Higl et al. 2021). Another approach consists in solving the set of MHD equations using the anelastic approximation (Glatzmaier 1984, 1985; Brun et al. 2004; Jones et al. 2009; Gastine & Wicht 2012; Smolarkiewicz & Charbonneau 2013; Featherstone & Hindman 2016), which filters out the fast magnetosonic waves, alleviating the overly strict constraint on the time step. However, such an approximation cannot model the excitation of the compressible pressure modes. Another way to overcome the constraint on the time step is to drastically reduce the speed of the fast magnetosonic waves (Rempel 2005; Hotta et al. 2015); again, at the cost of modifying the original set of MHD equations.

A numerical scheme that is capable of efficiently solving the fully compressible MHD equations at low sonic Mach numbers in strongly stratified setups is still missing. In this work we present a new method that aims to fill this gap. This can only be accomplished (i) by reducing the numerical dissipation, (ii) by overcoming the strict CFL condition, and (iii) by preserving the background stratification in MHSE over long timescales. For aspect (i), we use a low-Mach version of the five-wave HLLD solver (Minoshima & Miyoshi 2021), whose numerical dissipation is independent of the sonic Mach number of the modeled flow in subsonic regimes.

In order to deal with aspect (ii), time-implicit discretization techniques can be used. Most of the fully implicit (e.g., Aydemir & Barnes 1985; Charlton et al. 1990; Chacón 2008; Lütjens & Luciani 2010) and semi-implicit (e.g., Harned & Kerner 1985; Schnack et al. 1987; Lerbinger & Luciani 1991; Glasser et al. 1999; Jardin 2012; Fambri 2021) MHD schemes presented in the literature are designed to simulate magnetically confined plasmas and low- $\beta$  environments, where  $\beta$  is defined as the ratio of the gas pressure to the magnetic pressure:  $\beta = p/p_B$ . In such strongly magnetized plasmas, both fast magnetosonic and Alfvén waves put a strong limit on the time step. On the contrary, plasmas in stellar interiors are characterized by high  $\beta$  values (Mestel 1999)<sup>1</sup>, and the only source of stiffness is the generation of fast

magnetosonic waves. Thus, Alfvén waves do not need to be treated implicitly, which greatly simplifies the numerical problem. Recently, Dumbser et al. (2019) developed a semi-implicit conservative method that treats only the fast magnetosonic waves implicitly; however, that scheme cannot be implemented easily within the framework of our hydrodynamic code. In this work, we construct an alternative time-marching scheme suitable for modeling high- $\beta$  plasmas at low Mach numbers, based on the approach described by Fuchs et al. (2009), in which the induction equation is solved in a separate step and coupled to the rest of the system through Strang splitting (Strang 1968). As the high speed of the fast magnetosonic waves is mostly determined by the pressure flux in the momentum equation, we solve the subset containing the continuity, momentum, and energy equations implicitly, whereas the induction equation is integrated using an explicit time-stepper. For stability, the time step is now limited by the fastest fluid and Alfvén speeds on the grid; it is approximately  $1/M_{\text{son}}$  longer than that allowed by the CFL condition, which leads to a considerable speed-up when the Mach number of the flow is low. Since the update on the induction equation is performed in a separate step, the flux-Jacobian in the time-implicit part of the algorithm does not need to be evaluated with respect to the magnetic field components. This allows for more flexibility when choosing the method that evolves the magnetic field. In particular, we use a staggered formulation of constrained transport (CT-contact; Gardiner & Stone 2005) to keep  $\nabla \cdot \mathbf{B} = 0$  to machine precision, at least for a specific discretization of the divergence of the magnetic field.

Finally, aspect (iii) is solved by using the deviation well-balancing method (Berberich et al. 2021; Edelmann et al. 2021), which allows the a priori known background stratification in MHSE to be preserved, dramatically reducing the magnitude of numerical errors and the strength of spurious flows<sup>2</sup>. Recently, Canivete Cuissa & Teyssier (2022) performed fully compressible simulations of stellar magneto-convection at  $M_{\text{son}} \sim 10^{-3}$  using a well-balancing technique similar to the deviation method. However, their scheme relied on explicit time-steppers, and it was used to simulate only 2.5 convective turnovers. Moreover, they did not cure the excessive dissipation of the HLLD solver at low Mach numbers.

These methods have been implemented in the SEVEN-LEAGUE HYDRO (SLH) code, which has already been used in the past to simulate convective boundary mixing, shear instabilities, and wave excitation in stellar interiors, even in regimes of low Mach numbers (Miczek 2013; Edelmann 2014; Miczek et al. 2015; Edelmann & Röpke 2016; Edelmann et al. 2017; Horst et al. 2020, 2021; Andrassy et al. 2022). We stress that the current MHD implementation in SLH is not suitable for modeling low- $\beta$  plasmas. For simulating such regimes, a different method should be used instead, which is beyond the scope of this work.

In Sect. 2, we summarize the main properties of the fully compressible MHD equations with gravity. In Sects. 3 and 4, we provide details on the numerical algorithms implemented in SLH. In Sect. 5, several numerical experiments are run with the new MHD scheme in order to check its accuracy and efficiency in simulating flows at low Mach numbers, even in the

<sup>1</sup> Low- $\beta$  environments can be found in the outer layers of active stars, like the solar corona.

<sup>2</sup> A similar approach in which the states are split into a background component and deviations is described in Vögler et al. (2005), Khomenko & Collados (2006), Felipe et al. (2010), and Hotta et al. (2015).

presence of a steep stratification. Finally, in Sect. 6 we draw conclusions and summarize the fundamental aspects of the proposed algorithm.

## 2. Equations of compressible ideal MHD with gravity

The MHD scheme implemented in SLH is designed to solve the set of compressible ideal MHD equations with a (time-independent) gravitational source term<sup>3</sup>:

$$\frac{\partial \rho}{\partial t} + \nabla \cdot (\rho \mathbf{V}) = 0, \quad (1)$$

$$\frac{\partial(\rho \mathbf{V})}{\partial t} + \nabla \cdot [\rho \mathbf{V} \otimes \mathbf{V} + (p + p_B) \mathbf{I} - \mathbf{B} \otimes \mathbf{B}] = \rho \mathbf{g}, \quad (2)$$

$$\frac{\partial(\rho E_\phi)}{\partial t} + \nabla \cdot [(\rho E_\phi + p + p_B) \mathbf{V} - \mathbf{B}(\mathbf{B} \cdot \mathbf{V})] = 0, \quad (3)$$

$$\frac{\partial \mathbf{B}}{\partial t} + \nabla \cdot (\mathbf{V} \otimes \mathbf{B} - \mathbf{B} \otimes \mathbf{V}) = \mathbf{0}, \quad (4)$$

where  $\rho$  denotes the density,  $\mathbf{V} = (V_x, V_y, V_z)$  the velocity field,  $\mathbf{B} = (B_x, B_y, B_z)$  the magnetic field<sup>4</sup>,  $\mathbf{I}$  the unit tensor,  $\mathbf{g} = (g_x, g_y, g_z)$  the gravitational acceleration,  $p$  the gas pressure and  $p_B = |\mathbf{B}|^2/2$  the magnetic pressure. The total energy density  $\rho E_\phi$  is defined as

$$\rho E_\phi = \rho e_{\text{int}} + \frac{1}{2} \rho |\mathbf{V}|^2 + \frac{1}{2} |\mathbf{B}|^2 + \rho e_\phi, \quad (5)$$

where  $e_{\text{int}}$  and  $e_\phi$  are the specific internal and gravitational energies<sup>5</sup>.

The system is closed by an equation of state (EoS), which provides the numerical value of the gas pressure. Several different definitions for the EoS can be used in SLH, including a simple ideal gas law, radiation pressure, and a tabulated EoS (Helmholtz EoS; Timmes & Swesty 2000) that allows the effects of electron degeneracy and Coulomb corrections to be included, which are often needed to properly describe the thermodynamic conditions found in stellar material.

### 2.1. Eigenstructure of the MHD system and definition of Mach numbers

The homogeneous MHD system (left-hand side of Eqs. (1)–(4)) reduced to one spatial dimension has seven nonzero eigenvalues<sup>6</sup>,

$$\lambda_{1,7} = V_x \mp c_{f,x}, \quad \lambda_{2,6} = V_x \mp c_{a,x}, \quad \lambda_{3,5} = V_x \mp c_{s,x}, \quad \lambda_4 = V_x, \quad (6)$$

associated with different modes of propagation: left/right fast magnetosonic waves, left/right Alfvén waves, left/right slow

<sup>3</sup> However, other source terms can be added to the system depending on the problem at hand. These include energy generation by nuclear reactions, radiative transport of energy in the diffusion limit, neutrino cooling, and parabolic viscous terms.

<sup>4</sup> Throughout the paper we use the Lorentz-Heaviside notation:  $\mathbf{B} = \mathbf{b}/\sqrt{4\pi}$ .

<sup>5</sup> If the gravitational potential is time independent, solving the energy equation for  $\rho E_\phi$  instead of  $\rho E$  allows the  $\rho \mathbf{g} \cdot \mathbf{V}$  source term to be removed. This leads to more accurate results and better entropy- and energy-conservation properties in simulations of gas dynamics with gravity (Müller 2020; Edelmann et al. 2021).

<sup>6</sup> Here,  $x$  represents a generic direction.

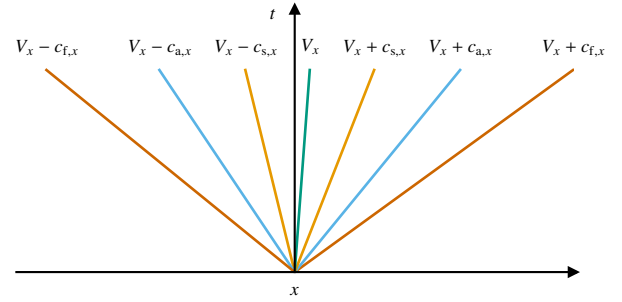


Fig. 1. Wave structure of the MHD system.

magnetosonic waves and one entropy wave.  $c_{s,x}$ ,  $c_{a,x}$ , and  $c_{f,x}$  are the slow magnetosonic, Alfvén, and fast magnetosonic speeds,

$$c_{f,s,x} = \left[ \frac{1}{2} \left( a^2 + \frac{|\mathbf{B}|^2}{\rho} \pm \sqrt{\left( a^2 + \frac{|\mathbf{B}|^2}{\rho} \right)^2 - 4a^2 c_{a,x}^2} \right) \right]^{\frac{1}{2}}, \quad (7)$$

$$c_{a,x} = |\mathbf{B}_x| / \sqrt{\rho}, \quad (8)$$

with the adiabatic sound speed  $a$  defined as

$$a = \left( \frac{\partial p}{\partial \rho} + \frac{p}{\rho^2} \frac{\partial p}{\partial e_{\text{int}}} \right)^{\frac{1}{2}}. \quad (9)$$

As illustrated in Fig. 1, the MHD wave pattern has a fixed ordering:

$$\lambda_1 < \lambda_2 < \lambda_3 < \lambda_4 < \lambda_5 < \lambda_6 < \lambda_7. \quad (10)$$

Alfvén waves correspond to incompressible modes of propagation, as they only carry perturbations in the velocity and magnetic field components orthogonal to the wave vector. Effects of compressibility are due to the propagation of slow and fast magnetosonic waves, while the entropy wave is simple advection of fluid.

In contrast to pure hydrodynamics, the more complex structure of the MHD waves allows several Mach numbers to be defined, depending on the considered reference velocity. In addition to  $\mathcal{M}_{\text{son}}$  (see Sect. 1), the Alfvén Mach number is defined as

$$\mathcal{M}_{\text{Alf}} = \frac{|\mathbf{V}|}{\sqrt{c_{a,x}^2 + c_{a,y}^2 + c_{a,z}^2}}, \quad (11)$$

while the directional slow and fast magnetosonic Mach numbers are given by

$$\mathcal{M}_{\text{slow,fast},x} = \frac{|V_x|}{c_{s,f,x}}. \quad (12)$$

### 2.2. Low-Mach limit of the MHD system

Magnetic fields amplified by dynamo mechanisms in deep convective layers of stars are likely to approach equipartition with respect to the kinetic energy content of the flow (Brandenburg & Subramanian 2005; Featherstone et al. 2009; Augustson et al. 2016; Hotta 2017; Käpylä 2019). To model such processes, the MHD system in Eqs. (1)–(4) must be solved in regimes of Mach numbers  $\mathcal{M}_{\text{fast},x} \lesssim \mathcal{M}_{\text{son}} \lesssim 10^{-2}$  and  $\mathcal{M}_{\text{Alf}} \sim 1$ . To infer the



structure of the solution under such conditions, it is useful to consider the nondimensional form of the fully compressible MHD equations<sup>7</sup>,

$$\frac{\partial \hat{\rho}}{\partial \hat{t}} + \hat{\nabla} \cdot (\hat{\rho} \hat{\mathbf{V}}) = 0, \quad (13)$$

$$\frac{\partial (\hat{\rho} \hat{\mathbf{V}})}{\partial \hat{t}} + \hat{\nabla} \cdot \left[ \hat{\rho} \hat{\mathbf{V}} \otimes \hat{\mathbf{V}} + \left( \frac{\hat{p}}{\hat{\mathcal{M}}_{\text{son}}^2} + \frac{\hat{p}_B}{\hat{\mathcal{M}}_{\text{Alf}}^2} \right) \mathbf{I} - \frac{\hat{\mathbf{B}} \otimes \hat{\mathbf{B}}}{\hat{\mathcal{M}}_{\text{Alf}}^2} \right] = \mathbf{0}, \quad (14)$$

$$\frac{\partial (\hat{\rho} \hat{\mathbf{E}})}{\partial \hat{t}} + \hat{\nabla} \cdot \left[ \left( \hat{\rho} \hat{\mathbf{E}} + \hat{p} + \hat{p}_B \frac{\hat{\mathcal{M}}_{\text{son}}^2}{\hat{\mathcal{M}}_{\text{Alf}}^2} \right) \hat{\mathbf{V}} - \hat{\mathbf{B}} (\hat{\mathbf{B}} \cdot \hat{\mathbf{V}}) \frac{\hat{\mathcal{M}}_{\text{son}}^2}{\hat{\mathcal{M}}_{\text{Alf}}^2} \right] = 0, \quad (15)$$

$$\frac{\partial \hat{\mathbf{B}}}{\partial \hat{t}} + \hat{\nabla} \cdot (\hat{\mathbf{V}} \otimes \hat{\mathbf{B}} - \hat{\mathbf{B}} \otimes \hat{\mathbf{V}}) = \mathbf{0}. \quad (16)$$

Here, the different variables have been rescaled by some reference quantity representative of the physical system of interest:  $x = \hat{x}x_r$ ,  $\rho = \hat{\rho}\rho_r$ ,  $\mathbf{V} = \hat{\mathbf{V}}V_r$ ,  $E = \hat{E}a_r^2$ ,  $p = \hat{p}\rho_r a_r^2$ ,  $\mathbf{B} = \hat{\mathbf{B}}B_r$ .  $\hat{\mathcal{M}}_{\text{son}} = |V_r|/a_r$  and  $\hat{\mathcal{M}}_{\text{Alf}} = |V_r|/(|B_r|/\sqrt{\rho_r})$  are the characteristic sonic and Alfvén Mach numbers of the flow.

In the limit of  $\hat{\mathcal{M}}_{\text{son}} \rightarrow 0$ , Eqs. (13)–(15) approach the incompressible regime (see [Matthaeus & Brown 1988](#)), in which the gas pressure is constant in space except for fluctuations  $\propto \hat{\mathcal{M}}_{\text{son}}^2$ . As this solution does not allow for compressible modes of propagation, only Alfvén and entropy waves can transport fluctuations in the state variables across the physical domain. In the regime we are interested in ( $\hat{\mathcal{M}}_{\text{Alf}} \sim 1$ ), these waves travel at similar speeds. However, the incompressible limit is not the only solution to the compressible MHD equations at  $\hat{\mathcal{M}}_{\text{son}} \ll 1$ . In fact, both slow and fast magnetosonic waves can be propagated with arbitrary small velocity fluctuations. Fast magnetosonic waves in particular travel at much higher speed than Alfvén waves and fluid motions in the low-Mach limit. If the plasma- $\beta$  is high, the large fast magnetosonic speed  $c_{f,x}$  is mostly determined by the pressure flux  $\hat{p}/\hat{\mathcal{M}}_{\text{son}}^2$  in Eq. (13). Since both slow incompressible flows and fast magnetosonic waves are permitted in the limit of  $\hat{\mathcal{M}}_{\text{son}} \rightarrow 0$ , the system of fully compressible MHD equations is stiff.

### 2.3. Magnetohydrostatic solutions

Magnetohydrostatic stratifications are a special class of solutions to the MHD system with gravitational source terms (see Eqs. (1)–(4)), where all the time derivatives are zero and the velocity is zero everywhere. Under these conditions, the distribution of density, pressure and magnetic field is given by the magnetohydrostatic equation

$$\nabla \cdot [(p + p_B)\mathbf{I} - \mathbf{B} \otimes \mathbf{B}] = \rho \mathbf{g}. \quad (17)$$

Any set  $(\rho, p, \mathbf{B})$  that solves Eq. (17) is called a ‘‘magnetohydrostatic solution’’. Equation (17) is undetermined, so a whole continuum of magnetohydrostatic solutions exists.

The stratification of stars is very well described by MHSE over a large fraction of their lifetime. Large deviations from MHSE are only expected in the late evolutionary stages of

<sup>7</sup> For simplicity, we only consider the homogeneous MHD system in this analysis.

massive stars, in atmospheric layers and in stellar winds. Even though their stratification is continuously perturbed by a whole variety of physical processes over fast dynamical timescales, the amplitude of such perturbations remains small, and the overall structure of the star can be considered to be in MHSE. Significant changes to the stratification only happen over the much longer thermal and nuclear timescales ([Kippenhahn et al. 2013](#)).

### 2.4. The solenoidal constraint

The magnetic field satisfies the solenoidal constraint

$$\nabla \cdot \mathbf{B} = 0. \quad (18)$$

This constraint has its origin in Maxwell’s equation and states that physically no magnetic monopoles can exist. Solutions to Eqs. (1)–(4) automatically satisfy this condition at all times if the initial field obeys the constraint. This can easily be illustrated by rewriting Eq. (4) into the equivalent form

$$\frac{\partial \mathbf{B}}{\partial t} + \nabla \times \mathcal{E} = 0, \quad (19)$$

where  $\mathcal{E} = -\mathbf{V} \times \mathbf{B}$  is the electromotive force. Applying the divergence to Eq. (19) results in

$$\frac{\partial (\nabla \cdot \mathbf{B})}{\partial t} = 0. \quad (20)$$

## 3. Spatial discretization

The system of partial differential equations (PDEs) described in Sect. 2 takes the general conservative form

$$\frac{\partial \mathbf{U}}{\partial t} + \frac{\partial \mathbf{F}(\mathbf{U})}{\partial x} + \frac{\partial \mathbf{G}(\mathbf{U})}{\partial y} + \frac{\partial \mathbf{H}(\mathbf{U})}{\partial z} = \mathbf{S}(\mathbf{U}), \quad (21)$$

with the respective vector of conservative variables  $\mathbf{U}$ , physical fluxes  $\mathbf{F}$ ,  $\mathbf{G}$ ,  $\mathbf{H}$  and source term  $\mathbf{S}$ . In SLH, Eq. (21) is solved numerically using the finite-volume method ([LeVeque 2002](#); [Toro 2009](#)), which is briefly summarized in the next section.

### 3.1. Finite-volume discretization

In a first step, the physical system is mapped on a 3D Cartesian grid<sup>8</sup> divided into  $N_x \times N_y \times N_z$  cells, whose spatial extent is given by  $[x_L, x_R] \times [y_L, y_R] \times [z_L, z_R]$ . Each cell in the computational domain is defined by the set of indices  $(i, j, k)$ , and its volume is given by the product of the spatial resolution elements along each axis:  $\Theta_{i,j,k} = \Delta x \Delta y \Delta z$ . Any quantity located at the center of the cell refers to the same indices, while quantities located at the cell boundaries are denoted by sets of indices like  $(i + 1/2, j, k)$ , which in this case defines the interface between cells  $(i, j, k)$  and  $(i + 1, j, k)$ .

Integrating Eq. (21) over the cell volume leads to

$$\begin{aligned} \frac{\partial \hat{\mathbf{U}}_{i,j,k}}{\partial t} = & -\frac{1}{\Delta x} (\hat{\mathbf{F}}_{i+1/2,j,k} - \hat{\mathbf{F}}_{i-1/2,j,k}) \\ & -\frac{1}{\Delta y} (\hat{\mathbf{G}}_{i,j+1/2,k} - \hat{\mathbf{G}}_{i,j-1/2,k}) \\ & -\frac{1}{\Delta z} (\hat{\mathbf{H}}_{i,j,k+1/2} - \hat{\mathbf{H}}_{i,j,k-1/2}) \\ & + \hat{\mathbf{S}}_{i,j,k}, \end{aligned} \quad (22)$$

<sup>8</sup> Here we describe the 3D algorithm; however, 1D and 2D Cartesian grids can also be used in SLH.

where  $\hat{U}_{i,j,k}$  is the volume-averaged vector of conserved quantities

$$\hat{U}_{i,j,k} = \frac{1}{\Theta_{i,j,k}} \int_{\Theta_{i,j,k}} U d\Theta. \quad (23)$$

The same procedure applies to  $\hat{S}_{i,j,k}$ , while the surface-averaged fluxes are defined as

$$\hat{F}_{i+1/2,j,k} = \frac{1}{A_{i+1/2,j,k}} \int_{A_{i+1/2,j,k}} \mathbf{F} \cdot \hat{\mathbf{n}} dA, \quad (24)$$

where  $A_{i+1/2,j,k}$  is the area of the interface  $(i + 1/2, j, k)$  and  $\hat{\mathbf{n}}$  is the normal to the surface pointing outward from the cell.

The right-hand side of Eq. (22) can be discretized in space if suitable numerical values for  $\hat{F}_{i+1/2,j,k}$  and  $\hat{S}_{i,j,k}$  are provided. For the latter, a typical choice consists in substituting the volume-averaged quantity with its value in the center of the cell, which is accurate to second order:

$$\hat{S}_{i,j,k} \approx S_{i,j,k}. \quad (25)$$

The computation of numerical fluxes, in contrast, needs more care, and upwind techniques must be used to achieve stability. The resulting system of ordinary differential equations (ODEs) is then discretized in time using the methods described in Sect. 4.

### 3.2. Numerical flux function

In order to get a proper estimate of the fluxes  $\hat{F}_{i+1/2,j,k}$ , we use the Godunov method (Godunov & Bohachevsky 1959). First, a pair of left and right states  $U_{i+1/2,j,k}^L, U_{i+1/2,j,k}^R$  is reconstructed<sup>9</sup> (through 1D sweeping) to the center of each cell boundary, starting from the cell-centered states  $\hat{U}_{i,j,k}$ . These states define a 1D Riemann problem, which can then be solved (either exactly or approximately) to provide the value of a flux function  $\mathcal{F}(U_{i+1/2,j,k}^L, U_{i+1/2,j,k}^R)$ . The surface-averaged flux is then approximated (to second-order accuracy) as

$$\hat{F}_{i+1/2,j,k} \approx \mathcal{F}(U_{i+1/2,j,k}^L, U_{i+1/2,j,k}^R). \quad (26)$$

Many MHD Riemann solvers used nowadays are designed to work in supersonic regimes. In order to achieve numerical stability, such solvers need to add upwind numerical diffusion terms to the physical fluxes<sup>10</sup>, which smear out any discontinuity present in the flow on a timescale comparable to the cell crossing time of the shock. The choice of these terms depends on the specific approximate Riemann solver used. In particular, the diffusion term associated with the pressure flux (see Eq. (2)) usually takes the form (see, e.g., Einfeldt et al. 1991; Cargo & Gallice 1997; Miyoshi & Kusano 2005)

$$D_p^x \propto -\bar{\rho} \bar{c}_f (V_x^R - V_x^L), \quad (27)$$

where  $\bar{\rho}$  and  $\bar{c}_f$  are suitable averages of the density and the fast magnetosonic speed at the cell interface. However, in low-Mach regimes, discontinuities in the flow are only transported by the linearly degenerate entropy and Alfvén waves. These modes

<sup>9</sup> Several spatial reconstruction routines are implemented in SLH, from simple constant extrapolation to the Piecewise Parabolic Method of Colella & Woodward (1984). These reconstruction schemes can be applied to both conservative and primitive variables.

<sup>10</sup> The physical fluxes are usually computed in Riemann solvers as some variation of the central flux  $(F_L + F_R)/2$ .

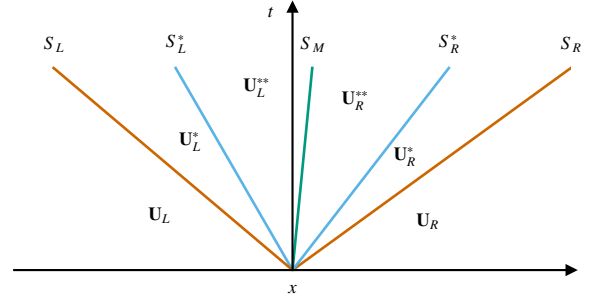


**Fig. 2.** Wave structure of HLLD-type solvers: only the fast magnetosonic ( $S_L, S_R$ ), Alfvén ( $S_L^*, S_R^*$ ), and entropy ( $S_M$ ) waves are considered in the computation of the states across the Riemann fan. The slow magnetosonic waves are discarded.

propagate with small speeds (see Sect. 2.2), and by the time they cross one cell in the computational grid they are strongly dissipated by the action of the numerical term in Eq. (27). This effect can also be explained by noticing that the pressure-diffusion coefficient scales as  $O(1/\mathcal{M}_{\text{fast},x})$ , so that it overwhelms the physical flux proportional to  $O(1)$  at low sonic Mach numbers. To remove this excessive dissipation, we use the low-dissipation HLLD solver (LHLLD) of Minoshima & Miyoshi (2021). This is a variation of the original five-wave HLLD solver (see Fig. 2) of Miyoshi & Kusano (2005). LHLLD introduces a Mach-dependent parameter  $\phi \propto \mathcal{M}_{\text{fast},x}$  in the intermediate state of the total pressure  $p_T = p + p_B$ :

$$p_T^* = \frac{(S_R - V_x^R) \rho_R p_T^L - (S_L - V_x^L) \rho_L p_T^R}{(S_R - V_x^R) \rho_R - (S_L - V_x^L) \rho_L} + \phi \frac{\rho_L \rho_R (S_R - V_x^R)(S_L - V_x^L)(V_x^R - V_x^L)}{(S_R - V_x^R) \rho_R - (S_L - V_x^L) \rho_L}. \quad (28)$$

In this context,  $S_L$  and  $S_R$  are conservative estimates of the speeds  $\lambda_{1,7}$ . In SLH they are evaluated as

$$\begin{aligned} S_L &= \min(V_x^L, V_x^R) - \max(c_{f,x}^L, c_{f,x}^R), \\ S_R &= \max(V_x^L, V_x^R) + \max(c_{f,x}^L, c_{f,x}^R). \end{aligned} \quad (29)$$

The low-Mach fix  $\phi$  is computed according to the following formulas:

$$\begin{aligned} c_u^L &= \left[ \frac{1}{2} \left( \frac{|B_L|^2}{\rho_L} + |V_L|^2 + \sqrt{\left( \frac{|B_L|^2}{\rho_L} + |V_L|^2 \right)^2 - 4 \frac{|V_L|^2 B_x^2}{\rho_L}} \right) \right]^{\frac{1}{2}}, \\ c_u^R &= \left[ \frac{1}{2} \left( \frac{|B_R|^2}{\rho_R} + |V_R|^2 + \sqrt{\left( \frac{|B_R|^2}{\rho_R} + |V_R|^2 \right)^2 - 4 \frac{|V_R|^2 B_x^2}{\rho_R}} \right) \right]^{\frac{1}{2}}, \\ \chi &= \max \left\{ \frac{c_u^L}{c_{f,x}^L}, \frac{c_u^R}{c_{f,x}^R} \right\}, \\ \phi &= \chi(2 - \chi). \end{aligned} \quad (30)$$

Since the fast magnetosonic wave speeds  $c_{f,x}^{L,R}$  and consequently also  $S_{L,R}$  scale as  $O(1/\mathcal{M}_{\text{fast},x})$ , the second term in Eq. (28) would scale as  $O(1/\mathcal{M}_{\text{fast},x})$  if  $\phi = 1$ , as in the original formulation of the HLLD solver. As previously described, this would lead to excessive numerical dissipation for small values of  $\mathcal{M}_{\text{fast},x}$ . Instead, by computing  $\phi$  according to Eq. (30), the



dissipation term becomes independent of the fast magnetosonic Mach number, since  $\phi \propto \mathcal{M}_{\text{fast},x}$ . This modification does not affect the other properties of the HLLD solver, such as preserving positivity of density and internal energy (Miyoshi & Kusano 2005; Minoshima & Miyoshi 2021). We note that the combined diffusion coefficient in Eq. (28) has a residual scaling  $O(1/\mathcal{M}_{\text{Alf}})$ , which would still introduce too much dissipation in very sub-Alfvén regimes. However, these are far from our main astrophysical applications.

### 3.3. Well-balancing method

As already noted in Sects. 1 and 3.1, hyperbolic fluxes and gravitational source terms are discretized with different methods. As a consequence, Godunov-type schemes do not automatically preserve magnetohydrostatic solutions on a discrete grid exactly. Therefore, whenever a stratification needs to be enforced to be in MHSE on the computational grid, we use the deviation well-balancing method (Berberich et al. 2021; Edelmann et al. 2021). The main ingredient of this method is an a priori known target state  $\tilde{U}$  that is a magnetohydrostatic solution to Eq. (21),

$$\frac{\partial \mathbf{F}(\tilde{U})}{\partial x} + \frac{\partial \mathbf{G}(\tilde{U})}{\partial y} + \frac{\partial \mathbf{H}(\tilde{U})}{\partial z} = \mathbf{S}(\tilde{U}), \quad (31)$$

with  $\tilde{V} = 0$ . Subtracting Eq. (31) from the original balance law in Eq. (21) yields a system of PDEs for the deviations from the target solution  $\Delta \mathbf{U} = \mathbf{U} - \tilde{U}$ :

$$\begin{aligned} \frac{\partial(\Delta \mathbf{U})}{\partial t} + \left( \frac{\partial \mathbf{F}(\tilde{U} + \Delta \mathbf{U})}{\partial x} - \frac{\partial \mathbf{F}(\tilde{U})}{\partial x} \right) \\ + \left( \frac{\partial \mathbf{G}(\tilde{U} + \Delta \mathbf{U})}{\partial y} - \frac{\partial \mathbf{G}(\tilde{U})}{\partial y} \right) \\ + \left( \frac{\partial \mathbf{H}(\tilde{U} + \Delta \mathbf{U})}{\partial z} - \frac{\partial \mathbf{H}(\tilde{U})}{\partial z} \right) = \mathbf{S}(\tilde{U} + \Delta \mathbf{U}) - \mathbf{S}(\tilde{U}). \end{aligned} \quad (32)$$

Now, to obtain a well-balanced method, Eq. (32) is discretized according to the finite-volume method described in Sect. 3.1, which leads to the semi-discrete form

$$\begin{aligned} \frac{\partial(\Delta \mathbf{U})_{i,j,k}}{\partial t} = & -\frac{1}{\Delta x} (\mathbf{F}_{i+1/2,j,k}^{\text{dev}} - \mathbf{F}_{i-1/2,j,k}^{\text{dev}}) \\ & -\frac{1}{\Delta y} (\mathbf{G}_{i,j+1/2,k}^{\text{dev}} - \mathbf{G}_{i,j-1/2,k}^{\text{dev}}) \\ & -\frac{1}{\Delta z} (\mathbf{H}_{i,j,k+1/2}^{\text{dev}} - \mathbf{H}_{i,j,k-1/2}^{\text{dev}}) \\ & + \mathbf{S}_{i,j,k}^{\text{dev}}. \end{aligned} \quad (33)$$

In this formulation, the deviation fluxes and source terms are defined by

$$\mathbf{F}_{i+1/2,j,k}^{\text{dev}} = \hat{\mathbf{F}}_{i+1/2,j,k} - \mathbf{F}(\tilde{U}_{i+1/2,j,k}), \quad (34)$$

$$\mathbf{G}_{i,j+1/2,k}^{\text{dev}} = \hat{\mathbf{G}}_{i,j+1/2,k} - \mathbf{G}(\tilde{U}_{i,j+1/2,k}), \quad (35)$$

$$\mathbf{H}_{i,j,k+1/2}^{\text{dev}} = \hat{\mathbf{H}}_{i,j,k+1/2} - \mathbf{H}(\tilde{U}_{i,j,k+1/2}), \quad (36)$$

$$\mathbf{S}_{i,j,k}^{\text{dev}} = \hat{\mathbf{S}}_{i,j,k} - \mathbf{S}(\tilde{U}_{i,j,k}), \quad (37)$$

where  $\hat{\mathbf{F}}_{i+1/2,j,k}$  is computed according to Eq. (26) in the states

$$\mathbf{U}_{i+1/2,j,k}^{\text{L,R}} = \tilde{U}_{i+1/2,j,k} + \Delta \mathbf{U}_{i+1/2,j,k}^{\text{L,R}}, \quad (38)$$

while  $\mathbf{F}(\tilde{U}_{i+1/2,j,k})$  corresponds to the physical fluxes in Eq. (21) evaluated in the target solution at the cell boundary. The deviations  $\Delta \mathbf{U}_{i,j,k}$ , rather than the states  $\mathbf{U}_{i,j,k}$ , are reconstructed to the boundary of the cell<sup>11</sup>. This guarantees that magnetohydrostatic solutions are preserved on the discrete grid, since in that case  $\Delta \mathbf{U}_{i,j,k} = \mathbf{0}$ , which leads to

$$\hat{\mathbf{F}}_{i+1/2,j,k} = \mathcal{F}(\tilde{U}_{i+1/2,j,k}, \tilde{U}_{i+1/2,j,k}) = \mathbf{F}(\tilde{U}_{i+1/2,j,k}). \quad (39)$$

Thus, the resulting method is well-balanced. Moreover, by removing the numerical errors arising from the magnetohydrostatic stratification, this method allows low-Mach flows to be simulated in stratified setups, which only cause small deviations from the MHSE state and would be completely dominated by spurious flows otherwise.

### 3.4. Constrained transport method

The divergence-free constraint described in Sect. 2.4 is not automatically satisfied if the induction equation is solved with Godunov-type schemes. As a result, magnetic monopoles are created locally at each time step and tend to accumulate, as they cannot be transported away by any of the MHD waves. If not properly treated, these artifacts can accelerate the flow along the magnetic field lines, generate wrong field topologies, and ultimately lead to severe stability problems (Brackbill & Barnes 1980).

Different strategies have been presented in the literature to cure this problem (for a review of these methods, see Tóth 2000). Among these, the eight-wave formulation (Powell 1997; Powell et al. 1999) modifies the MHD equations by including additional source terms that are proportional to  $\nabla \cdot \mathbf{B}$ . The modified system has an additional nonzero eigenvalue  $\lambda_8 = V_x$ , which transports jumps in the normal component (to the cell interface) of the magnetic field, so numerical monopoles are advected with the flow and do not accumulate over time.

Other solutions rely on divergence cleaning schemes (Dedner et al. 2002), where the divergence constraint is coupled to the MHD system using a generalized Lagrangian multiplier,  $\psi$ . This allows numerical monopoles to be transported with the maximum available speed on the grid and divergence errors to be damped at the same time.

One downside of both the eight-wave formulation and divergence cleaning is that they are not conservative and they cannot enforce any discretization of  $\nabla \cdot \mathbf{B}$  to zero. Furthermore, these methods are most effective when open boundaries are used, so that the magnetic monopoles can leave the domain. However, this is rarely the case for simulations of stellar interiors, where impermeable boundaries are often used to avoid a significant mass loss from the system.

Constrained transport methods based on a staggered formulation, instead, conserve the magnetic flux through the boundaries of each cell and force one particular discretization of  $\nabla \cdot \mathbf{B}$  to remain zero within round-off errors (Evans & Hawley 1988; Dai & Woodward 1998; Balsara & Spicer 1999; Tóth 2000; Londrillo & del Zanna 2004; Gardiner & Stone 2008; Mignone & Del Zanna 2021). Although a conservative scheme cannot guarantee that the discretized Lorentz force is orthogonal to the magnetic field lines in each cell of the computational grid (Tóth 2000), the magnitude of the parallel component of

<sup>11</sup> Deviations in the primitive variables can also be reconstructed if the corresponding equilibrium values are provided at the cell centers and at the cell boundaries.

the force acting on the fluid is much smaller than in other methods.

The key point of staggered constrained transport methods is to compute the surface integral of Eq. (19) over cell boundaries using Stokes's theorem, which leads to the finite-area equation<sup>12</sup>

$$\frac{\partial \hat{B}_{x,i+1/2,j,k}}{\partial t} = -\frac{1}{\Delta y} \left( \hat{\mathcal{E}}_{z,i+1/2,j+1/2,k} - \hat{\mathcal{E}}_{z,i+1/2,j-1/2,k} \right) + \frac{1}{\Delta z} \left( \hat{\mathcal{E}}_{y,i+1/2,j,k+1/2} - \hat{\mathcal{E}}_{y,i+1/2,j,k-1/2} \right). \quad (40)$$

Here,  $\hat{B}_{x,i+1/2,j,k}$  is the surface-averaged magnetic field component normal to the cell boundary

$$\hat{B}_{x,i+1/2,j,k} = \frac{1}{A_{i+1/2,j,k}} \int_{A_{i+1/2,j,k}} \mathbf{B} \cdot \hat{\mathbf{n}} dA, \quad (41)$$

while the line-averaged electromotive force is defined as

$$\hat{\mathcal{E}}_{z,i+1/2,j+1/2,k} = \frac{1}{\Delta z_{i+1/2,j+1/2,k}} \int_{\Delta z_{i+1/2,j+1/2,k}} \mathcal{E}_z dz. \quad (42)$$

Analogous formulas can be derived for the other components of the magnetic field and the electromotive force.

In order to solve Eq. (40) numerically, a proper estimate for  $\hat{B}_{x,i+1/2,j,k}$  and  $\hat{\mathcal{E}}_{z,i+1/2,j+1/2,k}$  must be provided. For the former, we approximate the surface-averaged quantity with its value at the center of the cell boundary,

$$\hat{B}_{x,i+1/2,j,k} \simeq B_{x,i+1/2,j,k}, \quad (43)$$

which is accurate to second order. In contrast to the standard finite-volume approach, here the magnetic field component normal to the interface is stored at cell boundaries, while the line-averaged electromotive force is evaluated at cell edges. Thus, the operation is performed on a staggered grid. Since the parallel magnetic field still needs to be reconstructed to compute the flux function, its value at cell-center locations is estimated as a simple arithmetic average between the neighboring cell interfaces:

$$\begin{aligned} \hat{B}_{x,i,j,k} &= \frac{1}{2} \left( \hat{B}_{x,i-1/2,j,k} + \hat{B}_{x,i+1/2,j,k} \right), \\ \hat{B}_{y,i,j,k} &= \frac{1}{2} \left( \hat{B}_{y,i,j-1/2,k} + \hat{B}_{y,i,j+1/2,k} \right), \\ \hat{B}_{z,i,j,k} &= \frac{1}{2} \left( \hat{B}_{z,i,j,k-1/2} + \hat{B}_{z,i,j,k+1/2} \right). \end{aligned} \quad (44)$$

To compute the line-averaged electromotive force in Eq. (42), in SLH we use the CT-contact algorithm of [Gardiner & Stone \(2005\)](#). In this method, the electric field at cell edges is computed as a simple arithmetic average of the four neighboring face-centered electromotive force components, with the addition of a diffusion term that helps removing spurious oscillations when the magnetic field is advected. For instance,  $\hat{\mathcal{E}}_{z,i+1/2,j+1/2,k}$

is approximated to second-order accuracy by

$$\begin{aligned} \hat{\mathcal{E}}_{z,i+1/2,j+1/2,k} &\simeq \frac{1}{4} \left( \bar{\mathcal{E}}_{z,i+1/2,j,k} + \bar{\mathcal{E}}_{z,i+1/2,j+1,k} \right. \\ &\quad \left. + \bar{\mathcal{E}}_{z,i,j+1/2,k} + \bar{\mathcal{E}}_{z,i+1,j+1/2,k} \right) \\ &\quad + \frac{\Delta y}{8} \left\{ \left( \frac{\partial \mathcal{E}_z}{\partial y} \right)_{i+1/2,j+1/4,k} - \left( \frac{\partial \mathcal{E}_z}{\partial y} \right)_{i+1/2,j+3/4,k} \right\} \\ &\quad + \frac{\Delta x}{8} \left\{ \left( \frac{\partial \mathcal{E}_z}{\partial x} \right)_{i+1/4,j+1/2,k} - \left( \frac{\partial \mathcal{E}_z}{\partial x} \right)_{i+3/4,j+1/2,k} \right\}, \end{aligned} \quad (45)$$

where  $\bar{\mathcal{E}}_z$  can be computed from the solution to the Riemann problem in Eq. (26). The calculation for the  $x$ - and  $y$ -component is again analogous. The upwind diffusion term enters in the derivatives of the electromotive force in Eq. (45), which are obtained according to the sign  $s_{i+1/2,j,k}$  of the entropy (contact) waves at the cell interfaces:

$$\begin{aligned} \left( \frac{\partial \mathcal{E}_z}{\partial y} \right)_{i+1/2,j+1/4,k} &= \frac{1 + s_{i+1/2,j,k}}{2} \left( \frac{\bar{\mathcal{E}}_{z,i,j+1/2,k} - \mathcal{E}_{z,i,j,k}^{\text{cc}}}{\Delta y/2} \right) \\ &\quad + \frac{1 - s_{i+1/2,j,k}}{2} \left( \frac{\bar{\mathcal{E}}_{z,i+1,j+1/2,k} - \mathcal{E}_{z,i+1,j,k}^{\text{cc}}}{\Delta y/2} \right). \end{aligned} \quad (46)$$

Here  $\mathcal{E}_{z,i,j,k}^{\text{cc}} = (-\mathbf{V}_{i,j,k} \times \mathbf{B}_{i,j,k})_z$  represents the  $z$ -component of the cell-centered electromotive force. The discretization of the line-averaged electromotive force leads to a semi-discrete form of Eq. (40) that can be integrated numerically in time. Any time-stepper that solves the resulting system of ODEs can keep the cell-volume average of  $\nabla \cdot \mathbf{B}$ ,

$$\begin{aligned} (\nabla \cdot \mathbf{B})_{i,j,k} &= \frac{\hat{B}_{x,i+1/2,j,k} - \hat{B}_{x,i-1/2,j,k}}{\Delta x} \\ &\quad + \frac{\hat{B}_{y,i,j+1/2,k} - \hat{B}_{y,i,j-1/2,k}}{\Delta y} \\ &\quad + \frac{\hat{B}_{z,i,j,k+1/2} - \hat{B}_{z,i,j,k-1/2}}{\Delta z}, \end{aligned} \quad (47)$$

within rounding errors.

#### 4. Time integration algorithm

The CFL constraint in time-explicit marching schemes restricts the time step to the crossing time of the fastest wave resulting from the underlying PDEs over a grid cell. In low-Mach-number flows, the fast magnetosonic wave speeds become very large, so that the time step needs to be reduced accordingly. Thus, simulating the evolution of slow fluid motions and Alfvén waves becomes expensive. In these regimes, implicit methods, in which the time step is not limited by stability conditions but only by the desired accuracy, represent an attractive alternative. When using such methods, the time step should be restricted to the shortest advection and Alfvén crossing time over one grid cell. If the sonic Mach number is small enough, the possibility of larger chosen time steps then outweighs the disadvantage of higher computational costs for a single time step by using the implicit solver.

As outlined in Sect. 1, we split the induction equation (see Eq. (4)) from the continuity, momentum and energy equations

<sup>12</sup> Here the calculation is made over the cell boundary  $(i + 1/2, j, k)$ .

(see Eqs. (1)–(3)), based on the approach described by Fuchs et al. (2009). This allows different spatial and temporal discretizations to be used depending on the problem at hand. In regimes of low Mach numbers and high  $\beta$  values, the stiffness is mostly generated by the pressure flux  $\propto 1/\hat{\mathcal{M}}_{\text{son}}^2$  in the momentum equation, while the nondimensional form of the induction equation does not depend on the Mach number of the flow (see Sect. 2.2). This suggests that implicit time discretization only needs to be applied to the subset of continuity, momentum and energy equations, whereas the induction equation can be solved with explicit time-steppers. These two updates can be combined to second-order accuracy with Strang splitting (Strang 1968):

$$\mathbf{U}^{n+1} = \mathcal{I}^{(\frac{1}{2}\Delta t)} \mathcal{H}^{(\Delta t)} \mathcal{I}^{(\frac{1}{2}\Delta t)} \mathbf{U}^n. \quad (48)$$

Here,  $\mathcal{I}$  represents a linear operator that updates only the magnetic field with an explicit marching scheme, while the nonlinear operator  $\mathcal{H}$  updates density, momentum and total energy (including source terms) using an implicit stepper. In each sub-step of Strang splitting, the discretization of the fluxes, source terms, and electromotive force is performed according to the methods described in Sect. 3.

In SLH, several implicit time-steppers can be used to solve the semi-discrete form of Eq. (22), such as first-order backward-Euler, higher-order ESDIRK schemes, and Crank-Nicolson. The resulting nonlinear system of equations is solved iteratively with a root-finding Raphson–Newton algorithm, which relies on the analytic formulation of the flux-Jacobian. Iterative linear solvers (such as BiCGSTAB(l), GMRES, and Multigrid) are used in combination with preconditioning techniques to solve each sub-step of the nonlinear solver<sup>13</sup>. In contrast, the semi-discrete form of the induction equation (see Eq. (40)) is solved with the time-explicit SSP-RK2 method of Shu & Osher (1988).

Numerical experiments performed with the proposed implicit–explicit Strang splitting (IESS) approach suggest that the maximum time step allowed for stability is approximately determined by

$$\Delta t = \min_{\Omega=(i,j,k)} \left\{ \frac{\Delta x}{|V_{x,\Omega}| + c_{a,x,\Omega}}, \frac{\Delta y}{|V_{y,\Omega}| + c_{a,y,\Omega}}, \frac{\Delta z}{|V_{z,\Omega}| + c_{a,z,\Omega}} \right\}, \quad (49)$$

so that the propagation of fluid motions and Alfvén waves is well resolved in time. This time step is approximately  $1/\mathcal{M}_{\text{son}}$  larger than that allowed by the conventional CFL condition if the plasma- $\beta$  is high, which considerably reduces the computational effort when simulating low-Mach-number flows. The price one has to pay is that the propagation of fast magnetosonic waves is not well resolved in time. Another advantage of IESS is that it can easily be implemented within the framework of the SLH code, which already had fully implicit time integration capabilities to solve the compressible Euler equations.

A single step of the described time-marching scheme can be summarized in the following way. First,  $\Delta t$  is obtained from Eq. (49) given  $\mathbf{B}^n$ ,  $\rho^n$ ,  $\rho \mathbf{V}^n$ , and  $\rho E_\phi^n$ . If gravity is not present,  $e_\phi$  does not appear in Eq. (5).

Second, SSP-RK2 and CT-contact are used to solve the induction equation over the first half of the time step,  $\Delta t/2$ . This results in an intermediate solution for the magnetic field,  $\mathbf{B}^{n+1/2}$ .

Third, this intermediate solution,  $\mathbf{B}^{n+1/2}$ , is used to solve the continuity, momentum, and energy equations over the full time step,  $\Delta t$ , with an implicit time-stepper. If gravity is present, then

the well-balancing method described in Sect. 3.3 can be used. Any other source term is also considered in this step. This allows the solution for density, momentum, and energy to be obtained at the next step,  $\rho^{n+1}$ ,  $\rho \mathbf{V}^{n+1}$ , and  $\rho E_\phi^{n+1}$ .

Fourth,  $\mathbf{B}^{n+1/2}$ ,  $\rho^{n+1}$ ,  $\rho \mathbf{V}^{n+1}$ , and  $\rho E_\phi^{n+1}$  are used to solve the induction equation over  $\Delta t/2$ . This yields the magnetic field at the final step  $\mathbf{B}^{n+1}$ .

The proposed MHD scheme is extremely modular, so different time-steppers, spatial reconstruction schemes and approximate Riemann solvers can be used in each sub-step of the algorithm, and well-balancing can be switched off if required. For instance, in addition to LHLLED, the original five-wave HLLD solver of Miyoshi & Kusano (2005) is also implemented in SLH. The performance and accuracy of both Riemann solvers are checked in some of the numerical experiments described in Sect. 5. Finally, in case slightly subsonic or transonic regimes need to be modeled with SLH, a fully un-split SSP-RK2 explicit time-stepper can be used.

## 5. Numerical tests

In order to assess the accuracy and performance of the newly implemented MHD algorithm, we have to rely on numerical experiments. Since the main purpose of the scheme is to be able to simulate MHD flows at low sonic Mach numbers in strong stratifications, we decide not to show the typical tests commonly run by other MHD codes. These usually include shock-tubes, supersonic vortices and magnetic blasts, which, however, are designed to test the shock-capturing capabilities of a numerical scheme. Instead, we ran a series of verification benchmarks that are more suited for testing the low-Mach properties of an MHD code.

As a first test, we solved the homogeneous MHD equations in three different cases (i, ii, and iii). In order to check the convergence and scaling of the methods for the whole MHD wave family, we performed a 1D linear analysis (i). The scaling was also checked against the advection of a stable MHD vortex in a wide range of Mach numbers (ii). Such a setup is particularly important as it resembles the typical vortex structures present in magneto-convection. The simulations were also run in fully-explicit mode using SSP-RK2, which allows the speed-up of IESS to be quantified as a function of the Mach number.

The ability of accurately evolving shear instabilities is fundamental in the context of simulations of turbulence as they generate additional vorticity, which leads to the cascade of energy. For this reason, we ran simulations of a magnetized Kelvin–Helmholtz instability (iii). We followed the growth and evolution of the instability in a resolution study from low-Mach to slightly subsonic regimes. A comparison between the HLLD and LHLLED solvers was performed to show the advantage of using low-dissipation fluxes over conventional methods in regimes of low Mach numbers.

Then we considered two setups in which gravity is present (iv, v). To check the entropy-conservation properties of the scheme based on the deviation well-balancing method, we modeled the rise of a parcel of fluid with higher entropy content than the (isentropic) background stratification, that is, a “hot bubble” (iv). By changing the magnitude of the entropy perturbation, we simulated different rise velocities of the bubble, down to Mach numbers of  $\mathcal{M}_{\text{son}} \sim 10^{-4}$ . To quantify the magnitude of the numerical errors generated by an unbalanced stratification,

<sup>13</sup> For more details on the implementation of implicit time stepping in SLH, see Miczek (2013) and Miczek et al. (2015).

we also simulated the rise of the bubble at  $\mathcal{M}_{\text{son}} \sim 10^{-2}$  without well-balancing.

Finally, we simulated a fully 3D small-scale dynamo (SSD) amplification in a star-like environment at moderate grid resolutions ( $v$ ). By changing the rate at which energy is injected in the system, we simulated progressively slower flows down to  $\mathcal{M}_{\text{son}} \sim 10^{-3}$ .

For all of the following tests, an ideal gas EoS was used with  $\gamma = 5/3$  except when specified otherwise. Within the framework of the IESS time-marching scheme described in Sect. 4, ESDIRK23 was chosen to treat the implicit part of the algorithm. This guarantees second-order accuracy in time. The time step in Eq. (49) was reduced by 20% to get a more conservative stability criterion. Finally, unlimited linear reconstruction, which is second-order accurate in space, was applied to primitive variables. Overall, the proposed scheme is (globally) second-order accurate.

### 5.1. Linear analysis

In this test, we followed the propagation of linear modes for all the MHD waves (see Sect. 2) as a way to get quantitative estimates of diffusion errors and to check the scaling of the numerical scheme. The setup is based on Stone et al. (2008), which we modified by considering much larger values of the gas pressure to increase the fast magnetosonic speed relative to the Alfvén and entropy wave speeds. Such a stiff system is characteristic of low-Mach flows in high- $\beta$  environments (see Sect. 2.2).

The homogeneous MHD equations were solved on a periodic 1D Cartesian grid divided into  $N$  cells, with the spatial domain ranging from 0 to  $L = 1$ . For the  $i$ th wave, the solution at  $t = 0$  was obtained by perturbing a uniform medium  $\mathbf{w}_0 = (1, 0, 0, 0, 10^3/\gamma, 1, \sqrt{2}, 1/2)$  with  $\delta\mathbf{w} = A\mathbf{R}_i(\mathbf{w}_0)\sin(2\pi x/L)$ , where  $\mathbf{w}$  is the vector of primitive variables ( $\rho, V_x, V_y, V_z, p, B_x, B_y, B_z$ ),  $A = 10^{-4}$  is the amplitude of the perturbation,  $x$  is the spatial coordinate and  $\mathbf{R}_i$  is the  $i$ th column of the right-eigenvector matrix (see Appendix A.3 in Stone et al. 2008). The chosen values for  $\mathbf{w}_0$  are such that  $c_{f,x} \approx 40.85$ ,  $c_{a,x} = 1$  and  $c_{s,x} \approx 0.99$ . For the entropy mode, we set  $V_x = 1$ , so the sonic Mach number of the wave is  $\mathcal{M}_{\text{son}} \approx 0.032$ . The simulations were run for one crossing time defined as  $t_c = L/\lambda_i$ , where  $\lambda_i$  is the wave speed. The  $L_1$  error was then computed for each primitive variable  $w_k$  as

$$L_{1,i}(w_k) = \frac{1}{N} \sum_j |w_{k,j}(t = t_c) - w_{k,j}(t = 0)|, \quad (50)$$

and the global error associated with the  $i$ th wave was then computed as

$$\delta_i = \frac{1}{A} \sqrt{\sum_k \left( \frac{L_{1,i}(w_k)}{\xi(w_{0,k})} \right)^2}, \quad (51)$$

with

$$\xi(w_{0,k}) = \begin{cases} w_{0,k}, & \text{for } w_{0,k} > 0, \\ 1, & \text{otherwise.} \end{cases} \quad (52)$$

In Eq. (50),  $j$  is the spatial index. The tolerance of the Raphson-Newton algorithm was set to  $10^{-10}$ , so that the errors computed using Eq. (51) were not dominated by the finite convergence of the nonlinear solver.

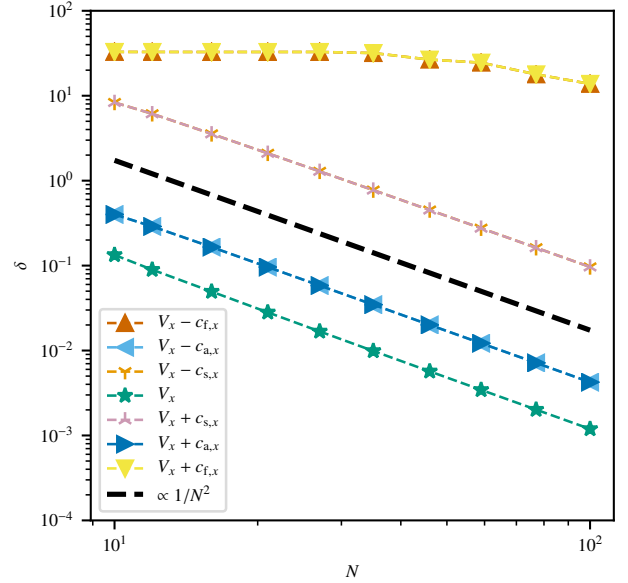


**Fig. 3.** Global error as a function of the grid resolution for the seven MHD waves after one crossing time,  $t_c$ . The dashed black line represents the second-order scaling.

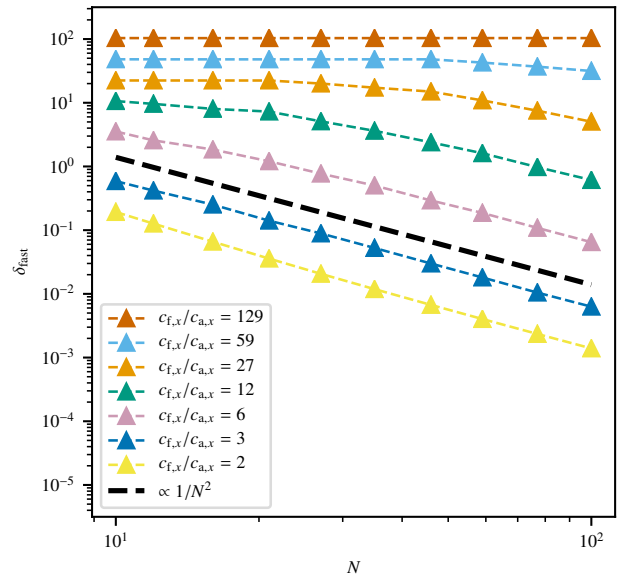


**Fig. 4.** Global error as a function of the grid resolution for the left-going fast magnetosonic wave. Different colors are associated with different values of  $c_{f,x}/c_{a,x}$ . The dashed black line is the second-order scaling.

Figure 3 shows the change of the global error as a function of  $N$  (ranging from 10 to 100) for all the seven MHD waves. Leftward and rightward propagating waves have identical errors. Since the MHD scheme relies on second-order methods to treat both the spatial and the temporal parts, the scheme converges with second-order accuracy for all waves except the fast magnetosonic waves, which are characterized by much larger errors. This is expected since IESS allows the MHD equations to be integrated over much longer time steps than the CFL constraint (see Sect. 4). As a consequence, the propagation of fast magnetosonic waves is not properly resolved in time and discretization errors strongly deteriorate the numerical solution. This effect is further quantified in Fig. 4, where we show the global error associated with the left-going fast magnetosonic wave as a



function of the grid resolution for different values of the gas pressure  $p$ , such that  $c_{f,x}/c_{a,x} = 2, 3, 6, 12, 27, 59, 129$ . Overall, the errors tend to decrease for smaller values of  $c_{f,x}/c_{a,x}$ , since the time step in Eq. (49) gets closer to the CFL time step and fast magnetosonic waves are progressively better resolved. Moreover, the simulations run with  $c_{f,x}/c_{a,x} \leq 27$  converge with second-order accuracy on the grids considered in this study.

## 5.2. Balsara vortex

In the previous section, we demonstrated that the current MHD scheme is capable of simulating linear waves with the expected (second-order) scaling with respect to resolution on 1D grids. In order to check the scaling in 2D and to test the low-Mach capabilities of the scheme, we considered the MHD vortex first described by Balsara (2004). This is an exact stationary solution of the ideal 2D homogeneous MHD equations, in which the distribution of the centrifugal acceleration, magnetic tension, gas and magnetic pressure gradients is such that the vortex is stable. The spatial domain is  $(x, y) \in [-5, 5] \times [-5, 5]$ , and we used  $64 \times 64$  grid cells with periodic boundaries in both directions. The initial conditions are given by

$$\begin{aligned} (V_x, V_y) &= \tilde{V} e^{\frac{1-r^2}{2}} (-y, x), \\ (B_x, B_y) &= \tilde{B} e^{\frac{1-r^2}{2}} (-y, x), \\ p &= 1 + \left[ \frac{\tilde{B}^2}{2} (1 - r^2) - \frac{\tilde{V}^2}{2} \right] e^{1-r^2}, \\ \rho &= 1, \end{aligned} \quad (53)$$

with  $r^2 = x^2 + y^2$ .  $\tilde{V}$  is the maximum rotational velocity of the vortex and  $\tilde{B}$  sets the value of the maximum Alfvén speed on the grid. To make this problem numerically more challenging, the vortex is advected along the diagonal of the computational grid, with  $|\mathbf{V}_{\text{adv}}| = \tilde{V}$ . The vortex is evolved for one advective crossing time  $t_{\text{adv}} = 10\sqrt{2}/\tilde{V}$ , after which it returns to the initial position. In this time interval, the vortex rotates 2.25 times.

We ran the grid of models

$$\begin{aligned} (\tilde{V}) \times (\beta_K) &= (10^{-5}, 10^{-4}, 10^{-3}, 10^{-2}, 10^{-1}) \\ &\times (10^{-2}, 10^{-1}, 1, 10^1, 10^2), \end{aligned} \quad (54)$$

with  $\beta_K = \tilde{B}^2/\tilde{V}^2$  being the ratio of the magnetic to the rotational kinetic energy, which is constant across the domain. Given this choice of parameters, the initial maximum Mach number  $\mathcal{M}_{\text{son}}$  ranges from  $1.55 \times 10^{-5}$  to  $1.55 \times 10^{-1}$ , so this parameter study covers both low Mach numbers and slightly subsonic regimes, in both weakly and strongly magnetized fluids.

Figure 5 shows the magnetic energy distribution after one advective crossing time  $t_{\text{adv}}$ . Numerical dissipation converts a fraction of kinetic and magnetic energy into internal energy, but the shape of the vortex is well preserved in all runs. The dissipation rate is virtually independent of  $\mathcal{M}_{\text{son}}$ . In contrast, dissipation of magnetic energy depends on the value of  $\beta_K$ . As already pointed out in Sect. 3.2, the pressure–diffusion coefficient in LHLLD has a residual scaling  $\mathcal{O}(1/\mathcal{M}_{\text{Alf}})$ . A larger value of  $\beta_K$  corresponds to lower  $\mathcal{M}_{\text{Alf}}$ , which then increases the magnitude of the numerical dissipation. The velocity field is progressively more diffused out and becomes less efficient in sustaining the magnetic field through induction against numerical resistivity.

To check the convergence of the scheme in 2D, we ran a vortex with  $\tilde{V} = 10^{-3}$  (corresponding to  $\max(\mathcal{M}_{\text{son}})_{t=0} = 1.55 \times 10^{-3}$ ) and  $\beta_K = 1$  at different resolutions<sup>14</sup>. At the end of the simulation, the  $L_1$  error was computed for each primitive variable  $w_k$  as

$$L_1(w_k) = \frac{1}{N^2} \sum_{i,j} |w_{k,i,j}(t = t_{\text{adv}}) - w_{k,i,j}(t = 0)|, \quad (55)$$

where  $i, j$  are the spatial indices. Figure 6 shows the convergence of the  $L_1$  error for different grids from  $N = 32$  up to  $N = 512$  cells per dimension. Convergence is second order for all primitive variables.

To compare the amount of numerical dissipation introduced by a standard and a low-Mach MHD flux function, we reran this last set of simulations with HLLD. In Fig. 7, we show the final rotational kinetic energy distribution obtained with the two methods:

$$E_R = \frac{1}{2}\rho \left[ (V_x - \tilde{V}/\sqrt{2})^2 + (V_y - \tilde{V}/\sqrt{2})^2 \right]. \quad (56)$$

At low resolution, HLLD considerably stretches the vortex and a large fraction of kinetic energy is dissipated into internal energy. In contrast, simulations run with LHLLD show mild dissipation and dispersion errors are only visible at the lowest resolutions. All simulations converge with increasing resolution, but the kinetic energy conservation in the vortex simulated with HLLD is still two orders of magnitude worse than that obtained with LHLLD at the highest resolution considered in this study.

As explained in Sect. 4, one advantage of IESS is that the MHD equations can be integrated on time steps longer than that allowed by the CFL condition without sacrificing stability. However, a single step of the proposed scheme is much more expensive than a single step of a more standard time-explicit marching scheme, as a large nonlinear system has to be solved iteratively with a Raphson–Newton method. Because of these competing effects, we expect the IESS scheme to be more efficient than an explicit time-stepper below a certain Mach number. To determine this threshold, we ran sets of simulations with the parameters

$$\begin{aligned} (\tilde{V}) \times (\beta_K) &= (10^{-4}, 10^{-3}, 10^{-2}, 10^{-1}) \\ &\times (10^{-1}, 1, 10^1), \end{aligned} \quad (57)$$

using both IESS and the explicit SSP-RK2<sup>15</sup> on  $40 \times 40$  grid cells. Every other sub-step of the Godunov method (like the spatial reconstruction, the LHLLD flux function and constrained transport) remained unchanged, so the only difference was in the time discretization. At the end of each simulation, the ratio of the wall-clock times  $\text{WCT}_{\text{SSP-RK2}}/\text{WCT}_{\text{IESS}}$  was taken as a measure of the relative efficiency between the marching schemes<sup>16</sup>. The results are shown in Fig. 8. As expected, the speed-up of IESS increases as the Mach number of the vortex is decreased. The simulations with  $\beta_K = 10$  are slower than the other cases, as the larger Alfvén speed considerably reduces the time step estimate

<sup>14</sup> We took these values as representative of the typical conditions found in stellar convection zones close to equipartition regimes (Augustson et al. 2016).

<sup>15</sup> For the time-explicit simulations, the CFL time step is reduced by 20%.

<sup>16</sup> No snapshots were saved throughout the simulations to minimize the cost of I/O operations.

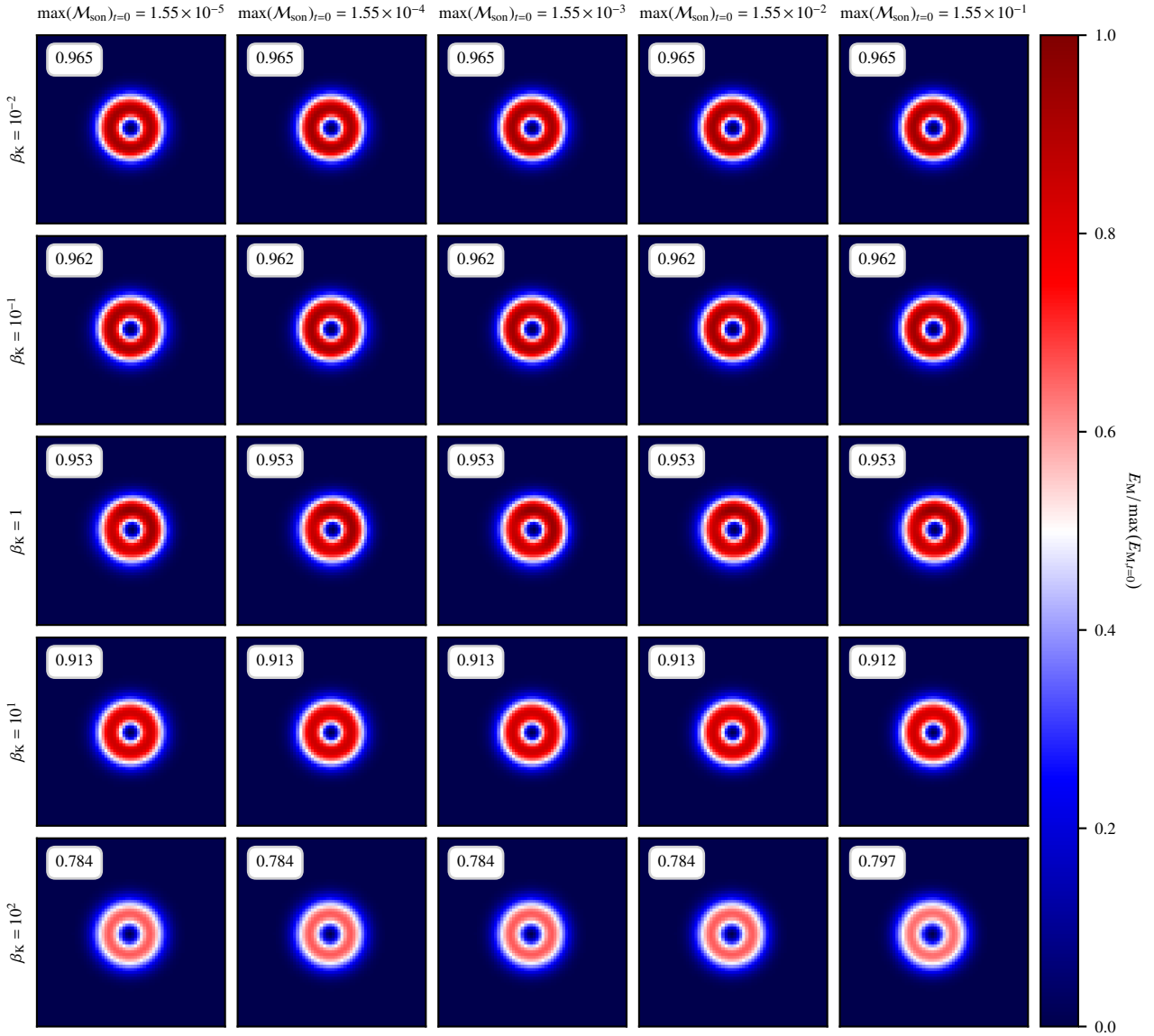


**Fig. 5.** Magnetic energy distribution of the Balsara vortex after one advective crossing time,  $t_{\text{adv}}$ , normalized by the maximum magnetic energy at  $t = 0$ . The ratio of the magnetic to the (rotational) kinetic energy of the vortex is varied along the  $y$ -axis (in descending order), while the initial maximum rotational velocity,  $\tilde{V}$ , varies along the  $x$ -axis. The inset in each subplot shows the ratio of the final to the initial magnetic energy. The vortex run with  $\tilde{V} = 10^{-1}$  and  $\beta_K = 10^2$  (bottom-right corner) has a maximum Mach number  $\max(\mathcal{M}_{\text{son}})_{t=0} = 1.65 \times 10^{-1}$ . In that system, the gas pressure drops in the regions around the center of the vortex to balance the large magnetic and centrifugal forces, which ultimately decreases the sound speed where the velocity is maximum.

in Eq. (49), while no significant difference is seen between  $\beta_K = 0.1$  and  $\beta_K = 1.0$ . IESS overtakes SSP-RK2 at  $\max(\mathcal{M}_{\text{son}})_{t=0} \simeq 4 \times 10^{-2}$  for  $\beta_K = (0.1, 1)$  and  $\max(\mathcal{M}_{\text{son}})_{t=0} \simeq 2 \times 10^{-2}$  for  $\beta_K = 10$ . At  $\max(\mathcal{M}_{\text{son}})_{t=0} = 10^{-3}$ , IESS is 10–20 times faster than SSP-RK2. This justifies the implementation efforts of a partially implicit time discretization algorithm for modeling slow flows.

### 5.3. Magnetized Kelvin–Helmholtz instability

For the following test, we ran MHD simulations of a Kelvin–Helmholtz instability. This is the primary instability that arises when there is a velocity shear within a continuous fluid, and it is the main source of vorticity that leads to the energy cascade in 3D turbulent flows. An accurate representation of this process is therefore a fundamental requirement for any numerical scheme

to be used for simulating magneto-convection. We considered a 2D domain with  $(x, y) \in [0, 2] \times [-0.5, 0.5]$ , mapped on a  $2N \times N$  grid. The horizontal velocity profile is given by

$$V_x = \mathcal{M}_x [1 - 2\eta(x)], \quad (58)$$

with

$$\eta(x) = \begin{cases} \frac{1}{2} \{1 + \sin[16\pi(y + 0.25)]\}, & \text{for } y > -\frac{9}{32} \text{ and } y < -\frac{7}{32}, \\ 1, & \text{for } y \geq -\frac{7}{32} \text{ and } y \leq \frac{7}{32}, \\ \frac{1}{2} \{1 - \sin[16\pi(y - 0.25)]\}, & \text{for } y > \frac{7}{32} \text{ and } y < \frac{9}{32}, \\ 0, & \text{otherwise.} \end{cases} \quad (59)$$

The parameter  $\mathcal{M}_x$  is the maximum sonic Mach number of the horizontal flow, and  $p = 1$  and  $\rho = \gamma$ , so initially the adiabatic

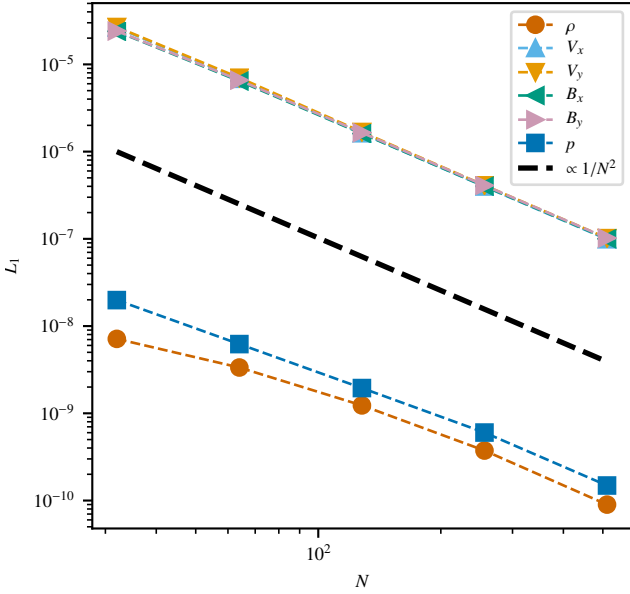


**Fig. 6.** Convergence of the  $L_1$  error in the Balsara vortex for each primitive variable as a function of resolution. For these simulations,  $\tilde{V} = 10^{-3}$  and  $\beta_K = 1$ . The dashed black line is the second-order scaling.

sound speed  $a$  is 1 everywhere. In this test,  $\gamma = 1.4$ . The magnetic field at  $t = 0$  is uniform and horizontal ( $B_x = 0.1M_x$ ), and the minimum Alfvén Mach number  $\mathcal{M}_{\text{Alf}}$  is 11.82 for all values of  $M_x$ .

It is well known that magnetic fields aligned with the shear flow have a stabilizing effect because they exert a restoring force on the perturbed interface (Chandrasekhar 1961). With a too strong field, the instability may reach saturation when the flow is still essentially laminar or it may be suppressed completely. Instead, weak magnetic stresses do not considerably affect the initial growth of the instability, so the flow can develop the typical vortex structures present in the pure hydrodynamic case. This leads to a much more complex evolution in the nonlinear phase (Frank et al. 1996). For this setup, nearly laminar flows are expected only when  $\min(\mathcal{M}_{\text{Alf}})_{t=0} \lesssim 1.1$ , as shown in Fig. A.1.

The instability is started by adding a perturbation to the  $y$ -velocity component in the initial state,  $V_y = 0.1M_x \sin(2\pi x)$  (see Fig. 9). The initial conditions are periodic in both directions. The evolution of the Kelvin–Helmholtz instability was studied for a wide range of Mach numbers and grid resolutions:

$$\begin{aligned}
 (\mathcal{M}_x) \times (N) &= (10^{-4}, 10^{-3}, 10^{-2}, 10^{-1}) \\
 &\times (32, 64, 128, 256, 512, 1024).
 \end{aligned}
 \tag{60}$$

The final time reached by each simulation was set according to the initial amplitude of the shear flow ( $t_{\text{max}} = 4.8/M_x$ ). The chosen initial conditions are such that the interface across the shear flow is smooth and resolved, which leads to convergent results at least in the early stages of the evolution of the flow. As in the previous test, we compared the results obtained with both the HLLD and LHLLD solvers.

Figures 10 and 11 show the time evolution of the  $y$ -direction kinetic energy  $E_{K,y} = \sum_{ij} (\rho V_y^2)_{ij} / 2$  and the total magnetic energy  $E_M = \sum_{ij} |\mathbf{B}_{ij}|^2 / 2$  for all the simulations considered in this study. As in the previous problem,  $i, j$  are the spatial indices. Because of stretching and wrapping of the field lines within the vortices, the magnetic energy slowly increases with time at the expense

of the kinetic energy content of the flow. After the primary rolls reach the top and bottom boundaries ( $t/t_{\text{max}} \approx 0.25$ ),  $E_{K,y}$  saturates due to the periodicity of the grid and starts to decrease. The secondary vortices keep winding up the magnetic field lines until Lorentz forces start to feedback on the velocity field, breaking down these inner structures. The two original shear interfaces get closer to each other (see Fig. A.3) until a strong numerical reconnection event happens at  $t/t_{\text{max}} \approx 0.45$ , which violently decouples the primary rolls and causes a secondary peak in  $E_{K,y}$  at  $t/t_{\text{max}} \approx 0.5$ . After this time, other reconnection events break down the flow into smaller structures, and both the magnetic and the kinetic energy are slowly dissipated away by the action of numerical resistivity and viscosity.

Since in this case we solved the ideal MHD equations, there is no characteristic scale on which magnetic and kinetic energy are dissipated into heat, so numerical effects play a significant role on progressively smaller scales at higher resolution. Thus, the amplification and dissipation of magnetic energy hardly converge for the resolutions considered in this study. The initial growth of  $E_{K,y}$ , in contrast, is not much influenced by the initial weak field, and it is mostly determined by the strength of the shear flows and the width of the shear interface, which is resolved. As a consequence,  $E_{K,y}$  converges until the major numerical reconnection event affects the velocity field. As shown in Fig. 10, the HLLD solver requires more resolution to reach convergence as the setup is run at progressively lower sonic Mach numbers. Eventually, the Mach-dependent pressure-diffusion coefficient in Eq. (27) completely dominates the evolution of the flow and deteriorates the numerical solution. For this reason, at  $M_x = 10^{-4}$  we were able to successfully run with HLLD only the  $64 \times 32$  and  $128 \times 64$  grids, while for higher resolutions the nonlinear solver failed to converge.

The effects of numerical dissipation are also shown in Fig. 12, where the distributions of the sonic Mach number obtained with HLLD and LHLLD are compared at fixed resolution ( $128 \times 64$  cells) for different values of  $M_x$  at  $t/t_{\text{max}} = 1/6$ . While in moderately subsonic regimes the large-scale structures in the flow are qualitatively similar, for lower Mach numbers HLLD introduces progressively more dissipation and the instability is eventually halted. When LHLLD is used instead, the morphology of the flow seems to be independent of the Mach number.

Finally, we performed a quantitative convergence study by computing the  $L_1$  error associated with  $E_{K,y}$  at  $t/t_{\text{max}} = 1/6$ . At this time, the first rolls have developed to considerable vertical wavelengths (see Fig. 12) so that the instability has already entered the nonlinear regime, and the flow is expected to converge as shown in Fig. 10. The  $L_1$  error was computed against a reference solution, which was taken from the highest grid resolution runs considered in this test ( $N = 1024$ ) using the LHLLD solver. All simulations (including the reference solutions) were down-sampled to a  $64 \times 32$  grid, so that the errors could directly be computed for different resolutions. This analysis was repeated for different values of  $M_x$  using both HLLD and LHLLD. The results are shown in Fig. 13. The errors are rescaled by  $M_x^2$  so that curves corresponding to different sonic Mach numbers lie on the same scale. Overall, the convergence is second-order with  $N$  for all simulations. LHLLD provides almost identical (rescaled) errors at given resolution in different regimes of Mach numbers. This is expected because the numerical dissipation introduced by this solver does not depend on  $M_{\text{son}}$ , thanks to the low-Mach fix in Eq. (30). Instead, the errors computed for the HLLD runs show a clear dependence on the sonic Mach number, and the errors get larger for slower flows. In particular, at  $M_x = 0.1$ ,

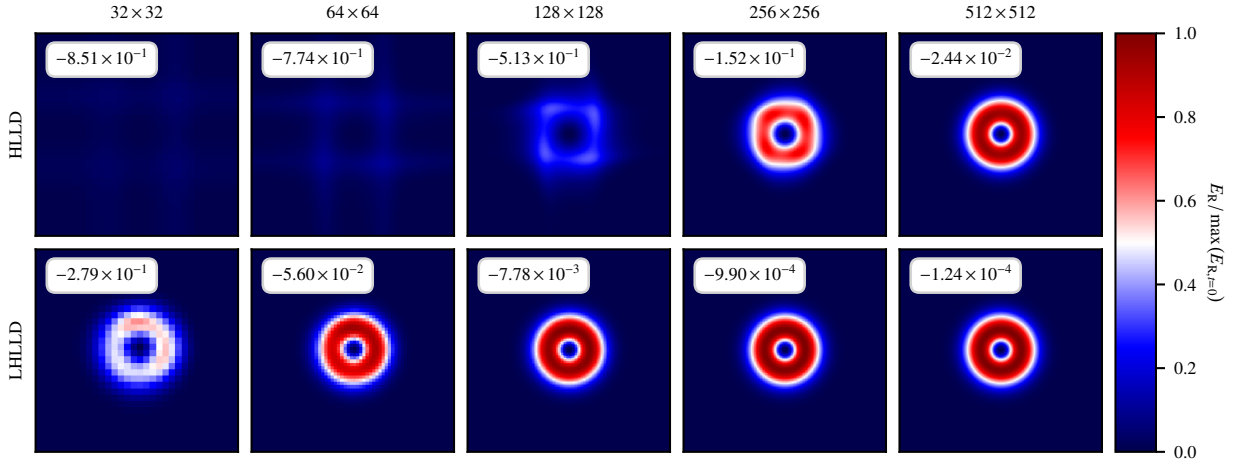


**Fig. 7.** Distribution of the rotational kinetic energy (normalized by the maximum initial value) of the Balsara vortex after one advective time,  $t_{\text{adv}}$ , at  $\tilde{V} = 10^{-3}$  and  $\beta_K = 1$ . The *top panels* show the vortices obtained with the HLLD flux function as a function of resolution, while the plots in the *bottom panels* are obtained with LHLLD. The insets show the fraction of rotational kinetic energy that has been dissipated by the end of the simulation:  $(E_{R,t=t_{\text{adv}}})_{\text{tot}} / (E_{R,t=0})_{\text{tot}} - 1$ .

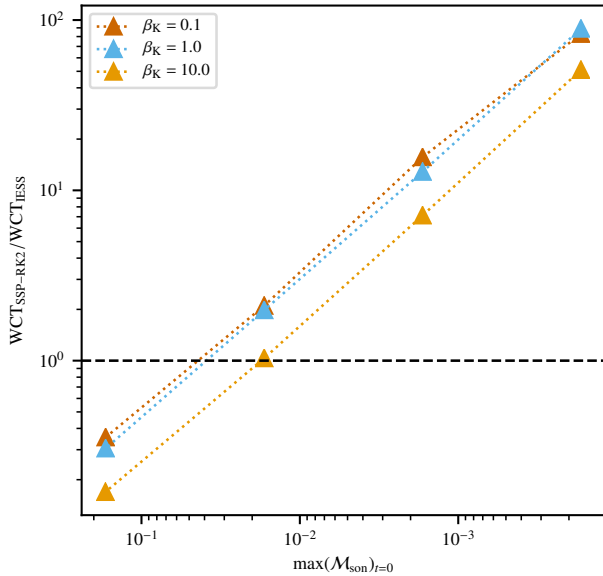


**Fig. 8.** Ratio of the wall clock times obtained with SSP-RK2 and IESS as a function of initial maximum sonic Mach number of the Balsara vortex for different magnetic to (rotational) kinetic energy ratios. The dashed black line is drawn to represent the same relative efficiency.

HLLD needs approximately 1.2 times the resolution of LHLLD to achieve the same accuracy, which justifies the use of HLLD in this regime of Mach numbers. Instead, when  $\mathcal{M}_x = 10^{-2}$  and  $\mathcal{M}_x = 10^{-3}$ , HLLD needs respectively twice or four times the resolution to be as accurate as the low-dissipation flux, which increases the amount of computing time by 8 or 64. Thus, the use of a low-Mach approximate Riemann solver becomes indispensable for providing accurate results in regimes of low sonic Mach numbers with moderate grid resolutions, which would be unfeasible with more standard solvers.

#### 5.4. Hot bubble

Flows in deep stellar convection zones are usually characterized by the presence of slow parcels of fluid that move in a stratification that is unstable against convection. In the absence of

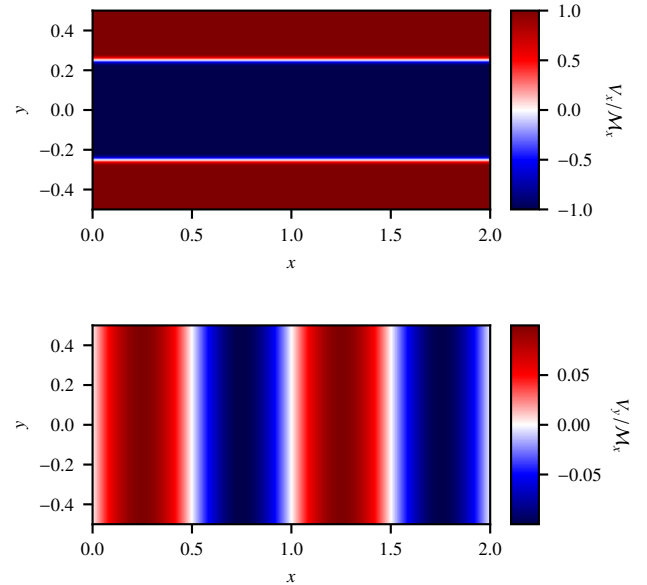


**Fig. 9.** Initial setups of  $V_x$  and  $V_y$  (here rescaled by  $\mathcal{M}_x$ ) used for simulating the growth of the Kelvin–Helmholtz instability.

volume heating and cooling processes, these packets of fluid preserve their entropy content until they mix with the surroundings. Therefore, a numerical scheme designed to simulate such flows should have good entropy-conservation properties. However, entropy conservation is hard to achieve if the density, temperature and pressure stratifications span several orders of magnitude and if the flows are very slow, since their entropy content would only be slightly higher or lower than the adiabatic surroundings<sup>17</sup>. Under these conditions, discretization errors caused by an imperfect balance of the background MHSE stratification can dominate the dynamics and deteriorate the numerical solution. As shown in Sect. 3.3, the magnitude of such errors can be drastically reduced by using well-balancing techniques.

<sup>17</sup> Better entropy-conservation properties can be achieved by directly evolving the specific entropy instead of  $\rho E_\phi$ . However, this approach does not conserve the total energy.



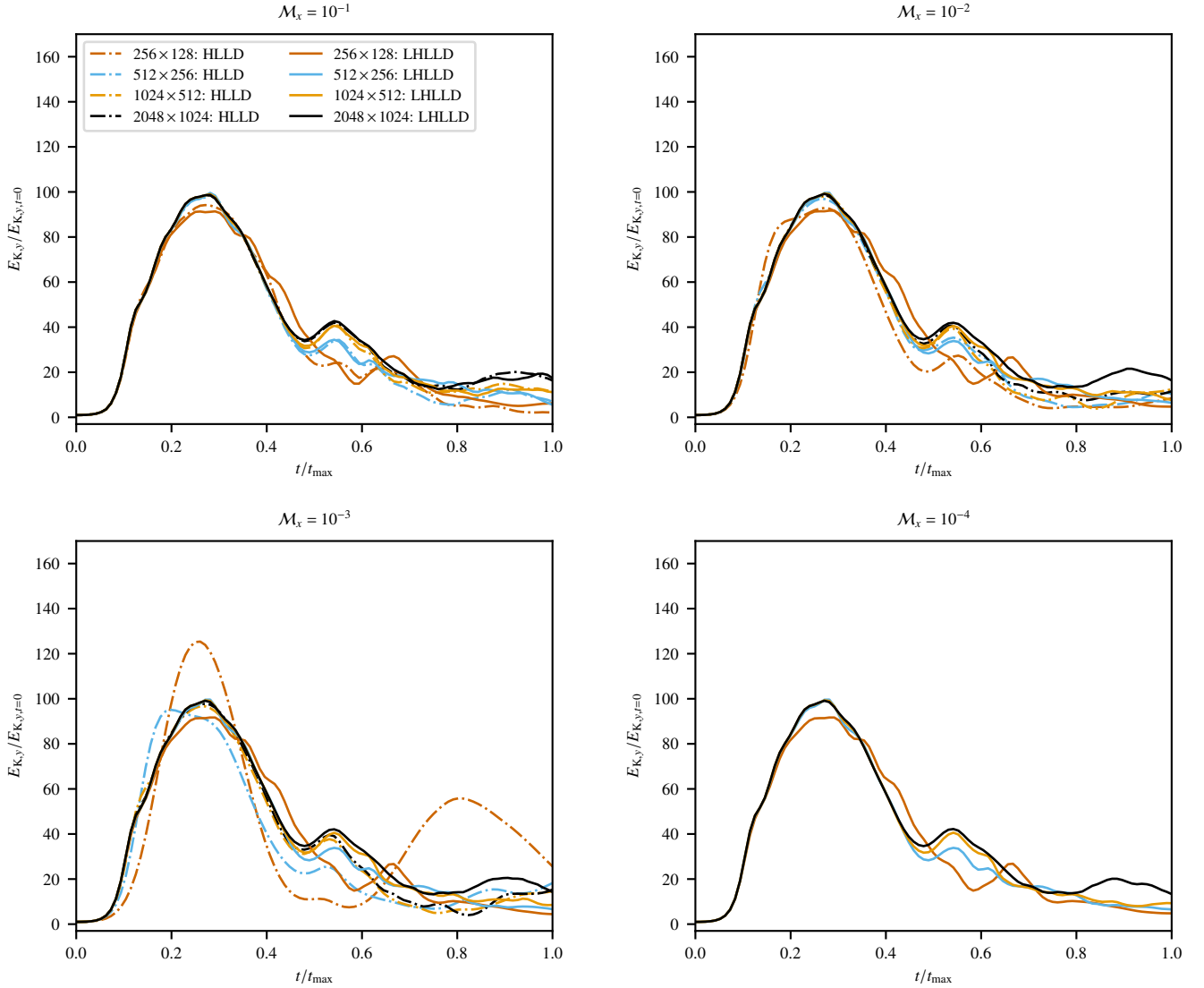


**Fig. 10.** Time evolution of the  $y$ -direction kinetic energy rescaled by its initial value in the magnetized Kelvin–Helmholtz instability test problem. Each panel corresponds to a different initial Mach number,  $\mathcal{M}_x$ . Different colors are used for different grid resolutions (the  $64 \times 32$  and  $128 \times 64$  grids cells have been left out for clarity). Results obtained with the HLLD solver are represented by dot-dashed lines, while solid lines are used for LHLLD. The solid black line in each panel is the reference solution. As explained in the text, the nonlinear solver does not converge when using HLLD at  $\mathcal{M}_x = 10^{-4}$  for  $N > 64$ .

In this section, we check the entropy-conservation properties of the MHD scheme implemented in SLH by running simulations of the hot bubble setup described by [Edelmann et al. \(2021\)](#), where a bubble of higher entropy content with respect to the surroundings buoyantly rises in an adiabatic stratification. The physical domain is mapped on a 2D Cartesian grid ( $N_x = 2/3 \times N_y$ ), and the background stratification is in MHSE. Boundary conditions are periodic everywhere and the gravitational acceleration takes the form

$$g_y(y) = g_0 \sin(k_y y), \quad (61)$$

where  $g_0 = -1.09904373 \times 10^5 \text{ cm s}^{-2}$ ,  $k_y = 2\pi/L_y$ ,  $y$  is the vertical spatial coordinate, and  $L_y$  is the vertical extent of the grid. The value of  $g_0$  is set such that the ratio of the maximum to the minimum gas pressure<sup>18</sup>  $p(y)$  is 100, which corresponds to

<sup>18</sup> More details on how to compute the pressure profile can be found in [Edelmann et al. \(2021\)](#).

4.6 pressure scale heights. The entropy profile inside the bubble is given by

$$A = A_0 \left\{ 1 + \left( \frac{\Delta A}{A} \right)_{t=0} \cos \left( \frac{\pi r}{2 r_0} \right)^2 \right\}, \quad (62)$$

where  $A_0$  is background entropy,  $r_0$  is the radius of the bubble,  $r$  is the distance from the center of the bubble and  $(\Delta A/A)_{t=0}$  is the initial entropy perturbation. The density is

$$\rho(y) = \left( \frac{p(y)}{A} \right)^{1/\gamma}, \quad (63)$$

so that the (initial) buoyant acceleration of the bubble is proportional to the entropy perturbation,

$$a_b = \frac{\Delta \rho}{\rho} g_y \propto \left( \frac{\Delta A}{A} \right)_{t=0}. \quad (64)$$

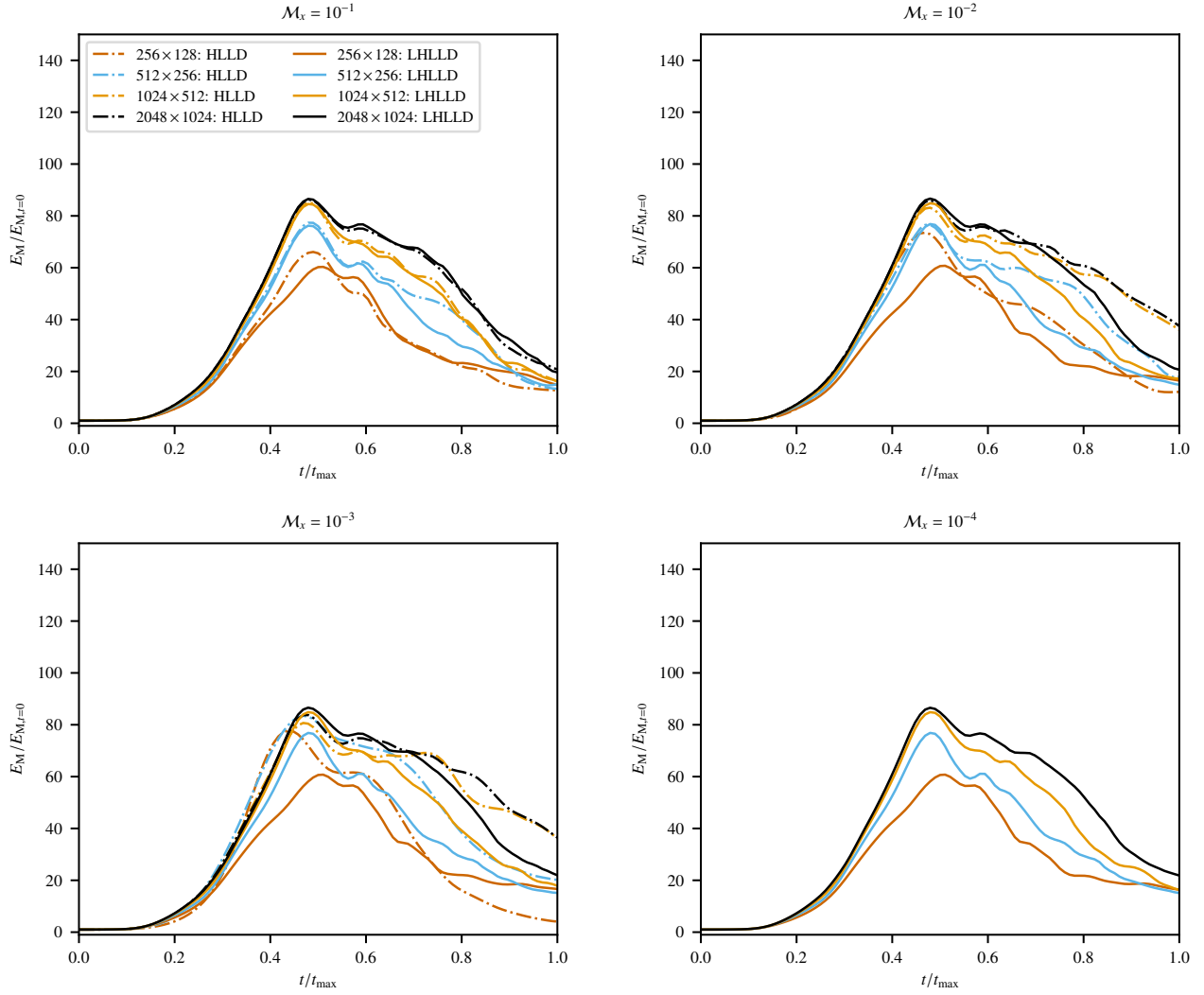


**Fig. 11.** Same as Fig. 10 but showing the total magnetic energy divided by its initial value.

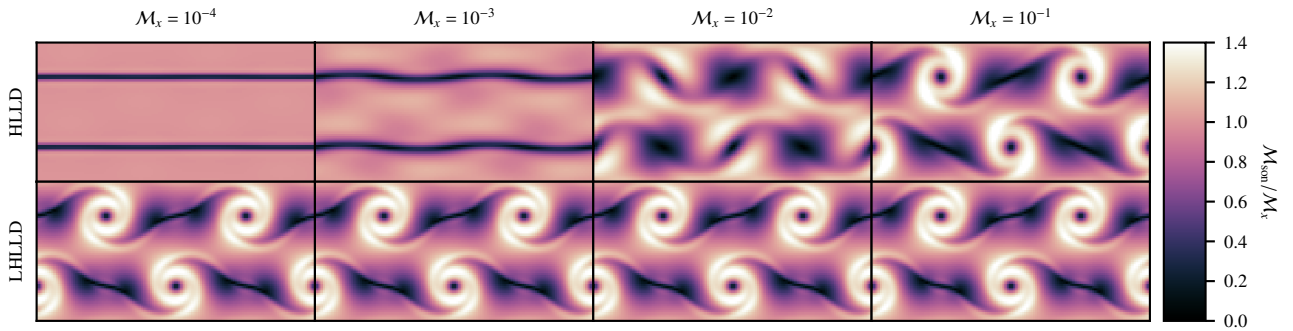


**Fig. 12.** Distribution of the sonic Mach number in the Kelvin–Helmholtz instability test at  $t/t_{\max} = 1/6$  obtained with the HLLD (top panels) and the LHLLD (bottom panels) solvers on a  $128 \times 64$  grid for different values of  $M_x$ . All panels are rescaled by the corresponding value of  $M_x$ .

We ran the models for the set of parameters

$$\left(\frac{\Delta A}{A}\right)_{t=0} \times (N_y) = (10^{-7}, 10^{-5}, 10^{-3}, 10^{-1}) \quad (65)$$

$$\times (96, 192, 384, 768),$$

and we set the maximum time such that in each run the bubble raised approximately the same distance  $l$ . This allowed different regimes of sonic Mach numbers to be simulated, as the velocity,

$V$ , reached by the bubble over a length,  $l$ , scales as

$$V \propto (a_b l)^{1/2}. \quad (66)$$

This ultimately leads to the relation

$$\mathcal{M}_{\text{son}} \propto \left(\frac{\Delta A}{A}\right)_{t=0}^{1/2}. \quad (67)$$

A uniform horizontal magnetic field was added to the system, and its strength was rescaled depending on the entropy

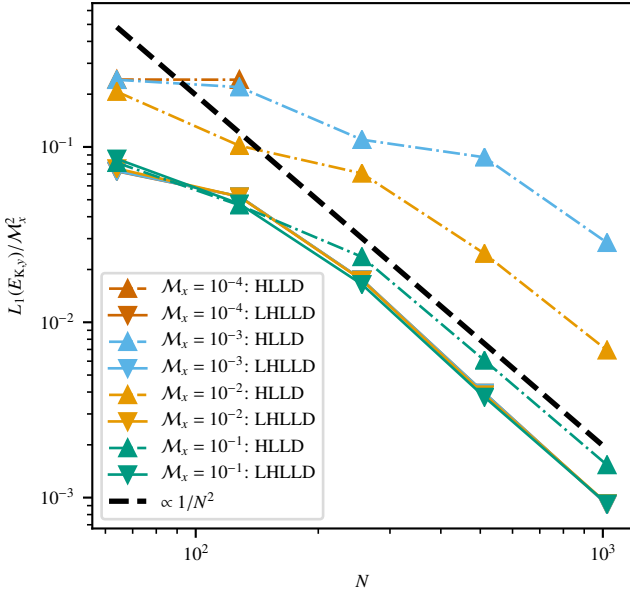


**Fig. 13.** Convergence with resolution  $N$  of the  $L_1$  error associated with  $E_{K,y}$  rescaled by  $M_x^2$  in the simulations of the Kelvin–Helmholtz instability. Different colors are used for different initial sonic Mach numbers  $M_x$  using the LHLLED (solid lines) and HLLD (dot-dashed lines) solvers. The dashed black line is the second-order scaling.

perturbation,

$$B_x = B_0 \left( \frac{\Delta A}{A} \right)_{t=0}^{1/2}. \quad (68)$$

This ensures that the relative magnitude of magnetic stresses compared to the ram pressure of the bubble remains the same for all simulations, and that the morphology of the flow is unaltered.  $B_0 = 47.3$  was chosen such that the final Alfvén Mach number at the position of largest entropy is in the range  $M_{\text{Alf}} \simeq 2\text{--}3$  depending on the grid resolution. Thus, magnetic fields are dynamically important but not strong enough to suppress buoyancy.

In Fig. B.1, we show the final entropy excess for all the simulations run in the parameter study. The center of the bubble accelerates faster than other regions as it is the point with maximum entropy, and the acceleration profile across the bubble leads to the development of shear at its outer edges. As the bubble rises in the stratification, the magnetic field lines are stretched into thin tubes, which locally amplifies the magnetic energy (see Fig. B.2). The amount of amplification depends on the numerical resistivity and so on resolution. In contrast to the pure hydrodynamic case studied by Edelmann et al. (2021), here the presence of a magnetic field suppresses the formation of vortices at the sides of the bubble. Overall, the entropy content of the bubble is well preserved even on the coarsest grid, but some negative entropy fluctuations are present at the very top of the bubble. These negative fluctuations are numerical artifacts. In fact, the entropy fluctuations may locally increase as a fraction of magnetic and kinetic energy is dissipated into internal energy, but they cannot become negative physically. These artifacts do not depend on the entropy perturbation, and they are limited to a very narrow region in the spatial domain that tends to shrink as the resolution is increased. All models converge upon grid refinement.

According to Eq. (67), the sonic Mach number of the bubble is expected to scale as the square root of the initial entropy

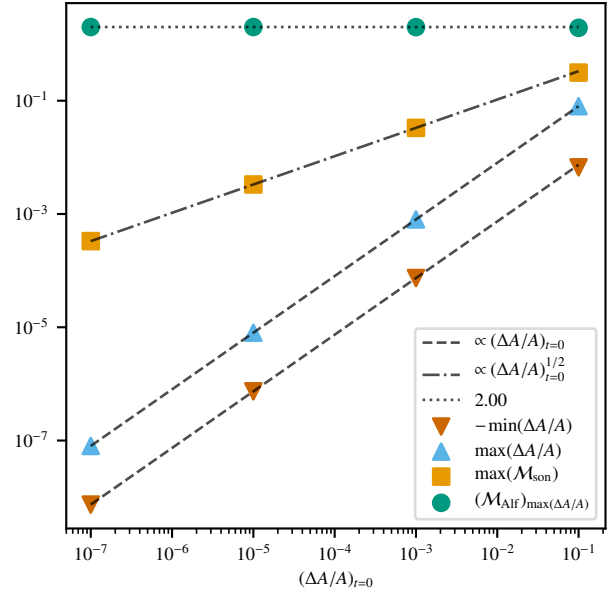


**Fig. 14.** Maximum sonic Mach number, minimum and maximum entropy fluctuations and Alfvén speed of the hot bubble as a function of the initial entropy perturbation obtained on a  $64 \times 96$  grid. The black lines represent the physical scalings.

perturbation. Any deviation from this relation, which has been obtained on the basis of physical arguments, can be due to difficulties in modeling slow flows in a stratified setup and the build-up of significant numerical errors. In Fig. 14, we show this scaling for the coarsest grid resolution. All data points overlap with the theoretical curve, and the minimum Mach number  $M_{\text{son}}$  achieved in this parameter study is  $3.32 \times 10^{-4}$  (see also Fig. B.3). The ratio of the rising velocity of the bubble to the Alfvén speed (in the point of maximum entropy) does not depend on the amplitude of the entropy perturbation. Since the initial magnetic field is proportional to  $(\Delta A/A)_{t=0}^{1/2}$ , the amount of amplification due to induction only depends on the velocity of the bubble  $V$  and the timescale over which magnetic induction operates ( $\propto 1/V$ ).

Finally, to quantify the strength of the spurious flows that are expected to arise if the stratification is left unbalanced, in Fig. 15 we show a comparison between simulations obtained with and without deviation well-balancing, where the vertical resolution  $N_y$  ranges from 96 to 768. For this comparison, we fixed  $(\Delta A/A)_{t=0}^{1/2} = 10^{-3}$  such that the maximum sonic Mach number of the bubble is approximately  $3 \times 10^{-2}$ . The unbalanced simulations develop large entropy fluctuations, both negative and positive, which strongly deteriorate the numerical solution. As the grid is refined, the simulations tend to converge, but wide regions of negative entropy fluctuations are still present even on the finest grid. Thus, this test demonstrates that well-balancing techniques are fundamental to correctly simulate the evolution of small entropy perturbations in steep isentropic stratifications and to reduce the effects of numerical errors when using moderately coarse grids.

### 5.5. Small-scale dynamo in a stratified setup

The previous tests demonstrated that the proposed MHD implementation can accurately simulate slow flows even in strongly stratified setups. As this numerical method will mostly be applied to simulate stellar interiors, it seems natural to test

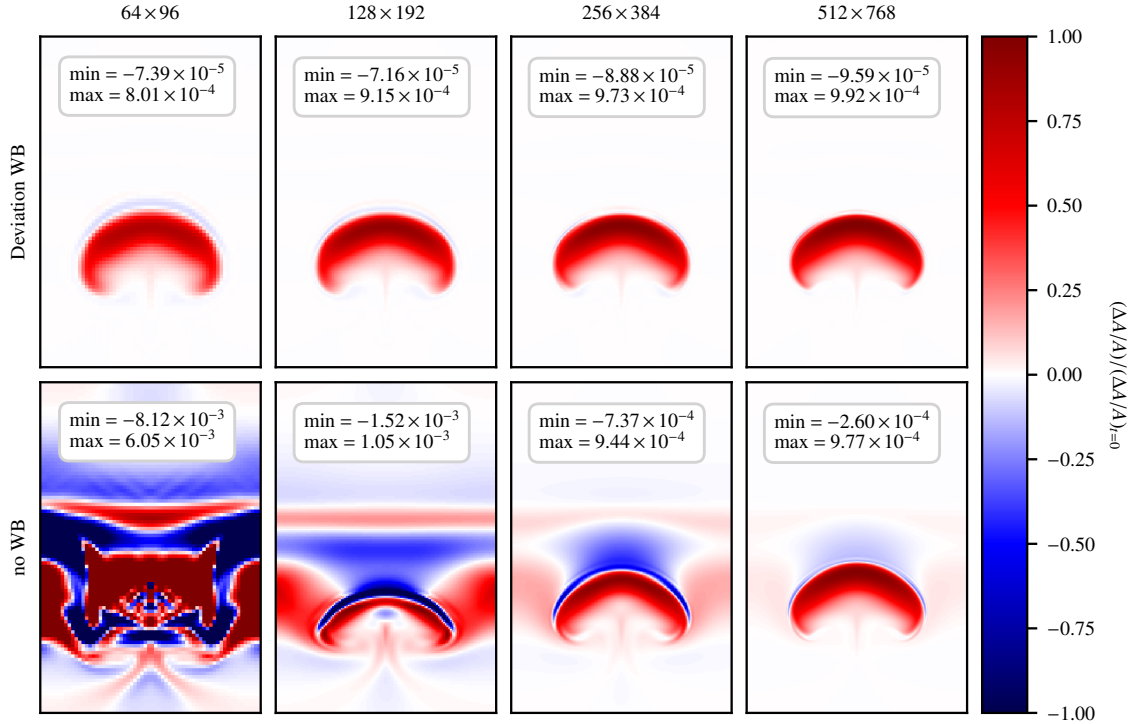


**Fig. 15.** Final distribution of the entropy fluctuations of the hot bubble for  $(\Delta A/A)_{t=0} = 10^{-3}$  at different grid resolutions. The entropy fluctuations are rescaled by  $(\Delta A/A)_{t=0}$ . The *top row* shows the results obtained with deviation well-balancing, whereas no well-balancing method was used in the simulations shown in the *bottom row*. The insets show the minimum and maximum values of the entropy fluctuation in each panel.

the scheme for dynamo amplification, which is the main cause for the generation of strong magnetic fields in a wide mass range of stars (see [Brun & Browning 2017](#), and references therein). In this section we focus on simulations of SSDs, where the magnetic energy is amplified on scales comparable to or smaller than the scales at which turbulence is forced ([Meneguzzi et al. 1981](#); [Schekochihin et al. 2004, 2007](#); [Brandenburg & Subramanian 2005](#); [Iskakov et al. 2007](#)), in contrast to large-scale dynamos where most of the magnetic energy is at scales larger than the forcing scale ([Brun et al. 2004](#); [Käpylä et al. 2008](#); [Charbonneau 2013](#); [Augustson et al. 2016](#)). Even though the efficiency of the dynamo amplification depends on many physical parameters, including the magnetic Prandtl number  $P_m = \nu/\eta$  ([Schekochihin et al. 2004, 2007](#); [Pietarila Graham et al. 2010](#); [Brandenburg 2011, 2014](#)), here we do not perform a parameter study for  $P_m$ , since in the current MHD scheme the viscosity ( $\nu$ ) and resistivity ( $\eta$ ) coefficients are not fixed, but are intrinsic to the underlying numerical methods, so they are not easy to constrain. Instead, we aim to check if it is possible to excite an SSD using the SLH code at low sonic Mach numbers.

We built the initial conditions based on the work of [Andrassy et al. \(2022\)](#), who performed a pure hydrodynamic study of a 3D convection zone with a stable layer on top of it, where the convective flows had a typical maximum Mach number  $\mathcal{M}_{\text{son}} \sim 0.1$ . The stratification of that model resembled oxygen shell burning in a massive star, even though some simplifications were adopted. Among these, an ideal gas EoS was used and effects of neutrino cooling were ignored. Here, we modified that setup even further by retaining only the convection zone and by decreasing the rate of energy injection to test our method in the low-Mach-number regime. Removing the stable layer greatly simplifies the problem at low Mach numbers, as the propagation of internal gravity waves does not need to be resolved. Since the wavelength

of these modes becomes shorter for progressively slower convective flows ([Sutherland 2010](#); [Edelmann et al. 2021](#)), high grid resolutions would be necessary to capture this process accurately at low Mach numbers, which would make the simulations very expensive.

For our experiment, we used  $N_x \times N_y \times N_z = 2N \times N \times 2N$  grid cells and the spatial domain (normalized by a characteristic length  $L = 4 \times 10^8$  cm) is  $-1 \leq x \leq 1$ ,  $1 \leq y \leq 2$ ,  $-1 \leq z \leq 1$ . Periodic boundaries were used in the horizontal directions, while reflecting boundaries were used in the vertical direction. The initial stratification is adiabatic and in MHSE, and it is given by the polytropic relation

$$\frac{d \ln p}{d \ln \rho} = \gamma. \quad (69)$$

The stratification spans 2.2 pressure scale heights. The gravitational acceleration takes the form

$$g(y) = g_0 f_g(y) y^{-5/4}, \quad (70)$$

where  $g_0 = 1.414870$ , and

$$f_g(y) = \begin{cases} \frac{1}{2} \left\{ 1 + \sin \left[ 16\pi \left( y - \frac{1}{32} \right) \right] \right\}, & \text{for } 1 \leq y < 1 + \frac{1}{16}, \\ 1, & \text{for } 1 + \frac{1}{16} \leq y < 2 - \frac{1}{16}, \\ \frac{1}{2} \left\{ 1 + \sin \left[ 16\pi \left( y - \frac{1}{32} \right) \right] \right\}, & \text{for } 2 - \frac{1}{16} \leq y < 2, \\ 0, & \text{otherwise.} \end{cases} \quad (71)$$

Moreover, in contrast to [Andrassy et al. \(2022\)](#), we are not interested in studying convective boundary mixing, so we only used a single species with mean molecular weight  $\mu = 1$ .

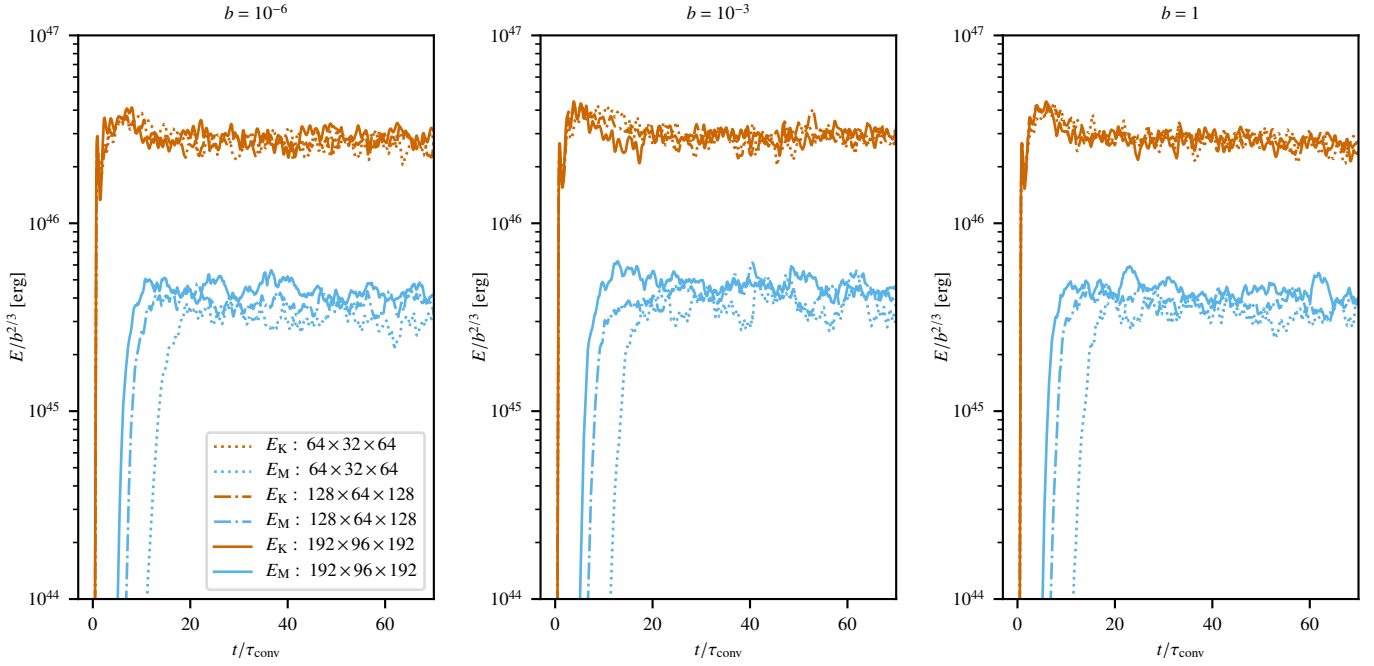


**Fig. 16.** Time evolution of the magnetic energy (sky blue) and kinetic energy (vermillion) in the simulations of the SSD for different grid resolutions (dotted:  $64 \times 32 \times 64$ , dot-dashed:  $128 \times 64 \times 128$ , solid:  $192 \times 96 \times 192$ ). Each panel shows the results obtained with a specific value of  $b$  (from left to right:  $b = 10^{-6}$ ,  $10^{-3}$ , 1). The time is expressed in units of the convective turnover, while the magnetic and kinetic energy curves are rescaled by  $b^{2/3}$  to take into account the different energy contents of the flows.

Convection is driven by a constant in time heat source  $\dot{q}(y)$  placed close to the bottom boundary,

$$\dot{q}(y) = \begin{cases} b\dot{q}_0 \sin(8\pi y), & \text{for } 1 \leq y \leq 1 + \frac{1}{8}, \\ 0, & \text{for } 1 + \frac{1}{8} < y \leq 2, \end{cases} \quad (72)$$

where  $\dot{q}_0 = 3.795720 \times 10^{-4} \text{ erg cm}^{-3} \text{ s}^{-1}$  and  $b$  is a nondimensional factor that allows the strength of the convective flows to be controlled through the scaling (see, e.g., Kippenhahn et al. 2013; Andrassy et al. 2020; Horst et al. 2021; Edelmann et al. 2021; Käpylä 2021)

$$\mathcal{M}_{\text{son}} \propto \dot{q}^{1/3} \propto b^{1/3}. \quad (73)$$

We considered the following grid of models:

$$(b) \times (N) = (10^{-6}, 10^{-3}, 1) \times (32, 64, 96). \quad (74)$$

We ran the simulations at nominal luminosity ( $b = 1$ ) with SSP-RK2, where the convective flows are characterized by a maximum  $\mathcal{M}_{\text{son}}$  of 0.1. In this regime of sonic Mach numbers, IESS is less efficient than explicit time-steppers (see Fig. 8). In contrast, the cases with  $b = 10^{-3}$  and  $b = 10^{-6}$  were run with IESS, since according to Eq. (73), the maximum  $\mathcal{M}_{\text{son}}$  is  $10^{-2}$  and  $10^{-3}$ , respectively.

In order to initiate an SSD, a weak seed magnetic field was added to the system<sup>19</sup>,

$$B_x(t = 0) = 10^5 b^{1/3}, \quad (75)$$

<sup>19</sup> As observed by Seta & Federrath (2020), the evolution of the dynamo in the nonlinear regime does not depend on the form of the seed field, as long as its magnitude is weak enough to not affect the development of convection.

where the dependence on  $b$  is such that the timescale on which the magnetic energy reaches saturation (expressed in units of convective turnovers) does not depend on the value of  $b$ . The convective turnover timescale was estimated as

$$\tau_{\text{conv}} = 2 \frac{L}{\langle \sigma_V \rangle_t}, \quad (76)$$

where

$$\sigma_V = \sqrt{\sigma_{V,x}^2 + \sigma_{V,y}^2 + \sigma_{V,z}^2} \quad (77)$$

is averaged over time, and  $\sigma_{V,x}^2$ ,  $\sigma_{V,y}^2$ ,  $\sigma_{V,z}^2$  represent the standard deviation of each velocity component computed over the whole domain. All simulations were run until  $t/\tau_{\text{conv}} = 70$ , with  $\tau_{\text{conv}} \simeq 5000, 500, 50 \text{ s}$  for  $b = 10^{-6}, 10^{-3}, 1$ , respectively. The initial MHSE density stratification was perturbed to initiate convection<sup>20</sup>. This perturbation leads to the development of buoyant structures that rise in the stratification until they hit the top boundary, after which they quickly become turbulent (see Fig. C.2). Convection fully develops after one convective turnover.

Figure 16 shows the time evolution of the kinetic and the magnetic energy for all the simulations run in the grid of models considered in this test. In the kinematic phase, the magnetic field is irrelevant to the dynamics, and it is amplified exponentially by the action of a dynamo process, with most of the magnetic energy distributed close to the resistive scale. As visible in the horizontal cuts shown in Fig. 17, the magnetic field distribution is characterized by small-scale structures with mixed polarity, while the velocity field is distributed on slightly larger scales, which suggests that  $P_m \gtrsim 1$ . The growth rate

<sup>20</sup> Details on how to compute the density perturbation can be found in Andrassy et al. (2022).



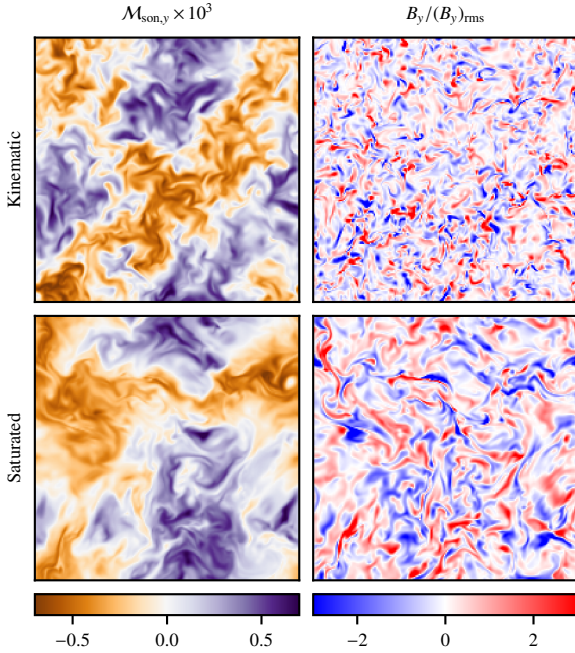


**Fig. 17.** Horizontal slices in the  $y = 1.5$  plane taken in the kinematic (upper plots) and saturated (lower plots) regimes of the SSD with  $b = 10^{-6}$  on the  $192 \times 96 \times 192$  grid. The panels on the left show the vertical sonic Mach number  $M_{\text{son},y} = V_y/a$  multiplied by  $10^3$ , while the plots on the right show the vertical magnetic field rescaled by the root mean square value across the plane.

**Table 1.** Time averages of  $E_M/b^{2/3}$  [ $10^{45} \times \text{erg}$ ] over the time interval  $20 < t/\tau_{\text{conv}} < 70$  for the different resolutions,  $N$ , and boost factors,  $b$ , considered in this study.

	$b = 10^{-6}$	$b = 10^{-3}$	$b = 1$
$N = 32$	$3.13 \pm 0.34$	$3.65 \pm 0.60$	$3.33 \pm 0.37$
$N = 64$	$3.73 \pm 0.32$	$4.31 \pm 0.55$	$3.78 \pm 0.31$
$N = 96$	$4.40 \pm 0.44$	$4.67 \pm 0.39$	$4.40 \pm 0.47$

**Notes.** The errors represent one standard deviation over the time series.

$\gamma_M = d(\ln E_M)/d\tau_{\text{conv}}$  increases with resolution (see also Fig. C.4), which is compatible with SSD amplification. In particular, we find that  $\gamma_M \propto \Delta x^{-0.8}$ . The dependence of the growth rate on  $\Delta x$  is weaker than  $\gamma_M \propto \Delta x^{-4/3}$ , which is typically observed in simulations of SSDs in solar and stellar convection zones (Pietarila Graham et al. 2010; Rempel 2014; Hotta et al. 2015; Riva & Steiner 2022; Canivete Cuissa & Teyssier 2022), and steeper than  $\gamma_M \propto \Delta x^{-2/3}$ , which is predicted by the Kazantsev dynamo theory (Kazantsev 1968; Brandenburg & Subramanian 2005).

When the magnetic field becomes strong enough, the Lorentz force starts to influence the evolution of the turbulent flows, damping the velocity on the small scales (see the bottom panels in Fig. 17). A statistically steady state configuration is then reached where the magnetic energy achieves sub-equipartition values  $E_M/E_K \simeq 0.1\text{--}0.2$ . In all simulations, an SSD is successfully excited, and the mean value of the amplified magnetic energy increases with resolution (see Table 1). In fact, the size of the resistive scale is smaller on finer grids, which in turn increases the maximal stretching rate of the field lines and the SSD becomes more efficient. In contrast, no systematic difference is observed in the magnetic to the kinetic energy

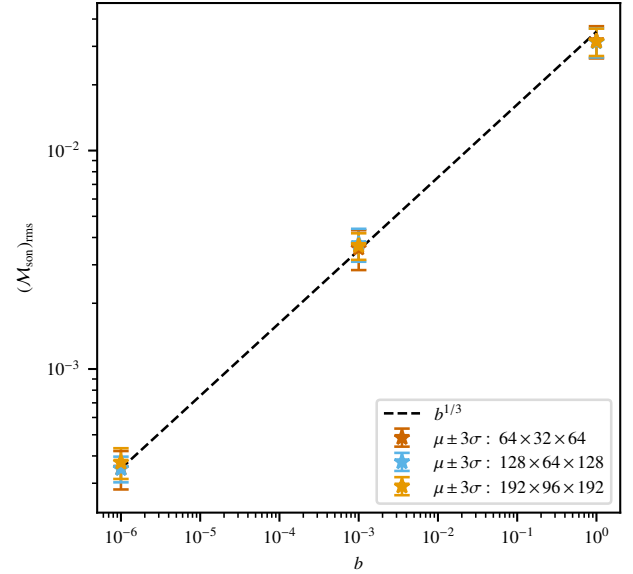


**Fig. 18.** Root mean square of the sonic Mach number as a function of the driving luminosity  $b$ . The data points are averages computed in the time interval  $20 < t/\tau_{\text{conv}} < 40$ . The error bars represent three standard deviations over the time series, while the dotted black line is the  $b^{1/3}$  scaling.

ratio in simulations run with the same resolution but different values of  $b$ . This is due to the fact that, thanks to the use of the LHLLED solver, the size of the viscous and resistive scales does not depend on the sonic Mach number of the flow, which is mostly determined by the chosen value of  $b$ . At given resolution, the SSD amplifies the magnetic field on the same spatial (resistive) scales, so the evolution of  $E_M/E_K$  becomes virtually independent of  $M_{\text{son}}$  (and so of  $b$ ) if the time is rescaled by the convective turnover  $\tau_{\text{conv}}$ , except for statistical fluctuations caused by the chaotic nature of the turbulent flows.

Figure 18 shows the root mean square sonic Mach number averaged over 20 convective turnovers in the saturated regime as a function of  $b$ . As noted in Edelmann et al. (2021), numerical errors introduced by an unbalanced stratification can cause deviations from the scaling in Eq. (73). In this case, the use of deviation well-balancing and LHLLED allows a good agreement between the computed Mach numbers and the scaling law to be reached, within three standard deviations. This proves that the convective flows are correctly simulated and are not dominated by numerical errors. The smallest  $(M_{\text{son}})_{\text{rms}}$  achieved in these runs is approximately  $3.7 \times 10^{-4}$ , which is close to what typically found in simulations of core-convective stars (Augustson et al. 2016; Edelmann et al. 2019; Horst et al. 2020; Higl et al. 2021).

Finally, Fig. 19 shows the kinetic and magnetic energy spectra (taken in the midplane of the box) in the saturated stage for different values of  $b$  and grid resolutions. Both spectra have been rescaled by  $b^{2/3}$  to take into account the different energy contents of the flows achieved with different values of  $b$ . The kinetic energy spectra converge to the  $k^{-5/3}$  Kolmogorov law (Kolmogorov 1941) upon grid refinement, and the dissipation range shifts toward progressively larger wave numbers  $k$ . The magnetic energy distributions peak in the inertial range, as expected in SSD simulations, and on the large scales they show a shallower dependence on  $k$  than the Kazantsev isotropic dynamo theory,  $k^{3/2}$  (Kazantsev 1968). This can be explained by the fact that, in this setup, turbulence is not isotropic, and large-scale anisotropic convective flows are present because of the

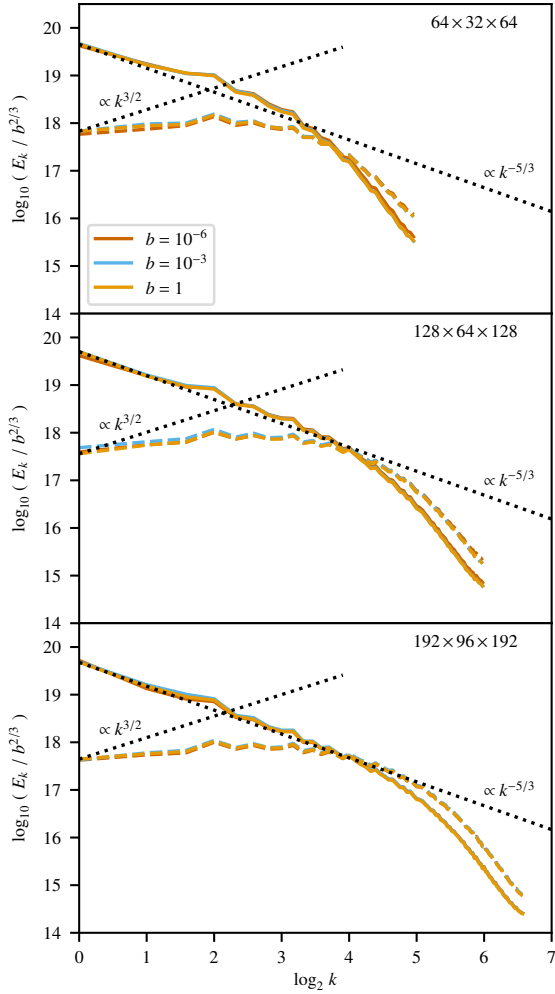


**Fig. 19.** Kinetic (solid lines) and magnetic (dashed lines) energy spectra as a function of the wave number  $k$  obtained in a horizontal slice of the convective box at  $y = 1.5$ . All spectra are averaged over the time interval  $20 < t/\tau_{\text{conv}} < 40$  and are rescaled by  $b^{2/3}$ . The three panels show the results for different numbers of grid cells (from top to bottom:  $64 \times 32 \times 64$ ,  $128 \times 64 \times 128$ ,  $192 \times 96 \times 192$ ). The dotted black lines are the Kolmogorov ( $k^{-5/3}$ ) and Kazantsev ( $k^{3/2}$ ) scalings.

steep stratification and the use of closed vertical boundaries (see Fig. C.2). Magnetic and kinetic energy achieve equipartition at the bottom of the inertial range, except for the simulations run on  $64 \times 32 \times 64$  grid cells, in which equipartition is reached only in the dissipation range. The maximum magnetic to kinetic energy ratio is around 3 in the dissipation range for the highest resolution considered in this study. Again, since the numerical diffusion of the MHD scheme is Mach-independent, the shape and amplitude of the rescaled spectra do not depend on  $b$  on any of the three grids. Thus, this test indicates that SLH is capable of correctly simulating fully compressible magneto-convection and SSDs in regimes of low sonic Mach numbers even with moderate grid resolutions.

## 6. Summary and conclusions

In this work, we have presented a new finite-volume scheme for solving the fully compressible MHD equations with gravity in regimes of low sonic Mach numbers and high- $\beta$  environments, which is suitable for simulating magneto-convection and dynamo processes in deep layers of stars. This method relies on

a low-dissipation MHD Riemann solver (LHLLD; Minoshima & Miyoshi 2021) to avoid the excessive numerical dissipation typical of high-resolution, shock-capturing solvers as  $\mathcal{M}_{\text{son}} \rightarrow 0$ .

The strict CFL condition on the time step is overcome by using an implicit–explicit time discretization algorithm, for which the induction equation is integrated using an explicit time-stepper, while the rest of the MHD system is integrated implicitly. The solutions to the two subsets of equations are coupled through Strang splitting following the prescription of Fuchs et al. (2009). The combined marching scheme has a less restrictive condition on the time step, which is limited only by the fastest fluid and Alfvén speeds instead of the fast magnetosonic speed, leading to a considerable speed-up in regimes of low sonic Mach numbers.

Whenever required, a magnetohydrostatic solution can be enforced on the discrete grid with the deviation well-balancing method (Berberich et al. 2021; Edelmann et al. 2021). This technique leads to better entropy-conservation properties of the numerical scheme, even in cases where the pressure and density stratifications span several orders of magnitude across the computational domain. Finally, the  $\nabla \cdot \mathbf{B} = 0$  condition is enforced using the CT-contact method (Gardiner & Stone 2005). This new scheme is implemented in the SLH code, and it has been tested in five numerical experiments.

First, we checked the global convergence of the methods by following the propagation of linear modes for all the MHD waves on a 1D grid. This test proves that the scheme is globally second-order accurate.

For the second test, we ran simulations of an MHD vortex advected along the diagonal of a square 2D grid. The characteristic velocities involved in the problem were varied such that the maximum Mach number,  $\mathcal{M}_{\text{son}}$ , ranged from  $1.55 \times 10^{-5}$  to  $1.55 \times 10^{-1}$ . This experiment showed that the MHD scheme also scales with second-order accuracy on 2D grids and that the numerical dissipation is independent of  $\mathcal{M}_{\text{son}}$ , even though it becomes larger for lower  $\mathcal{M}_{\text{Aif}}$ . However, we observed a considerable dissipation only when the magnetic energy of the vortex was 100 times its rotational kinetic energy. This regime is far from our main astrophysical applications. The dissipation of kinetic energy for both the LHLLD and the standard HLLD solvers has been quantified for different resolutions at a maximum Mach number  $\mathcal{M}_{\text{son}} = 1.55 \times 10^{-3}$ . Even though all the results converged upon grid refinement, conservation of rotational kinetic energy was two orders of magnitude worse when using the HLLD flux instead of LHLLD. We also quantified the efficiency of IESS over a standard SSP-RK2 as a function of  $\mathcal{M}_{\text{son}}$ . When the maximum sonic Mach number of the flow is below  $(2-5) \times 10^{-2}$ , IESS becomes considerably more efficient than explicit time-steppers.

In the third experiment we considered the growth of a Kelvin–Helmholtz instability under the effects of a weak magnetic field parallel to the shear flow, which is known to generate more complex vortex structures than the case with a strong magnetic field (Frank et al. 1996). The second-order convergence of the  $y$ -direction kinetic energy was checked using both the LHLLD and HLLD solvers for different shear velocities, such that the corresponding sonic Mach number ranged from  $10^{-4}$  to  $10^{-1}$ . Again, we observed that the amount of dissipation was virtually independent of  $\mathcal{M}_{\text{son}}$  for LHLLD, while the numerical solution obtained with HLLD was progressively more degraded as the Mach number was further decreased. This test showed that HLLD needed twice or four times the resolution to be as accurate as LHLLD when  $\mathcal{M}_{\text{son}} \sim 10^{-3}$  and  $\mathcal{M}_{\text{son}} \sim 10^{-2}$ , while it only needed 20% more resolution at  $\mathcal{M}_{\text{son}} \sim 10^{-1}$ .

In our fourth test we simulated the rise of a hot bubble in an adiabatic stratification in MHSE. The initial magnetic field was horizontal and uniform. Different entropy perturbations were considered to test the capabilities of the MHD scheme in modeling slow flows in steep stratifications (in this case, the vertical domain spanned 4.6 pressure scale heights). Overall, the entropy content of the bubble was very well preserved and all results converged upon grid refinement. Thanks to the deviation method, we were able to successfully simulate the rise of the bubble for entropy perturbations as low as  $10^{-7}$ , leading to typical sonic Mach numbers of  $3 \times 10^{-4}$ . A relation between the rise velocity of the bubble and the entropy perturbation has been obtained on the basis of physical considerations. We show that the results obtained with this MHD scheme could satisfy that relation even on coarse grids, which suggests that discretization errors arising from the background stratification did not play any significant role in the evolution of the bubble. For comparison, we also ran the same setup at an intermediate entropy perturbation without well-balancing. The unbalanced states led to the generation of large pressure jumps at the cell interfaces, which launched strong waves that degraded the numerical solution at low resolution. Even when the magnitude of these errors was progressively reduced at higher resolution, they were still significant on the finest grid.

Lastly, we ran a fully convective box on a 3D Cartesian grid (with  $2N \times N \times 2N$  grid cells) to simulate an SSD. The initial stratification was in MHSE and it resembled the thermodynamic conditions found in oxygen shell burning in a massive star (Andrassy et al. 2022). Convection was driven by a heat source placed at the bottom of the box, and a weak seed magnetic field was planted in the system to initiate the dynamo. By changing the rate of energy injection, we were able to study different velocity regimes. In particular, we simulated three different cases, with  $M_{\text{son}} \sim 10^{-3}$ ,  $10^{-2}$ , and  $10^{-1}$ . We only considered moderate grid resolutions ( $N = 32, 64, 96$ ). In the kinematic phase, the magnetic field energy was exponentially amplified on the smallest scales of the turbulent flow, with a higher growth rate in finer grids, which is consistent with SSD amplification. When the Lorentz force started to affect the evolution of the fluid, the saturated nonlinear phase began. Because of the use of a low-Mach Riemann solver, the amount of magnetic energy amplified (compared to the kinetic energy content of the flow) did not depend on the sonic Mach number of convection and achieved sub-equipartition values for the resolutions considered in this study ( $E_M/E_K \simeq 0.1\text{--}0.2$ ).

Overall, the results obtained in these tests demonstrate that the numerical methods implemented in SLH can accurately and efficiently tackle a variety of MHD processes that act in stellar interiors, in regimes that are inaccessible to conventional methods.

*Acknowledgements.* The work of G.L. and F.K.R. is supported by the German Research Foundation (DFG) through the grant RO 3676/3-1. The work of C.B. and C.K. is supported by DFG through the grant KL 566/22-1. P.V.F.E. was supported by the US Department of Energy through the Los Alamos National Laboratory (LANL). LANL is operated by Triad National Security, LLC, for the National Nuclear Security Administration of the US Department of Energy (Contract No. 89233218CNA000001). G.L., R.A., J.H., G.W., and F.K.R. acknowledge support by the Klaus Tschira Foundation. This work has been assigned a document release number LA-UR-22-27864.

## References

Andrassy, R., Herwig, F., Woodward, P., & Ritter, C. 2020, *MNRAS*, **491**, 972  
 Andrassy, R., Higl, J., Mao, H., et al. 2022, *A&A*, **659**, A193  
 Augustson, K. C., Brun, A. S., & Toomre, J. 2016, *ApJ*, **829**, 92

Aydemir, A. Y., & Barnes, D. C. 1985, *J. Comput. Phys.*, **59**, 108  
 Balsara, D. S. 2004, *ApJS*, **151**, 149  
 Balsara, D. S., & Spicer, D. S. 1999, *J. Comput. Phys.*, **149**, 270  
 Berberich, J. P., Chandrashekar, P., & Klingenberg, C. 2021, *Comput. Fluids*, **219**, 104858  
 Brackbill, J. U., & Barnes, D. C. 1980, *J. Comput. Phys.*, **35**, 426  
 Brandenburg, A. 2011, *ApJ*, **741**, 92  
 Brandenburg, A. 2014, *ApJ*, **791**, 12  
 Brandenburg, A., & Subramanian, K. 2005, *Phys. Rep.*, **417**, 1  
 Brown, B. P., Browning, M. K., Brun, A. S., Miesch, M. S., & Toomre, J. 2010, *ApJ*, **711**, 424  
 Browning, M. K. 2008, *ApJ*, **676**, 1262  
 Browning, M. K., Miesch, M. S., Brun, A. S., & Toomre, J. 2006, *ApJ*, **648**, L157  
 Brun, A. S., & Browning, M. 2017, *Living Rev. Sol. Phys.*, **14**, 4  
 Brun, A. S., Miesch, M. S., & Toomre, J. 2004, *ApJ*, **614**, 1073  
 Brun, A. S., Browning, M. K., & Toomre, J. 2005, *ApJ*, **629**, 461  
 Canivete Cuissa, J. R., & Teyssier, R. 2022, *A&A*, **664**, A24  
 Cargo, P., & Gallice, G. 1997, *J. Comput. Phys.*, **136**, 446  
 Chacón, L. 2008, *Phys. Plasmas*, **15**, 056103  
 Chandrasekhar, S. 1961, *Hydrodynamic and hydromagnetic stability* (Oxford University Press)  
 Charbonneau, P. 2013, *Solar and Stellar Dynamos* (Springer-Verlag)  
 Charlton, L. A., Holmes, J. A., Lynch, V. E., Carreras, B. A., & Hender, T. C. 1990, *J. Comput. Phys.*, **86**, 270  
 Colella, P., & Woodward, P. R. 1984, *J. Comput. Phys.*, **54**, 174  
 Courant, R., Friedrichs, K., & Lewy, H. 1928, *Math. Ann.*, **100**, 32  
 Dai, W., & Woodward, P. R. 1998, *ApJ*, **494**, 317  
 Dedner, A., Kemm, F., Kröner, D., et al. 2002, *J. Comput. Phys.*, **175**, 645  
 Dumbser, M., Balsara, D. S., Tavelli, M., & Fambri, F. 2019, *Int. J. Numer. Methods Fluids*, **89**, 16  
 Edelmann, P. V. F. 2014, Dissertation, Technische Universität München, Germany  
 Edelmann, P. V. F., & Röpke, F. K. 2016, in *JUQUEEN Extreme Scaling Workshop 2016*, eds. D. Brömmel, W. Frings, & B. J. N. Wylie (Jülich Supercomputing Centre)  
 Edelmann, P. V. F., Röpke, F. K., Hirschi, R., Georgy, C., & Jones, S. 2017, *A&A*, **604**, A25  
 Edelmann, P. V. F., Ratnasingam, R. P., Pedersen, M. G., et al. 2019, *ApJ*, **876**, 4  
 Edelmann, P. V. F., Horst, L., Berberich, J. P., et al. 2021, *A&A*, **652**, A53  
 Einfeldt, B., Roe, P. L., Munz, C. D., & Sjogreen, B. 1991, *J. Comput. Phys.*, **92**, 273  
 Evans, C. R., & Hawley, J. F. 1988, *ApJ*, **332**, 659  
 Fambri, F. 2021, *Int. J. Numer. Methods Fluids*, **93**, 3447  
 Featherstone, N. A., & Hindman, B. 2016, *ApJ*, **818**, 32  
 Featherstone, N. A., Browning, M. K., Brun, A. S., & Toomre, J. 2009, *ApJ*, **705**, 1000  
 Felipe, T., Khomenko, E., & Collados, M. 2010, *ApJ*, **719**, 357  
 Frank, A., Jones, T. W., Ryu, D., & Gaalaas, J. B. 1996, *ApJ*, **460**, 777  
 Fuchs, F. G., Mishra, S., & Risebro, N. H. 2009, *J. Comput. Phys.*, **228**, 641  
 Gardiner, T. A., & Stone, J. M. 2005, *J. Comput. Phys.*, **205**, 509  
 Gardiner, T. A., & Stone, J. M. 2008, *J. Comput. Phys.*, **227**, 4123  
 Gastine, T., & Wicht, J. 2012, *Icarus*, **219**, 428  
 Ghizaru, M., Charbonneau, P., & Smolarkiewicz, P. K. 2010, *ApJ*, **715**, L133  
 Glasser, A. H., Sovinec, C. R., Nebel, R. A., et al. 1999, *Plasma Phys. Controlled Fusion*, **41**, A747  
 Glatzmaier, G. A. 1984, *J. Comput. Phys.*, **55**, 461  
 Glatzmaier, G. A. 1985, *ApJ*, **291**, 300  
 Godunov, S. K., & Bohachevsky, I. 1959, *Matematicheskij Sbornik*, **47**, 271  
 Harned, D. S., & Kerner, W. 1985, *J. Comput. Phys.*, **60**, 62  
 Higl, J., Müller, E., & Weiss, A. 2021, *A&A*, **646**, A133  
 Horst, L., Edelmann, P. V. F., Andrassy, R., et al. 2020, *A&A*, **641**, A18  
 Horst, L., Hirschi, R., Edelmann, P. V. F., Andrassy, R., & Roepke, F. K. 2021, *A&A*, **653**, A55  
 Hotta, H. 2017, *ApJ*, **843**, 52  
 Hotta, H., Rempel, M., & Yokoyama, T. 2015, *ApJ*, **803**, 42  
 Isakov, A. B., Schekochihin, A. A., Cowley, S. C., McWilliams, J. C., & Proctor, M. R. E. 2007, *Phys. Rev. Lett.*, **98**, 208501  
 Jardin, S. C. 2012, *J. Comput. Phys.*, **231**, 822  
 Jones, C. A., Kuzanyan, K. M., & Mitchell, R. H. 2009, *J. Fluid Mech.*, **634**, 291  
 Käpylä, P. J. 2011, *Astron. Nachr.*, **332**, 43  
 Käpylä, P. J. 2019, *A&A*, **631**, A122  
 Käpylä, P. J. 2021, *A&A*, **651**, A66  
 Käpylä, P. J., Korpi, M. J., & Brandenburg, A. 2008, *A&A*, **491**, 353  
 Käpylä, P. J., Mantere, M. J., & Brandenburg, A. 2011, *Astron. Nachr.*, **332**, 883  
 Käpylä, P. J., Mantere, M. J., & Brandenburg, A. 2012, *ApJ*, **755**, L22



- Käpylä, P. J., Mantere, M. J., Cole, E., Warnecke, J., & Brandenburg, A. 2013, *ApJ*, 778, 41
- Käpylä, P. J., Gent, F. A., Olsper, N., Käpylä, M. J., & Brandenburg, A. 2020, *Geophys. Astrophys. Fluid Dyn.*, 114, 8
- Karak, B. B., Käpylä, P. J., Käpylä, M. J., et al. 2015, *A&A*, 576, A26
- Kazantsev, A. P. 1968, *Sov. J. Exp. Theor. Phys.*, 26, 1031
- Khomenko, E., & Collados, M. 2006, *ApJ*, 653, 739
- Kippenhahn, R., Weigert, A., & Weiss, A. 2013, *Stellar Structure and Evolution* (Springer)
- Kolmogorov, A. 1941, *Akad. Nauk SSSR Dokl.*, 30, 301
- Kupka, F., & Muthsam, H. J. 2017, *Living Rev. Comput. Astrophys.*, 3, 1
- Lerbinger, K., & Luciani, J. F. 1991, *J. Comput. Phys.*, 97, 444
- LeVeque, R. J. 2002, *Finite Volume Methods for Hyperbolic Problems*, *Cambridge Texts in Applied Mathematics* (Cambridge University Press)
- Londrillo, P., & del Zanna, L. 2004, *J. Comput. Phys.*, 195, 17
- Lütjens, H., & Luciani, J.-F. 2010, *J. Comput. Phys.*, 229, 8130
- Masada, Y., Yamada, K., & Kageyama, A. 2013, *ApJ*, 778, 11
- Matthaeus, W. H., & Brown, M. R. 1988, *Phys. Fluids*, 31, 3634
- Meneguzzi, M., Frisch, U., & Pouquet, A. 1981, *Phys. Rev. Lett.*, 47, 1060
- Mestel, L. 1999, *Stellar Magnetism* (Oxford University Press)
- Miczek, F. 2013, Dissertation, Technische Universität München, Germany
- Miczek, F., Röpke, F. K., & Edelmann, P. V. F. 2015, *A&A*, 576, A50
- Mignone, A., & Del Zanna, L. 2021, *J. Comput. Phys.*, 424, 109748
- Minoshima, T., & Miyoshi, T. 2021, *J. Comput. Phys.*, 446, 110639
- Minoshima, T., Kitamura, K., & Miyoshi, T. 2020, *ApJS*, 248, 12
- Miyoshi, T., & Kusano, K. 2005, *J. Comput. Phys.*, 208, 315
- Müller, B. 2020, *Living Rev. Comput. Astrophys.*, 6, 3
- Pietarila Graham, J., Cameron, R., & Schüssler, M. 2010, *ApJ*, 714, 1606
- Powell, K. G. 1997, in *Upwind and High-Resolution Schemes*, eds. M.Y. Hussaini, B. van Leer, J. Van Rosendale (Springer), 570
- Powell, K. G., Roe, P. L., Linde, T. J., Gombosi, T. I., & De Zeeuw, D. L. 1999, *J. Comput. Phys.*, 154, 284
- Rempel, M. 2005, *ApJ*, 622, 1320
- Rempel, M. 2014, *ApJ*, 789, 132
- Rempel, M. 2018, *ApJ*, 859, 161
- Riva, F., & Steiner, O. 2022, *A&A*, 660, A115
- Rogers, T. M., Lin, D. N. C., McElwaine, J. N., & Lau, H. H. B. 2013, *ApJ*, 772, 21
- Schekochihin, A. A., Cowley, S. C., Taylor, S. F., Maron, J. L., & McWilliams, J. C. 2004, *ApJ*, 612, 276
- Schekochihin, A. A., Iskakov, A. B., Cowley, S. C., et al. 2007, *N. J. Phys.*, 9, 300
- Schnack, D., Barnes, D., Mikic, Z., Harned, D. S., & Caramana, E. 1987, *J. Comput. Phys.*, 70, 330
- Seta, A., & Federrath, C. 2020, *MNRAS*, 499, 2076
- Shu, C.-W., & Osher, S. 1988, *J. Comput. Phys.*, 77, 439
- Smolarkiewicz, P. K., & Charbonneau, P. 2013, *J. Comput. Phys.*, 236, 608
- Stone, J. M., Gardiner, T. A., Teuben, P., Hawley, J. F., & Simon, J. B. 2008, *ApJS*, 178, 137
- Strang, G. 1968, *SIAM J. Numer. Anal.*, 5, 506
- Sutherland, B. R. 2010, *Internal Gravity Waves* (Cambridge University Press)
- Timmes, F. X., & Swesty, F. D. 2000, *ApJS*, 126, 501
- Toro, E. F. 2009, *Riemann Solvers and Numerical Methods for Fluid Dynamics: A Practical Introduction* (Springer)
- Tóth, G. 2000, *J. Comput. Phys.*, 161, 605
- Viallet, M., Baraffe, I., & Walder, R. 2011, *A&A*, 531, A86
- Viviani, M., Käpylä, M. J., Warnecke, J., Käpylä, P. J., & Rheinhardt, M. 2019, *ApJ*, 886, 21
- Vögler, A., Shelyag, S., Schüssler, M., et al. 2005, *A&A*, 429, 335
- Warnecke, J., Käpylä, P. J., Käpylä, M. J., & Brandenburg, A. 2016, *A&A*, 596, A115
- Yadav, R. K., Christensen, U. R., Wolk, S. J., & Poppenhaeger, K. 2016, *ApJ*, 833, L28

### Appendix A: Magnetized Kelvin–Helmholtz instability

This appendix explores the effects of the grid resolution and strength of the initial magnetic field on the evolution of the Kelvin–Helmholtz instability shown in Sect. 5.3.

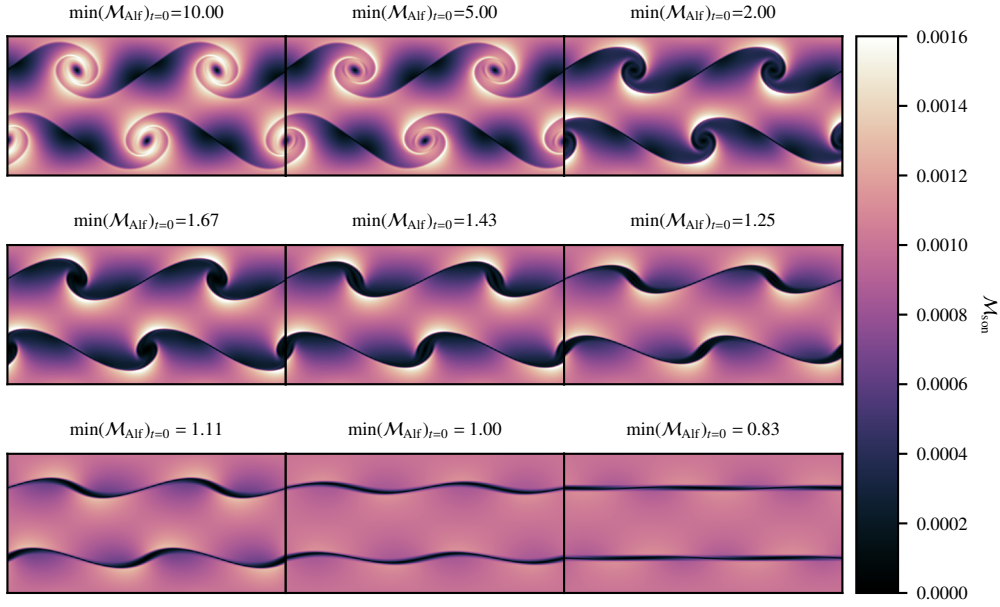


**Fig. A.1.** Distribution of the sonic Mach number in the simulations of the Kelvin–Helmholtz instability at  $t/t_{\max} = 1/6$  for different values of the initial magnetic field,  $B_x$ , computed as  $B_x = \sqrt{\gamma}\alpha$ , with  $\alpha = (0.1, 0.2, 0.5, 0.6, 0.7, 0.9, 0.9, 1.0, 1.2)$ . These simulations were performed on a  $512 \times 256$  grid with  $M_x = 10^{-3}$ . The title in each panel is the corresponding minimum Alfvén Mach number of the flow at  $t = 0$ . For a strong enough initial magnetic field, the magnetic stresses prevent the growth of the instability.

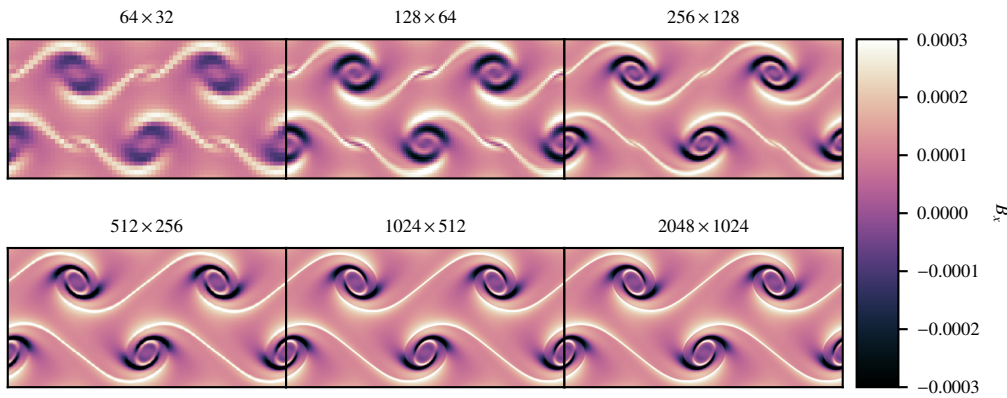


**Fig. A.2.** Distribution of  $B_x$  in the simulations of the Kelvin–Helmholtz instability at  $t/t_{\max} = 1/6$  for different grid resolutions, starting from the initial conditions described in Sect. 5.3 with  $M_x = 10^{-3}$ . On grids with  $N \leq 128$ , numerical discretization errors generate grid-scale vorticity, which leads to the growth of secondary instabilities in the regions between the primary rolls. This effect does not appear in better converged simulations.

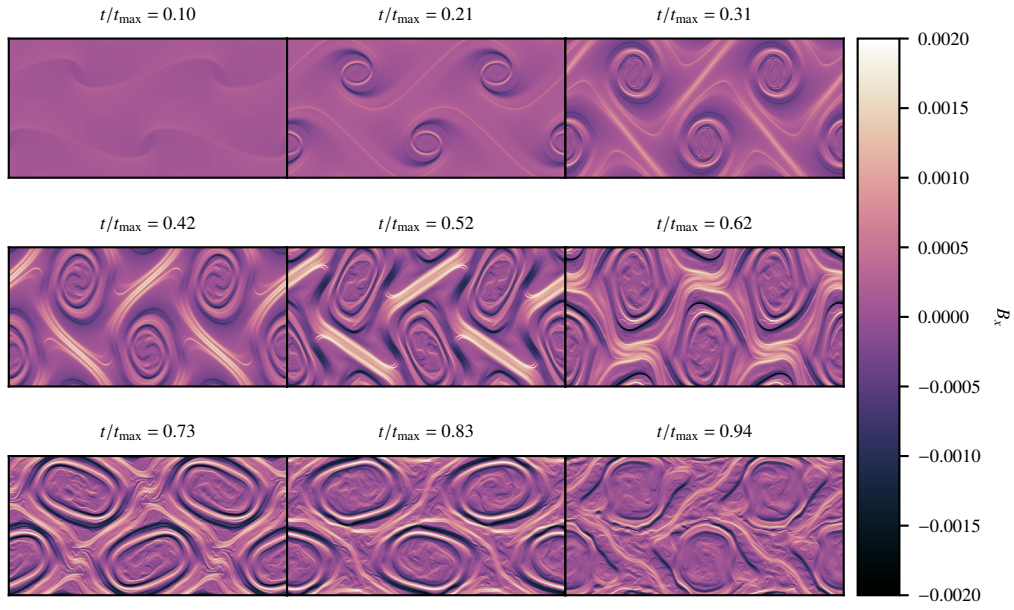


**Fig. A.3.** Time evolution of  $B_x$  in the simulations of the Kelvin–Helmholtz instability starting from the initial conditions described in Sect. 5.3 with  $\mathcal{M}_x = 10^{-3}$ . The grid is  $2048 \times 1024$ .

## Appendix B: Hot bubble

Here, we extend the study described in Sect. 5.4. In particular, we show the dependence of the entropy fluctuations,  $\mathcal{M}_{\text{son}}$ , and  $p_B$  on the magnitude of the initial entropy perturbation  $(\Delta A/A)_{t=0}$ .

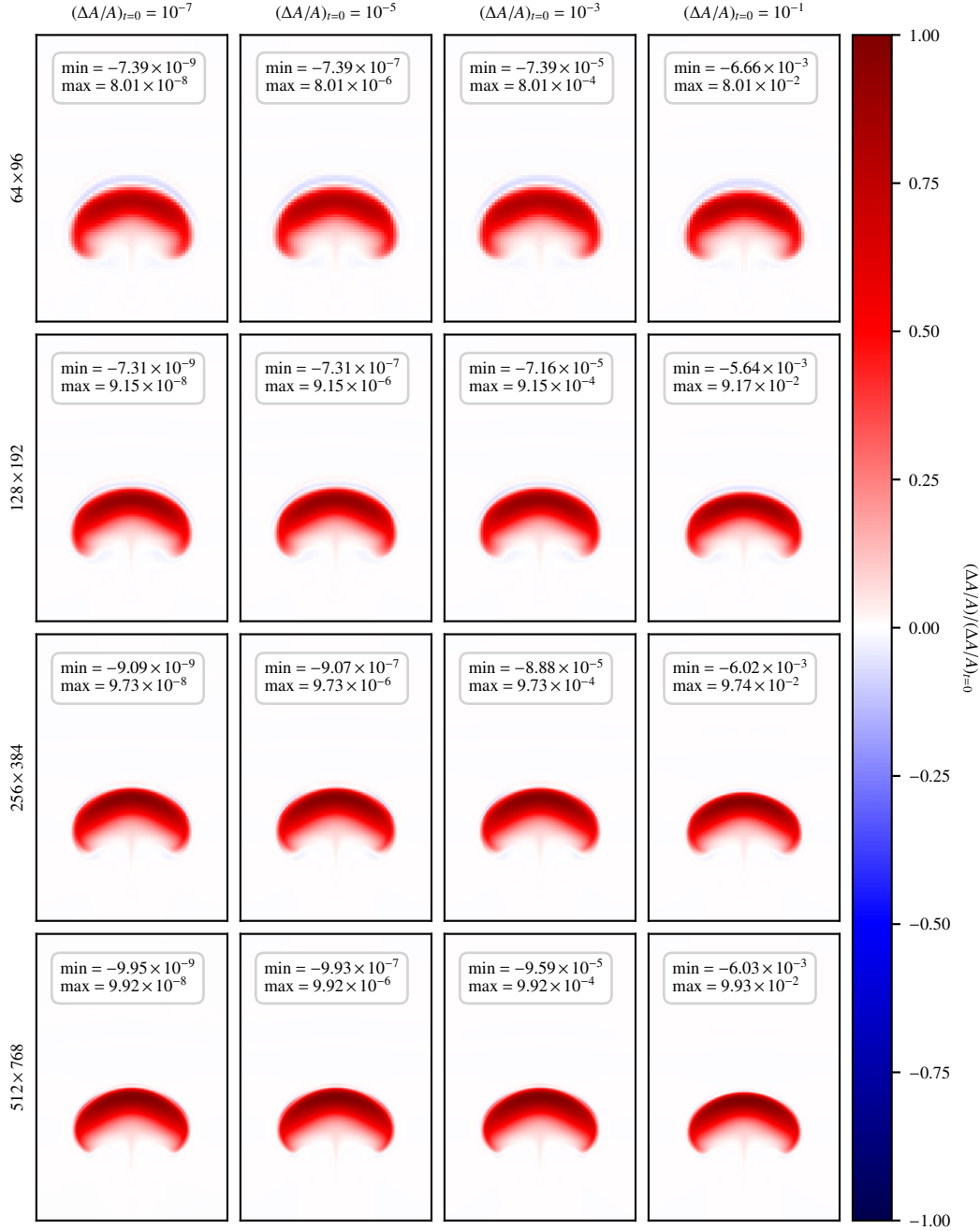


**Fig. B.1.** Final distribution of the entropy fluctuations,  $\Delta A/A$ , of the hot bubble for different values of  $(\Delta A/A)_{t=0}$  and grid resolutions. Each panel is rescaled by the corresponding value of  $(\Delta A/A)_{t=0}$ . The insets provide the minimum and maximum values of the entropy fluctuations in each plot.

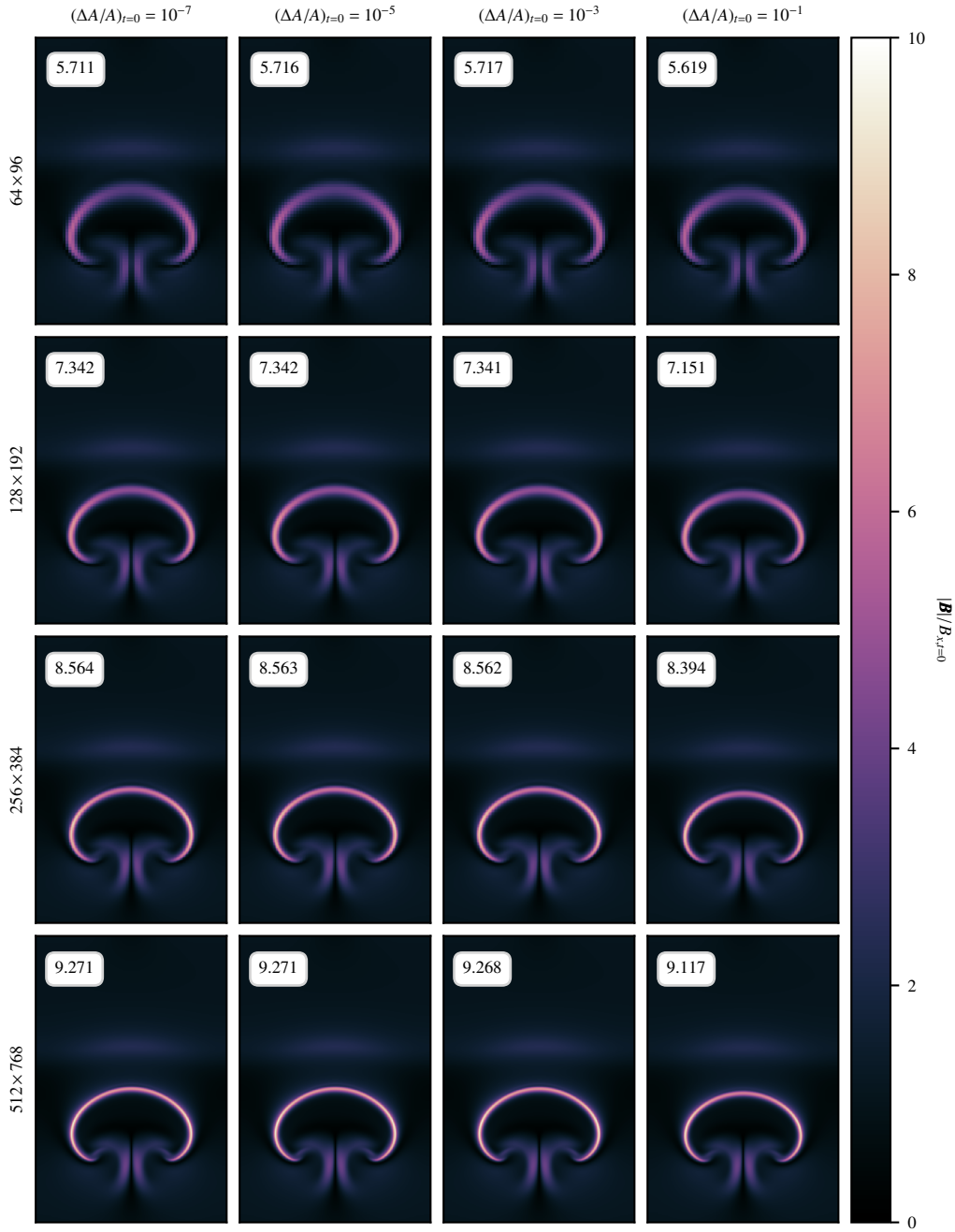


**Fig. B.2.** Final distribution of  $|B|/B_{x,t=0}$  for different values of  $(\Delta A/A)_{t=0}$  and grid resolutions in the simulations of the hot bubble. The insets show the maximum ratio in each panel. The amount of numerical resistivity decreases upon grid refinement, which leads to the generation of narrower stripes with stronger magnetic fields.

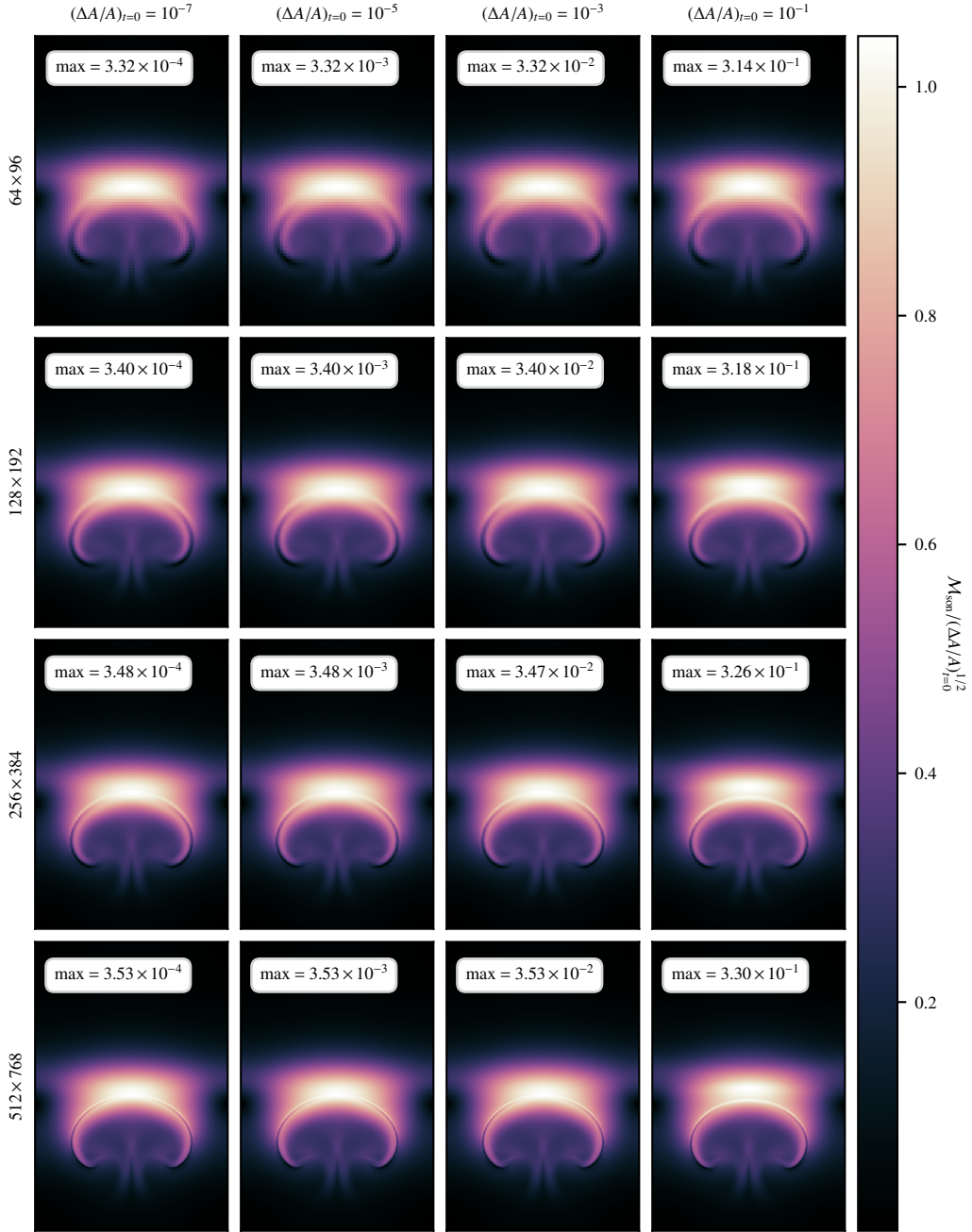


**Fig. B.3.** Final distribution of the sonic Mach number of the hot bubble for different values of  $(\Delta A/A)_{t=0}$  and different grid resolutions. Each panel is rescaled by the corresponding value of  $(\Delta A/A)_{t=0}^{1/2}$ . The insets show the maximum sonic Mach number. An entropy perturbation of  $(\Delta A/A)_{t=0} = 0.1$  drives flows that are far from the low-Mach-number regime. In this case, effects of compressibility caused by the high ram pressure of the bubble are large enough to cause a 6–7% deviation from the theoretical scaling discussed in Sect. 5.4.

### Appendix C: Small-scale dynamo

In this section we extend the analysis of the SSD test described in Sect. 5.5. In particular, we show 1D vertical averages of the

velocity and magnetic field distributions, the time evolution of the numerical divergence of the magnetic field, vertical cuts of the sonic Mach number distribution and the time evolution of the total magnetic energy in the kinematic phase.

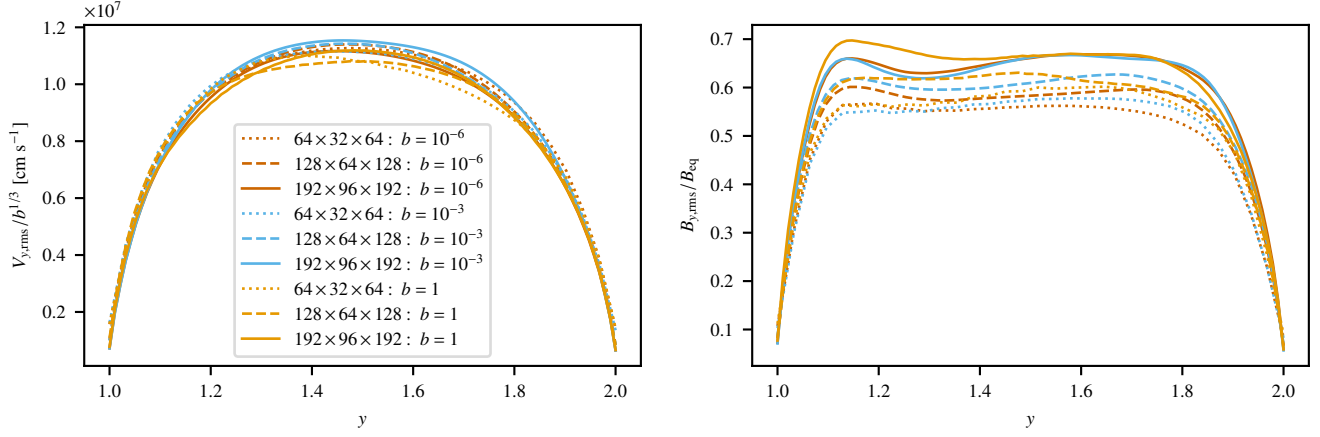


**Fig. C.1.** Vertical profiles of  $V_y$  (left) and  $B_y$  (right) in the simulations of the SSD, averaged over  $20 < t/\tau_{conv} < 40$ . Different colors represent different grid resolutions, while different line styles are used for representing different values of  $b$ . The vertical velocity is rescaled by  $b^{2/3}$  to remove the dependence of the energy injection rate, while  $B_y$  is rescaled by the corresponding equipartition value,  $B_{eq} = \sqrt{\rho}|\mathbf{V}|_{rms}$ .

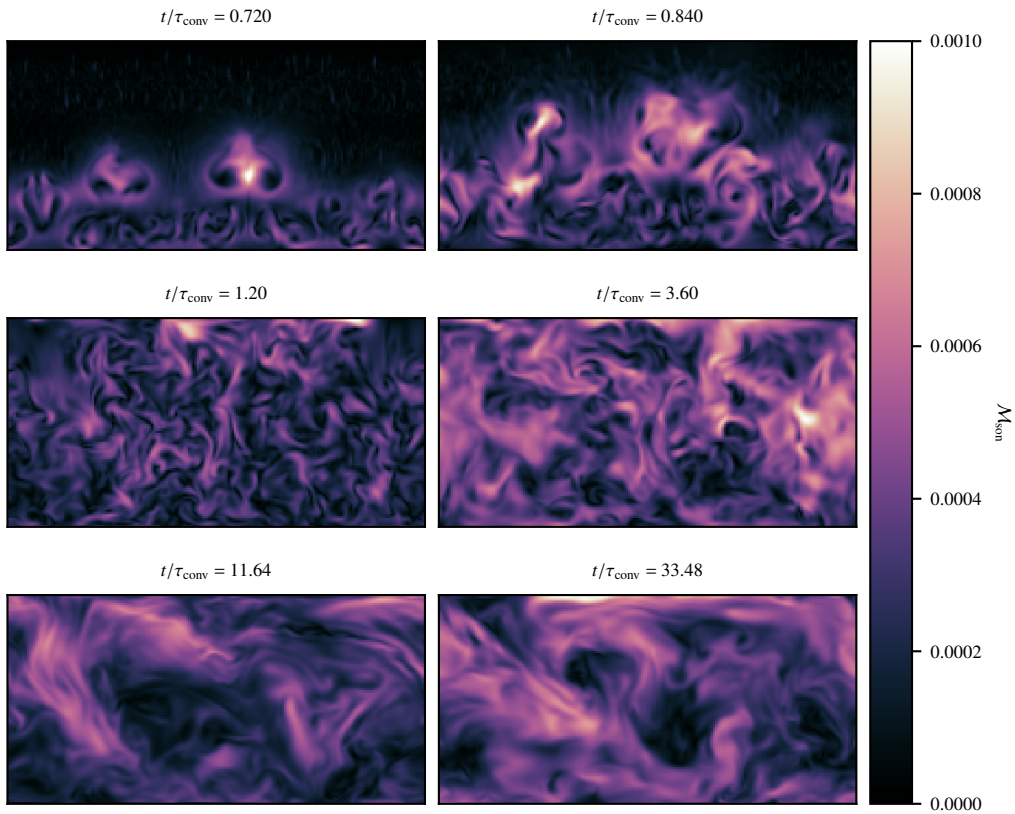


**Fig. C.2.** Vertical cuts of the sonic Mach number taken at  $z = 0$  in the simulations of the SSD run with  $b = 10^{-6}$  on the  $192 \times 96 \times 192$  grid. Each panel is taken at a different moment in time, which is given in the title. As the SSD approaches the saturated regime, the small-scale structures in the velocity field are damped by the Lorentz force, and vertical motions mainly happen in the form of large-scale flows.



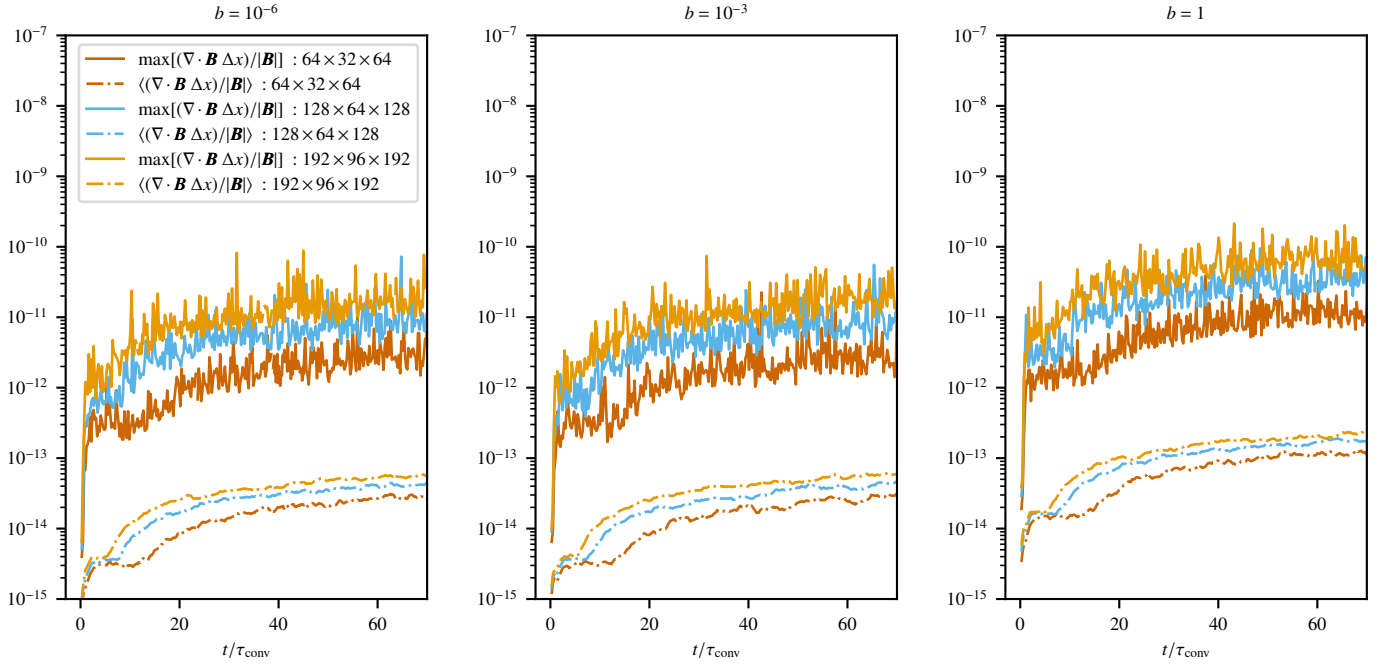


**Fig. C.3.** Time evolution of the maximum (solid line) and mean (dot-dashed) relative divergence of the magnetic field in the simulations of the SSD. Since the induction equation is solved using a staggered constrained transport method, the update on the magnetic field keeps the divergence in Eq. (47) within round-off error. Although these errors accumulate in time, by the end of the simulation magnetic monopoles are still irrelevant to the dynamics of the SSD.

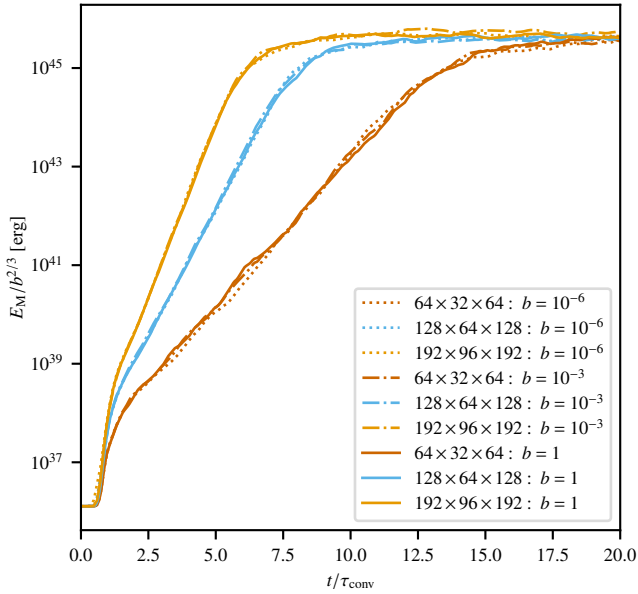


**Fig. C.4.** Time evolution of the magnetic energy in the simulations of the SSD up to  $t/\tau_{\text{conv}} = 20$ . Each line style represents a specific value of the boost factor,  $b$ , while different colors are used for different numbers of grid cells.



## 3.2 Publication II: Comparison of different Godunov-like methods in simulations of astrophysical subsonic flows

The study presented in Sect. 3.1 demonstrated the significance of employing low-dissipation Riemann solvers in simulations of low-Mach-number MHD flows. At the same time, it was shown that the use of partially implicit time discretization can drastically diminish the computational cost of simulations for Mach numbers lower than  $\approx 0.05$ . To limit the size of the parameter space, no emphasis was put on the spatial reconstruction method. A second-order accurate, unlimited scheme was used to reconstruct the pair of Riemann states at cell boundaries in all tests.

However, the choice of the reconstruction function plays a key role in determining both the accuracy and performance of the code. In simulations of astrophysical flows, the question of what combination of the Riemann solver and spatial reconstruction will produce the desired solution at minimal computational cost is crucial. In fact, these simulations often require huge amounts of computational resources, pushing the limits of even big computing centers. Finding the ingredients in the Godunov algorithm that minimize the effort to compute a given solution is non-trivial. As explained in section 2.3.1, simply increasing the order of the reconstruction polynomial does not necessarily produce more accurate results, especially when the flows are discontinuous or show other nonlinearities. Also, higher-order TVD methods such as PPM involve several conditional statements that break vectorization, so they tend to be more expensive than lower-order or unlimited methods.

This paper aims to quantify the properties of 18 different combinations of methods in the Godunov algorithm with a special focus on subsonic flows, which are particularly relevant to stellar and geophysical hydrodynamics. In particular, 6 spatial reconstruction schemes (ranging from unlimited linear to a 7<sup>th</sup>-order accurate method) and 3 Riemann solvers (Rusanov, HLLC, and a low-dissipation solver) are tested using two verification benchmarks: a 2D, Kelvin–Helmholtz instability, where the Mach number of the shear layers varies from  $10^{-3}$  to 0.1, and an astrophysical setup, namely an idealized oxygen-burning shell of a massive star, which involves 3D turbulent convection, convective boundary mixing processes, and excitation of internal waves.

This work is limited to purely hydrodynamic flows (i.e., without magnetic fields). An analogous comparison of MHD methods would require taking into account the way the divergence-free property of the magnetic field is characterized by the numerical scheme, which would considerably increase the complexity of the study. However, the main results obtained in this paper are general and also apply to MHD flows.

## **Title**

Performance of high-order Godunov-type methods in simulations of astrophysical low Mach number flows

## **Authors**

G. Leidi, R. Andrassy, W. Barsukow, J. Higl, P. V. F. Edelmann, and F. K. Röpke

## **Publication status**

The manuscript was accepted for publication in February 2024.

## **DOI**

<https://doi.org/10.48550/arXiv.2402.16706>

<https://doi.org/10.1051/0004-6361/202348882>

## **Author's contribution**

GL is the main author of this paper. GL implemented most of the numerical methods used in the proposed comparison study and ran simulations of the test problem involving turbulent convection and excitation of internal waves. GL further analyzed the simulation results and wrote most of the manuscript. The project idea originated during discussions with RA, who also constructed the PSH method presented in this study, ran simulations of the Kelvin–Helmholtz instability, and contributed parts of the theory sections. PFVE and JH provided parts of the computational resources. All authors contributed to the manuscript by suggesting content and improvements.

## **Credit**

Leidi et al., 2024, arXiv e-prints, arXiv:2402.16706

# Performance of high-order Godunov-type methods in simulations of astrophysical low Mach number flows

G. Leidi<sup>1</sup>, R. Andrassy<sup>1</sup>, W. Barsukow<sup>2</sup>, J. Higl<sup>1,3</sup>, P. V. F. Edelman<sup>4</sup>, and F. K. Röpke<sup>1,5</sup>

<sup>1</sup> Heidelberger Institut für Theoretische Studien, Schloss-Wolfsbrunnenweg 35, D-69118 Heidelberg, Germany  
e-mail: giovanni.leidi@h-its.org

<sup>2</sup> Bordeaux Institute of Mathematics, Bordeaux University and CNRS/UMR5251, Talence, 33405 France

<sup>3</sup> High-Performance Computing Center Stuttgart, Nobelstraße 19, 70569 Stuttgart, Germany

<sup>4</sup> Computer, Computational and Statistical Sciences (CCS) Division and Center for Theoretical Astrophysics (CTA), Los Alamos National Laboratory, Los Alamos, PO Box 1663, NM 87545, USA

<sup>5</sup> Zentrum für Astronomie der Universität Heidelberg, Institut für Theoretische Astrophysik, Philosophenweg 12, D-69120 Heidelberg, Germany

Received 8 December 2023 / Accepted 23 February 2024

## ABSTRACT

High-order Godunov methods for gas dynamics have become a standard tool for simulating different classes of astrophysical flows. Their accuracy is mostly determined by the spatial interpolant used to reconstruct the pair of Riemann states at cell interfaces and by the Riemann solver that computes the interface fluxes. In most Godunov-type methods, these two steps can be treated independently, so that many different schemes can in principle be built from the same numerical framework. Because astrophysical simulations often test out the limits of what is feasible with the computational resources available, it is essential to find the scheme that produces the numerical solution with the desired accuracy at the lowest computational cost. However, establishing the best combination of numerical options in a Godunov-type method to be used for simulating a complex hydrodynamic problem is a nontrivial task. In fact, formally more accurate schemes do not always outperform simpler and more diffusive methods, especially if sharp gradients are present in the flow. In this work, we use our fully compressible SEVEN-LEAGUE HYDRO (SLH) code to test the accuracy of six reconstruction methods and three approximate Riemann solvers on two- and three-dimensional (2D and 3D) problems involving subsonic flows only. We consider Mach numbers in the range from  $10^{-3}$  to  $10^{-1}$ , which are characteristic of many stellar and geophysical flows. In particular, we consider a well-posed, 2D, Kelvin–Helmholtz instability problem and a 3D turbulent convection zone that excites internal gravity waves in an overlying stable layer. Although the different combinations of numerical methods converge to the same solution with increasing grid resolution for most of the quantities analyzed here, we find that (i) there is a spread of almost four orders of magnitude in computational cost per fixed accuracy between the methods tested in this study, with the most performant method being a combination of a “low-dissipation” Riemann solver and a sextic reconstruction scheme, (ii) the low-dissipation solver always outperforms conventional Riemann solvers on a fixed grid when the reconstruction scheme is kept the same, (iii) in simulations of turbulent flows, increasing the order of spatial reconstruction reduces the characteristic dissipation length scale achieved on a given grid even if the overall scheme is only second order accurate, (iv) reconstruction methods based on slope-limiting techniques tend to generate artificial, high-frequency acoustic waves during the evolution of the flow, (v) unlimited reconstruction methods introduce oscillations in the thermal stratification near the convective boundary, where the entropy gradient is steep.

**Key words.** Convection – Hydrodynamics – Instabilities – Methods: numerical – Turbulence – Waves

## 1. Introduction

High-resolution schemes for gas dynamics (see, e.g., van Leer 1979; Colella & Woodward 1984; Harten et al. 1987; Colella 1990; Liu et al. 1994; Jiang & Shu 1996; Colella & Sekora 2008; Toro 2009; Balsara 2017) are routinely used for modeling a broad variety of astrophysical flow phenomena. Their popularity derives from their conservation properties and robustness, which allow them to accurately capture both smooth and discontinuous solutions on the same computational grid without sacrificing numerical stability.

These schemes are based on higher-order extensions of the original first-order accurate method of Godunov (1959) and their time-integration algorithm is typically carried out in three steps. First, a pair of Riemann states is reconstructed at each grid cell interface by applying high-order monotonic interpolants to a set of cell-averaged hydrodynamic quantities. Second, the resulting

Riemann problems are solved (either exactly or approximately) to obtain fluxes across every cell boundary. Finally, the cell surface integral of the fluxes is evaluated, allowing the cell-volume-averaged state quantities to be advanced in time<sup>1</sup>.

In most high-order Godunov schemes, the solution strategy of the Riemann problem is independent of the spatial interpolant used for reconstructing the Riemann states. Therefore, many different schemes can be built from the same numerical framework. The choices made in the construction of a particular scheme, however, do have a strong effect on its accuracy, that is the dif-

<sup>1</sup> High-resolution schemes for gas dynamics can be fully discrete, where the system of equations is discretized both in space and time, or semi-discrete, where spatial discretization is performed first while leaving the problem continuous in time. In the latter approach, state quantities are then advanced in time using any standard numerical solver for systems of ordinary differential equations.

ference between the numerical ( $U$ ) and the true ( $u$ ) solution,

$$\|U - u\| = O(\Delta x^m) + O(\Delta t^n), \quad (1)$$

computed in some norm  $\|\cdot\|$  (see, e.g., [LeVeque 2002](#)). Here,  $\Delta x$  is the width of the grid cell and  $\Delta t$  is the time step. Although the formal order of the spatial and temporal accuracy of a Godunov-like scheme, “ $m$ ” and “ $n$ ” in Eq. (1), can be derived for smooth flows, they do not give any information about the magnitude of the numerical errors generated on a given grid, which is problem-dependent. The convergence rates can also be significantly lower than the formal order of accuracy of the scheme for problems that admit non-smooth solutions. Consequently, formally higher-than-second-order interpolants do not always outperform simpler linear spatial reconstruction schemes when large gradients or discontinuities are present in the flow ([Greenough & Rider 2003](#)). Moreover, if the flow is stochastic or chaotic, like in the case of turbulence, convergence may not be achieved in the sense of Eq. (1), but rather the quality of the numerical results can only be judged in terms of global or ensemble-averaged quantities that characterize the flow and its evolution.

Given these considerations, it is impossible to generalize the convergence properties of a certain combination of numerical methods in a Godunov-type scheme, so they have to be explored by running numerical tests. Such tests, to be significant, have to be challenging enough and close to the actual application case. The performance of the numerical scheme is another crucial aspect to be considered alongside its accuracy, especially in astrophysical simulations, which often test out the limits of what is feasible nowadays with available computational resources. Therefore, the question arises of what combination of different ingredients in a Godunov-type scheme should be used to produce the desired solution at a minimal computational cost.

Several comparison studies have been presented in the literature with the aim of shedding light on the behavior of different high-resolution schemes in simulations of complex hydrodynamic phenomena, such as forced turbulence ([Klingenberg et al. 2007](#); [Kritsuk et al. 2011](#); [San & Kara 2015](#); [Radice et al. 2015](#); [Seo & Ryu 2023](#)), convection ([Müller 2020](#)), jet evolution ([Beckwith & Stone 2011](#); [Musoke et al. 2020](#)), magneto-rotational instabilities in accretion disks ([Flock et al. 2010](#)), Richtmyer-Meshkov instabilities ([Latini et al. 2007](#)), and shear instabilities ([McNally et al. 2012](#); [Lecoanet et al. 2017](#)). These numerical experiments focused on supersonic or mildly subsonic flow regimes, for which Godunov-type methods are highly optimized (see, e.g., [LeVeque 2002](#); [Toro 2009](#)). Nonetheless, high-resolution schemes have been proven to be a powerful tool also for modeling regimes of low Mach numbers ( $\mathcal{M} := |V|/c \lesssim 0.1$ , where  $V$  is the fluid velocity and  $c$  is the sound speed), especially in simulations of terrestrial (see, e.g., [Day & Bell 2000](#); [Klein 2009](#); [Dumbser et al. 2009](#); [Motheau et al. 2018](#)) and stellar (see, e.g., [Meakin & Arnett 2007](#); [Muthsam et al. 2010](#); [Woodward et al. 2014](#); [Goffrey et al. 2017](#); [Müller 2020](#); [Horst et al. 2021](#); [Canivete Cuissa & Teyssier 2022](#)) flows. To our knowledge, other than idealized tests, no extensive work along the line of the aforementioned comparison studies has been presented for low-Mach-number flows yet. Only a few studies evaluated the impact of the order of the spatial and temporal discretization in the numerical scheme on the properties of highly subsonic turbulent flows, but they kept the Riemann solver fixed ([Wongwathanarat et al. 2016](#); [Teyssier & Müller 2023](#)).

In this work, we use our fully compressible SEVEN-LEAGUE HYDRO (SLH) code to test 18 different combinations of spatial reconstruction schemes and Riemann solvers on two test problems

in which flows are highly subsonic ( $10^{-3} \lesssim \mathcal{M} \lesssim 10^{-1}$ ). In particular, we consider a two-dimensional (2D) Kelvin–Helmholtz instability with smooth initial conditions and a 3D, turbulent convection zone that entrains material from an upper, stably stratified layer, where internal waves are free to propagate. The initial conditions of the latter test are adopted from the work of [Andrassy et al. \(2022\)](#). Here, we opt to reduce the strength of the heat source driving the convection in order to achieve lower convective speeds than those obtained by [Andrassy et al. \(2022\)](#). Also, contrary to that work, we provide performance measurements for all the methods tested in our study. In both tests, we conduct a resolution study to analyze the convergence of the numerical results obtained by each method.

The paper is structured as follows: in Sect. 2, we provide a detailed description of the equations solved and the numerical methods included in this study. In Sect. 3, we measure the convergence properties of different Godunov-type schemes for the 2D, Kelvin–Helmholtz instability test problem (see Sect. 3.1) and for the 3D setup involving turbulent convection, convective boundary mixing, and wave excitation (see Sect. 3.2). In Sect. 4, we use the kinetic energy spectrum of the convective flows simulated in the latter test, which is close to a real astrophysical application, to provide measurements of the computational cost per fixed accuracy for each method. Finally, in Sect. 5, we summarize the main results and we give some guidance on which methods to use for specific applications.

## 2. Methods

### 2.1. Governing equations

We solve the fully compressible, inviscid Euler equations with a source term  $S$  in the integral form

$$\frac{1}{|\Omega|} \frac{\partial}{\partial t} \left( \int_{\Omega} U \, d\Omega \right) + \frac{1}{|\Omega|} \oint_{\partial\Omega} \mathbb{T} \cdot \mathbf{n} \, dA = \frac{1}{|\Omega|} \int_{\Omega} S \, d\Omega, \quad (2)$$

where

$$U = \begin{bmatrix} \rho \\ \rho u \\ \rho v \\ \rho w \\ \rho e_{\text{tot}} \\ \rho X \end{bmatrix} \quad (3)$$

is the set of conserved quantities,  $|\Omega|$  is the volume of a fluid element  $\Omega$  enclosed by a surface  $\partial\Omega$ ,  $\mathbf{n}$  is the outward normal vector to the surface, and  $\mathbb{T} = [\mathbf{F}|\mathbf{G}|\mathbf{H}]$  is a tensor defined by the flux vectors

$$\mathbf{F} = \begin{bmatrix} \rho u \\ \rho u^2 + p \\ \rho uv \\ \rho uw \\ (\rho e_{\text{tot}} + p)u \\ \rho Xu \end{bmatrix}, \quad \mathbf{G} = \begin{bmatrix} \rho v \\ \rho v^2 + p \\ \rho vw \\ (\rho e_{\text{tot}} + p)v \\ \rho Xv \end{bmatrix}, \quad \mathbf{H} = \begin{bmatrix} \rho w \\ \rho w^2 + p \\ \rho vw \\ (\rho e_{\text{tot}} + p)w \\ \rho Xw \end{bmatrix}. \quad (4)$$

Here,  $\rho$  denotes the mass density,  $\mathbf{V} = (u, v, w)$  the velocity field,  $e_{\text{tot}} = e_{\text{int}} + \frac{1}{2}|\mathbf{V}|^2$  the total energy per unit mass,  $e_{\text{int}}$  the specific internal energy, and  $X$  the mass fraction of a passive scalar used as a tracer advected with the fluid. The system represented by Eq. (2) is closed by an equation of state (EoS), which gives the gas pressure as a function of the density and internal energy,

$$p = p(\rho, e_{\text{int}}). \quad (5)$$

In this work, we only consider a perfect gas with a given adiabatic index  $\gamma$ , for which

$$p(\rho, e_{\text{int}}) = (\gamma - 1)\rho e_{\text{int}}. \quad (6)$$

For modeling the test problem introduced in Sect. 3.2, which involves the presence of a gravitational field,  $\mathbf{g} = (g_x, g_y, g_z)$ , the corresponding source term,

$$\mathbf{S}_{\text{grav}} = \begin{bmatrix} 0 \\ \rho g_x \\ \rho g_y \\ \rho g_z \\ \rho \mathbf{g} \cdot \mathbf{V} \\ 0 \end{bmatrix}, \quad (7)$$

must be included in the right-hand-side term of Eq. (2). Because we assume  $\mathbf{g}$  to be time-independent, we opt to solve an equivalent form of Eq. (2), in which the gravitational potential  $\phi$  is directly added to  $e_{\text{tot}}$ , eliminating the  $\rho \mathbf{g} \cdot \mathbf{V}$  source term from the energy equation,

$$e_{\text{tot}} \mapsto e_{\text{tot}} + \phi, \quad \mathbf{S}_{\text{grav}} = \begin{bmatrix} 0 \\ \rho g_x \\ \rho g_y \\ \rho g_z \\ \rho \mathbf{g} \cdot \mathbf{V} \\ 0 \end{bmatrix} \mapsto \begin{bmatrix} 0 \\ \rho g_x \\ \rho g_y \\ \rho g_z \\ 0 \\ 0 \end{bmatrix}. \quad (8)$$

Numerical schemes that solve this form of Eq. (2) are capable of conserving the total energy of the system over time exactly. Such a property is particularly important in low-Mach-number hydrodynamics, where even small energy conservation errors can become comparable to the kinetic energy content of the flows (Müller 2020; Edelmann et al. 2021).

## 2.2. Seven-League Hydro code

In our study, Eq. (2) is solved numerically using the SEVEN-LEAGUE HYDRO code (SLH, Miczek 2013; Edelmann 2014), which was originally developed to model the broad variety of hydrodynamic processes that characterize the deep interiors of stars, such as shear instabilities (Edelmann et al. 2017), excitation of internal waves (Horst et al. 2020), convective boundary mixing (Horst et al. 2021; Andrassy et al. 2022, 2023), and turbulent dynamos (Leidi et al. 2022, 2023). SLH makes use of the finite-volume discretization on an arbitrarily curvilinear, but logically rectangular, Eulerian grid to retain the conservation properties of the fluid-dynamics equations. Numerical solutions to Eq. (2) are computed by means of Godunov-type methods based on the definition of Riemann problems at cell interfaces. The code is parallelized using the Message Passing Interface (MPI) and it has been proven to scale up to several hundred thousand processes (Edelmann & Röpke 2016).

SLH allows the user to choose among many different numerical options at compile time, which makes this code perfectly suited to run the comparison study introduced in Sect. 1. In particular, in addition to the well-known Rusanov (Rusanov 1962), Roe (Roe 1981), and Harten-Lax-van Leer-Contact (HLLC, Toro et al. 1994) approximate Riemann solvers, SLH adopts special low-Mach-number methods (Liou 2006; Miczek et al. 2015; Minoshima & Miyoshi 2021) to reduce the excessive numerical dissipation introduced by shock-capturing schemes at low Mach numbers (see Sect. 2.4). A wide spectrum of spatial reconstruction methods can be used to generate a pair or Riemann states

at each grid cell interface, ranging from (first-order accurate) constant reconstruction to very high order methods, some of which are described in Sect. 2.3. In problems involving the presence of a gravitational field, the deviation well-balancing method (Berberich et al. 2021; Edelmann et al. 2021) is used to preserve hydrostatic solutions and to reduce the strength of spurious flows generated by grid discretization errors in strongly stratified media.

In SLH, the cell-volume-averaged source term and the cell-surface-averaged fluxes are approximated using the midpoint method, making the code at best second-order accurate in space. On a 3D, evenly spaced Cartesian grid, the final expressions for these integrals read

$$\frac{1}{\Delta V} \int_{\Omega_{i,j,k}} \mathbf{S} \, dx dy dz = \mathcal{S}_{i,j,k} + \mathcal{O}(\Delta x^2), \quad (9)$$

$$\frac{1}{\Delta A} \int_{\Delta A_{i+1/2,j,k}} \mathbf{F} \, dy dz = \mathcal{F}_{i+1/2,j,k} + \mathcal{O}(\Delta x^2), \quad (10)$$

$$\frac{1}{\Delta A} \int_{\Delta A_{i,j+1/2,k}} \mathbf{G} \, dx dz = \mathcal{G}_{i,j+1/2,k} + \mathcal{O}(\Delta x^2), \quad (11)$$

$$\frac{1}{\Delta A} \int_{\Delta A_{i,j,k+1/2}} \mathbf{H} \, dx dy = \mathcal{H}_{i,j,k+1/2} + \mathcal{O}(\Delta x^2), \quad (12)$$

where  $\mathcal{S}_{i,j,k}$  is the point value of the source term  $\mathbf{S}$  at the center of the cell represented by the set of indices  $(i, j, k)$  and vector quantities such as  $\mathcal{F}_{i+1/2,j,k}$  refer to the face-centered value of the flux at the boundary between two adjacent cells, in this case  $(i, j, k)$  and  $(i + 1, j, k)$ . The volume of the cell and the surface of a cell face are  $\Delta V = \Delta x^3$  and  $\Delta A = \Delta x^2$ , respectively. The discretized source term and fluxes in Eqs. (9)–(12) are used to build a semi-discrete version of Eq. (2) which leaves the problem continuous in time, following the method of lines (see, e.g., LeVeque 2002),

$$\begin{aligned} \frac{\partial \bar{U}_{i,j,k}}{\partial t} = & -\frac{1}{\Delta x} \left( \mathcal{F}_{i+1/2,j,k} - \mathcal{F}_{i-1/2,j,k} \right. \\ & + \mathcal{G}_{i,j+1/2,k} - \mathcal{G}_{i,j-1/2,k} \\ & + \mathcal{H}_{i,j,k+1/2} - \mathcal{H}_{i,j,k-1/2} \left. \right) \\ & + \mathcal{S}_{i,j,k}. \end{aligned} \quad (13)$$

The time update on the cell-volume-averaged conserved variables,  $\bar{U}_{i,j,k}$ , is then carried out in a dimensionally unsplit fashion using explicit or implicit time stepping. Here, we only consider a limited set of all of the numerical methods available in SLH to avoid constructing a too large parameter space. In the following sections, we provide a detailed description of the algorithms that we use for running the tests presented in Sect. 3.1 and 3.2.

## 2.3. Spatial reconstruction methods

We use six reconstruction methods as summarized in Table 1. We do not attempt to be exhaustive in the choice of our methods, which is why, for example, essentially non-oscillatory (ENO) and weighted ENO (WENO) schemes (see, e.g., Liu et al. 1994; Jiang & Shu 1996; Shu 2009) are left out from our comparison study<sup>2</sup>. We also exclude multidimensional reconstruction methods. However, the methods we do include cover a wide range in

<sup>2</sup> The influence of the parameter that occurs in the smoothness indicators of the compact third order WENO scheme of Kolb (2014) on the generation of sound waves by turbulent flows is discussed in Appendix C.



complexity and formal order of accuracy and several of them are often used in stellar hydrodynamics.

The simplest are unlimited linear (LIN) and parabolic (PAR) methods, which have proved to be well-behaved in implicit simulations of slow flows using our SLH code (e.g. Horst et al. 2020, 2021; Andrassy et al. 2023). Their main disadvantage – the generation of artificial oscillations around steep gradients – can be eliminated using slope limiters. Out of a wide spectrum of limiters available, we have decided to include the popular van Leer limiter (van Leer 1974) in combination with linear reconstruction (LIN+VL). This limiter has the total-variation-diminishing (TVD) property and eliminates the oscillations completely.<sup>3</sup> As examples of higher-order methods with limiters, we include two versions of the widely used piecewise-parabolic method (PPM): Colella & Woodward (1984, CW84 hereinafter) and Colella & Sekora (2008, CS08 hereinafter), for which we introduce the acronyms PPM84 and PPM08, respectively. We also construct a hybrid method, which we name piecewise sextic hybrid (PSH). It combines unlimited sextic reconstruction for dynamic variables ( $\rho$ ,  $V$ ,  $p$ ) with the PPM08 method for passive scalars. We provide lower-order alternatives to the PSH method in Appendix A, although we do not test them in this study.

In the remainder of this section, we provide detailed descriptions of all the six reconstruction methods in unified notation. We do this to (i) maximise the reproducibility of our work, (ii) simplify the methods' more general original forms (e.g. for non-uniform grids), (iii) make clear what choices we make if several options are available, and (iv) to point out a few typographic mistakes in the original works.

We refer to the variable being reconstructed as  $a$  in Sections 2.3.1–2.3.6. Although reconstruction can be performed in physical coordinates, we chose to do it in logical coordinates defined by the cell index  $i$ , which leads to much simpler expressions. This choice does not influence our results in any way since we use uniform Cartesian grids. In some cases, we introduce the continuous linear logical coordinate  $\zeta$  such that the coordinate of the centre of cell  $i$  is  $\zeta_i = i$  and the left and right cell interfaces are located at  $\zeta_{i-1/2} = i - \frac{1}{2}$  and  $\zeta_{i+1/2} = i + \frac{1}{2}$ , respectively. The reconstruction is usually discontinuous at the interfaces. We use the notation  $a_{i+1/2,L}$  and  $a_{i+1/2,R}$  to denote the reconstructed states on the left and right side of the interface at  $\zeta_{i+1/2}$ , respectively. Reconstruction is performed along each spatial axis separately, i.e. the reconstruction procedure is always one-dimensional. To highlight the difference between cell averages and point values, we use the notation  $\bar{a}_i$  for the average value of  $a$  within cell  $i$ .

In this work, we always reconstruct the set of cell-volume-averaged primitive variables  $\bar{q}$ , where  $q = (\rho, V, p, X)$ , because it helps reducing oscillations near discontinuities as compared to reconstructing cell-volume-averaged conserved quantities  $\bar{U}$ . In SLH, transformations between  $\bar{q}$  and  $\bar{U}$  are performed using 2<sup>nd</sup>-order approximations,

$$\begin{aligned} \bar{q} &= \xi(\bar{U}) + O(\Delta x^2), \\ \bar{U} &= \xi^{-1}(\bar{q}) + O(\Delta x^2), \end{aligned} \quad (14)$$

<sup>3</sup> This formally holds for linear advection in one spatial dimension. In practice, we do not observe oscillations even when the LIN+VL method is applied to a multi-dimensional system of conservation laws, see Sect. 3.1.

where  $\xi$  is a nonlinear, invertible transformation,

$$\xi(\mathbf{U}) = \begin{bmatrix} U_1 \\ U_2/U_1 \\ U_3/U_1 \\ U_4/U_1 \\ (\gamma - 1) \left( U_5 - \frac{1}{2U_1} (U_2^2 + U_3^2 + U_4^2) \right) \\ U_6/U_1 \end{bmatrix}, \quad (15)$$

and  $U_i$  is the  $i$ -th component of  $\mathbf{U}$ .

### 2.3.1. The LIN method

The unlimited linear reconstruction method is based on a linear approximation to the underlying function  $a(\zeta)$ . Its slope  $\delta_i$  (in cell-index coordinates) is estimated using the central difference (the Fromm method)

$$\delta_i = \frac{\bar{a}_{i+1} - \bar{a}_{i-1}}{2} = \Delta x \partial_x a|_{x_i} + O(\Delta x^3), \quad (16)$$

using which we obtain the reconstructed states

$$a_{i-1/2,R} = \bar{a}_i - \frac{\delta_i}{2} + O(\Delta x^2), \quad (17)$$

$$a_{i+1/2,L} = \bar{a}_i + \frac{\delta_i}{2} + O(\Delta x^2). \quad (18)$$

The LIN method is exact wherever  $a(\zeta)$  is locally linear, 2<sup>nd</sup>-order accurate for general but smooth functions  $a(\zeta)$ , and it requires two ghost cells at domain boundaries.<sup>4</sup>

### 2.3.2. The LIN+VL method

The van-Leer-limited linear reconstruction method is particularly easy to describe in terms of the 2<sup>nd</sup>-order-accurate, interface-centred slopes

$$\delta_{i-1/2} = \bar{a}_i - \bar{a}_{i-1}, \quad (19)$$

$$\delta_{i+1/2} = \bar{a}_{i+1} - \bar{a}_i. \quad (20)$$

The final slope  $\delta_{i,\text{lim}}$  is then obtained by applying the limiter of van Leer (1974),

$$\delta_{i,\text{lim}} = \begin{cases} \frac{2\delta_{i-1/2}\delta_{i+1/2}}{\delta_{i-1/2} + \delta_{i+1/2}} & \text{if } \delta_{i-1/2}\delta_{i+1/2} > 0, \\ 0 & \text{otherwise,} \end{cases} \quad (21)$$

which gives the reconstructed states

$$a_{i-1/2,R} = \bar{a}_i - \frac{\delta_{i,\text{lim}}}{2} + O(\Delta x^2), \quad (22)$$

$$a_{i+1/2,L} = \bar{a}_i + \frac{\delta_{i,\text{lim}}}{2} + O(\Delta x^2). \quad (23)$$

The limiter makes the slope less steep where  $a(\zeta)$  is strongly curved and flat at local extrema. With a smooth and monotonic function  $a(\zeta)$ , the effect of the limiter weakens upon grid refinement and the left and right states converge to those provided by the LIN method. This makes the LIN+VL method formally 2<sup>nd</sup>-order accurate away from any extrema. Two ghost cells are required at domain boundaries.

<sup>4</sup> Although the method only uses the cells  $i - 1$ ,  $i$ , and  $i + 1$ , reconstruction must also be performed in the first ghost cell to fully define the Riemann problem at the domain boundary.

**Table 1.** Overview of spatial reconstruction methods used in this work.

ID	Theoretical order	Practical order	Number of ghost cells	Description
LIN	2	2.0	2	piecewise linear, no limiter
LIN+VL	2	2.0	2	piecewise linear, van Leer limiter
PAR	3	3.0	2	piecewise parabolic, no limiter
PPM84	4	2.3, 1.6	3	PPM method of <a href="#">Colella &amp; Woodward (1984)</a>
PPM08	6	6.0	4	PPM method of <a href="#">Colella &amp; Sekora (2008)</a>
PSH	7	7.0	4	hybrid piecewise sextic with no limiter for dynamic variables and PPM08 for passive scalars

**Notes.** ID: identifier; Theoretical order: formal order of accuracy for smooth and monotonic solutions in 1D; Practical order: asymptotic order obtained in the 1D experiments reported in Appendix B (smooth but non-monotonic solutions). In the case of PPM84, the higher order of accuracy corresponds to linear advection and the lower one to the propagation of a sound wave using the LHLLC flux function, see Appendix B for details.

### 2.3.3. The PAR method

The unlimited parabolic method assumes that  $a(\zeta)$  can within cell  $i$  be described using the parabola

$$a(\zeta) = \sum_{n=0}^2 c_n (\zeta - \zeta_i)^n. \quad (24)$$

The three coefficients  $c_n$  are uniquely determined by the requirement that the averages of  $a(\zeta)$  in cells  $i-1$ ,  $i$ , and  $i+1$  equal  $\bar{a}_{i-1}$ ,  $\bar{a}_i$ , and  $\bar{a}_{i+1}$ , respectively. The reconstructed states are then obtained by evaluating Eq. (24) at  $\zeta_{i-1/2}$  and  $\zeta_{i+1/2}$ , respectively. The resulting expressions are

$$a_{i-1/2,R} = \frac{1}{6} (2\bar{a}_{i-1} + 5\bar{a}_i - \bar{a}_{i+1}) + O(\Delta x^3), \quad (25)$$

$$a_{i+1/2,L} = \frac{1}{6} (-\bar{a}_{i-1} + 5\bar{a}_i + 2\bar{a}_{i+1}) + O(\Delta x^3). \quad (26)$$

The PAR method is exact wherever  $a(\zeta)$  is locally parabolic, 3<sup>rd</sup>-order accurate for general but smooth functions  $a(\zeta)$ , and it requires two ghost cells at domain boundaries.

### 2.3.4. The PPM84 method

The piecewise parabolic reconstruction of CW84 is a two-step process. The first is based on the 4<sup>th</sup>-order-accurate interpolation formula

$$a_{i+1/2} = \frac{1}{2} (\bar{a}_i + \bar{a}_{i+1}) - \frac{1}{6} (\delta_{i+1} - \delta_i) = a|_{x_{i+1/2}} + O(\Delta x^4). \quad (27)$$

This expression is the equivalent of Eq. 1.6 of CW84 in the special case of a uniform grid. CW84 then replace  $\delta_i$  by the limited value

$$\delta_{i,\text{lim}} = \begin{cases} \text{sgn}(\delta_i) \min(|\delta_i|, 2|\delta_{i-1/2}|, 2|\delta_{i+1/2}|) & \text{if } \delta_{i-1/2} \delta_{i+1/2} > 0 \\ 0 & \text{otherwise,} \end{cases} \quad (28)$$

which is the monotonised central limiter of [van Leer \(1977\)](#). In our implementation, we do not set  $\delta_{i,\text{lim}} = 0$  if  $\delta_{i-1/2} \delta_{i+1/2} \leq 0$  (i.e. at local extrema). We have tested that, thanks to the presence of another limiter in PPM84 (see below), this modification has essentially no influence on the results. However, it makes the code faster because it removes three conditional expressions per reconstruction step (we need  $\delta_{i-1,\text{lim}}$ ,  $\delta_{i,\text{lim}}$ , and  $\delta_{i+1,\text{lim}}$  to obtain  $a_{i-1/2}$  and  $a_{i+1/2}$ ).

The interpolated value  $a_{i+1/2}$  is initially assigned to both  $a_{i+1/2,L}$  and  $a_{i+1/2,R}$ , i.e. there is no discontinuity at the interface. However, CW84 approximate the distribution of variable  $a$  in cell  $i$  by the parabola uniquely defined by  $a_{i-1/2,R}$ ,  $a_{i+1/2,L}$ , and the cell average  $a_i$ . This parabola may in some cases take on values outside of the interval defined by  $a_{i-1/2,R}$  and  $a_{i+1/2,L}$ , i.e. overshoots may appear within the cell. To prevent this, a second limiting step is introduced. We express it in terms of the differences

$$a_i^- = a_{i-1/2,R} - \bar{a}_i, \quad (29)$$

$$a_i^+ = a_{i+1/2,L} - \bar{a}_i. \quad (30)$$

The limiter is then defined by the variable replacements

$$\begin{aligned} a_i^- &\mapsto 0, \quad a_i^+ \mapsto 0 & \text{if } a_i^- a_i^+ \geq 0, \\ a_i^- &\mapsto -2a_i^+ & \text{if } |a_i^-| > 2|a_i^+|, \\ a_i^+ &\mapsto -2a_i^- & \text{if } |a_i^+| > 2|a_i^-|. \end{aligned} \quad (31)$$

The reconstructed states  $a_{i-1/2,R}$  and  $a_{i+1/2,L}$  are recovered using Eqs. (29) and (30). Equation (31) is equivalent to Eq. 1.10 of CW84. This second limiter introduces discontinuities at cell interfaces in regions where the gradient of  $a(\zeta)$  changes rapidly and it flattens the assumed parabola at local extrema.

Unlike CW84, we do not use the parabolic model of  $a(\zeta)$  inside the cell in any way. We only need the states at the two sides of each interface to construct Riemann problems and time integration is done using a Runge-Kutta scheme (see Sect. 2.5 for details). However, the second limiter (Eq. (31)), which is based on the parabolic model, is still needed to remove oscillations and to introduce dissipation where necessary.

Although the interpolation formula that PPM84 starts with is 4<sup>th</sup>-order accurate, the slope flattening introduced at all extrema reduces the practically attainable order of accuracy substantially for non-monotonic solutions even if they are smooth. Our 1D experiment in Sect. B.1 gives the order of 2.3 whereas [Colella & Sekora \(2008\)](#) reach the order of 2.6 in a similar advection experiment with a Gaussian-shaped profile and PPM84 reconstruction. The PPM84 method requires three ghost cells at domain boundaries.

### 2.3.5. The PPM08 method

The piecewise parabolic method of CS08 is based on ideas similar to those of CW84 in constructing the PPM84 scheme and PPM08 also contains two limiters. However, the limiters are

modified such that PPM08 models smooth extrema instead of flattening them.

In PPM08, the first estimate of  $a_{i+1/2}$  is obtained using the 6<sup>th</sup>-order-accurate interpolation formula (c.f. Eq. 17 of CS08)

$$a_{i+1/2} = \frac{37}{60}(\bar{a}_i + \bar{a}_{i+1}) - \frac{2}{15}(\bar{a}_{i-1} + \bar{a}_{i+2}) + \frac{1}{60}(\bar{a}_{i-2} + \bar{a}_{i+3}) \quad (32)$$

$$= a|_{x_{i+1/2}} + O(\Delta x^6). \quad (33)$$

If  $a_{i+1/2}$  does not satisfy the condition (c.f. Eq. 13 of CS08)

$$\min(\bar{a}_i, \bar{a}_{i+1}) \leq a_{i+1/2} \leq \max(\bar{a}_i, \bar{a}_{i+1}) \quad (34)$$

a limiter is applied. It is based on three 2<sup>nd</sup>-order-accurate second derivatives,

$$(\mathcal{D}^2 a)_{i+1/2} = 3(\bar{a}_i - 2a_{i+1/2} + \bar{a}_{i+1}) = \partial_x^2 a|_{x_{i+1/2}} \Delta x^2 + O(\Delta x^4), \quad (35)$$

$$(\mathcal{D}^2 a)_i = \bar{a}_{i-1} - 2\bar{a}_i + \bar{a}_{i+1} = \partial_x^2 a|_{x_i} \Delta x^2 + O(\Delta x^4), \quad (36)$$

$$(\mathcal{D}^2 a)_{i+1} = \bar{a}_i - 2\bar{a}_{i+1} + \bar{a}_{i+2} = \partial_x^2 a|_{x_{i+1}} \Delta x^2 + O(\Delta x^4). \quad (37)$$

In Eq. (35), the more common finite difference formula with a prefactor 4 would arise if the involved quantities were of the same kind, i.e. all three point values, or all three averages. These derivatives are combined to obtain a limited derivative  $(\mathcal{D}^2 a)_{i+1/2,\text{lim}}$  such that

$$(\mathcal{D}^2 a)_{i+1/2,\text{lim}} = \text{sgn} \left[ (\mathcal{D}^2 a)_{i+1/2} \right] \min \left( \left| (\mathcal{D}^2 a)_{i+1/2} \right|, C \left| (\mathcal{D}^2 a)_i \right|, C \left| (\mathcal{D}^2 a)_{i+1} \right| \right) \quad (38)$$

if all three derivatives have the same sign and

$$(\mathcal{D}^2 a)_{i+1/2,\text{lim}} = 0 \quad (39)$$

otherwise. We use  $C = 1.25$  in Eq. (38). The limited derivative is then used to modify the value of  $a_{i+1/2}$ ,

$$a_{i+1/2} \mapsto \frac{1}{2}(\bar{a}_i + \bar{a}_{i+1}) - \frac{1}{6}(\mathcal{D}^2 a)_{i+1/2,\text{lim}}. \quad (40)$$

Equation 19 of CS08 is equivalent to our Eq. (40) except for the factor in front of the second term, which is  $\frac{1}{3}$  in CS08. This is likely a typographical error because the factor of  $\frac{1}{6}$  is needed to obtain the original, unlimited value of  $a_{i+1/2}$  when the solution is so smooth that the limiter does not change the second derivative significantly.

Just like in the PPM84 method, the interpolated value  $a_{i+1/2}$  is initially assigned to both  $a_{i+1/2,\text{L}}$  and  $a_{i+1/2,\text{R}}$ , i.e. there is no discontinuity at the interface. The second limiting step depends on whether cell  $i$  is in the vicinity of a local extremum or not. If (c.f. Eq. 20 of CS08)

$$(\bar{a}_i - a_{i-1/2,\text{R}})(a_{i+1/2,\text{L}} - \bar{a}_i) \leq 0 \quad \text{or} \quad (\bar{a}_i - \bar{a}_{i-1})(\bar{a}_{i+1} - \bar{a}_i) \leq 0, \quad (41)$$

cell  $i$  is close to a local extremum, which should be preserved if smooth enough. The second derivatives

$$(\mathcal{D}^2 a)_i^* = 6(a_{i-1/2,\text{R}} - 2\bar{a}_i + a_{i+1/2,\text{L}}), \quad (42)$$

$$(\mathcal{D}^2 a)_{i-1} = \bar{a}_{i-2} - 2\bar{a}_{i-1} + \bar{a}_i, \quad (43)$$

$$(\mathcal{D}^2 a)_i = \bar{a}_{i-1} - 2\bar{a}_i + \bar{a}_{i+1}, \quad (44)$$

$$(\mathcal{D}^2 a)_{i+1} = \bar{a}_i - 2\bar{a}_{i+1} + \bar{a}_{i+2}. \quad (45)$$

are combined to judge the solution's smoothness (CS08 have one wrong index in their equivalent of our Eq. (43), c.f. their Eq. 21). We then set

$$(\mathcal{D}^2 a)_{i,\text{lim}}^* = \text{sgn} \left[ (\mathcal{D}^2 a)_i^* \right] \min \left( \left| (\mathcal{D}^2 a)_i^* \right|, C \left| (\mathcal{D}^2 a)_{i-1} \right|, C \left| (\mathcal{D}^2 a)_i \right|, C \left| (\mathcal{D}^2 a)_{i+1} \right| \right) \quad (46)$$

if all four second derivatives have the same sign and

$$(\mathcal{D}^2 a)_{i,\text{lim}}^* = 0 \quad (47)$$

otherwise. Finally, the reconstructed states are updated,

$$a_{i-1/2,\text{R}} \mapsto \bar{a}_i + (a_{i-1/2,\text{R}} - \bar{a}_i) \frac{(\mathcal{D}^2 a)_{i,\text{lim}}^*}{(\mathcal{D}^2 a)_i^*}, \quad (48)$$

$$a_{i+1/2,\text{L}} \mapsto \bar{a}_i + (a_{i+1/2,\text{L}} - \bar{a}_i) \frac{(\mathcal{D}^2 a)_{i,\text{lim}}^*}{(\mathcal{D}^2 a)_i^*}. \quad (49)$$

If  $\left| (\mathcal{D}^2 a)_i^* \right| < \varepsilon = 10^{-12}$  we do not modify the reconstructed states in this step. Equations (48) and (49) are equivalent to Eq. 23 of CS08.

If the condition in Eq. (41) is not satisfied, i.e. cell  $i$  is not in the vicinity of a local extremum, we use Eqs. (29)-(31) instead of Eqs. (48) and (49) to limit the reconstructed states. CS08 propose to use a slightly less restrictive limiter away from extrema (their Eq. 26), but that limiter produces oscillations with our time-discretization scheme and we do not use it.

Just as we do in the case of PPM84, we only use the reconstructed states and not the assumed parabolic model of  $a(\zeta)$  within the cell, see Sect. 2.3.4 for details. The PPM08 method is 6<sup>th</sup>-order accurate for smooth functions  $a(\zeta)$  even if they are not monotonic. Our 1D experiment in Sect. B.1 confirms this. The PPM08 method requires four ghost cells at domain boundaries.

### 2.3.6. The PSH method

Whereas all of the previous reconstruction methods are applied to all variables in the same way, the PSH method is hybrid: it is an unlimited piecewise-sextic method for all dynamic variables combined with PPM08 for passive scalars. This allows us to eliminate certain issues that occur with methods containing limiters when applied to slow flows (see Sect. 3.1 for details) while essentially eliminating oscillations in the passive scalars, which could represent mass fractions. The piecewise sextic reconstruction assumes that within cell  $i$   $a(\zeta)$  can be described by the sextic polynomial

$$a(\zeta) = \sum_{n=0}^6 c_n (\zeta - \zeta_i)^n. \quad (50)$$

The seven coefficients  $c_n$  are uniquely determined by the requirement that the averages of  $a(\zeta)$  in cells  $i - 3 + n$  equal  $\bar{a}_{i-3+n}$  for  $n = 0, 1, \dots, 6$ . The reconstructed states are then obtained by evaluating Eq. (50) at  $\zeta_{i-1/2}$  and  $\zeta_{i+1/2}$ , respectively. The result-



ing expressions are

$$a_{i-1/2,R} = \frac{1}{420} \left( 4\bar{a}_{i-3} - 38\bar{a}_{i-2} + 214\bar{a}_{i-1} + 319\bar{a}_i - 101\bar{a}_{i+1} + 25\bar{a}_{i+2} - 3\bar{a}_{i+3} \right) + O(\Delta x^7), \quad (51)$$

$$a_{i+1/2,L} = \frac{1}{420} \left( -3\bar{a}_{i-3} + 25\bar{a}_{i-2} - 101\bar{a}_{i-1} + 319\bar{a}_i + 214\bar{a}_{i+1} - 38\bar{a}_{i+2} + 4\bar{a}_{i+3} \right) + O(\Delta x^7), \quad (52)$$

The method is exact wherever  $a(\zeta)$  is locally a sextic polynomial, 7<sup>th</sup>-order accurate for general but smooth functions  $a(\zeta)$ , and it requires four ghost cells at domain boundaries.

#### 2.4. Approximate Riemann solvers

The reconstructed pair of primitive state quantities,  $\mathbf{q}_{i+1/2,L,R}$ , defines a Riemann problem at the cell interface  $i + 1/2$ , which SLH solves by means of 1D approximate Riemann solvers to obtain the face-centered value of the fluxes  $\mathcal{F}_{i+1/2}$ . We run the tests presented in Sect. 3 using two widely popular flux functions, namely the RUSANOV and HLLC solvers. Because in this work we only focus on simulations of subsonic flows, for comparison we also build a low-dissipation version of HLLC following the approach of Minoshima & Miyoshi (2021), who modified the Harten-Lax-van Leer-Discontinuities (HLLD, Miyoshi & Kusano 2005) scheme for magnetohydrodynamics to diminish the magnitude of the numerical dissipation for low-Mach-number flows. The authors called this low-dissipation flux ‘‘LHLLD’’, so, for consistency, we will refer to the low-dissipation HLLC solver as ‘‘LHLLC’’ throughout the text<sup>5</sup>. In the rest of this section, we summarize the main aspects of each of these solvers and provide the implementation details whenever several choices can be made for specifying the value of a certain quantity that is needed to evaluate the numerical flux.

##### 2.4.1. RUSANOV

The RUSANOV flux is computed by adding an upwind, numerical diffusive term proportional to the maximum wave speed at the cell interface,  $S_{\max}$ , to every component of the central flux. The final expression for the numerical flux reads<sup>6</sup>

$$\mathcal{F}(U_L, U_R) = \frac{1}{2} [\mathbf{F}(U_L) + \mathbf{F}(U_R)] - \frac{1}{2} S_{\max} (U_R - U_L), \quad (53)$$

where  $U_{L,R}$  are the left and right sets of conserved quantities, respectively. In SLH,  $S_{\max}$  is estimated as

$$S_{\max} = \max(|u_L| + c_L, |u_R| + c_R), \quad (54)$$

where  $c = (\gamma p / \rho)^{1/2}$  is the sound speed. The diffusive term in Eq. (53) scales with the Mach number of the flow  $\mathcal{M}$  and allows

<sup>5</sup> Although SLH was already equipped with several low-Mach solvers, like AUSM<sup>+</sup>-up (Liou 2006) and Miczek-Roe (Miczek et al. 2015), we decide not to use them in this study because they all suffer from a more restrictive stability criterion on the time step than LHLLC when used in combination with explicit time steppers, whilst all of these fluxes provide very similar results in terms of accuracy.

<sup>6</sup> For sake of clarity, here we assume that the fluxes are computed in the  $x$  direction and dropped the indices, but analogous expressions can be obtained for the  $y$  and  $z$  directions.

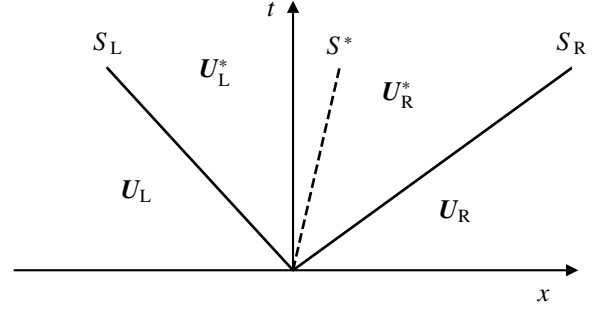


**Fig. 1.** Space-time diagram showing the wave structure of the HLLC solver for a Riemann problem of gas dynamics.  $S_{L,R}$  are the two outer sonic waves (solid lines), while  $S^*$  is the speed of the linearly degenerate contact and shear waves (dashed line) that separate the two intermediate ‘‘star’’ states,  $U_{L,R}^*$ .

the scheme to achieve numerical stability by smearing out any discontinuity that may arise in the vector of state quantities  $U$ .

The RUSANOV solver is one of the simplest schemes that can be used to approximate the fluxes at grid cell interfaces, which makes it very efficient in terms of Floating Point Operations per Second. However, it does not take into account the complex structure of the solution arising from the Riemann problem of gas dynamics (see, e.g., Toro 2009), so the states between the two outer waves in the Riemann fan are averaged out. For this reason, this flux function is particularly diffusive for transporting contact and shear waves, which lack the self-steepening property of sound waves.

##### 2.4.2. HLLC

Different from RUSANOV, the HLLC solver restores the linearly degenerate contact and shear waves back to the structure of the solution of the Riemann problem (see Fig. 1). In this method, the numerical flux is chosen according to the sign of the wave speeds in the Riemann fan,

$$\mathcal{F}(U_L, U_R) = \begin{cases} \mathbf{F}_L & \text{if } 0 \leq S_L, \\ \mathbf{F}_L^* & \text{if } S_L < 0 \leq S^*, \\ \mathbf{F}_R^* & \text{if } S^* < 0 \leq S_R, \\ \mathbf{F}_R & \text{if } S_R < 0. \end{cases} \quad (55)$$

While the computation of the physical fluxes  $\mathbf{F}_L = \mathbf{F}(U_L)$  and  $\mathbf{F}_R = \mathbf{F}(U_R)$  is trivial, the fluxes in the intermediate regions,  $\mathbf{F}_L^*$  and  $\mathbf{F}_R^*$ , are obtained by solving the Rankine–Hugoniot jump conditions across the two outer sonic waves,

$$S_L U_L^* - \mathbf{F}_L^* = S_L U_L - \mathbf{F}_L, \quad (56)$$

$$S_R U_R^* - \mathbf{F}_R^* = S_R U_R - \mathbf{F}_R. \quad (57)$$

Here,  $U_L^*$  and  $U_R^*$  represent the state quantities in the star regions. In order to solve Eqs. (56)–(57), proper estimates of the wave speeds  $S_L$  and  $S_R$  must be provided beforehand. SLH computes these wave speeds as

$$S_L = \min(u_L, u_R) - \max(c_L, c_R), \quad (58)$$

$$S_R = \max(u_L, u_R) + \max(c_L, c_R). \quad (59)$$

After some assumptions and algebraic manipulations (see Toro 2009), these estimates allow Eqs. (56)–(57) to be solved for the

star states  $\mathbf{U}_{L,R}^*$ ,

$$(\rho)_{L,R}^* = \tilde{\alpha}_{L,R}, \quad (60)$$

$$(\rho u)_{L,R}^* = \tilde{\alpha}_{L,R} S^*, \quad (61)$$

$$(\rho v)_{L,R}^* = \tilde{\alpha}_{L,R} v_{L,R}, \quad (62)$$

$$(\rho w)_{L,R}^* = \tilde{\alpha}_{L,R} w_{L,R}, \quad (63)$$

$$(\rho e_{\text{tot}})_{L,R}^* = \tilde{\alpha}_{L,R} \frac{(\rho e_{\text{tot}})_{L,R}}{\rho_{L,R}} + \tilde{\alpha}_{L,R} (S^* - u_{L,R}) \left[ S^* + \frac{p_{L,R}}{\rho_{L,R} (S_{L,R} - u_{L,R})} \right], \quad (64)$$

$$(\rho X)_{L,R}^* = \tilde{\alpha}_{L,R} X_{L,R}, \quad (65)$$

with

$$\tilde{\alpha}_{L,R} = \rho_{L,R} \left( \frac{S_{L,R} - u_{L,R}}{S_{L,R} - S^*} \right), \quad (66)$$

and  $S^*$  being the speed of the intermediate wave,

$$S^* = \frac{p_R - p_L + \rho_L u_L (S_L - u_L) - \rho_R u_R (S_R - u_R)}{\rho_L (S_L - u_L) - \rho_R (S_R - u_R)}. \quad (67)$$

The gas pressure is preserved across the middle wave and takes the value

$$p^* = \frac{1}{2} \left[ p_L + p_R + \rho_L (S_L - u_L) (S^* - u_L) + \rho_R (S_R - u_R) (S^* - u_R) \right]. \quad (68)$$

These expressions are then inserted back into Eqs. (56)–(57) to compute  $\mathbf{F}_L^*$  and  $\mathbf{F}_R^*$ . Finally, the interface flux is chosen according to Eq. (55).

In our study, we use a variant of the original HLLC solver of Toro et al. (1994), which allows the low-Mach correction presented in the next section to be implemented trivially into the solver. In particular, we directly evaluate the physical fluxes in the selected state of the Riemann fan,

$$\mathcal{F}(\mathbf{U}_L, \mathbf{U}_R) = \begin{cases} \mathbf{F}_L & \text{if } 0 \leq S_L, \\ \mathbf{F}(\mathbf{U}_L^*) & \text{if } S_L < 0 \leq S^*, \\ \mathbf{F}(\mathbf{U}_R^*) & \text{if } S^* < 0 \leq S_R, \\ \mathbf{F}_R & \text{if } S_R < 0, \end{cases} \quad (69)$$

and we compute  $p^*$  using a linearized Riemann solver for the equations of gas dynamics (see, e.g., Toro 1991),

$$p^* = \frac{1}{2} (p_L + p_R) - \frac{1}{2} \tilde{\rho} \tilde{c} (u_R - u_L), \quad (70)$$

where  $\tilde{c} = (c_L + c_R)/2$  and  $\tilde{\rho} = (\rho_L + \rho_R)/2$ . The system in Eq. (69) is consistent with the physical fluxes in the sense that

$$\mathcal{F}(\mathbf{U}, \mathbf{U}) = \mathbf{F}(\mathbf{U}) \quad (71)$$

and it satisfies the Rankine–Hugoniot jump conditions across the contact wave  $S^*$  as the original solver,

$$S^* \mathbf{U}_R^* - \mathbf{F}_R^* = S^* \mathbf{U}_L^* - \mathbf{F}_L^*. \quad (72)$$

Diagnostic tests of the Kelvin–Helmholtz instability problem, described in Sect. 3.1, show that the numerical solutions computed with our modified version and the original solver of Toro et al. (1994) are virtually indistinguishable for subsonic flows. We stress, however, that the fluxes in Eq. (69) do not satisfy the jump conditions across the sonic waves  $S_L$  and  $S_R$  (see Eqs. (56) and (57)). Therefore, there is no guarantee that the resulting scheme preserves positivity of density and internal energy when the flow is nearly transonic, in which case effects of compressibility and nonlinearities can become dominant. Such a flow regime, however, is not considered in this study.

### 2.4.3. LHLLC

As discussed in Sect. 2.4.2, HLLC restores the intermediate, linearly degenerate waves, so it is generally more accurate than two-wave solvers like RUSANOV or HLL (Harten et al. 1983) in simulations involving the presence of material interfaces or the propagation of entropy waves. However, the effects of the numerical dissipation introduced by HLLC on the evolution of the flow become progressively more dominant as  $\mathcal{M} \rightarrow 0$ , thus producing unnecessarily large diffusive errors in highly subsonic velocity regimes (see, e.g., Fleischmann et al. 2020). In our variant of HLLC, this behavior is caused by the upwind term in the expression for  $p^*$  (see Eq. (70)),

$$D(p^*) = -\frac{1}{2} \tilde{\rho} \tilde{c} (u_R - u_L). \quad (73)$$

This term scales with  $\mathcal{M}$ , which is inconsistent with the scaling of pressure fluctuations dynamically generated by subsonic flows. In fact, in the asymptotic limit  $\mathcal{M} \rightarrow 0$ , the solution to the compressible Euler equations approaches the incompressible regime (Guillard & Viozat 1999), in which the gas pressure is homogeneous in space except for fluctuations proportional to  $\mathcal{M}^2$ . At low Mach numbers, the numerical term in Eq. (73) can eventually become larger than the physical pressure fluctuation at the cell interface, thus leading to an highly inaccurate pressure flux estimation.

In order to correct for the flawed scaling of the numerical dissipation introduced by HLLC-like methods, we here follow the approach described in Minoshima & Miyoshi (2021), who proposed to multiply the diffusive term in Eq. (73) by a factor  $\phi$  proportional to the local Mach number of the flow<sup>7</sup>. Such a correction was originally applied to the magnetohydrodynamic solver HLLD, but it can easily be used in HLLC by setting all magnetic field components to zero, resulting in

$$\phi = \chi(2 - \chi), \quad (74)$$

with

$$\chi = \min \left\{ 1, \max \left( \frac{|\mathbf{V}_L|}{c_L}, \frac{|\mathbf{V}_R|}{c_R} \right) \right\}. \quad (75)$$

The final expression for  $p^*$  then reads

$$p^* = \frac{1}{2} (p_L + p_R) - \phi \frac{1}{2} \tilde{\rho} \tilde{c} (u_R - u_L). \quad (76)$$

The resulting upwind term in this “low-dissipation” version of the HLLC flux (LHLLC) scales with  $\mathcal{M}^2$  when the flow is subsonic, so the ratio of the numerical diffusive term to the amplitude of pressure fluctuations is independent of  $\mathcal{M}$ .

We note that the same fix cannot equally be applied to the RUSANOV flux without sacrificing numerical stability. In particular, a diffusive coefficient proportional to  $\mathcal{M}^2$  would result in too little dissipation for sound waves. This is not the case for LHLLC, in which the complex upwinding performed in Eq. (69) guarantees that the scheme remains stable for the propagation of sound waves (see also Appendix B.1).

<sup>7</sup> Other low-Mach corrections for the HLLC Riemann solver can be found, e.g., in Thornber et al. (2008); Rieper (2011); Xie et al. (2019); Chen et al. (2020); Fleischmann et al. (2020).

## 2.5. Time discretization

Because the acoustic Courant-Friedrichs-Lewy (CFL, Courant et al. 1928) criterion on the time step becomes excessively strict in regimes of very low Mach numbers, implicit time discretization techniques are typically better suited for simulating the evolution of such slow flows (see, e.g., Viallet et al. 2011; Miczek et al. 2015; Dumbser et al. 2019). However, we recognize that most hydrodynamic codes nowadays do not have time-implicit integration capabilities, whose implementation requires a considerable effort from code developers. Thus, to make our study easily reproducible, we decide to target in our test setups, see Sect. 3.1 and 3.2, flows with Mach numbers in the range  $10^{-3} \lesssim \mathcal{M} \lesssim 10^{-1}$ , where simple time-explicit marching schemes are still competitive with implicit ones. In this work, explicit time integration is performed in a semi-discrete fashion, in which the cell-surface integral of the fluxes and the cell-volume integral of the source terms in Eq. (2) are first separately discretized in space whilst the system is left continuous in time according to the method of lines (see Sect. 2.2). The resulting system of ordinary differential equations (see Eq. (13)), is then solved numerically to advance the cell-volume-averaged state quantities in time. To solve Eq. (13), we use the third-order accurate, strong stability preserving (SSP) RK3 method of Shu & Osher (1988), in which the update on  $\bar{U}_{i,j,k}^{(n)}$  from time  $t_n$  to time  $t_{n+1} = t_n + \Delta t$  is performed in three stages,

$$\bar{U}_{i,j,k}^{(1)} = \bar{U}_{i,j,k}^{(n)} - \mathcal{R}(\bar{U}_{i,j,k}^{(n)})\Delta t, \quad (77)$$

$$\bar{U}_{i,j,k}^{(2)} = \frac{3}{4}\bar{U}_{i,j,k}^{(n)} + \frac{1}{4}\bar{U}_{i,j,k}^{(1)} - \frac{1}{4}\mathcal{R}(\bar{U}_{i,j,k}^{(1)})\Delta t, \quad (78)$$

$$\bar{U}_{i,j,k}^{(n+1)} = \frac{1}{3}\bar{U}_{i,j,k}^{(n)} + \frac{2}{3}\bar{U}_{i,j,k}^{(2)} - \frac{2}{3}\mathcal{R}(\bar{U}_{i,j,k}^{(2)})\Delta t. \quad (79)$$

In particular, we compute the spatial residuals at stage  $s$ ,

$$\begin{aligned} \mathcal{R}(\bar{U}_{i,j,k}^{(s)}) = & \frac{1}{\Delta x} \left( \mathcal{F}_{i+1/2,j,k}^{(s)} - \mathcal{F}_{i-1/2,j,k}^{(s)} \right. \\ & + \mathcal{G}_{i,j+1/2,k}^{(s)} - \mathcal{G}_{i,j-1/2,k}^{(s)} \\ & + \mathcal{H}_{i,j,k+1/2}^{(s)} - \mathcal{H}_{i,j,k-1/2}^{(s)} \\ & \left. - \mathcal{S}_{i,j,k}^{(s)} \right), \end{aligned} \quad (80)$$

using the numerical techniques described in Sects. 2.3 and 2.4. Finally, in order to achieve numerical stability, we limit the time step according to

$$\Delta t = \frac{\text{CFL}}{N_{\text{dim}}} \min_{i,j,k} \left( \frac{\Delta x}{|\mathbf{V}|_{i,j,k} + c_{i,j,k}} \right), \quad (81)$$

where  $N_{\text{dim}}$  is the number of spatial dimensions. In all the tests presented in Sect. 3, we always adopt  $\text{CFL} = 0.8$ . We prefer to use a third-order accurate time stepper over less computationally expensive (but more inaccurate) methods, such as the ‘‘Midpoint rule’’ or SSP-RK2 (Shu & Osher 1988), so that the spatial instead of the temporal discretization would contribute most to the building up of global truncation errors.

## 3. Convergence properties of different Godunov-type methods

In this section, we check if the methods included in our study (described in Sect. 2) converge to the same numerical solution for several physical quantities of interest. In particular, we test a

Kelvin–Helmholtz instability and a more complex setup characterized by the presence of turbulent convective flows, turbulent entrainment, and wave excitation. The results of the latter set of simulations allow us to estimate the computational cost per fixed accuracy for any given scheme, which we show in Sect. 4.

### 3.1. Kelvin–Helmholtz instability

We first test all of our 18 combinations of numerical schemes as described in Sects. 2.3 and 2.4 on a 2D Kelvin–Helmholtz problem with the initial condition

$$\rho = \gamma, \quad (82)$$

$$u = \mathcal{M}_0 [1 - 2\eta(y)], \quad (83)$$

$$v = \frac{\mathcal{M}_0}{10} \sin(2\pi x), \quad (84)$$

$$p = 1, \quad (85)$$

$$X = \eta(y), \quad (86)$$

where  $\gamma = 1.4$  and

$$\eta(y) = \begin{cases} \frac{1}{2} \{ 1 + \sin [16\pi(y + 0.25)] \}, & \text{for } y > -\frac{9}{32} \text{ and } y < -\frac{7}{32}, \\ 1, & \text{for } y \geq -\frac{7}{32} \text{ and } y \leq \frac{7}{32}, \\ \frac{1}{2} \{ 1 - \sin [16\pi(y - 0.25)] \}, & \text{for } y > \frac{7}{32} \text{ and } y < \frac{9}{32}, \\ 0, & \text{otherwise.} \end{cases} \quad (87)$$

The smooth function  $\eta(y)$  provides a resolvable transition between layers moving in opposite horizontal directions. The initial speed of sound is unity, so  $\mathcal{M}_0$  is a tunable initial Mach number of the shear flow. We discuss solutions with  $\mathcal{M}_0 = 10^{-1}$ ,  $10^{-2}$ , and  $10^{-3}$ . In Eq. (84), a smooth initial perturbation with an amplitude of  $\mathcal{M}_0/10$  is included as a velocity component perpendicular to the shear flow. The computational domain, assumed to be periodic in both  $x$  and  $y$ , spans  $0 \leq x \leq 2$ ,  $-0.5 \leq y \leq 0.5$ .

The fact that the transition function  $\eta(y)$  between the shear layers is smooth<sup>8</sup> allows us to compute numerically converged solutions even in the absence of physical viscosity as long as the simulations are stopped before the flow field becomes chaotic (see also Robertson et al. 2010; McNally et al. 2012; Lecoanet et al. 2017; Berlok & Pfrommer 2019). Each of the two transitions spans only  $1/16$  of the domain height and is poorly resolved on the coarser grids used in our tests. Therefore, we improve the accuracy of the initial cell averages that involve  $\eta(y)$  by averaging  $\eta(y)$  over 100 points uniformly distributed in the  $y$ -range covered by each cell. We measure numerical errors with respect to a reference solution computed using PSH reconstruction and the LHLLC flux function on a  $8192 \times 4096$  grid. The solution for  $\mathcal{M}_0 = 10^{-2}$  is shown in Fig. 2 at four points in time<sup>9</sup>. As the instability grows in amplitude, the sinusoidal initial perturbation is rolled up into a series of vortices. Parts of the initial shear layers are stretched and become trapped in the centres of the vortices. Other parts of the shear layers become substantially narrower. We quantify this phenomenon by computing the minimum scale height  $\min(H_X) \equiv 1/\max(|\nabla X|)$  of the passive scalar  $X$ . Figure 3 shows that this quantity drops by as much as a factor of 28 between  $t = 0$  and  $t = 0.8\mathcal{M}_0^{-1}$ . At the

<sup>8</sup>  $\eta(y)$  and its first derivative are continuous but the second derivative is not.

<sup>9</sup> We give the time in units of  $\mathcal{M}_0^{-1}$  such that the same numerical value corresponds to the same evolutionary stage of the instability at all three initial Mach numbers we use.

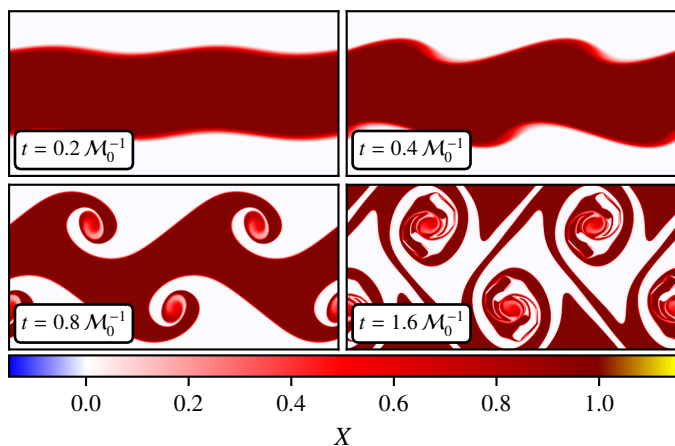


**Fig. 2.** Reference solution to the Kelvin–Helmholtz problem with initial Mach number  $\mathcal{M}_0 = 10^{-2}$ . The solution was computed using PSH reconstruction and the LHLLC flux function on an  $8192 \times 4096$  grid. The mass fraction  $X$  of the passive scalar is shown at four points in time: late in the linear growth of the instability ( $t = 0.2 \mathcal{M}_0^{-1}$ ), at an early stage of non-linear evolution ( $t = 0.4 \mathcal{M}_0^{-1}$ ), at a stage when the primary vortices have fully formed ( $t = 0.8 \mathcal{M}_0^{-1}$ ; the final time for all of our other Kelvin–Helmholtz simulations), and at a late stage when fine threads have formed inside the primary vortices ( $t = 1.6 \mathcal{M}_0^{-1}$ ). We use the same colour scale as in Figs. 4, D.2, and D.1, although  $0 \leq X \leq 1$  in the reference solution.

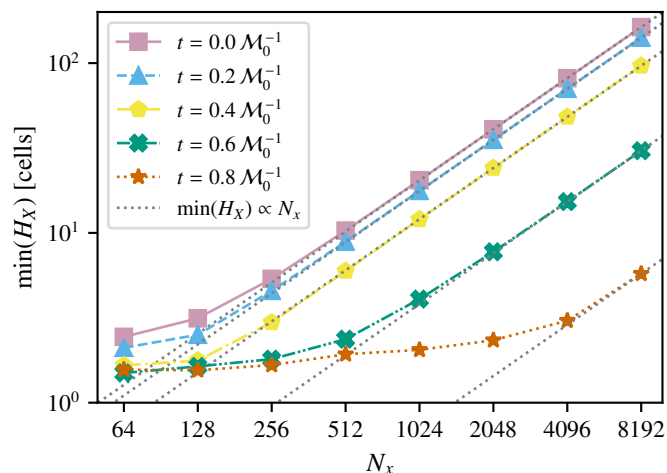


**Fig. 3.** Resolution dependence of the minimum scale height  $\min(H_x)$  of the passive scalar in the Kelvin–Helmholtz problem expressed in units of the computational cell width and shown at five points in time. Grid resolution is given by the number  $N_x$  of computational cells along the  $x$  axis. The initial Mach number is  $\mathcal{M}_0 = 10^{-2}$  and we use PSH reconstruction and the LHLLC flux function in this series of simulations. Once the steepest gradients in  $X$  become resolved the minimum scale height starts to follow the linear scaling relations shown.

latter point in time, the minimum scale height is only 5.75 computational cells on the  $8192 \times 4096$  reference grid. Extremely thin and difficult-to-resolve filaments appear at even later times (see Fig. 2). Therefore, we compare the solutions at  $t = 0.8 \mathcal{M}_0^{-1}$ , making the problem non-linear and challenging enough but not computationally prohibitive. The maximum Mach number in the flow field is  $1.8 \mathcal{M}_0$  at this point in time.

Figure 4 compares the distributions of the passive scalar in simulations with  $\mathcal{M}_0 = 10^{-2}$  computed on a  $128 \times 64$  grid. The steepest gradients are strongly under-resolved on this grid (see Fig. 3), which increases the amplitude and visibility of small-

scale artefacts produced by different methods. All of the six reconstruction functions lead to extremely diffusive solutions with the RUSANOV flux, although high-order methods with limiters (PPM84, PPM08, PSH) still preserve steep gradients at some places. Numerical diffusion is strongly suppressed with the HLLC flux function owing to the explicit treatment of the contact wave in HLLC. The three highest-order methods (PPM84, PPM08, PSH) reproduce the structure of the primary vortices (c.f. Fig. 2) much more closely than the lower-order methods (LIN, LIN+VL, PAR). However, the two PPM methods develop secondary instabilities around the primary vortices. This effect, not present in the reference solution, occurs also with the LHLLC flux function (see also McNally et al. 2012). The secondary instabilities become the dominant source of numerical errors. We find that these instabilities tend to grow when excessive velocity shear is generated at the grid scale and there is not enough numerical dissipation to suppress their growth. Therefore, the excitation of artificial, short wavelength Kelvin–Helmholtz instabilities is favored on coarser grids, which generate larger shear at the grid scale across the poorly resolved slip line, and by less dissipative Riemann solvers. For the same reason, simulations run with the HLLC solver are more prone to developing secondary instabilities at higher rather than lower Mach numbers, as HLLC introduces less numerical diffusion into the system when modeling faster flows (see, e.g., the panels for PPM84+HLLC in Fig. 4 and Fig. D.1). As the grid is refined, the shear layers are progressively better resolved thus reducing grid scale shear and suppressing the growth of the secondary instabilities. Not surprisingly, the smooth interiors of the primary vortices are best represented with the highest-order method PSH (c.f. Fig. 2). Figures D.1 and D.2, respectively, show that the differences between the three flux functions become smaller with  $\mathcal{M}_0 = 10^{-1}$  and much larger with  $\mathcal{M}_0 = 10^{-3}$ . This is expected because the amount of numerical dissipation (relative to the flow of interest) introduced by the RUSANOV and HLLC flux functions increases with decreasing Mach number of the flow, see Sect. 2.4. With  $\mathcal{M}_0 = 10^{-3}$ , only the PSH method reproduces the basic structure of the primary vortices when combined with the HLLC flux. Comparing Fig. 4 with Fig. D.2, we see that the LHLLC flux produces results independent of the initial Mach number  $\mathcal{M}_0$  because all of the flows are considerably subsonic. All of the methods we test converge to the same flow pattern with  $\mathcal{M}_0 = 10^{-2}$ , see Fig. D.7 for solutions computed on the  $4096 \times 2048$  grid<sup>10</sup>.

The magnitude of the largest overshoot (or undershoot) in the passive scalar is shown in the insets in Figs. 4, D.1, and D.2. Thanks to their use of limiters, the LIN+VL, PPM84, PPM08, and PSH methods largely eliminate the overshoots, making the methods useful for the advection of mass fractions. We observe only some accumulation of round-off-level overshoots (up to  $\approx 10^{-14}$ ) with LIN+VL, independently of the initial Mach number or grid resolution. The PPM84, PPM08, and PSH methods produce small but finite overshoots. At  $t = 0.8 \mathcal{M}_0^{-1}$ , the magnitude of the largest overshoots is  $\approx 10^{-4}$  with PPM84,  $\approx 10^{-2}$  with PPM08, and  $\approx 10^{-6}$  with PSH across all grids and all initial Mach numbers. However, they only occur in a few cells or groups of cells scattered across the computational grid, so the total mass affected by this effect is negligibly small. Moreover, the amplitude of such overshoots, drops to the round-off level in many of our simulations as the resolution is increased. Unlim-

<sup>10</sup> Similar plots for all initial Mach numbers and all computational grids are available on Zenodo (<https://zenodo.org/doi/10.5281/zenodo.10280900>).



ited methods produce substantially larger overshoots, reaching 8% and 17% for LIN and PAR, respectively. They are the result of the dispersion errors characteristic of linear schemes of 2<sup>nd</sup> or higher order, so they are nearly always present around sharp structures and affect a much larger amount of mass than the sporadic and isolated overshoots produced by PPM84, PPM08, and PSH. The benefits of the hybrid approach in PSH thus become obvious – secondary instabilities are suppressed (as compared with PPM84 and PPM08) thanks to the absence of limiters for dynamic variables while mass fractions, for which limiters are used, are well behaved.

We quantify numerical convergence of all of our methods by measuring  $L_1$  errors with respect to the reference solution in the density  $\rho$ , kinetic energy  $E_{k,y}$ , associated with motions perpendicular to the initial shear flow, and mass fraction  $X$  of the passive scalar. We define the relative  $L_1$  error for any quantity  $q$  as

$$L_1 = \frac{1}{\sigma^{\text{ref}}} \frac{\sum_{i=1}^{N_x} \sum_{j=1}^{N_y} |q_{i,j} - q_{i,j}^{\text{ref}}|}{N_x N_y}, \quad (88)$$

where  $q^{\text{ref}}$  is the reference solution and the sums run over the whole computational grid of  $N_x \times N_y$  cells. The error is normalised using the standard deviation  $\sigma^{\text{ref}}$  of  $q^{\text{ref}}$ . This choice is motivated by the fact that density fluctuations are much smaller than the mean density in our setup. The reference solution is always re-binned from its original,  $8192 \times 4096$  grid, by repeatedly averaging groups of  $2 \times 2$  neighbouring cells until the desired grid resolution is achieved.

The  $L_1$  errors for the set of simulations with the initial Mach number  $\mathcal{M}_0 = 10^{-2}$  are shown in Fig. 5. We first focus on the kinetic energy  $E_{k,y}$  and mass fraction  $X$ . The solutions computed using the LHLLC flux approach 2<sup>nd</sup>-order convergence, as expected. Only the PPM84 reconstruction method gives a slight decrease in the convergence rate in  $E_{k,y}$  on the finest of our grids. The same effect is observed in the sets of simulations with  $\mathcal{M}_0 = 10^{-1}$  (Fig. D.3) and  $\mathcal{M}_0 = 10^{-3}$  (Fig. D.4). The convergence rate of PPM08 also decreases on very fine grids in the latter case. Apart from this, the convergence curves are nearly independent of the initial Mach number with the LHLLC flux (c.f. Figs. 5, D.3, and D.4), confirming its low-Mach property. The highest-order reconstruction methods usually (but not always) produce the smallest errors on a given and sufficiently fine grid. The errors differ by up to one order of magnitude, although the overall 2D scheme is 2<sup>nd</sup>-order accurate in all of the cases.

The magnitude of numerical errors strongly increases when we decrease initial Mach number with the non-low-Mach flux functions RUSANOV and HLLC. As described above, the spatial structure of errors produced by linear methods differs from that produced by methods with limiters. Figures 5, D.3, and D.4 show that the linear methods LIN, PAR, and for dynamic variables also PSH approach 2<sup>nd</sup>-order convergence on sufficiently fine grids even if the magnitude of the errors is much larger than what we obtain with the LHLLC flux function.

The two PPM methods converge poorly in  $\rho$  at low Mach numbers (Figs. 5 and D.4). Because the initial density is constant everywhere, all of the density fluctuations are the integrated effects of the divergence (or convergence) of the velocity field in the continuity equation. The magnitude of the velocity divergence in simulations computed on the  $512 \times 256$  grid is shown in Figs. 6, D.5, and D.6. The solutions computed using the LIN, PAR, and PSH methods clearly show the structure of the primary vortices with some oscillations in the shear layers and a background of relatively weak, large-scale sound waves. On the

other hand, the solutions computed using the PPM84 and PPM08 methods show a large amount of small-scale “numerical noise”. After inspecting the time dependence of these artificial structures<sup>11</sup>, we conclude that some of these structures travel with the flow while others have the character of small-scale sound waves. We believe that both originate from cumulative effects of the limiters switching their local state many times over the time span of the simulation<sup>12</sup>. The switching can result in rapid changes in the magnitude of the discontinuities at cell faces and, consequently, in the amount of dissipation applied in the Riemann solver (i.e. the numerical flux function). This effect is weakest with the low-dissipation flux function LHLLC but it is still clearly present on the  $4096 \times 2048$  grid, see Fig. D.8. The structures disappear when we disable the limiters in PPM84 and PPM08 (not shown in the figures). We do not observe the fast-propagating, small-scale sound waves with LIN+VL but the method does produce thin structures in the velocity divergence around the primary vortices, which follow the flow.

Overall, the PSH method produces by far the smallest errors with the RUSANOV and HLLC flux functions and initial Mach numbers  $\mathcal{M}_0 \leq 10^{-2}$  (Figs. 5 and D.4). The only exception is the poor convergence (or even divergence) in the passive tracer  $X$  observed with the PSH+RUSANOV combination in simulations with  $\mathcal{M}_0 \leq 10^{-2}$  performed on very fine grids. This effect is also likely related to the limiters switching their local state many times over the time span of the simulation but we did not investigate it further.

### 3.2. 3D simulations of convection, turbulent entrainment, and wave excitation

In this section, we consider a test problem in which a variety of complex hydrodynamic phenomena can be captured on the same computational grid. These include convective transport of energy, turbulent mixing at a convective boundary, and the propagation of internal waves in a stably stratified layer, all of which are often encountered in simulations of geophysical and stellar hydrodynamics. The initial conditions for this test are adopted from the work of [Andrassy et al. \(2022\)](#) and they represent a hydrostatic solution of Eq. (2). In particular, the thermodynamic conditions in this setup are similar to those found in an oxygen-burning shell of a massive star. We map the hydrostatic stratification (see Fig. 7) on an evenly spaced, 3D, Cartesian grid defined by  $(x, y, z) \in [-1, 1] \times [1, 3] \times [-1, 1]$ . The gravitational acceleration points downward in the  $y$ -direction,

$$g_y = g_0 f_g(y) y^{-5/4}, \quad (89)$$

where  $g_0 = -1.414870$  and

$$f_g(y) = \begin{cases} \frac{1}{2} \left\{ 1 + \sin \left[ 16\pi \left( y - \frac{1}{32} \right) \right] \right\}, & \text{for } 1 \leq y < 1 + \frac{1}{16}, \\ 1, & \text{for } 1 + \frac{1}{16} \leq y \leq 3 - \frac{1}{16} \\ \frac{1}{2} \left\{ 1 + \sin \left[ 16\pi \left( y - \frac{1}{32} \right) \right] \right\}, & \text{for } 3 - \frac{1}{16} < y \leq 3. \end{cases} \quad (90)$$

As in [Andrassy et al. \(2022\)](#), we work with rescaled quantities such that the speed of sound and the density at the base of the

<sup>11</sup> See an animation available on Zenodo (<https://zenodo.org/doi/10.5281/zenodo.10280900>).

<sup>12</sup> The animations show high values of the velocity divergence developing early on where the second derivative of the transition function  $\eta(y)$  (Eq. (87)) is discontinuous. This higher-order discontinuity may influence the behaviour of limiters.

box are taken as units of velocity and density, and the thickness of the convective oxygen shell as unit of length. A detailed list of units with the associated values can be found in Table 1 of [Andrassy et al. \(2022\)](#).

The initially hydrostatic stratification is described by a piecewise-polytropic relation in the form

$$\frac{\partial \ln p}{\partial \ln \rho} = \begin{cases} \gamma_0, & \text{for } 1 \leq y < 2 - \frac{1}{16}, \\ \gamma_0 + \eta(y)(\gamma_1 - \gamma_0), & \text{for } 2 - \frac{1}{16} \leq y \leq 2 + \frac{1}{16}, \\ \gamma_1, & \text{for } 2 + \frac{1}{16} < y \leq 3, \end{cases} \quad (91)$$

where  $\gamma_0 = 5/3$ ,  $\gamma_1 = 1.3$ , and  $\eta(y)$  is a smooth function,

$$\eta(y) = \begin{cases} 0, & \text{for } 1 \leq y < 2 - \frac{1}{16}, \\ \frac{1}{2}[1 + \sin(8\pi y)], & \text{for } 2 - \frac{1}{16} \leq y \leq 2 + \frac{1}{16}, \\ 1, & \text{for } 2 + \frac{1}{16} < y \leq 3. \end{cases} \quad (92)$$

The adiabatic index is  $\gamma = \gamma_0$ . In this work, we assume periodic boundary conditions in the horizontal  $x$ - and  $z$ -direction, whereas reflecting, stress-free boundaries are used in the vertical  $y$ -direction. This problem is set up such that turbulent convective flows develop in the lower half of the domain, which is initially adiabatic, while internal gravity waves are free to propagate in the upper, stably stratified layer. To keep track of the position of the upper convective boundary, at  $t = 0$  we fill the stable layer with a passive scalar whose abundance smoothly turns to 0 across the upper boundary of the adiabatic region according to  $X = \eta(y)$ .

In order to drive the convection, we include a time-independent heat source that continuously injects energy into the system close to the base of the box. The rate of energy released per unit volume,

$$\dot{q}(y) = \begin{cases} \dot{q}_0 \sin(8\pi y) \frac{\sin(4\pi\Delta x)}{(4\pi\Delta x)}, & \text{for } 1 \leq y < 1 + \frac{1}{8}, \\ 0, & \text{for } 1 + \frac{1}{8} \leq y \leq 3, \end{cases} \quad (93)$$

is added to the right-hand side of Eq. (2) as

$$\mathbf{S} \mapsto \mathbf{S} + \begin{bmatrix} 0 \\ 0 \\ 0 \\ 0 \\ \dot{q} \\ 0 \end{bmatrix}. \quad (94)$$

In the work of [Andrassy et al. \(2022\)](#), the amplitude of the heat source was  $\dot{q}_0 = 3.795720 \times 10^{-4}$ , which gave rise to convective flows with a root-mean-square Mach number  $\mathcal{M}_{\text{rms}} \approx 0.04$ . To make the problem more challenging, here we decrease  $\dot{q}$  by a factor of ten, so  $\dot{q}_0 = 3.795720 \times 10^{-5}$ . The lower heating rate, according to the well-established  $\mathcal{M} \propto \dot{q}_0^{1/3}$  relation (see, e.g., [Woodward et al. 2014](#); [Käpylä 2021](#); [Horst et al. 2021](#)), should drive convection at  $\mathcal{M}_{\text{rms}} \approx 0.02$ .

In this setup, internal gravity waves (IGWs) are excited by the interaction of the convective flows with the bottom boundary of the stably stratified layer. The wavelength of IGWs in the direction of gravity becomes shorter when the waves are excited at progressively lower temporal frequencies ([Sutherland 2010](#)). At the heating rate we consider, the most prominent IGWs that originate at the convective boundary are only barely spatially resolved on the coarsest of our grids with  $128^3$  cells. Therefore, we decide not to decrease  $\dot{q}_0$  even further for these simulations because it would give rise to convective flows with lower characteristic frequencies and lead to the generation of unresolved

IGWs in the stable layer. Due to the fully compressible nature of SLH, we also expect short-wavelength sound waves to be generated, although at much lower amplitudes than those of IGWs at the typical Mach numbers encountered in this test problem ([Lighthill 1952](#)).

As done for the test described in Sect. 3.1, here we run simulations for each of the 18 considered combinations of Riemann solvers and spatial reconstruction schemes. To judge the numerical convergence of our results, each combination of methods is run on grids with  $128^3$  and  $256^3$  cells. Additionally, we run a single simulation on a  $512^3$  grid using the LHLLC Riemann solver and the PAR reconstruction scheme, which we consider the reference solution for this test problem. However, because of the chaotic nature of the turbulent flows that arise in the convective layer, convergence is not expected in the exact flow morphology, so we do not compute  $L_1$  errors as done in Sect. 3.1. Instead, we analyze the convergence of the numerical results in terms of ensemble-averaged quantities that are representative of the dynamical properties of the system, such as kinetic energy spectra computed in the convective and stable layers.

To break the initial symmetry, we add a perturbation to the hydrostatic density stratification in the form

$$\Delta\rho = 1.1 \times 10^{-5} \frac{\dot{q}(y)}{\dot{q}_0} [\sin(3\pi x) + \cos(\pi x)] [\sin(3\pi z) - \cos(\pi z)]. \quad (95)$$

The subsequent evolution of the system and the development of convection is shown in Fig. 8. The density perturbation, alongside the action of the heat source, generate packets of fluid with higher entropy content than the adiabatic surroundings. The packets of hot and low-density material buoyantly rise in the adiabatic stratification until they reach  $y \approx 2$ . At this height, the temperature stratification turns subadiabatic and the buoyant force acting on the rising plumes changes sign, forcing them to overturn. IGWs excited at the bottom boundary of the subadiabatic region propagate upward in the stratification (with characteristic Mach numbers in the range from 0.005 to 0.01) and are subsequently reflected at the top boundary of the domain. Shear instabilities break the large-scale buoyant structures that arise in the adiabatic layer and initiate the cascade of kinetic energy toward smaller scales. Turbulent convection fully develops after approximately one convective turnover time scale,  $\tau_{\text{conv}} = 133$  time units, which we define according to

$$\tau_{\text{conv}} = \frac{2L_{\text{conv}}}{\langle |V|_{\text{rms}} \rangle}. \quad (96)$$

In Eq. (96), the root-mean-square convective speed is averaged over several convective turnover time scales and  $L_{\text{conv}} = 1$  is taken as representative of the vertical extent of the convection zone. In our reference simulation, the root-mean-square Mach number in the convection zone is<sup>13</sup>  $\mathcal{M}_{\text{rms}} = 0.019 \pm 0.001$ , which is in agreement with the value predicted by the  $\mathcal{M}_{\text{rms}} \propto \dot{q}_0^{1/3}$  scaling relation. All simulations are run until  $t_{\text{max}} = 32\tau_{\text{conv}}$  to have a proper coverage of the dynamical evolution of the system and to compute meaningful time averages needed for the following analysis.

### 3.2.1. Flow morphology and spatial kinetic energy spectra

In Fig. 9, we show snapshots of the Mach number taken at the vertical plane  $z = 0$ , obtained at the final time  $t = 32\tau_{\text{conv}}$

<sup>13</sup> The error bar represents one standard deviation computed over the last 20 convective turnovers.

with all the methods tested here. Although all panels show results computed using the same grid resolution ( $256^3$ ), there is a vast difference between the methods in terms of effects induced by numerical dissipation. With the RUSANOV flux, convection mainly happens in the form of large-scale plumes and IGWs are barely excited in the stable layer except when high-order methods such as PSH or PPM08 are used to reconstruct the Riemann states. Smaller-scale structures typical of turbulent flows become progressively more visible in the convection zone with higher-order reconstruction methods and less dissipative solvers. Internal waves with progressively shorter wavelengths also tend to be more visible in the stable layer with less dissipative methods.

The effects of the numerical dissipation on the properties of the flow are better quantified in Fig. 10 and 11, where we show the power spectra of kinetic energy extracted from a horizontal plane in the middle of the convection zone ( $y = 1.5$ ) and stable layer ( $y = 2.5$ ) as functions of the horizontal wavenumber,

$k_h = \sqrt{k_x^2 + k_z^2}$ . We compute  $k_x$  and  $k_z$  as

$$k_x = \begin{cases} m, & \text{for } 0 \leq m \leq \lfloor \frac{N_x-1}{2} \rfloor, \\ -N_x + m, & \lfloor \frac{N_x-1}{2} \rfloor < m < N_x, \end{cases} \quad (97)$$

$$k_z = \begin{cases} n, & \text{for } 0 \leq n \leq \lfloor \frac{N_z-1}{2} \rfloor, \\ -N_z + n, & \lfloor \frac{N_z-1}{2} \rfloor < n < N_z, \end{cases} \quad (98)$$

where  $\lfloor \cdot \rfloor$  represents the floor function and  $N_x$  and  $N_z$  are the numbers of cells in the  $x$ - and  $z$ -direction, respectively. The spectra are averaged over the time interval  $t \in (10\tau_{\text{conv}}, 32\tau_{\text{conv}})$ . In the convection zone, all of the curves approximately agree with the Kolmogorov scaling law ( $k_h^{-5/3}$ ) on some intermediate scales. We notice that the kinetic energy spectra shown in Fig. 10 present a pile-up of kinetic energy at the bottom of the inertial range. This phenomenon, also known as ‘‘bottleneck effect’’, is often observed both in hydrodynamic simulations (see, e.g., Dobler et al. 2003) and experimental studies (see, e.g., K uchler et al. 2019) of turbulent flows. The extent of the inertial range of the turbulent kinetic energy spectrum greatly differs from method to method. With a fixed spatial reconstruction scheme, the kinetic energy spectrum obtained with LHLLC enters the viscous sub-range (where the kinetic energy of the turbulent eddies is dissipated into internal energy of the gas) at higher wavenumbers as compared to both HLLC and RUSANOV. Reconstruction schemes based on slope limiters are characterized by shallower spectra in the viscous sub-range than those generated by unlimited schemes. In the stable layer (see Fig. 11), RUSANOV and HLLC generate much weaker IGWs than the reference run even on large scales, except when used in combination with PSH. Both in the convective and stable layers, all spectra converge to the reference solution if the order of the spatial reconstruction method or the grid resolution are increased.

### 3.2.2. Turbulent entrainment at the convective boundary

The overturning of the convective flows at the upper convective boundary gives rise to a variety of hydrodynamic processes (including shear instabilities, convective overshoot, and breaking of surface waves) that lead to the entrainment of material from the upper, stably stratified layer into the convection zone. The conglomeration of these processes is known in the literature as ‘‘convective boundary mixing’’ (see, e.g., Meakin & Arnett 2007; Andrassy et al. 2020; Horst et al. 2021; Anders & Pedersen 2023) and it increases the size of convective regions over time. As part of our comparison study, we quantify the impact of the choice

of a specific combination of methods in Godunov-type schemes on the evolution of the convective boundary. At any given point in time, we assume that the vertical coordinate of the boundary between the convective and stable layer,  $y_{\text{cb}}$ , is the position at which the horizontal average of the passive scalar  $X$  takes the value

$$\bar{X} = \frac{1}{2}(X_{\text{min}} + X_{\text{max}}), \quad (99)$$

where  $X_{\text{min}}$  and  $X_{\text{max}}$  are the minimum and maximum values of  $X$ , respectively. Such a choice for  $y_{\text{cb}}$  is justified by the fact that the initial abundance of the passive scalar,  $X$ , smoothly transitions from 0 to 1 at  $y \approx 2$ , which is the boundary of the initially adiabatic layer where convection sets in first. The time evolution of  $y_{\text{cb}}$  is shown in Fig. 12 for all of our combinations of methods. We note that PPM-based methods used in combination with RUSANOV do not show signs of numerical convergence to the reference solution. Also, the other reconstruction schemes used with RUSANOV seem to accelerate the mixing at the convective boundary with respect to the reference run, especially on the  $128^3$  grid. In reality, this is an artifact of the method used to estimate the position of the convective boundary  $y_{\text{cb}}$ . In fact, because RUSANOV does not resolve shear or contact waves (see Sect. 2.4), the initial gradient in  $X$  at the convective boundary is further smoothed out by the effects of numerical dissipation. When convection fully develops, it mixes the passive scalar that has diffused inside the convection zone and homogenizes its abundance, thus shifting the formal position of  $X = \bar{X}$  outward. This effect is further enhanced with the most diffusive reconstruction methods tested here. Therefore, with the RUSANOV solver, entrainment of material from the stable to the convective layer is mostly determined by numerical diffusion rather than turbulent mixing and the distribution of the passive tracer is not representative of  $y_{\text{cb}}$ . On the other hand, all of the other methods tested here quickly achieve numerical convergence to the reference solution with increasing grid resolution, the order of the reconstruction scheme, or by using progressively less dissipative Riemann solvers. Among the data sets obtained with the six reconstruction schemes, the maximum relative deviation of  $y_{\text{cb}}$  from the reference solution at the final time is 20% and 15% with HLLC on the  $128^3$  and  $256^3$  grids, respectively, while with LHLLC it decreases from 12% to 5% with increasing grid resolution.

### 3.2.3. Shape of the convective boundary

The properties of the upper convective boundary are also studied by means of horizontal averages in the Brunt-V ais al a frequency, which determines both the spectrum of convectively driven IGWs (see, e.g., Sutherland 2010) and the rate of mass entrainment from the stable layer according to the bulk-Richardson-number mixing model (see, e.g., Meakin & Arnett 2007; Andrassy et al. 2020; Rizzuti et al. 2023). Here, the Brunt-V ais al a frequency is computed as

$$N_{\text{BV}} = \left[ -\frac{g_y}{H_p} (\nabla_{\text{ad}} - \nabla) \right]^{1/2}, \quad (100)$$

where

$$\nabla = \frac{d \ln T}{d \ln p}, \quad (101)$$



$T = p/\rho$  is the temperature of the gas<sup>14</sup>,  $H_p = -(\mathrm{d} \ln p/\mathrm{d}y)^{-1}$  is the local pressure scale height, and  $\nabla_{\mathrm{ad}} = 0.4$  is the adiabatic temperature gradient. We average the profiles of  $N_{\mathrm{BV}}$  over  $t \in (30\tau_{\mathrm{conv}}, 32\tau_{\mathrm{conv}})$  so that the change in the position of the convective boundary is smaller than its width. At the same time, the chosen averaging time interval is long enough to partly suppress the statistical fluctuations induced by the turbulent nature of the convective flows. The results are shown in Fig. 13. As convection sets in and entrains material from the upper, stably stratified layer, it steepens the vertical entropy gradient  $\mathrm{d}s/\mathrm{d}y$  across the convective boundary. Therefore, due to the  $N_{\mathrm{BV}}^2 \propto \mathrm{d}s/\mathrm{d}y$  proportionality (see, e.g., Maeder 2009), the vertical profile of the Brunt-Väisälä frequency develops a spike in the region close to the convective boundary and it quickly approaches  $N_{\mathrm{BV}}^{\prime=0}$  in the rest of the stable layer. The fact that, in this setup,  $N_{\mathrm{BV}}$  is characterized by large vertical gradients near the convective boundary (at least with HLLC and LHLLC), makes this quantity particularly suited to measure the amplitude of numerical undershoots or overshoots generated by the methods included in our study. In the regions right above the position of the spike in  $N_{\mathrm{BV}}$ , limited reconstruction methods (i.e., LIN + VL, PPM08, and PPM08) do not generate undershoots below the curve  $N_{\mathrm{BV}}^{\prime=0}$ , except for dynamical fluctuations smaller than 2% induced by the flows in the stable layer. On the other hand, reconstruction schemes that do not use limiters for dynamic variables (i.e., LIN, PAR, and PSH) produce undershoots whose amplitude is considerably larger than that of the dynamical fluctuations. The values of the largest undershoots relative to  $N_{\mathrm{BV}}^{\prime=0}$  are shown in the insets of Fig. 13. Overall, the amplitude of the undershoots increases with the order of the unlimited reconstruction method, and it ranges from  $\approx 7\%$  with LIN to almost 40% with PSH. The profiles of  $N_{\mathrm{BV}}$  obtained on the  $128^3$  grid, not shown here (but available on Zenodo<sup>15</sup>), reveal that the amplitude of the undershoots slightly increases from the  $128^3$  to the  $256^3$  grid for LIN and PAR, although the undershoot region becomes narrower on progressively finer grids. We note that, despite the large-amplitude undershoots generated by some of our unlimited reconstruction methods, such numerical errors do not have any significant impact on the growth of the convection zone, as shown in Fig. 12. Nonetheless, they could still affect the frequency spectrum of IGWs in the stable layer, although the spatial spectra from the stable layer (see Fig. 11) do show any such effect and converge to the reference solution. If numerical undershoots are largely to be avoided whilst generating a steep convective boundary, PPM84 + LHLLC or PPM08 + LHLLC could be the methods of choice.

### 3.3. Frequency power spectra

Finally, in Fig. 14, we show the frequency power spectrum of the vertical velocity component,  $v$ , obtained in the middle of the stable layer for all of our 18 Godunov-type schemes. In particular, the frequency power spectra shown in Fig. 14 are Fourier projections of an array<sup>16</sup> containing the value of  $v$  at  $(x, y, z) = (-0.2, 2.5, -0.2)$  at each time step. There is a clear distinction between the frequency range corresponding to the regime of IGWs ( $\omega < N_{\mathrm{BV}}$ ), where all spectra are almost flat, and the high-frequency range ( $\omega > N_{\mathrm{BV}}$ , where only sound

waves are non-evanescent) in which the spectra are characterized by a steep decrease in power (although non monotonic) toward higher frequencies. The forest of lines visible at frequencies in the range from 1 to 50 correspond to the resonant pressure modes of the cavity as predicted by the linear wave theory in the Cowling approximation (Aerts 2021, see also Fig. 15). In the frequency regime of IGWs, the power spectrum seems to converge to the reference solution when increasing the grid resolution or when using less dissipative Riemann solvers. A more quantitative analysis of the IGW spectrum would require substantially longer simulations, which would benefit from more time averaging as well as reach higher frequency resolution.

On the other hand, the high-frequency domain is well resolved even in simulations run on the  $128^3$  grid, and differences between the spectra are clearly visible. Overall, there is a large spread in power (by almost 20 orders of magnitude at the Nyquist frequency) among the different methods tested in our study, which does not decrease with grid resolution. Therefore, numerical convergence is not achieved at high frequencies. We note that the spectra with the highest power density in the high-frequency range are always those obtained with limited reconstruction methods, in particular PPM84 and PPM08, while unlimited reconstruction methods tend to generate much “quieter” spectra and that are closer to the reference solution. In the simulations of the Kelvin–Helmholtz instability shown in Sect. 3.1, we find that a power excess in high-frequency, short-wavelength sound waves is generated by the complex limiting procedure performed in PPM84 and PPM08 to reconstruct the Riemann states at cell interfaces. In this setup, a similar phenomenon is likely responsible for generating an acoustic power excess close to the Nyquist frequency, where the spread between the spectra is maximum. The power excess, however, is still large down to frequencies similar to the that of the fundamental oscillation mode of the cavity  $\omega_0 = 1.1$ . Also, PPM-based methods used in combination with HLLC excite much stronger resonant lines than those generated with LHLLC, and their peak power density is almost as high as the flat part of the spectrum associated with IGWs. When used with PPM84, both RUSANOV and LHLLC produce a broad feature in the frequency spectrum whose peak is at  $\omega_{\mathrm{peak}} \approx 50$  and 100 on the  $128^3$  and  $256^3$  grids, respectively. If these were sound waves, their wavelength  $\lambda$  would be

$$\lambda = \frac{2\pi}{\omega_{\mathrm{peak}}} c_{\mathrm{sound}}(y = 2.5) \approx 2.7\Delta x, \quad (102)$$

which is close to the Nyquist frequency in space. Therefore, such a feature in the spectrum may be caused by odd-even cell decoupling traveling at the local speed of sound. Additional peaks are observed at even higher frequencies than the frequency of the least resolvable sound wave on the grid (with a wavelength of two cells), so these are most likely numerical artifacts. Tests performed with lower CFL factors of 0.4 and 0.2 show that the amplitude of these peaks is slightly reduced when using shorter time steps in the simulation, but the level of the continuum in the power spectrum remains essentially unaltered. In light of these results, we advise against using PPM-based methods in simulations of sound generation by low-Mach-number turbulence.

## 4. Performance metrics

After proving that all of the methods tested in our study converge to the correct solution for most of the physical quantities of inter-

<sup>14</sup> Here, we assume that the gas constant is unity.

<sup>15</sup> <https://zenodo.org/doi/10.5281/zenodo.10280900>

<sup>16</sup> The array of the values of  $v$  obtained at each time step is multiplied by the Hanning window function to reduce the amplitude of the discontinuities in the signal at the boundaries of the time domain.

est<sup>17</sup>, we can now search for the most efficient way to generate a numerical solution at the desired accuracy. In principle, one could use the  $L_1$  errors computed from the simulations of the Kelvin–Helmholtz instability (see Sect. 3.1) to find the resolution of the grid on which the scheme achieves a given level of accuracy. Then, the computational cost of the simulation run on such a grid can be estimated if the wall-clock time spent by the program to perform a single cell update is known. Here, we prefer to use the results from the test problem involving turbulent convective flows and wave excitation (see Sect. 3.2), which is more challenging than the Kelvin–Helmholtz instability test and much closer to a real application of stellar hydrodynamics. However, due to the chaotic nature of the turbulent flows that develop in the convection zone, convergence in the  $L_1$  error norm cannot be achieved. Therefore, rather than measuring the computational cost per fixed accuracy in the sense of  $L_1$  errors, we opt to measure the computational cost of a simulation run with a specific combination of numerical methods that achieves a given level of effective resolution of the turbulent flows,  $N_{\text{eff}}$ . We estimate the effective resolution obtained on a given grid with  $N_x^3$  cells as

$$N_{\text{eff}}(N_x) = \frac{2L_{\text{conv}}}{\lambda_{\text{vis}}(N_x)}, \quad (103)$$

where  $\lambda_{\text{vis}}(N_x)$  is a characteristic dissipation length scale in the turbulent kinetic energy spectrum. In high-resolution schemes, the amount of kinematic viscosity introduced into the system is not fixed, but rather its value depends on the local dynamical properties of the flow and it is often found to be a steep function of the spatial wavenumber (see, e.g., Porter & Woodward 1994). Therefore,  $\lambda_{\text{vis}}(N_x)$  cannot be defined uniquely. Here, we choose

$$\lambda_{\text{vis}}(N_x) \approx \frac{2L_{\text{conv}}}{k_{h,10}(N_x)} \quad (104)$$

as a representative value for the dissipation length scale, with  $k_{h,10}(N_x)$  being the spatial wavenumber at which the kinetic power spectrum rescaled by the Kolmogorov law drops by one dex from its maximum. In this approximation, the effective resolution is simply given by

$$N_{\text{eff}}(N_x) = k_{h,10}(N_x). \quad (105)$$

To perform a more precise measurement of  $N_{\text{eff}}(N_x)$ , both the array of wavenumbers and of the kinetic energy spectrum are linearly interpolated on a finer grid. The values of the effective resolution (rescaled by the grid resolution  $N_x$ ) obtained in the simulations included in our study are collected in Table 2. There is a clear trend toward higher effective resolution when using progressively higher-order reconstruction methods or less dissipative Riemann solvers.

By combining the values of  $N_{\text{eff}}(N_x)$  and the average wall-clock time  $\delta t(N_x)$  spent by the program to perform a single cell update, shown in Table 3, it is possible to estimate the computational effort required by each combination of numerical options to achieve the effective resolution of PPM08 + LHLLC<sup>18</sup> as

$$\Theta(N_x) = \frac{\delta t(N_x)}{\delta t(N_x)_{\text{PPM08+LHLLC}}} \left( \frac{N_{\text{eff}}(N_x)}{N_{\text{eff,PPM08+LHLLC}}(N_x)} \right)^{-4}. \quad (106)$$

<sup>17</sup> A prominent example of a nonconvergent numerical solution is the frequency power spectrum of sound waves in the test problem of turbulent convection and mass entrainment shown in Sect. 3.2.

<sup>18</sup> In the following expression, we make use of the fact that the complexity of a 3D, Godunov algorithm, such as that implemented in SLH, scales with  $N_x^4$ , with  $N_x$  being the number of grid cells per dimension.

Equation (106) is rescaled such that the cost of the simulation run with PPM08 + LHLLC on any given grid is unity. All values of  $\Theta(N_x = 128)$  and  $\Theta(N_x = 256)$  are shown in Table 4. The spread of almost four orders of magnitude in the relative computational cost among the different methods is due to the steep dependence of  $\Theta(N_x)$  on  $N_{\text{eff}}(N_x)$ , which varies by as much as a factor of 10 (see Table 2). On the other hand,  $\Theta(N_x)$  only scales linearly with  $\delta t(N_x)$ , which in our simulations varies at most by a factor of  $\approx 3$  (with LIN + RUSANOV and PPM84 + LHLLC achieving the lowest and highest wall-clock time per cell-update, respectively). The most expensive combination of methods among those tested in our study (in terms of computational cost per fixed resolving power) is LIN + VL + RUSANOV,  $\sim 1000$  times as expensive as PPM08 + LHLLC. The strong numerical dissipation generated by RUSANOV leads to very poor performance of the finite-volume scheme even when used in combination with PPM-based reconstruction methods. Only with the unlimited PSH method such a flux function is capable of achieving acceptable performance ( $\Theta(N_x) \approx 4$ ). When the reconstruction scheme is kept the same, using progressively less dissipative Riemann solvers decreases the cost of reaching the same effective resolution. At the typical Mach numbers encountered in the convection zone ( $M \approx 0.02$ ), the combination of HLLC and second-order reconstruction schemes or PAR is considerably more expensive than PPM08 + LHLLC ( $\Theta(N_x)$  in the range from 10 to 30). The performance of the scheme increases when HLLC is used with PPM-based reconstruction schemes ( $\Theta(N_x)$  in the range from 2 to 6) and it is even higher than that of PPM08 + LHLLC when coupled to PSH. PSH + LHLLC is the most performant method on both grids according to the chosen metric. Overall, the computational cost of the finite-volume scheme is considerably reduced when using the low-dissipation solver (by a factor from 2 to 10 with respect to a scheme using HLLC and the same spatial reconstruction method). The relative performance of the scheme only varies slightly when LHLLC is used in combination with reconstruction methods less accurate than PSH, with the worst performance being achieved by LIN + VL ( $\Theta(N_x) \approx 3$ ).

We note that, for most methods, the value of  $\Theta(N_x)$  sensibly increases (by as much as a factor of  $\approx 2$ ) from the  $128^3$  to the  $256^3$  grid. Such differences are due to the small but systematic decrease of the rescaled effective resolution  $N_{\text{eff}}(N_x)/N_x$  with increasing the grid resolution (this behavior is also confirmed by the reference solution computed on the  $512^3$  grid, see Table 2). Although the differences observed in  $N_{\text{eff}}(N_x)/N_x$  among the two grids are at most 20%, they are significantly amplified after applying the steep scaling relation between  $\Theta(N_x)$  and  $N_{\text{eff}}(N_x)$ . However, this effect is negligible if compared to the large spread obtained in the values of  $\Theta(N_x)$  on a given grid. Furthermore, we stress that our measure of  $\Theta(N_x)$  is based on a crude approximation of effective resolution of the turbulent flows, so the values provided in Table 4 should only be taken as estimates of the relative performance of different Godunov-type methods in simulations of turbulent convection. The measurements of the absolute performance provided in Table 3, which are needed to estimate  $\Theta(N_x)$ , may also depend on the parallelization strategy and the number of cores used to run the simulations, especially for the methods that require many ghost cells (e.g., PPM08 and PSH) and are therefore characterized by higher communication costs.

## 5. Summary and conclusions

High-resolution, finite-volume schemes are popular methods for simulating the behaviour of astrophysical fluids. There is a wide range of spatial-reconstruction schemes, numerical flux

**Table 2.** Effective resolution  $N_{\text{eff}}(N_x)$  as defined in Sect. 3.2 for all of the 18 Godunov-type methods tested in our study on grids with  $N_x = 128$  and  $N_x = 256$  cells per dimension. Here, all numbers are given as a percentage of the grid resolution  $N_x$  for an easier comparison between different grids. In this metric, the rescaled effective resolution of the reference run (PAR + LHLLC + 512<sup>3</sup>) is 24.43.

128 <sup>3</sup>	RUSANOV	HLLC	LHLLC
LIN	6.21	14.45	24.68
LIN+VL	5.24	13.53	21.97
PAR	7.04	16.68	29.05
PPM84	10.62	24.15	31.47
PPM08	14.21	28.42	33.85
PSH	20.47	37.24	49.22
256 <sup>3</sup>	RUSANOV	HLLC	LHLLC
LIN	5.47	12.61	23.30
LIN+VL	4.38	11.08	19.75
PAR	6.35	14.28	26.16
PPM84	10.10	21.23	29.06
PPM08	13.55	27.00	32.02
PSH	19.90	35.08	47.00

**Table 3.** Mean wall-clock time spent by the program to advance the solution by one time step with RK3 in a single cell of the computational grid, in units of  $\mu\text{s}$ . The numbers provided in the tables are averages of five measurements, each of which is obtained by evolving the setup described in Sect. 3.2 for 100 steps. Relative errors in the averages (in the sense of  $1\sigma$ ) are smaller than 2% in all cases. Every simulation run for this analysis is MPI parallelized using grids with 32<sup>3</sup> cells per task. Computations are performed on 2.3 GHz Intel Xeon, Skylake-based processors.

128 <sup>3</sup>	RUSANOV	HLLC	LHLLC
LIN	1.47	1.68	1.70
LIN+VL	1.57	1.80	1.89
PAR	1.47	1.74	1.78
PPM84	4.12	4.30	4.31
PPM08	3.57	3.75	3.83
PSH	2.01	2.36	2.41
256 <sup>3</sup>	RUSANOV	HLLC	LHLLC
LIN	1.60	1.73	1.77
LIN+VL	1.73	1.87	1.88
PAR	1.60	1.81	1.86
PPM84	4.23	4.40	4.47
PPM08	3.79	4.03	4.00
PSH	2.24	2.47	2.52

functions and time-integration methods that can be combined into a numerically stable and robust, finite-volume scheme. Focusing on subsonic flows, we have analysed the accuracy and computational cost of all possible combinations of six spatial-reconstruction schemes and three numerical flux functions, i.e. 18 methods in total. The numerical solution was marched in time with a semi-discrete scheme based on a third-order Runge–Kutta method. This choice was motivated by our focus on the spatial accuracy of the schemes and the related need to suppress time-stepping errors.

We consider two main test problems. The first is a Kelvin–Helmholtz instability problem, in which the initial shear flows have Mach numbers of  $10^{-1}$ ,  $10^{-2}$ , and  $10^{-3}$ . We use a smooth

**Table 4.** Relative computational cost of each Godunov-type method considered in this study to achieve the same effective resolution as the PPM08 + LHLLC combination ( $\Theta$ , see Eq. (106)) in the simulations described in Sect. 3.2. Here all numbers are rounded to two significant figures.

128 <sup>3</sup>	RUSANOV	HLLC	LHLLC
LIN	340	13.0	1.60
LIN+VL	710	18.0	2.80
PAR	210	7.70	0.86
PPM84	110	4.30	1.50
PPM08	30.0	2.00	1.00
PSH	3.90	0.42	0.14
256 <sup>3</sup>	RUSANOV	HLLC	LHLLC
LIN	470	18.0	1.60
LIN+VL	1200	33.0	3.30
PAR	260	11.0	1.00
PPM84	110	5.70	1.60
PPM08	30.0	2.00	1.00
PSH	3.80	0.43	0.14

initial condition to make it possible to obtain numerically convergeable solutions to the inviscid Euler equations at a fixed point in time in the non-linear phase of the instability. We characterise the accuracy of the solutions by (i) performing a qualitative assessment of the spatial structure of the solutions and (ii) by measuring  $L_1$  errors with respect to a reference solution obtained on a fine grid of  $8192 \times 4096$  cells.

The low-Mach flux function LHLLC is found to be much less dissipative and much more accurate than the HLLC and RUSANOV flux functions at the two lowest Mach numbers considered. Even though the overall 2D numerical scheme is 2<sup>nd</sup>-order accurate, the errors produced by different spatial reconstruction schemes span as much as an order of magnitude. Unlimited reconstruction schemes of increasing order, up to 7<sup>th</sup>, provide progressively more accurate results when the solution is sufficiently well resolved. However, these schemes are of limited use for the advection of mass fractions due to the oscillations and overshoots they produce around discontinuities. This issue is largely eliminated by the use of limiters in the schemes LIN+VL, PPM84, and PPM08. However, we find that the switching behaviour of the limiters introduces spurious structures and small-scale sound waves to the solutions, which severely reduce the accuracy of the methods when applied to slow flows. Our hybrid method PSH, which combines unlimited, 7<sup>th</sup>-order reconstruction for dynamic variables with PPM08 for mass fractions, is found to provide the most accurate solutions in nearly all of our simulations of the Kelvin–Helmholtz instability.

Our second test problem, chosen to be as close as possible to practical applications in the dynamics of stellar interiors, involves stratified turbulent convection generating waves in and entraining mass from an overlying stably stratified layer. The typical Mach number of the convection is  $\approx 0.02$ . The turbulent nature of the convective flow makes the solutions chaotic but space- and time-averaged quantities can still be meaningfully compared between different simulations. We run the simulations on grids of 128<sup>3</sup> and 256<sup>3</sup> cells with one additional simulation on a 512<sup>3</sup> grid serving as a reference solution.

Qualitatively speaking, the solutions match the trends seen in the simulations of the Kelvin–Helmholtz instability, i.e. combinations of the least dissipative flux functions with the highest-



order reconstruction schemes provide the highest resolving power in both the convective and stable layers. Spatial spectra of kinetic energy computed in the convective and stable layers converge toward the reference solution with any of the 18 methods but the least dissipative combinations (especially PSH+LHLLC) are much closer to the reference solution than the most dissipative ones (especially LIN+VL+RUSANOV). The spatial spectrum in both layers obtained with PSH+LHLLC on a  $256^3$  grid is essentially the same as that with PAR+LHLLC on a  $512^3$  grid.

The growth rate of the convective layer converges upon grid refinement with all 6 reconstruction schemes and both the HLLC and LHLLC flux function but the convergence is significantly faster with the low-Mach flux function LHLLC. The RUSANOV flux function produces extremely viscous flows and large deviations from the reference solution in terms of the position of the upper convective boundary.

We show that schemes that do not use limiting for dynamic variables (LIN, PAR, PSH), unlike those that do (LIN+VL, PPM84, PPM08), produce overshoots in the Brunt-Väisälä frequency at the relatively sharp convective boundary. The magnitude of the overshoots increases with increasing order of accuracy of the method, as expected. Neither the growth rate of the convective layer, nor the temporal and spatial spectra of internal gravity waves are affected by this phenomenon in our simulations but we recommend careful testing when such high-order methods are applied to other setups or used to derive quantities not investigated here.

Temporal spectra of the vertical component of velocity in the stable layer show that all six reconstruction schemes produce qualitatively similar, flat and featureless spectra in the regime of internal gravity waves. On the other hand, the spectra of pressure (i.e. high frequency) waves are sensitive to the choice of the reconstruction scheme even with the low-Mach flux function LHLLC. The spectra also reinforce our conclusions based on the Kelvin-Helmholtz problem that methods that apply limiters to dynamic variables generate much more acoustic “noise” than methods that do not. This includes the popular methods PPM84 and PPM08. Although we do not know what the acoustic spectrum in our problem should look like, we show that the frequencies of vertical resonant modes agree with 1D linear wave theory.

Finally, we use the steep drop-off of the spatial kinetic energy spectra in the convective layer close to the grid scale to define a measure of effective resolution. Rescaling the wall-clock time of our  $128^3$  and  $256^3$  simulations, we estimate the computational cost of matching the same effective resolution using our 18 methods. The cost is found to span almost four orders of magnitude. The largest cost reduction comes from choosing the least dissipative flux function, which is LHLLC in our study. We show that the reconstruction schemes PSH, PAR, and PPM08, in order of increasing cost, are the cheapest at the same effective resolution.

Our study demonstrates that it is generally advisable to use low-dissipation Riemann solvers in Godunov-type finite-volume schemes for simulating low-Mach-number flows. The low-Mach fix  $\phi$  in Eq. (76) can easily be implemented in any HLLC-type scheme without affecting the absolute performance of the code, and it reduces the amount of computation required to achieve the same accuracy as HLLC by a factor ranging from 2 to 10 at typical Mach numbers of  $\approx 0.01$ . At Mach numbers of  $\approx 10^{-4}$  or  $\approx 10^{-3}$ , like those encountered in the convective cores of main sequence stars, the usage of a low-Mach solver decreases the computational cost per fixed accuracy with respect to a conventional Riemann solver by even larger factors (Leidi et al. 2022). Although low-dissipation Riemann solvers such as

LHLLC bring clear advantages in simulations of subsonic flows when used in Eulerian codes, their robustness and accuracy properties in quasi-Lagrangian, moving-mesh schemes still has to be verified. We note that such schemes hold promise for a particularly significant improvement because mesh motions aim at reducing advection errors by minimizing the velocities relative to the cell interfaces. This naturally leads to low-Mach-number flows in the comoving frame, which are better modeled by low-Mach-number Riemann solvers. We are currently testing an implementation of the LHLLC/D solvers of Minoshima & Miyoshi (2021) in the moving-mesh MHD code AREPO (Springel 2010), which we will report in a forthcoming study.

On the other hand, the choice of the spatial reconstruction scheme depends on the physical application of interest. Overall, second-order reconstruction methods lead to the generation of considerably more inaccurate results than higher-order schemes when the Mach number of the flow is low. If numerical overshoots have to be suppressed whilst retaining high resolving power, PPM84 and PPM08 should be the methods of choice. However, higher-order unlimited reconstruction methods should be preferred over PPM-based methods in simulations of sound wave generation by subsonic turbulence because they generate much less numerical “noise” in the acoustic spectrum. Less oscillatory alternatives to the hybrid PSH method, such as the 3<sup>th</sup>-order piecewise parabolic hybrid (PPH) or the 5<sup>th</sup>-order piecewise quartic hybrid (PQH) methods described in Appendix A, could offer the best compromise between the complete removal of numerical overshoots and reduction of acoustic noise.

Finally, we note that there are complex astrophysical environments where both high- and low-Mach-number flows can co-exist. This scenario often occurs, for instance, in accretion disks (see, e.g., Klessen & Hennebelle 2010), star forming regions (see, e.g., Wang et al. 2024), or outer layers of stars (see, e.g., Wedemeyer et al. 2017). To model such diverse flow regimes, the simple use of unlimited higher-order reconstructions and low-dissipation solvers may give rise to numerical instabilities, especially in the proximity of shock fronts. To cure this problem, an alternative approach based on the local dynamical properties of the flow is needed (see, e.g., Mignone et al. 2011; Fleischmann et al. 2020). One possibility is to add a selection criterion to the function that computes the flux at a cell interface such that the LHLLC solver is used if the Mach number of the flow is lower than a conservative threshold (e.g.,  $\mathcal{M} \lesssim 0.6$ ), whereas a proper shock-capturing method (e.g., HLL or HLLC) is chosen for modeling faster flows. A similar argument can be made for the choice of the spatial reconstruction scheme. To avoid introducing large oscillations in the state quantities near large, non-linear discontinuities, schemes that are more dissipative and possibly close to being TVD (such as LIN+VL, PPM84, PPM08, or WENO) should be preferred over high order unlimited methods.

*Acknowledgements.* The work of GL and FKR is supported by the German Research Foundation (DFG) through the grant RO 3676/3-1. We acknowledge support by the Klaus Tschira Foundation. This work is funded by the Deutsche Forschungsgemeinschaft (DFG, German Research Foundation) under Germany’s Excellence Strategy EXC 2181/1 - 390900948 (the Heidelberg STRUCTURES Excellence Cluster). The authors gratefully acknowledge the Gauss Centre for Supercomputing e.V. (www.gauss-centre.eu) for funding this project by providing computing time on the GCS Supercomputer SuperMUC-NG at Leibniz Supercomputing Centre (www.lrz.de). PVFE was supported by the U.S. Department of Energy through the Los Alamos National Laboratory (LANL). LANL is operated by Triad National Security, LLC, for the National Nuclear Security Administration of the U.S. Department of Energy (Contract No. 89233218CNA000001). This work has been assigned a document release number LA-UR-23-33257.

## References

- Aerts, C. 2021, *Rev. Mod. Phys.*, 93, 015001
- Anders, E. H. & Pedersen, M. G. 2023, *Galaxies*, 11
- Andrassy, R., Herwig, F., Woodward, P., & Ritter, C. 2020, *MNRAS*, 491, 972
- Andrassy, R., Higl, J., Mao, H., et al. 2022, *A&A*, 659, A193
- Andrassy, R., Leidi, G., Higl, J., et al. 2023, arXiv e-prints, arXiv:2307.04068
- Balsara, D. S. 2017, *Living Reviews in Computational Astrophysics*, 3, 2
- Beckwith, K. & Stone, J. M. 2011, *The Astrophysical Journal Supplement Series*, 193, 6
- Berberich, J. P., Chandrashekar, P., & Klingenberg, C. 2021, *Computers & Fluids*, 219, 104858
- Berlok, T. & Pfrommer, C. 2019, *MNRAS*, 485, 908
- Canivete Cuissa, J. R. & Teyssier, R. 2022, *A&A*, 664, A24
- Chen, S., Lin, B., Li, Y., & Yan, C. 2020, *SIAM Journal on Scientific Computing*, 42, B921
- Colella, P. 1990, *Journal of Computational Physics*, 87, 171
- Colella, P. & Sekora, M. D. 2008, *Journal of Computational Physics*, 227, 7069
- Colella, P. & Woodward, P. R. 1984, *Journal of Computational Physics*, 54, 174
- Courant, R., Friedrichs, K., & Lewy, H. 1928, *Mathematische Annalen*, 100, 32
- Day, M. S. & Bell, J. B. 2000, *Combustion Theory and Modelling*, 4, 535
- Dobler, W., Haugen, N. E., Yousef, T. A., & Brandenburg, A. 2003, *Phys. Rev. E*, 68, 026304
- Dumbser, M., Balsara, D. S., Tavelli, M., & Fambri, F. 2019, *International Journal for Numerical Methods in Fluids*, 89, 16
- Dumbser, M., Castro, M., Parés, C., & Toro, E. F. 2009, *Computers & Fluids*, 38, 1731
- Edelmann, P. V. F. 2014, Dissertation, Technische Universität München
- Edelmann, P. V. F., Horst, L., Berberich, J. P., et al. 2021, *A&A*, 652, A53
- Edelmann, P. V. F. & Röpke, F. K. 2016, in *JUQUEEN Extreme Scaling Workshop 2016*, ed. D. Brömmel, W. Frings, & B. J. N. Wylie, *JSC Internal Report No. FZJ-JSC-IB-2016-01*, 63–67
- Edelmann, P. V. F., Röpke, F. K., Hirschi, R., Georgy, C., & Jones, S. 2017, *A&A*, 604, A25
- Fleischmann, N., Adami, S., & Adams, N. A. 2020, *Journal of Computational Physics*, 423, 109762
- Flock, M., Dzyurkevich, N., Klahr, H., & Mignone, A. 2010, *A&A*, 516, A26
- Godunov, S. K. 1959, *Matematicheskii Sbornik*, 89, 271
- Goffrey, T., Pratt, J., Viallet, M., et al. 2017, *A&A*, 600, A7
- Greenough, J. A. & Rider, W. J. 2003, *Journal of Computational Physics*, 196
- Guillard, H. & Viozat, C. 1999, *Computers & Fluids*, 28, 63
- Harten, A., Engquist, B., Osher, S., & Chakravarthy, S. R. 1987, *Journal of Computational Physics*, 71, 231
- Harten, A., Lax, P. D., & Leer, B. V. 1983, *SIAM Review*, 25, 35
- Horst, L., Edelmann, P. V. F., Andrassy, R., et al. 2020, *A&A*, 641, A18
- Horst, L., Hirschi, R., Edelmann, P. V. F., Andrassy, R., & Röpke, F. K. 2021, *A&A*, 653, A55
- Jiang, G.-S. & Shu, C.-W. 1996, *Journal of Computational Physics*, 126, 202
- Käpylä, P. J. 2021, *A&A*, 651, A66
- Klein, R. 2009, *Theoretical and Computational Fluid Dynamics*, 23, 161
- Klessen, R. S. & Hennebelle, P. 2010, *A&A*, 520, A17
- Klingenberg, C., Schmidt, W., & Waagan, K. 2007, *Journal of Computational Physics*, 227, 12
- Kolb, O. 2014, *SIAM Journal on Numerical Analysis*, 52, 2335
- Kritsuk, A. G., Åke Nordlund, Collins, D., et al. 2011, *The Astrophysical Journal*, 737, 13
- Küchler, C., Bewley, G., & Bodenschatz, E. 2019, *Journal of Statistical Physics*, 175, 617
- Latini, M., Schilling, O., & Don, W. S. 2007, *Journal of Computational Physics*, 221, 805
- Lecoanet, D., McCourt, M., Quataert, E., et al. 2017, *MNRAS*, 455, 4274
- Leidi, G., Andrassy, R., Higl, J., Edelmann, P. V. F., & Röpke, F. K. 2023, *A&A*, 679, A132
- Leidi, G., Birke, C., Andrassy, R., et al. 2022, *A&A*, 668, A143
- LeVeque, R. J. 2002, *Finite Volume Methods for Hyperbolic Problems*, Cambridge Texts in Applied Mathematics (Cambridge University Press)
- Lighthill, M. J. 1952, *Proceedings of the Royal Society of London Series A*, 211, 564
- Liou, M.-S. 2006, *Journal of Computational Physics*, 214, 137
- Liu, X.-D., Osher, S., & Chan, T. 1994, *Journal of Computational Physics*, 115, 200
- Maeder, A. 2009, *Physics, Formation and Evolution of Rotating Stars*
- McNally, C. P., Lyra, W., & Passy, J.-C. 2012, *ApJS*, 201, 18
- Meakin, C. A. & Arnett, D. 2007, *ApJ*, 667, 448
- Miczek, F. 2013, Dissertation, Technische Universität München
- Miczek, F., Röpke, F. K., & Edelmann, P. V. F. 2015, *A&A*, 576, A50
- Mignone, A., Zanni, C., Tzeferacos, P., et al. 2011, *The Astrophysical Journal Supplement Series*, 198, 7
- Minoshima, T. & Miyoshi, T. 2021, *Journal of Computational Physics*, 446, 110639
- Miyoshi, T. & Kusano, K. 2005, *Journal of Computational Physics*, 208, 315
- Motheau, E., Duarte, M., Almgren, A., & Bell, J. B. 2018, *Journal of Computational Physics*, 372, 1027
- Müller, B. 2020, *Living Reviews in Computational Astrophysics*, 6, 3
- Musoke, G., Young, A. J., & Birkinshaw, M. 2020, *Monthly Notices of the Royal Astronomical Society*, 498, 3870
- Muthsam, H. J., Kupka, F., Löw-Baselli, B., et al. 2010, *New A*, 15, 460
- Porter, D. H. & Woodward, P. R. 1994, *ApJS*, 93, 309
- Radice, D., Couch, S. M., & Ott, C. D. 2015, *Computational Astrophysics and Cosmology*, 2, 7
- Rieper, F. 2011, *Journal of Computational Physics*, 230, 5263
- Rizzuti, F., Hirschi, R., Arnett, W. D., et al. 2023, *Monthly Notices of the Royal Astronomical Society*, 523, 2317
- Robertson, B. E., Kravtsov, A. V., Gnedin, N. Y., Abel, T., & Rudd, D. H. 2010, *MNRAS*, 401, 2463
- Roe, P. L. 1981, *Journal of Computational Physics*, 43, 357
- Rusanov, V. 1962, *USSR Computational Mathematics and Mathematical Physics*, 1, 304
- San, O. & Kara, K. 2015, *Computers & Fluids*, 117, 24
- Seo, J. & Ryu, D. 2023, *The Astrophysical Journal*, 953, 39
- Shu, C.-W. 2009, *SIAM Review*, 51, 82
- Shu, C.-W. & Osher, S. 1988, *Journal of Computational Physics*, 77, 439
- Springel, V. 2010, *MNRAS*, 401, 791
- Sutherland, B. R. 2010, *Internal Gravity Waves* (Cambridge University Press)
- Teissier, J.-M. & Müller, W.-C. 2023, arXiv e-prints, arXiv:2306.09856
- Thornber, B., Mosedale, A., Drikakis, D., Youngs, D., & Williams, R. 2008, *Journal of Computational Physics*, 227, 4873
- Toro, E. F. 1991, *Proceedings of the Royal Society of London Series A*, 434, 683
- Toro, E. F. 2009, *Riemann Solvers and Numerical Methods for Fluid Dynamics: A Practical Introduction* (Berlin Heidelberg: Springer)
- Toro, E. F., Spruce, M., & Speares, W. 1994, *Shock Waves*, 4, 25
- van Leer, B. 1974, *Journal of Computational Physics*, 14, 361
- van Leer, B. 1977, *Journal of Computational Physics*, 23, 276
- van Leer, B. 1979, *Journal of Computational Physics*, 32, 101
- Viallet, M., Baraffe, I., & Walder, R. 2011, *A&A*, 531, A86
- Wang, C., Wang, K., Xu, F.-W., et al. 2024, *A&A*, 681, A51
- Wedemeyer, S., Kučinskas, A., Klevas, J., & Ludwig, H.-G. 2017, *A&A*, 606, A26
- Wongwathanarat, A., Grimm-Strele, H., & Müller, E. 2016, *A&A*, 595, A41
- Woodward, P. R., Herwig, F., & Lin, P.-H. 2014, *The Astrophysical Journal*, 798, 49
- Xie, W., Zhang, R., Lai, J., & Li, H. 2019, *International Journal for Numerical Methods in Fluids*, 89, 430

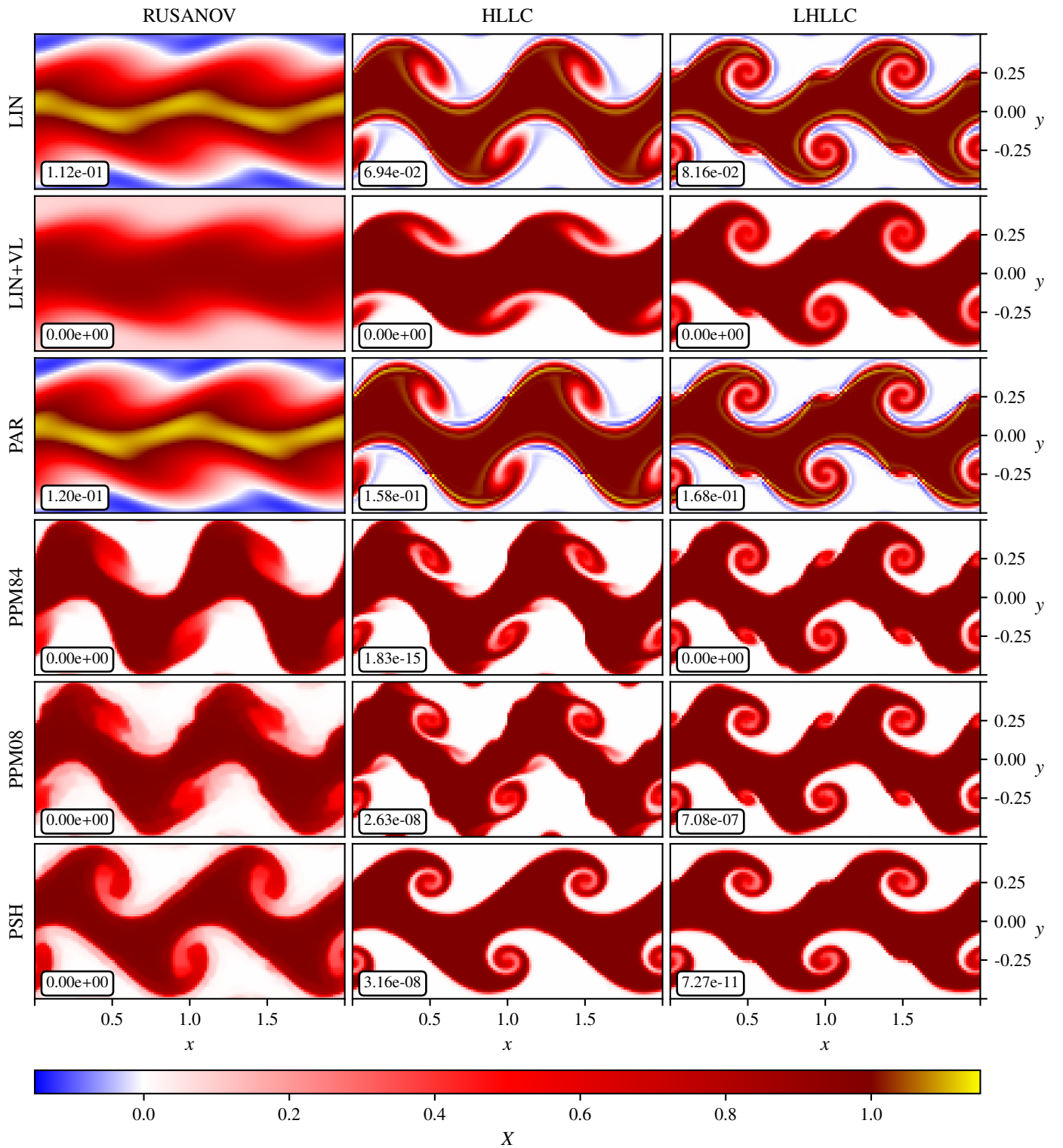


**Fig. 4.** Distributions of the mass fraction  $X$  of the passive scalar in simulations of the Kelvin–Helmholtz instability with the initial Mach number  $\mathcal{M}_0 = 10^{-2}$  on a  $128 \times 64$  grid. The results are shown at  $t = 0.8 \mathcal{M}_0^{-1}$ . Rows and columns show different reconstruction schemes and numerical flux functions, respectively. The colour scale intentionally shows values  $X < 0$  and  $X > 1$  to highlight the overshoots that some of the schemes produce. The absolute value of the largest overshoot outside of this range is given in each panel.



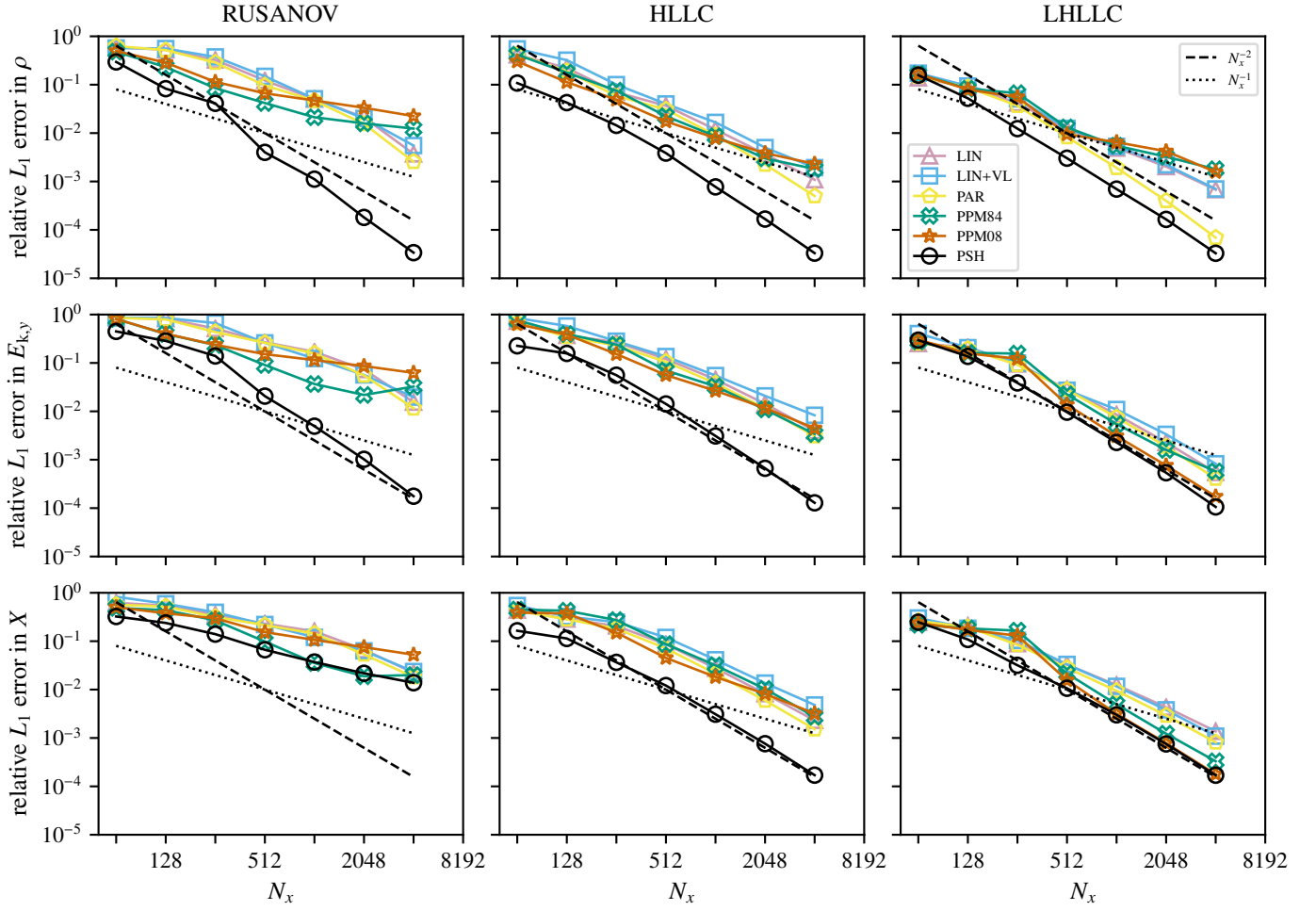


**Fig. 5.** Relative  $L_1$  errors for different variables (rows), flux functions (columns), and reconstruction methods (legend) as functions of grid resolution in the simulations of the Kelvin–Helmholtz instability with the initial Mach number  $\mathcal{M}_0 = 10^{-2}$ . The dashed and dotted lines, which are at the same locations in all of the panels, show the 1<sup>st</sup>- and 2<sup>nd</sup>-order scalings to guide the eye.

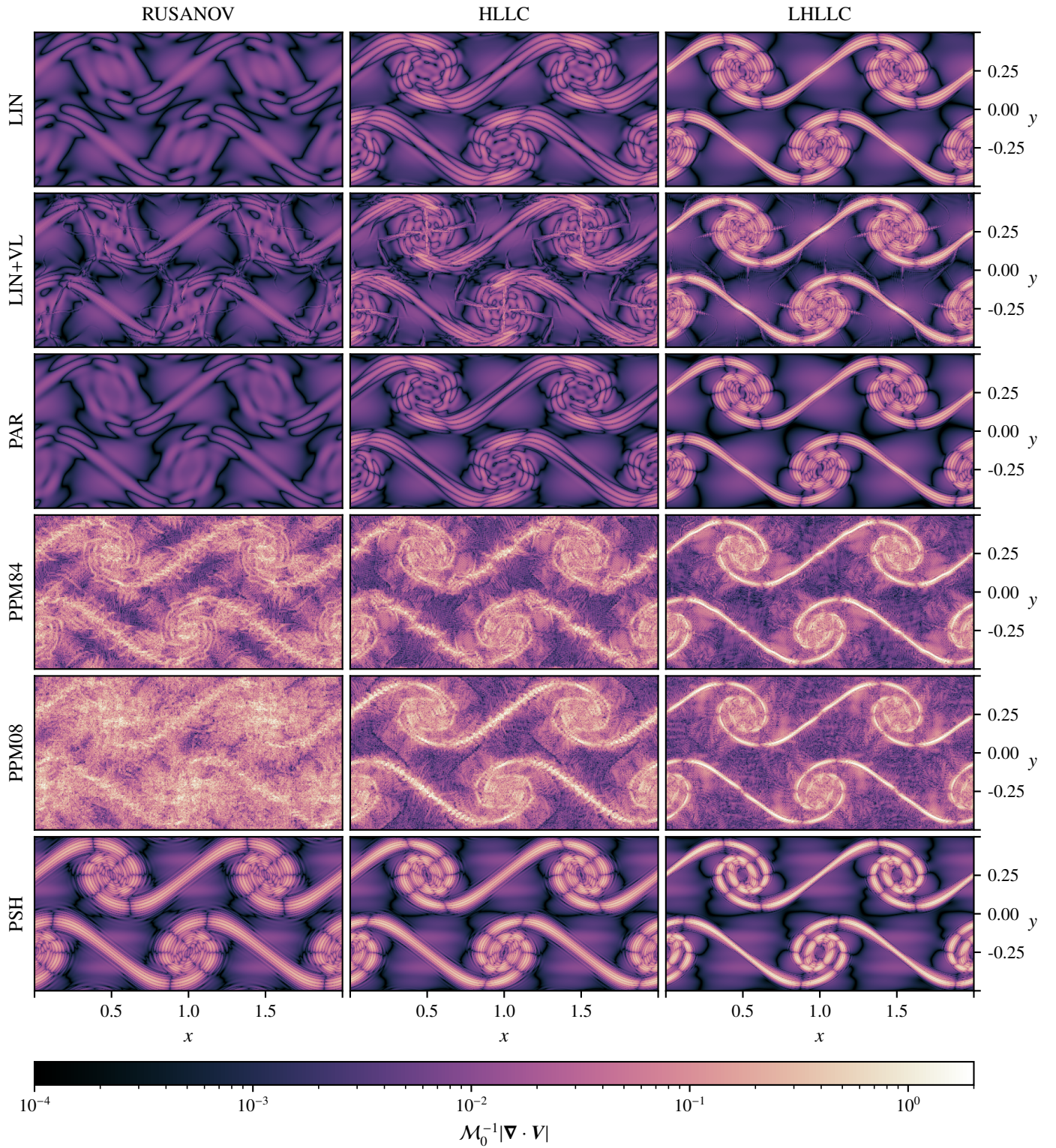


**Fig. 6.** Magnitude of velocity divergence in simulations of the Kelvin–Helmholtz instability with the initial Mach number  $\mathcal{M}_0 = 10^{-2}$  on a  $512 \times 256$  grid. The results are shown at  $t = 0.8 \mathcal{M}_0^{-1}$ . Rows and columns show different reconstruction schemes and numerical flux functions, respectively. The small-scale structure produced by the LIN+VL, PPM84, and PPM08 schemes, which does not occur with the LIN, PAR, and PSH schemes, is caused by the use of limiters.

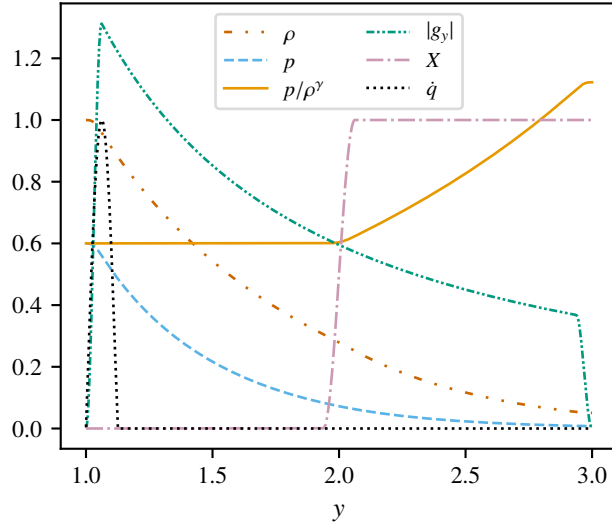


**Fig. 7.** Hydrostatic stratification of density, gas pressure, pseudo-entropy ( $p/\rho^\gamma$ ), and gravity at  $t = 0$  in the problem of turbulent convection and wave excitation at a convective boundary, based on the initial conditions provided in [Andrassy et al. \(2022\)](#). The distribution of the mass fractional abundance of a passive tracer ( $X$ ) and the heat source ( $\dot{q}$ ) are also shown, here represented by a dash-dotted pink and dashed black line, respectively. In this setup, the gravitational acceleration smoothly turns to zero at the bottom and top boundaries of the spatial domain to make the problem consistent with the usage of reflecting, stress free boundary conditions, which for the gas pressure imply  $\partial p/\partial y = 0$ .

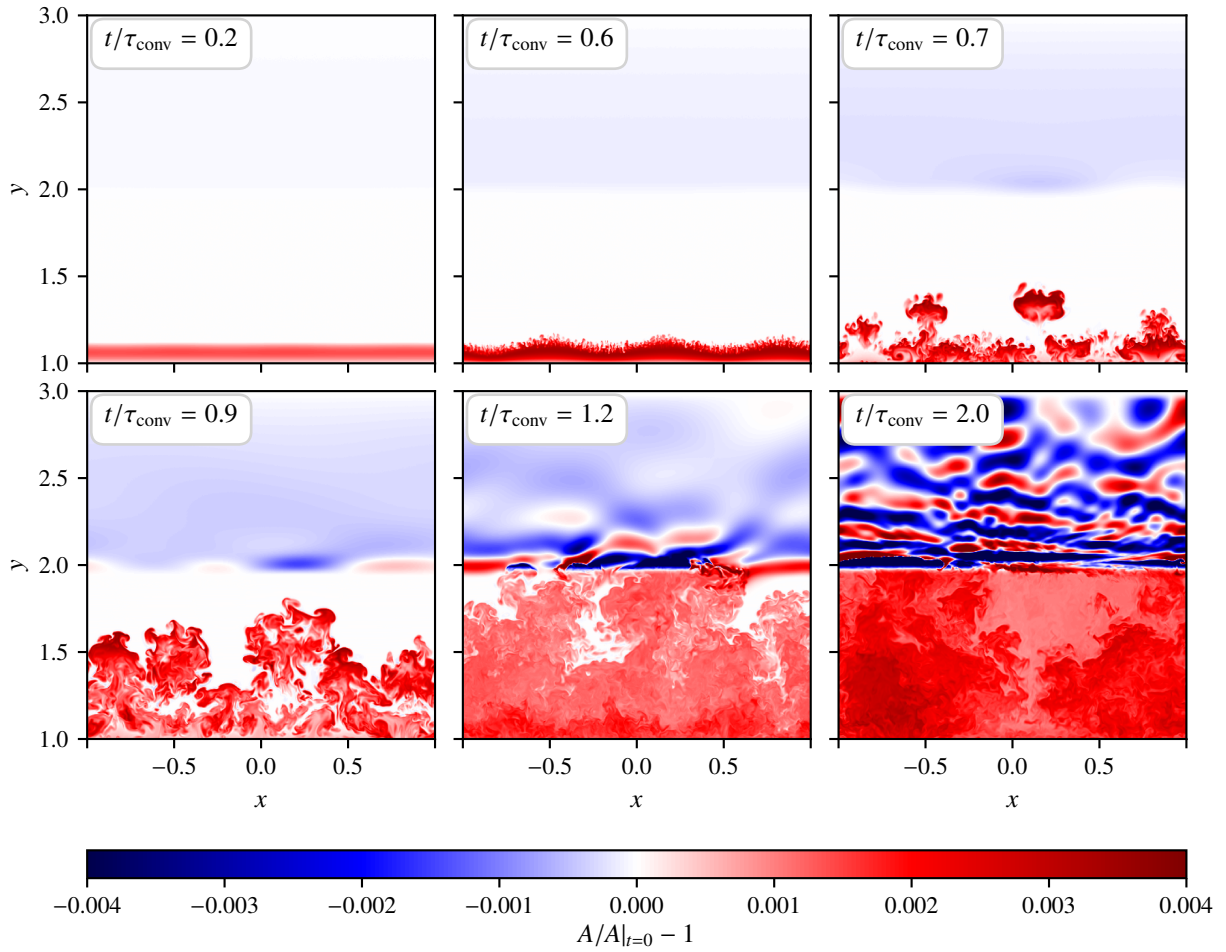


**Fig. 8.** Pseudo-entropy ( $A = p/\rho^\gamma$ ) fluctuations with respect to the hydrostatic, background state computed at different times during the development of the convection, as indicated by the insets, in the problem of turbulent convection and wave excitation. Data are visualized in the  $z = 0$  plane. This simulation was run using the PAR method and LHLLC on a  $512^3$  grid and we consider it our reference solution. Convective plumes start exciting IGWs at the upper convective boundary by  $t \approx \tau_{\text{conv}}$  (see center bottom panel).



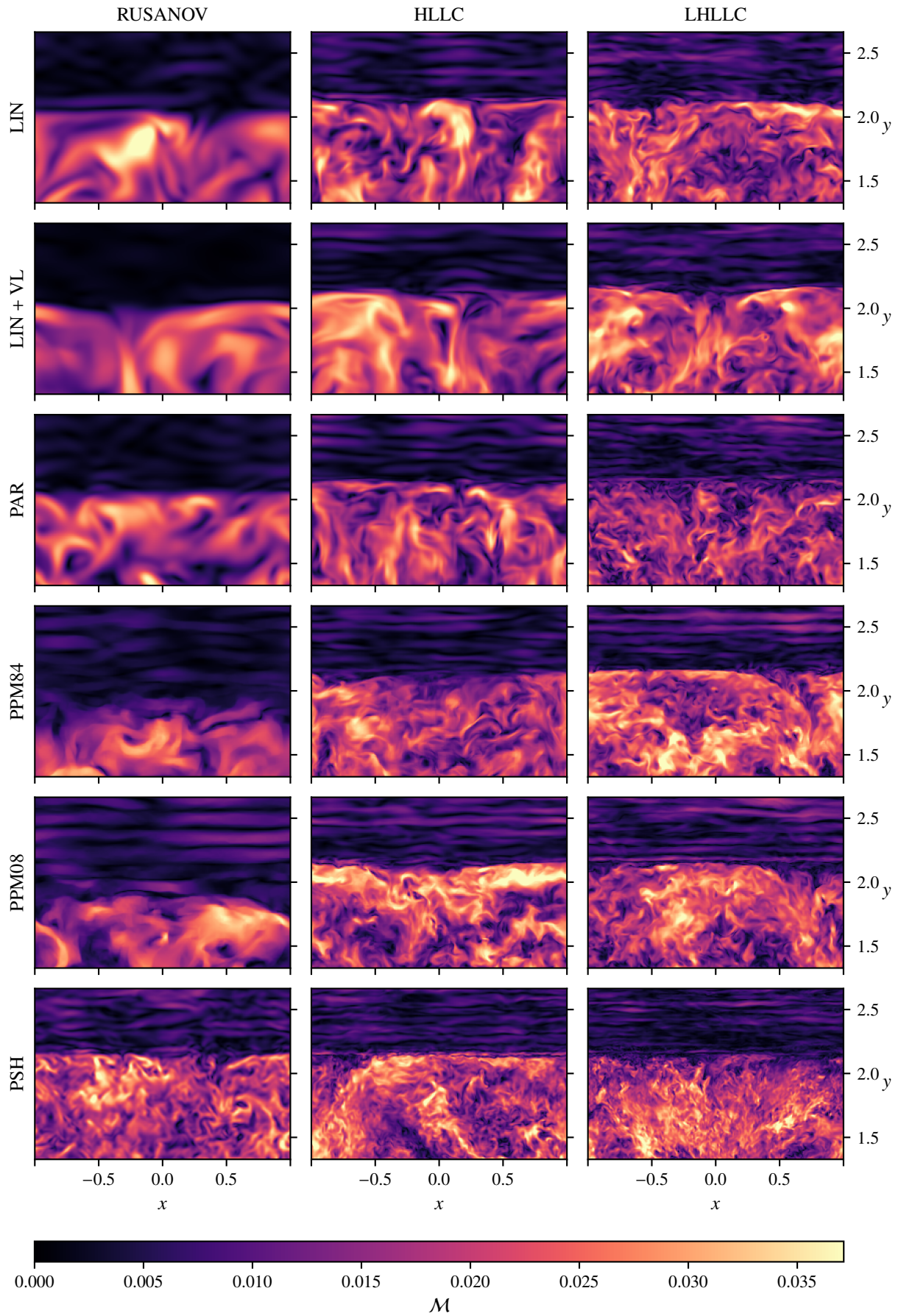


**Fig. 9.** Snapshots obtained at the final simulation time ( $t = 32\tau_{\text{conv}}$ ) showing the distribution of the Mach number at  $z = 0$  in the simulations of turbulent convection and wave propagation in a 3D box. The grid resolution is  $256^3$ . Each panel is cut between  $y = 1.3$  and  $y = 2.7$  for a better visualization of the flows in the proximity of the upper convective boundary.

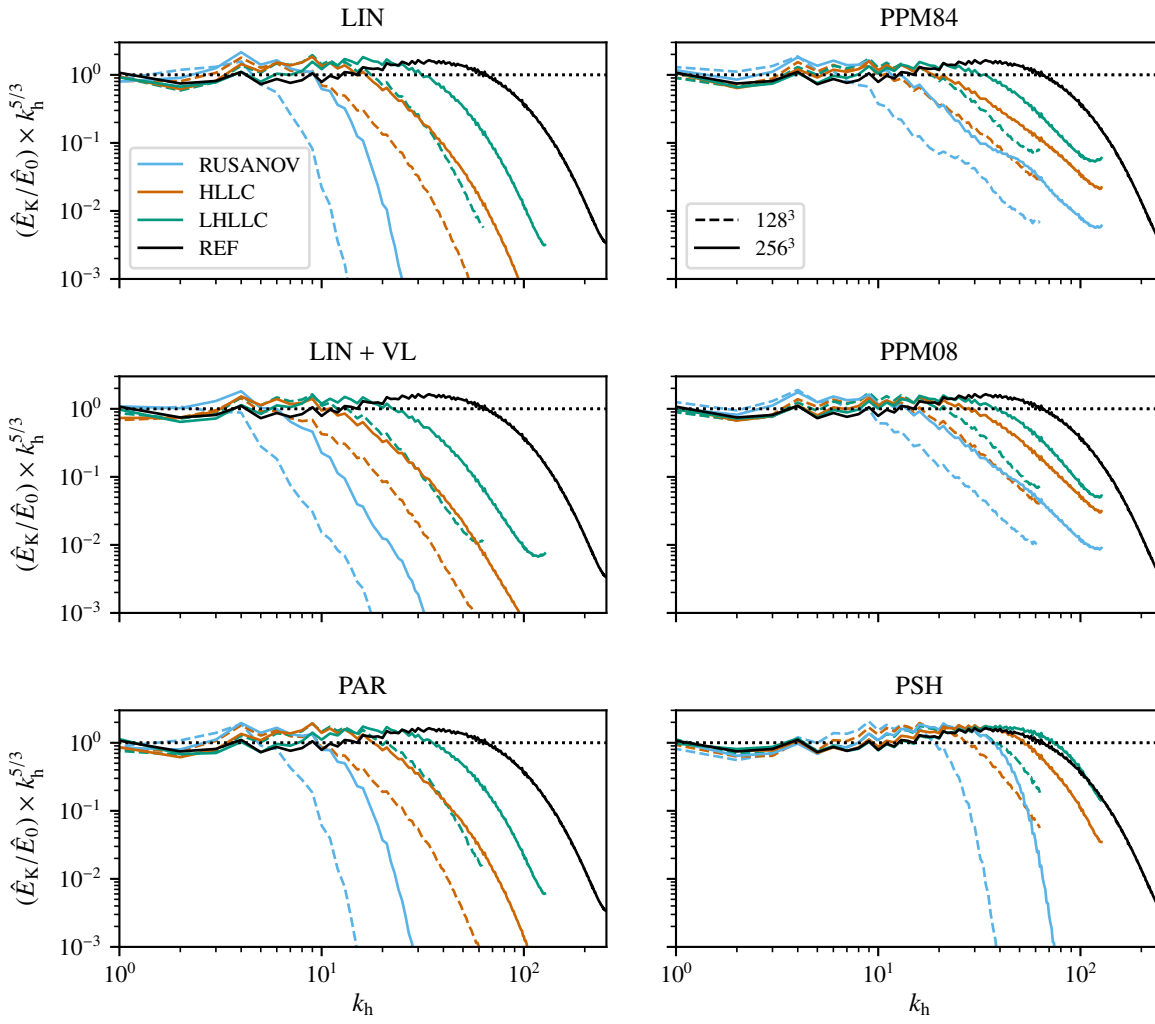


**Fig. 10.** Kinetic energy spectra computed on the horizontal plane  $y = 1.5$  of the convective layer for all of our 18 combinations of Riemann solvers and spatial reconstruction schemes in the problem of turbulent convection and wave excitation. The spectra have been averaged over the time interval  $t \in (10\tau_{\text{conv}}, 32\tau_{\text{conv}})$  and rescaled by the Kolmogorov law ( $k_h^{-5/3}$ ) and by the value  $\hat{E}_0$  of the spectral energy density of the reference run at  $k_h = 15$ .



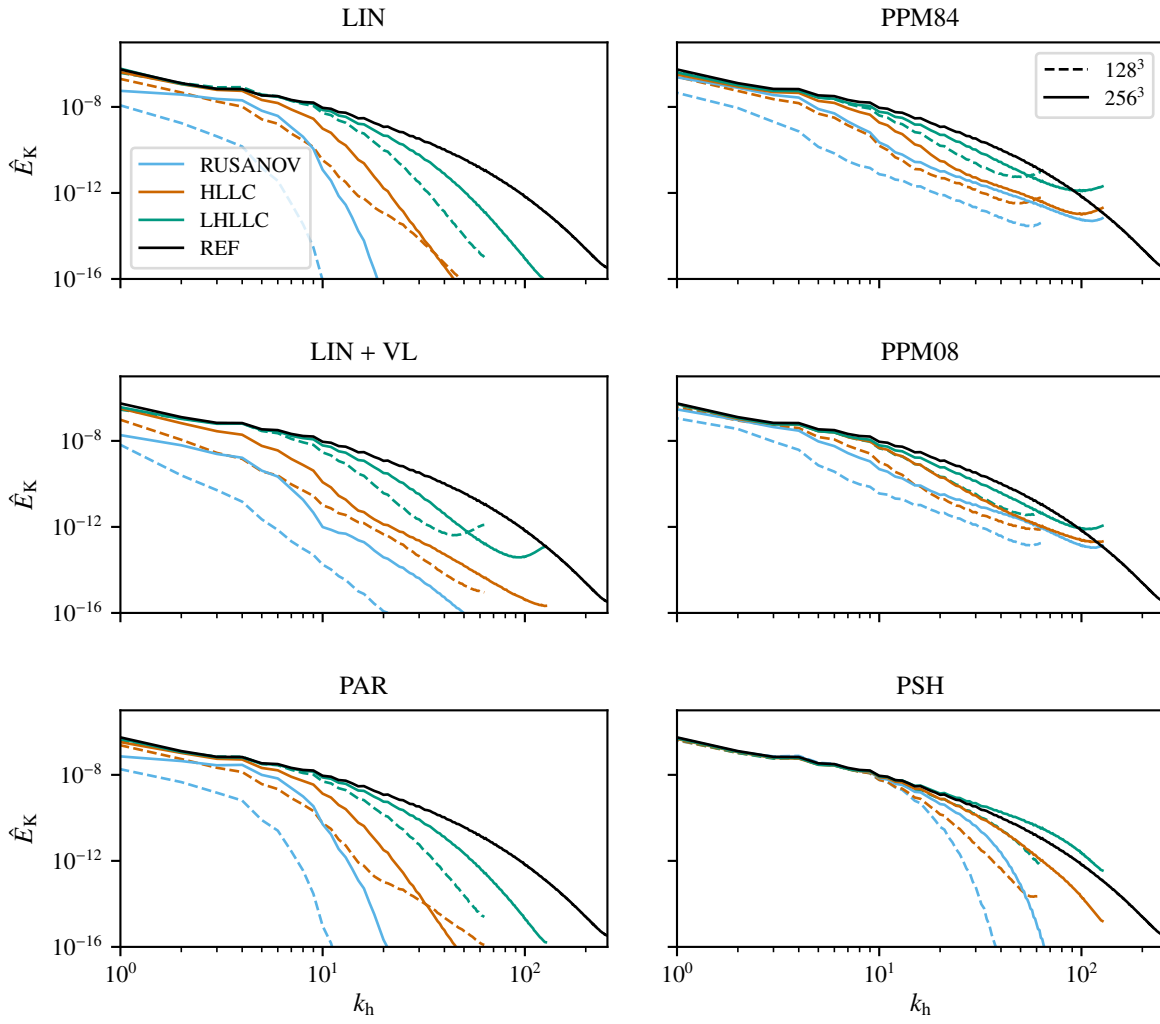


**Fig. 11.** Kinetic energy spectra computed on the horizontal plane  $y = 2.5$  of the stable layer for all of our 18 combinations of Riemann solvers and spatial reconstruction schemes in the problem of turbulent convection and wave excitation. The spectra have been averaged over the time interval  $t \in (10\tau_{\text{conv}}, 32\tau_{\text{conv}})$ . The black solid line represents the reference run (REF), which is computed using the LHLLC Riemann solver and the PAR reconstruction scheme on a  $512^3$  grid.

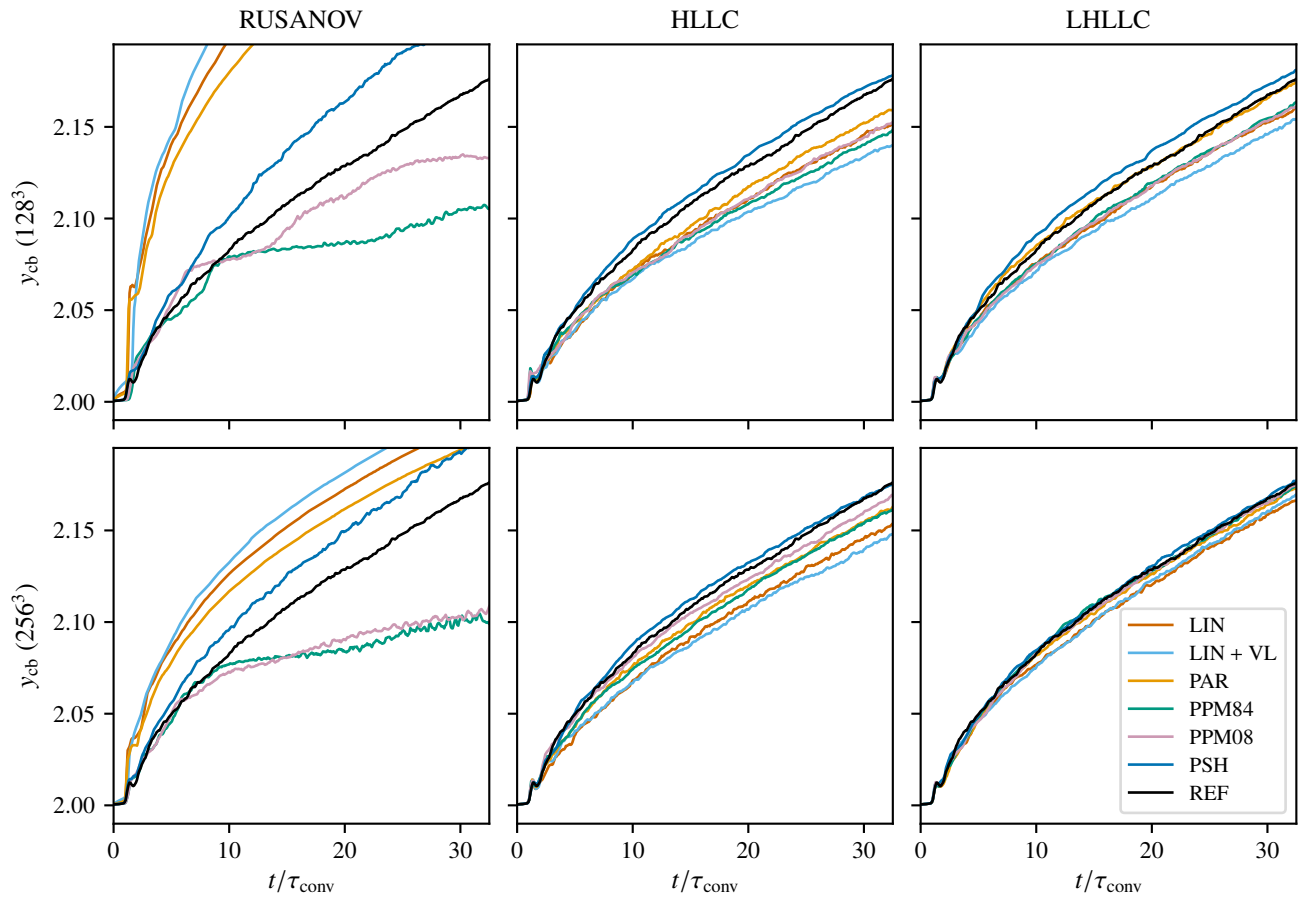


**Fig. 12.** Time evolution of the position of the upper convective boundary ( $y_{cb}$ ) in the problem of turbulent convection and entrainment described in Sect. 3.2. The top and bottom rows show results from  $128^3$  and  $256^3$  simulations, respectively. The black solid line represents the reference run (REF).

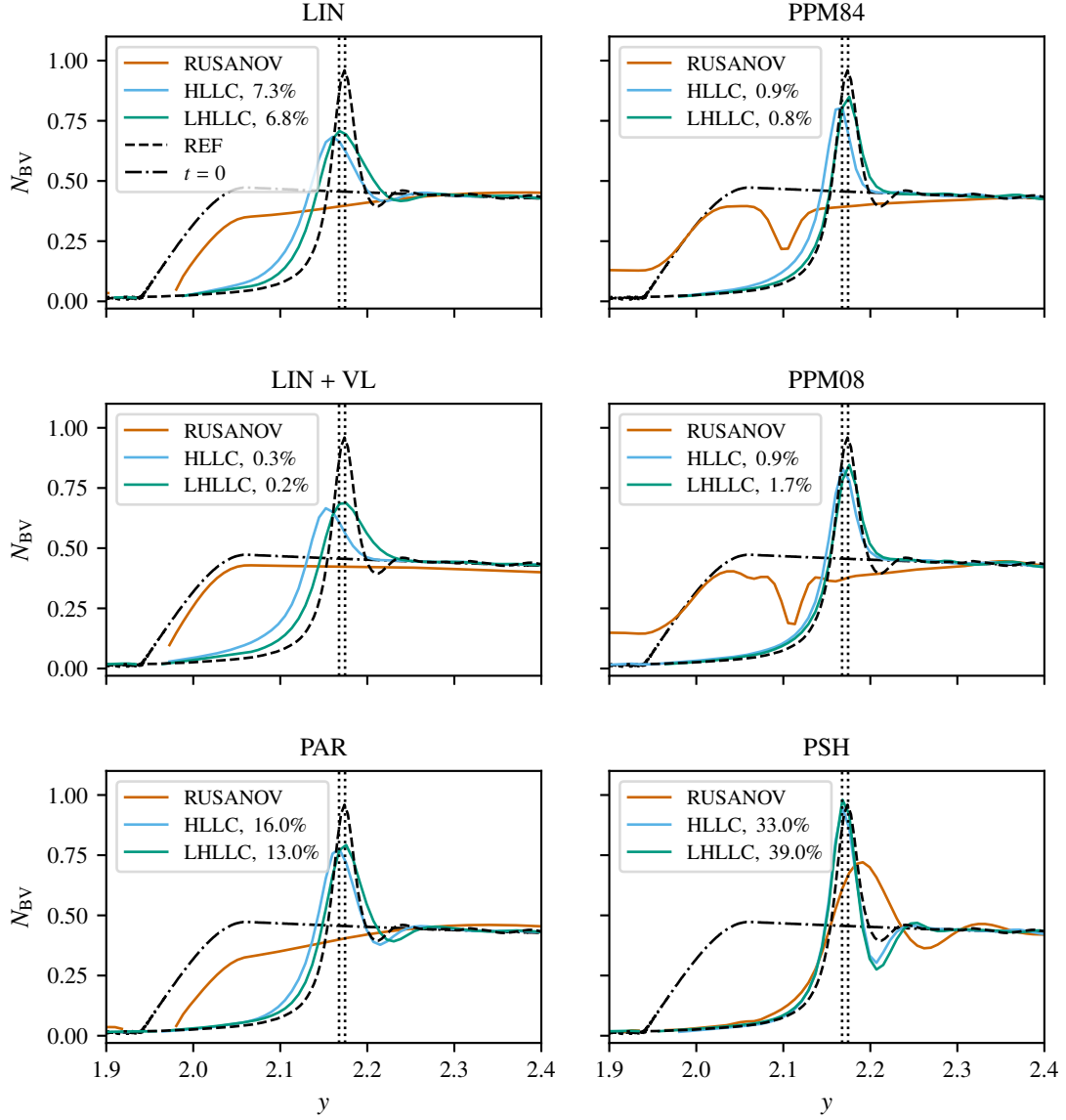


**Fig. 13.** Vertical profiles of the Brunt-Väisälä frequency ( $N_{BV}$ ) averaged over the time interval  $t \in (30\tau_{\text{conv}}, 32\tau_{\text{conv}})$  in the problem of turbulent convection and wave excitation. Each panel shows the results of simulations run using the same reconstruction scheme but different Riemann solvers. Here, we only show results from the  $256^3$  grid to avoid cluttering the figures. The reference run (REF) is represented by a black dashed line. The black dash-dotted line is the profile of the Brunt-Väisälä frequency at  $t = 0$ , and the vertical black dotted lines represent the position of the convective boundary at the beginning and the end of the chosen averaging time interval in the reference run,  $y = 2.168$  and  $y = 2.174$ , respectively. The percentages shown in the insets for simulations run with the HLLC and LHLLC solvers represent the amplitude of the largest undershoot in  $N_{BV}$  relative to  $N_{BV,t=0}$ , in the spatial range  $y \in (2.15, 2.40)$ . The amplitude of the largest undershoot in the reference run is 12%.

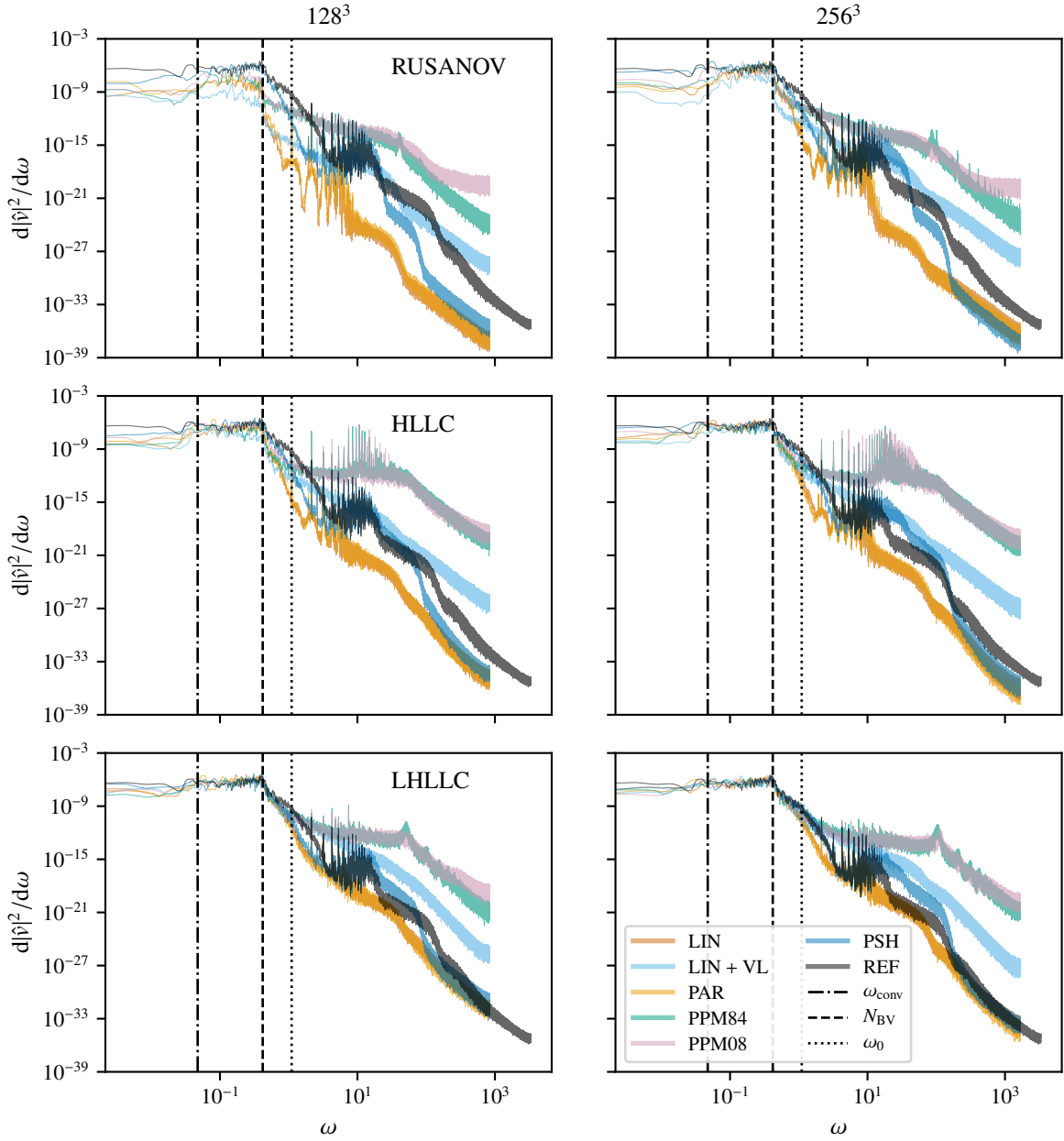


**Fig. 14.** Frequency power spectrum of the vertical velocity component  $v$  extracted in the middle of the stable layer at  $(x, y, z) = (-0.2, 2.5, -0.2)$  over the time series  $t \in (10\tau_{\text{conv}}, 32\tau_{\text{conv}})$  in the problem of turbulent convection and wave excitation. The left and right panels show results obtained on the  $128^3$  and the  $256^3$  grid, respectively. Each row of panels shows the results of simulations run using 6 reconstruction schemes with the same Riemann solver. The reference solution (indicated with REF) is the black curve. The convective turnover frequency ( $\omega_{\text{conv}} = 2\pi/\tau_{\text{conv}}$ ), the Brunt-Väisälä frequency at  $(x, y, z) = (-0.2, 2.5, -0.2)$  ( $N_{\text{BV}}$ ), and the frequency of the fundamental oscillation mode of the cavity ( $\omega_0 = 1.1$ ) are represented by the black dashed-dotted, dashed, and dotted lines, respectively.

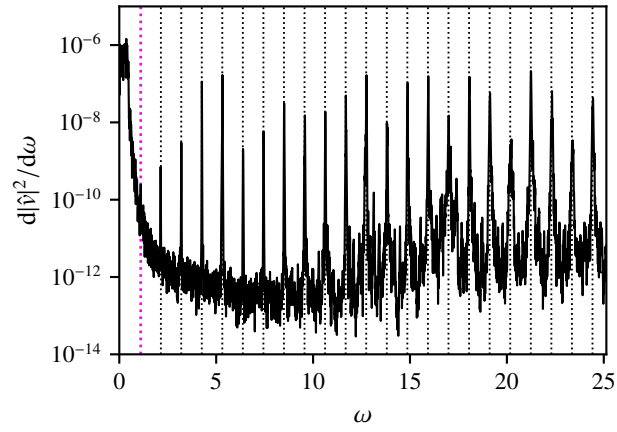


**Fig. 15.** Frequency power spectrum of  $v$  as in Fig. 14 but showing only the results of PPM08 + HLLC on the  $256^3$  grid. The vertical black dotted lines represent the resonant modes of the cavity which we derived from the theory of linear oscillations in Cowling approximation (see, e.g., Aerts 2021). The pink line at  $\omega = 1.1$  is the frequency of the fundamental oscillation mode of the cavity.

## Appendix A: The PPH and PQH methods

The idea of applying limiters to passive scalars (or mass fractions) only, which lead us to formulating the PSH method (Sect. 2.3.6), can be applied at any order of accuracy. In this section, we provide two methods that can be seen as lower-order alternatives to PSH. Their potential advantages include a lower amplitude of overshoots in dynamic quantities and the need for fewer ghost cells.

We start with the unlimited parabolic method PAR (Sect. 2.3.3) and apply a two-step limiter to passive scalars. The first step is defined by the variable replacements

$$a_{i-1/2,L/R} \mapsto \text{median}(a_{i-1}, a_{i-1/2,L/R}, a_i). \quad (\text{A.1})$$

These replacements are followed by the application of the PPM84 limiter defined by Eq. (31). We call the resulting method piecewise parabolic hybrid (PPH). The PPH method is exact wherever  $a(\zeta)$  is locally parabolic, 3<sup>rd</sup>-order accurate for general but smooth functions  $a(\zeta)$ , and it requires two ghost cells at domain boundaries.

A more accurate method, which we call piecewise quartic hybrid (PQH), can be obtained by assuming that within cell  $i$   $a(\zeta)$  can be described by the quartic polynomial

$$a(\zeta) = \sum_{n=0}^4 c_n (\zeta - \zeta_i)^n. \quad (\text{A.2})$$

The five coefficients  $c_n$  are uniquely determined by the requirement that the averages of  $a(\zeta)$  in cells  $i - 2 + n$  equal  $\bar{a}_{i-2+n}$  for  $n = 0, 1, \dots, 4$ . The reconstructed states are then obtained by evaluating Eq. (A.2) at  $\zeta_{i-1/2}$  and  $\zeta_{i+1/2}$ , respectively. The resulting expressions are

$$a_{i-1/2,R} = \frac{1}{60} \left( -3\bar{a}_{i-2} + 27\bar{a}_{i-1} + 47\bar{a}_i - 13\bar{a}_{i+1} + 2\bar{a}_{i+2} \right), \quad (\text{A.3})$$

$$a_{i+1/2,L} = \frac{1}{60} \left( 2\bar{a}_{i-2} - 13\bar{a}_{i-1} + 47\bar{a}_i + 27\bar{a}_{i+1} - 3\bar{a}_{i+2} \right). \quad (\text{A.4})$$

The limiter we apply to passive scalars in the PQH method is the same as that in the PPH method, see above. The PQH method is exact wherever  $a(\zeta)$  is locally a quartic polynomial, 5<sup>th</sup>-order accurate for general but smooth functions  $a(\zeta)$ , and it requires three ghost cells at domain boundaries.

We have only performed a small number of tests with these two methods. Specifically, we ran simulations of the Kelvin-Helmholtz problem (Sect. 3.1) with the initial Mach number of  $\mathcal{M}_0 = 10^{-3}$  and the HLLC flux function on grids of  $64 \times 32$  and  $128 \times 64$  cells. There were no overshoots in the passive tracer in the results of these tests.

## Appendix B: 1D test cases

We use two simple 1D experiments – linear advection and the propagation of a linear sound wave – to compare the accuracy that the six reconstruction schemes can reach if not constrained by the 2<sup>nd</sup>-order accuracy limit imposed by our multidimensional scheme.

### B.1. Linear advection

The initial conditions in this experiment correspond to a right-going contact wave:

$$\rho(x) = \gamma [1 + 0.01 \sin(2\pi x)], \quad (\text{B.1})$$

$$u(x) = 0.1, \quad (\text{B.2})$$

$$p(x) = 1. \quad (\text{B.3})$$

We consider the interval  $0 \leq x \leq 1$  with periodic boundary conditions and the equation of state of an ideal gas with the ratio of specific heats  $\gamma = 1.4$ . The average speed of sound is unity and it varies by 0.5% due to the density variation. The solution is sought at  $t = 10$ , when the sinusoid has been advected by one period and the analytic solution becomes identical to the initial condition. This makes the quantification of numerical errors trivial.

We use the same code for this experiment as we do for all the other experiments reported in this work. Since some of the schemes tested exceed 2<sup>nd</sup> order of accuracy, cell averages cannot be approximated by sampling the initial condition at cell centres. We initialise the discrete density profile using the formula

$$\rho_i = \gamma \left[ 1 + 0.01 \frac{\sin(\pi \Delta x)}{\pi \Delta x} \sin(2\pi x_i) \right], \quad (\text{B.4})$$

where  $\Delta x$  is the constant grid spacing and  $x_i$  the location of  $i$ -th cell's centre. This formula is easily obtained by analytically averaging Eq. (B.1) in the interval  $x_i - \Delta x/2 \leq x \leq x_i + \Delta x/2$ . We suppress time-stepping errors by using the RK3 scheme with CFL = 0.01. Because the Mach number of the flow is 0.1, this means that the wave is advected by only  $10^{-3} \Delta x$  during every 3<sup>rd</sup>-order-accurate time step. We use the LHLLC flux function for this experiment.

The  $L^1$  errors we obtain on grids with different numbers of cells  $N_x$  are shown in Fig. B.1. We test the LIN, LIN+VL, PAR, and PPM84 schemes on grids with 8 to 512 cells. We are forced to stop at grids of 64 cells for the most accurate schemes PPM08 and PSH, because the errors rapidly become dominated by the finite precision of floating-point arithmetic. The asymptotic orders of accuracy based on  $L^1$  errors measured on the three finest grids available are reported in Table 1. Both LIN and LIN+VL reach the expected 2<sup>nd</sup> order of accuracy. The absolute errors produced by LIN+VL are somewhat larger as compared with LIN because of the presence of the van Leer limiter. The PPM84 scheme is formally 4<sup>th</sup>-order accurate but that only holds for monotonic solutions. PPM84 contains a limiter that flattens the slope at local extrema and that reduces the scheme's asymptotic order to 2.3 in this test case. We have experimentally turned off both limiters present in PPM84, which increased the asymptotic order of accuracy to 4.0, as expected. The PAR, PPM08, and PSH methods reach the asymptotic orders of 3.0, 6.0, and 7.0, also matching theoretical expectations.

### B.2. Sound wave

The initial conditions in this experiment correspond to a right-going sound wave:

$$\rho(x) = \rho_0 [1 + \gamma^{-1} \Psi(x)], \quad (\text{B.5})$$

$$u(x) = \gamma^{-1} c_0 \Psi(x), \quad (\text{B.6})$$

$$p(x) = p_0 [1 + \Psi(x)], \quad (\text{B.7})$$

where

$$\Psi(x) = \Psi_0 \sin(2\pi x). \quad (\text{B.8})$$



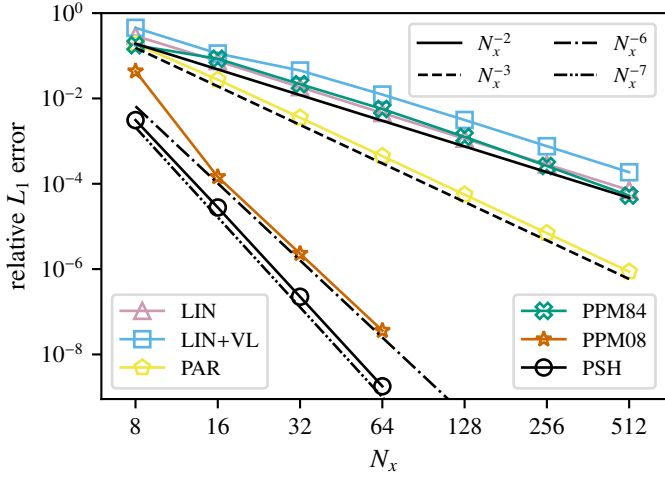


**Fig. B.1.** Relative  $L_1$  errors obtained by advecting a sinusoid by one period on 1D grids with  $N_x$  cells using different reconstruction schemes. A few scaling relations are shown to guide the eye.

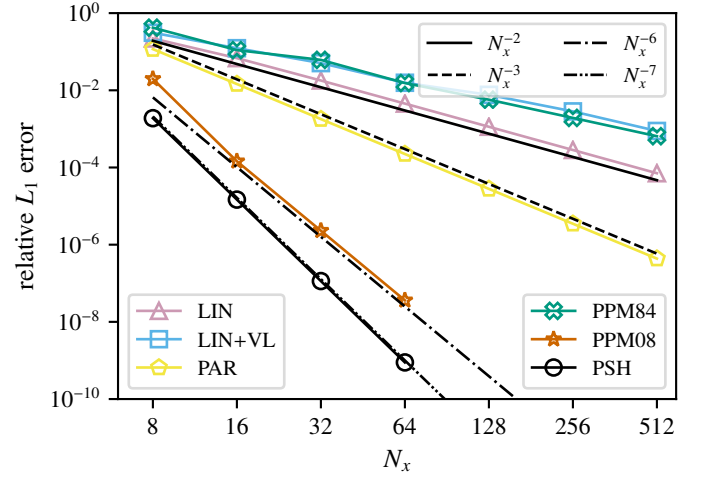


**Fig. B.2.** Relative  $L_1$  errors in velocity  $u$  obtained by propagating a sinusoidal sound wave by one period on 1D grids with  $N_x$  cells using different reconstruction schemes. A few scaling relations are shown to guide the eye.

We use  $\rho_0 = \gamma$ ,  $p_0 = 1$  and the equation of state of an ideal gas with the ratio of specific heats  $\gamma = 1.4$ , so that the unperturbed speed of sound is  $c_0 = 1$ . We set the amplitude  $\Psi_0 = 10^{-10}$  to suppress non-linear effects. This allows us to avoid accuracy constraints imposed by our 2<sup>nd</sup>-order-accurate transformations between primitive and conserved variables. Round-off errors are suppressed by using 128-bit floating point numbers. In a way analogous to Eq. (B.4), we initialise the discrete wave such that the cell average of  $\Psi(x)$  in cell  $i$  is<sup>19</sup>

$$\Psi_i = \frac{\sin(\pi\Delta x)}{\pi\Delta x} \Psi(x_i). \quad (\text{B.9})$$

The simulations are stopped at  $t = 1$ , when the sound wave has propagated by a single wavelength around the periodic domain  $0 \leq x \leq 1$ . Neglecting non-linear effects, which are of order  $\Psi_0^2 = 10^{-20}$ , the evolved solution is expected to be identical to the initial condition. Timestepping errors are suppressed by using the RK3 scheme with CFL = 0.001, i.e. the wave moves by only  $10^{-3}\Delta x$  per time step. We use the LHLLC flux function for this experiment.

We show  $L^1$  errors in the velocity  $u$  on grids with 8 to 512 cells in Fig. B.2. The simulation series with the most accurate PPM08 and PSH schemes are stopped at grids of 64 cells, because the absolute errors rapidly approach  $10^{-20}$ , i.e. the magnitude of the residual non-linear effects. The asymptotic orders of accuracy, as defined by the  $L^1$  errors measured on the three finest grids available, are 2.0, 3.0, 6.0, and 7.0 for the LIN, PAR, PPM08, and PSH methods, respectively, matching theoretical expectations. The LIN+VL and PPM84 methods only reach the order of 1.6, which seems to be caused by the combination of the low-Mach flux function LHLLC with the limiters contained in these two methods. We have checked that both methods reach the order of 2.0 with the RUSANOV and HLLC flux functions (PPM84 flattens the slope at local extrema, which reduces its order, see also Sect. B.1).

The  $L^1$  errors discussed so far do not distinguish between amplitude and phase errors. We quantify amplitude errors by computing the relative loss of the total kinetic energy from  $t = 0$

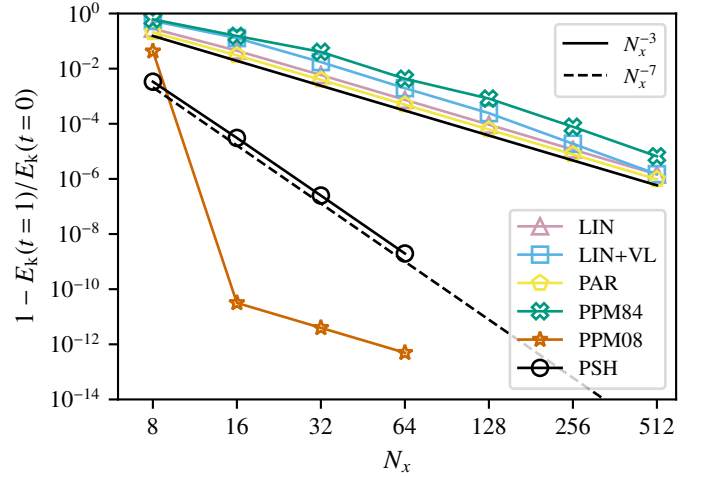


**Fig. B.3.** Relative decrease in kinetic energy after propagating a sinusoidal sound wave by one period on 1D grids with  $N_x$  cells using different reconstruction schemes. Two scaling relations are shown to guide the eye.

to  $t = 1$ , see Fig. B.3. Some kinetic energy is lost in all of the simulations, which is a sign of stability. The amount of energy dissipated decreases with the 3<sup>rd</sup> power of the grid spacing for LIN, LIN+VL, PAR, and PPM84. It is not immediately clear why this is the case given that the methods have different orders of accuracy, but we did not investigate this further. In case of PSH, the dissipation rate decreases with the 7<sup>th</sup> power of the grid spacing, matching the method's order of accuracy. PPM08 is a special case – the method preserves extrema and sinusoids resolved by 16 or more cells per wavelength turn out to be smooth enough not to trigger any of the method's limiters. PPM08 reduces to a simple interpolation function in this special case, eliminating jumps at all cell interfaces, see Sect. 2.3.5. This, in turn, eliminates all explicit dissipative terms in the flux function. The dissipation rate drops by many orders of magnitude and timestepping errors start to dominate.

<sup>19</sup> We do not average the  $\Psi^2$  term, which would appear in the product  $\rho u$ , because the term is only  $\approx 10^{-20}$  with  $\Psi_0 = 10^{-10}$ . This term must be kept small or other non-linear effects would also cease to be negligible in the range of relative  $L_1$  errors we explore.

### Appendix C: Sound wave generation with a compact third order WENO scheme

The results presented in Sects. 3.1 and 3.2 reveal that nonlinear, switching reconstruction schemes (such as LIN+VL, PPM84, and PPM08) generate excess acoustic power which is not present in simulations run with unlimited (linear) reconstruction methods. The question naturally arises whether nonlinear but non-switching schemes (e.g., WENO) also generate artificial sound waves in simulations of low-Mach-number flows. In this Appendix we try to answer this question using the compact third order (CTO) WENO scheme of Kolb (2014). This scheme reconstructs the quantity  $a$  within the cell  $i$  using a weighted sum of three polynomials,  $a_{L,R,C}(\zeta)$ . The ultimate expression for the underlying function  $a(\zeta)$  reads

$$a(\zeta) = w_L a_L(\zeta) + w_C a_C(\zeta) + w_R a_R(\zeta). \quad (\text{C.1})$$

The weighting coefficients are computed as

$$w_m = \frac{\alpha_m}{\sum_{k \in \{L,C,R\}} \alpha_k}, \quad (\text{C.2})$$

where

$$\alpha_m = \frac{c_m}{(\epsilon_{\text{WENO}} + \text{IS}_m)^p}, \quad (\text{C.3})$$

$m \in \{L, C, R\}$ ,  $c_L = c_R = 0.25$ ,  $c_C = 0.5$ , and  $\text{IS}_m$  are the smoothness indicators of the scheme<sup>20</sup>,

$$\text{IS}_L = (\bar{a}_i - \bar{a}_{i-1})^2, \quad (\text{C.4})$$

$$\text{IS}_R = (\bar{a}_{i+1} - \bar{a}_i)^2, \quad (\text{C.5})$$

$$\text{IS}_C = \frac{13}{12c_C^2} (\bar{a}_{i+1} - 2\bar{a}_i + \bar{a}_{i-1})^2 + \frac{1}{4} (\bar{a}_{i+1} - \bar{a}_{i-1})^2. \quad (\text{C.6})$$

In Eq. (C.3), we set  $p = 2$ . The functions  $a(\zeta)_{L,R}$  are one-sided linear reconstructions

$$a_L(\zeta) = \bar{a}_i + (\bar{a}_i - \bar{a}_{i-1})(\zeta - \zeta_i), \quad (\text{C.7})$$

$$a_R(\zeta) = \bar{a}_i + (\bar{a}_{i+1} - \bar{a}_i)(\zeta - \zeta_i), \quad (\text{C.8})$$

whereas  $a_C(\zeta)$  is defined such that

$$a_{\text{opt}}(\zeta) = c_L a_L(\zeta) + c_C a_C(\zeta) + c_R a_R(\zeta) \quad (\text{C.9})$$

is the unique parabola that conserves the cell volume averages  $\bar{a}_{i-1}$ ,  $\bar{a}_i$ , and  $\bar{a}_{i+1}$  over cells  $i-1$ ,  $i$ , and  $i+1$ , respectively. This constraint implies

$$a_{\text{opt}}(\zeta) = a_i + \left. \frac{\partial a}{\partial \zeta} \right|_{\zeta_i} (\zeta - \zeta_i) + \left. \frac{1}{2} \frac{\partial^2 a}{\partial \zeta^2} \right|_{\zeta_i} (\zeta - \zeta_i)^2, \quad (\text{C.10})$$

with

$$a_i = \bar{a}_i - \frac{1}{24} (\bar{a}_{i+1} - 2\bar{a}_i + \bar{a}_{i-1}), \quad (\text{C.11})$$

$$\left. \frac{\partial a}{\partial \zeta} \right|_{\zeta_i} = \frac{\bar{a}_{i+1} - \bar{a}_{i-1}}{2}, \quad (\text{C.12})$$

$$\left. \frac{\partial^2 a}{\partial \zeta^2} \right|_{\zeta_i} = \bar{a}_{i+1} - 2\bar{a}_i + \bar{a}_{i-1}. \quad (\text{C.13})$$

The smoothness indicators  $\text{IS}_{L,R,C}$  are such that the smoothest among the polynomials  $a(\zeta)_{L,R,C}$  has the largest weight in

Eq. (C.1). This feature allows CTO-WENO to achieve third-order spatial accuracy in smooth parts of the flow while at the same time it remains robust near discontinuities. The parameter  $\epsilon_{\text{WENO}}$  that appears in the denominator of  $\alpha_m$  avoids division by zero in the case a smoothness indicator  $\text{IS}_m = 0$ . Thus, the oscillatory behavior of  $a(\zeta)$  is also determined by the value of this parameter. In fact, when  $\epsilon_{\text{WENO}} \gg \text{IS}_{L,R,C}$ , the weighting coefficients become almost equal and the scheme is unlimited even near discontinuities, making it similar to our PAR method. On the other hand, if  $\epsilon_{\text{WENO}} \ll \text{IS}_m$ , the weighting coefficients are only determined by  $\text{IS}_{L,R,C}$  and the scheme becomes close to being TVD near discontinuities or in poorly resolved parts of the flow.

Although CTO-WENO, unlike LIN+VL or the PPM methods, does not involve any conditional statements, the weighting coefficients that occur in  $a(\zeta)$  can still abruptly change from time step to time step if a barely resolved wave or feature in the flow crosses that particular cell. Such a rapid change in the form of the polynomial  $a(\zeta)$  can generate high-frequency perturbations in the state quantities on the grid scale and affect the propagation of sound waves. Therefore, we expect a version of CTO-WENO that uses small values of  $\epsilon_{\text{WENO}}$  to generate artificial acoustic noise, whereas large values of  $\epsilon_{\text{WENO}}$  should generate results closer to our unlimited reconstruction methods.

To test this hypothesis, we run a series of simulations of the setup involving turbulent convective flows and excitation of internal waves described in Sect. 3.2. We fix the grid resolution to  $128^3$  cells and the Riemann solver is LHLLC. We run one simulation for each value of  $\epsilon_{\text{WENO}} \in (10^{-12}, 10^{-10}, 10^{-8}, 10^{-6}, 10^{-4}, 10^2)$ , so that several intermediate cases between the two extreme behaviors of the scheme (close to being TVD and fully oscillatory) are considered. We extract the frequency spectrum of the vertical velocity component from the middle of the stable layer as done for the analysis in Sect. 3.3. The results are shown in Fig. C. As expected, the power stored in sound waves is considerably increased when very small values of  $\epsilon_{\text{WENO}}$  are used. For  $\epsilon_{\text{WENO}} = 10^{-12}$ , the power spectrum obtained using CTO-WENO resembles that produced by LIN+VL. Decreasing the value of  $\epsilon_{\text{WENO}}$  progressively reduces (in a monotonic way) the energy of the sound waves and eventually the continuum of the power spectrum converges for  $\epsilon_{\text{WENO}} \gtrsim 10^{-4}$ . In the study performed by Kolb (2014), the value of  $\epsilon_{\text{WENO}}$  that achieves the optimal order of accuracy lies within the range<sup>21</sup>  $\Delta x^3 \lesssim \epsilon_{\text{WENO}} \lesssim \Delta x^2$ , which, for this setup, corresponds to  $10^{-6} \lesssim \epsilon_{\text{WENO}} \lesssim 10^{-4}$ . However, we note that, in this test, the values of the primitive variables reconstructed at the grid cell interfaces span several orders of magnitude. Therefore, using a unique value of  $\epsilon_{\text{WENO}}$  could potentially result in different oscillatory properties of the scheme depending on which variable is being reconstructed. One way to avoid this problem is to rescale the reconstructed quantity  $a$  such that its mean value across the stencil is close to unity. However, we decide not to investigate this effect on the generation of artificial sound waves further.

### Appendix D: Additional plots for the Kelvin–Helmholtz problem

<sup>20</sup> For a formal derivation of these indicators, see Sect. 2.1 of Kolb (2014).

<sup>21</sup> Here we assume that the reconstructed variable  $a$  is dimensionless.

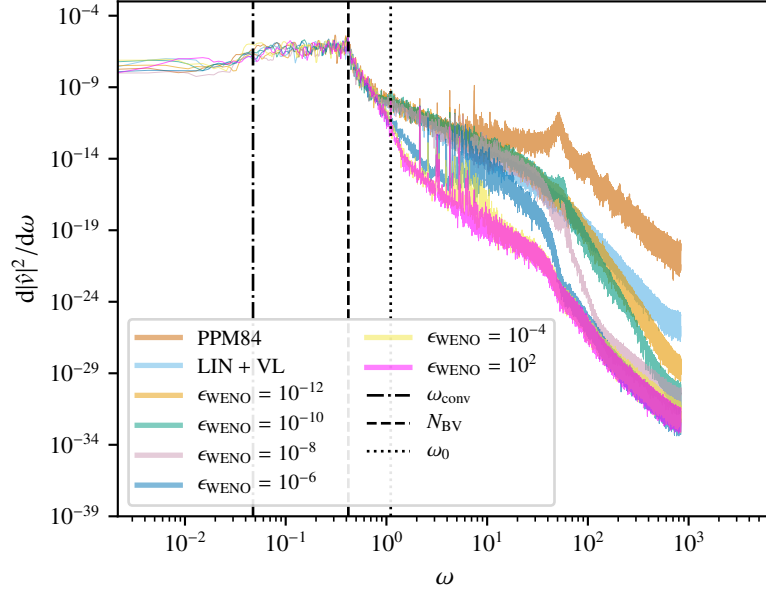


**Fig. C.1.** Frequency power spectrum of the vertical velocity component  $v$  extracted in the middle of the stable layer at  $(x, y, z) = (-0.2, 2.5, -0.2)$  over the time series  $t \in (10\tau_{\text{conv}}, 32\tau_{\text{conv}})$  in the problem of turbulent convection and wave excitation described in Sect. 3.2. These results are obtained on a grid with  $128^3$  cells, using the LLLC Riemann solver and the CTO-WENO scheme of Kolb (2014) for different values of the parameter  $\epsilon_{\text{WENO}}$  occurring in the smoothness indicators of the scheme (see Sect. C), ranging from  $10^{-12}$  to  $10^2$ . As a reference, power spectra obtained with the numerical options LLLC + PPM84 and LLLC + LIN + VL are also shown. The convective turnover frequency ( $\omega_{\text{conv}} = 2\pi/\tau_{\text{conv}}$ ), the Brunt-Väisälä frequency at the location of the point probe ( $N_{\text{BV}}$ ), and the frequency of the fundamental oscillation mode of the cavity ( $\omega_0 = 1.1$ ) are represented by the black dashed-dotted, dashed, and dotted lines, respectively.

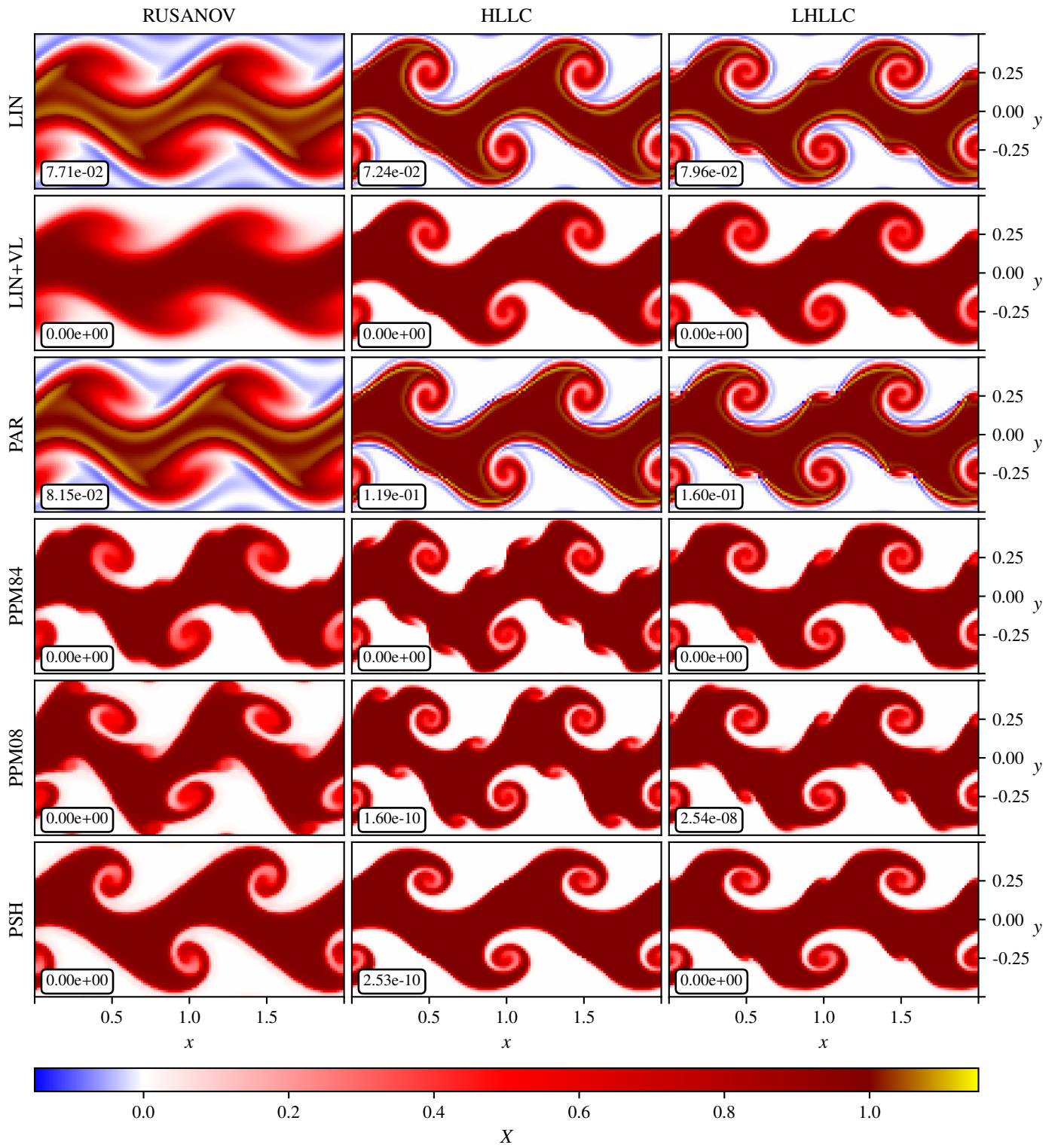


Fig. D.1. As Fig. 4 but with the initial Mach number  $\mathcal{M}_0 = 10^{-1}$ .

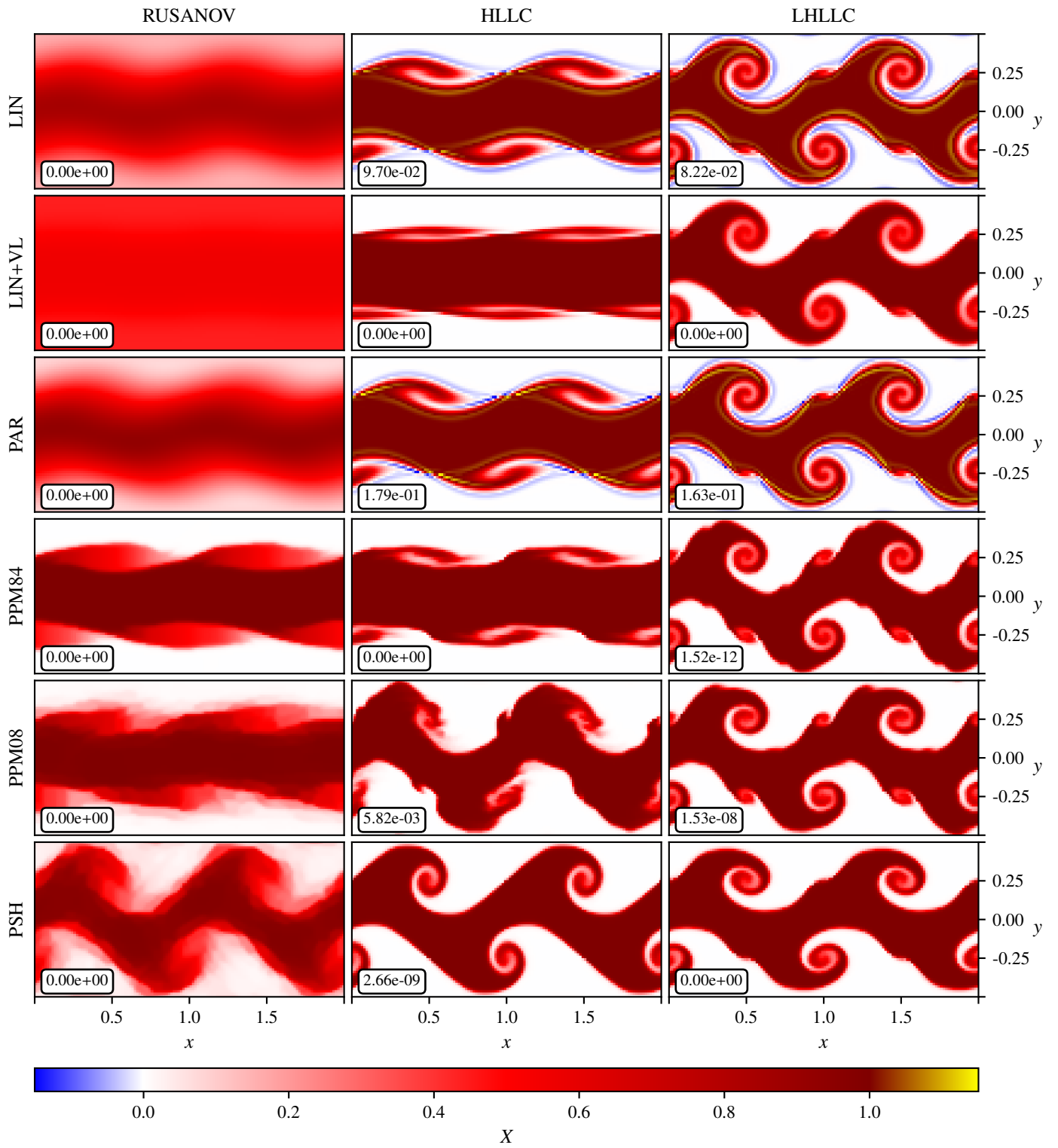
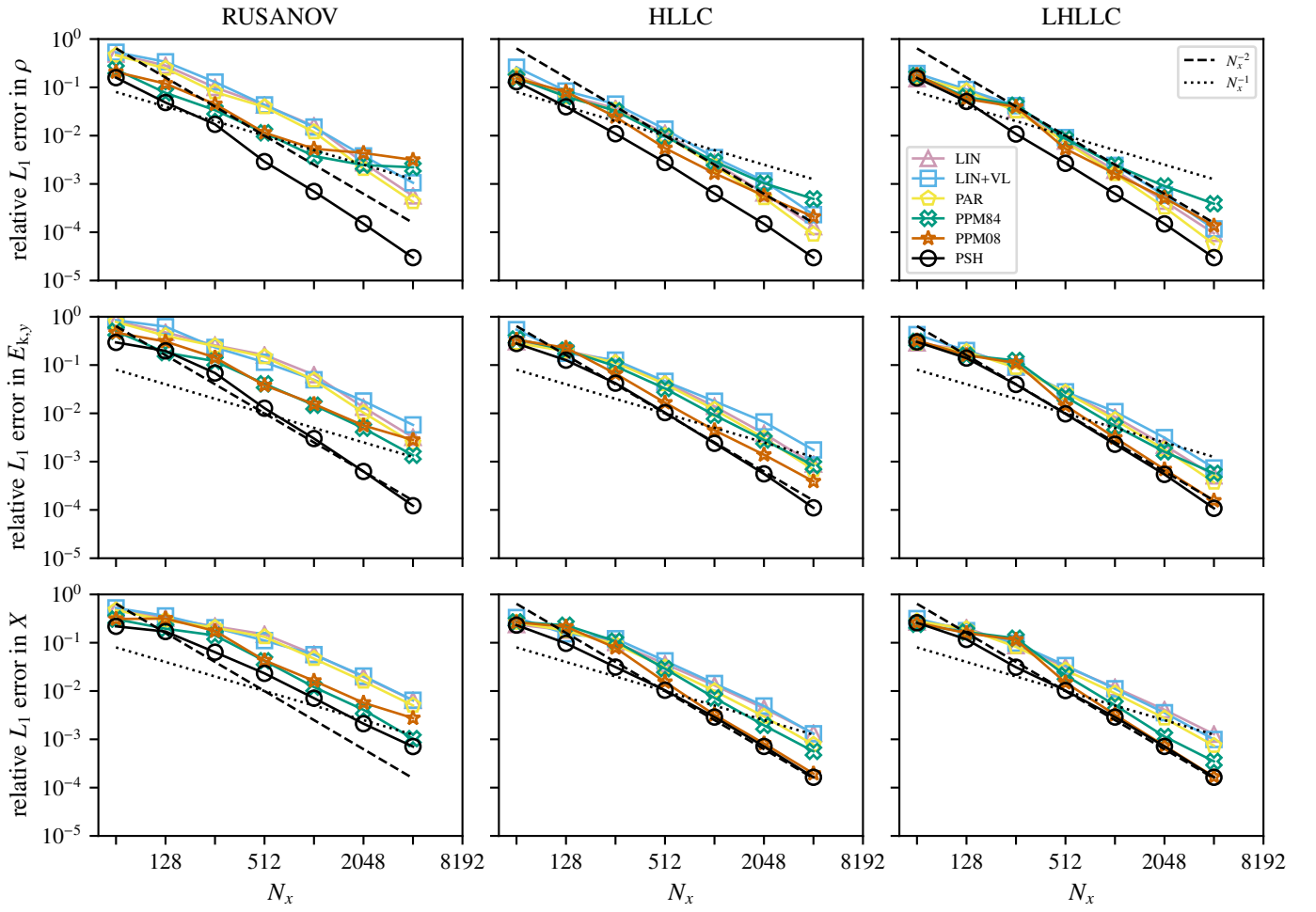
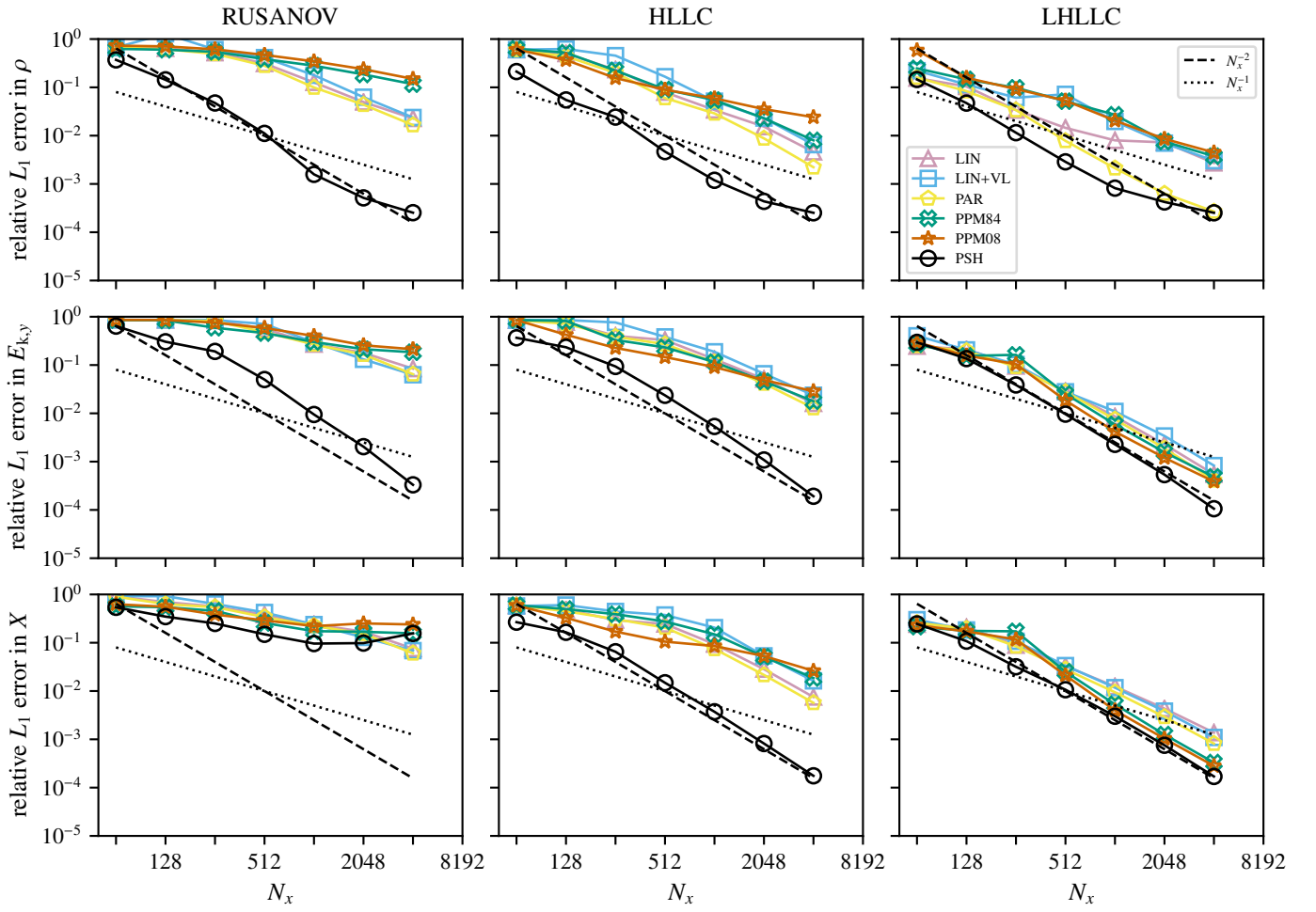


Fig. D.2. As Fig. 4 but with the initial Mach number  $\mathcal{M}_0 = 10^{-3}$ .



**Fig. D.3.** As Fig. 5 but with the initial Mach number  $M_0 = 10^{-1}$ .





**Fig. D.4.** As Fig. 5 but with the initial Mach number  $\mathcal{M}_0 = 10^{-3}$ .

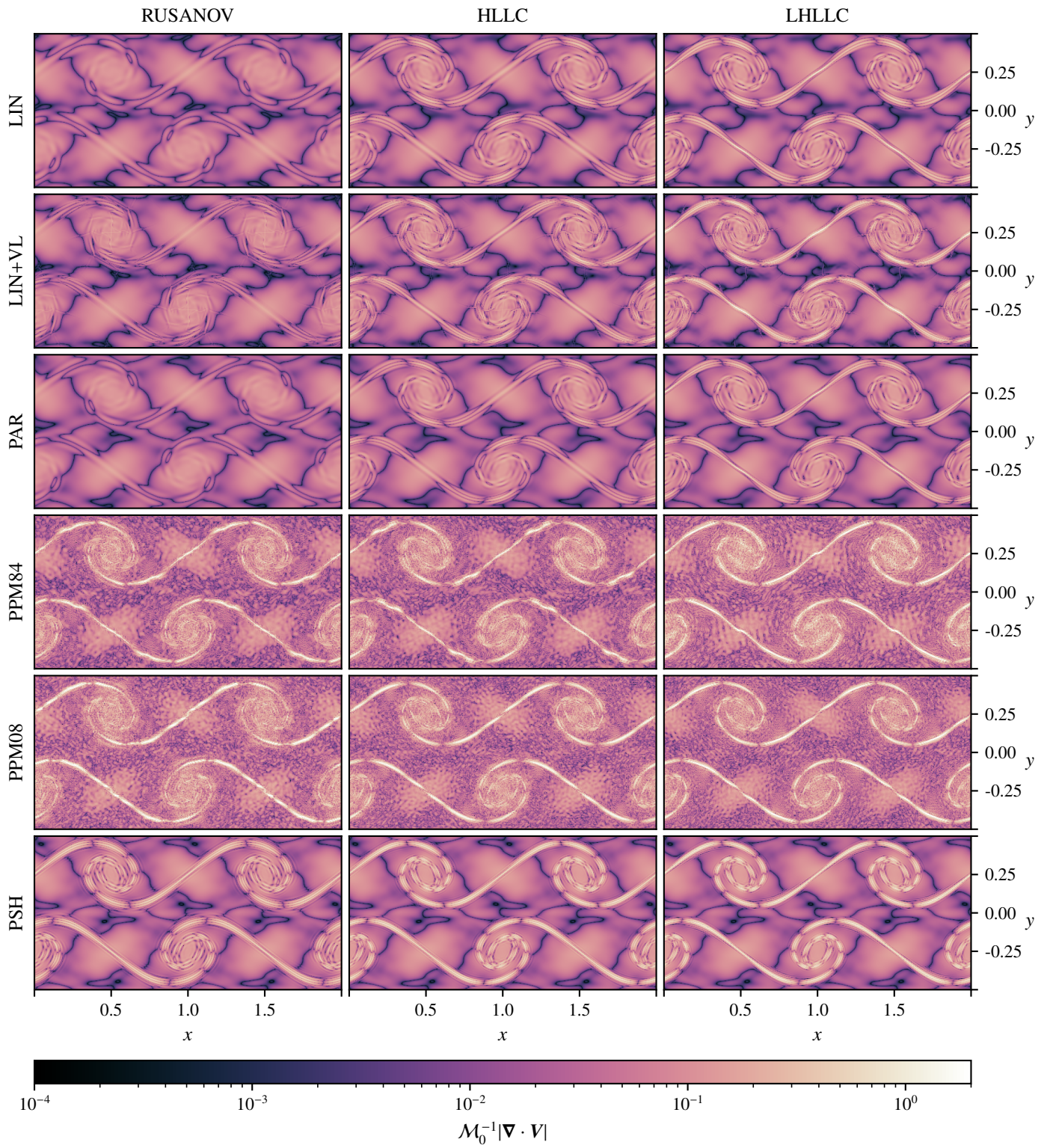


**Fig. D.5.** As Fig. 6 but with the initial Mach number  $\mathcal{M}_0 = 10^{-1}$ .



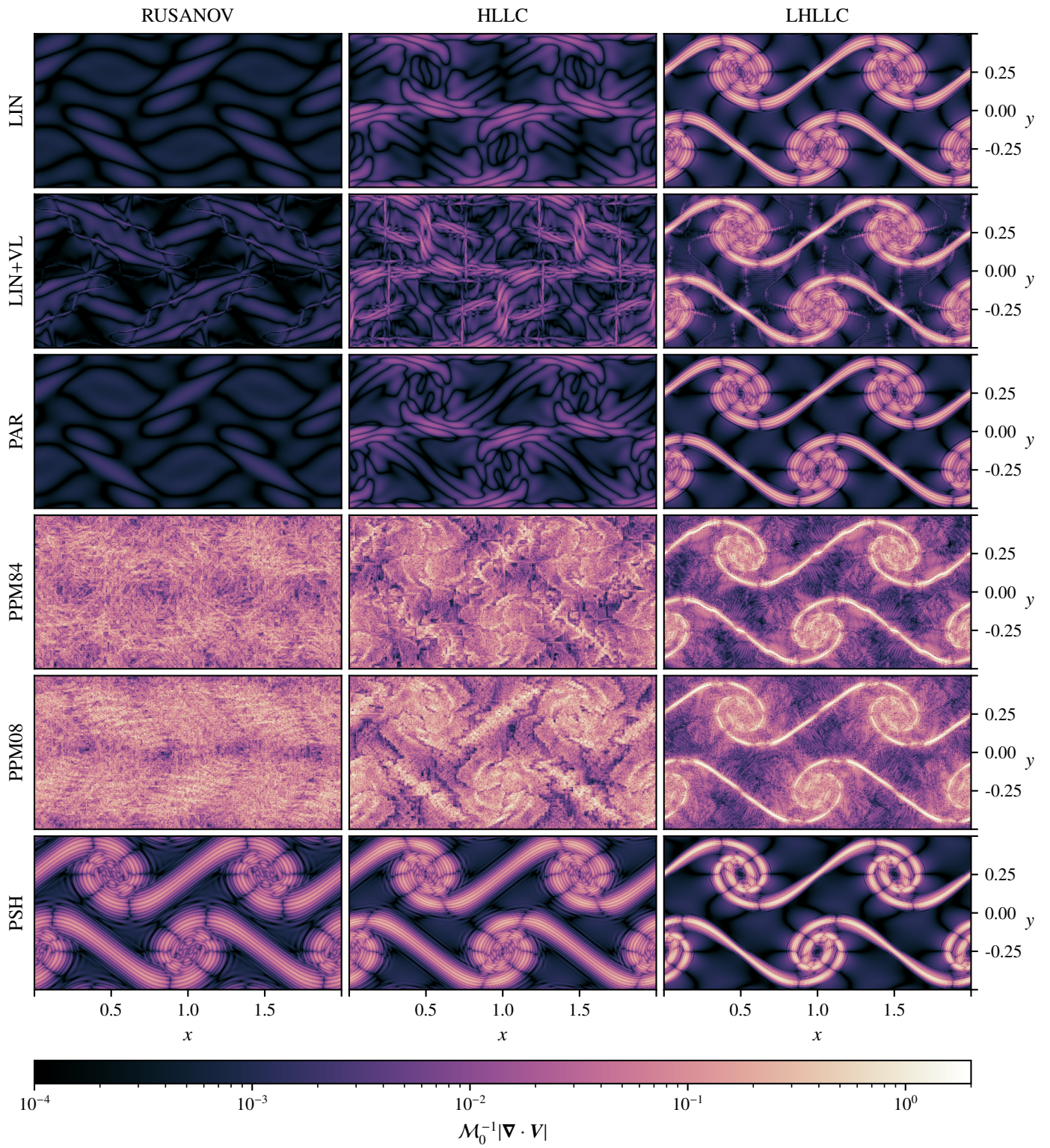


**Fig. D.6.** As Fig. 6 but with the initial Mach number  $\mathcal{M}_0 = 10^{-3}$ .

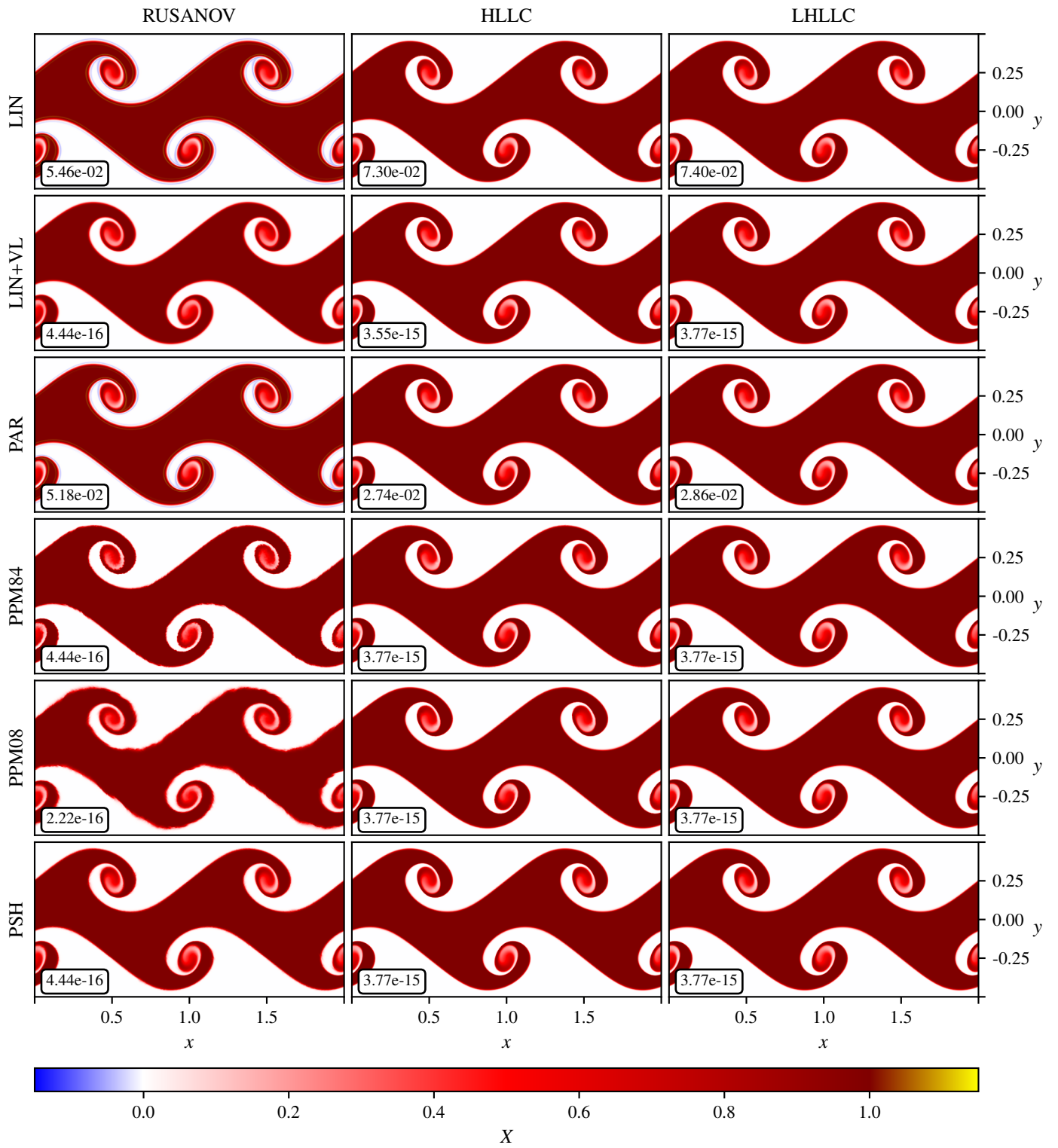
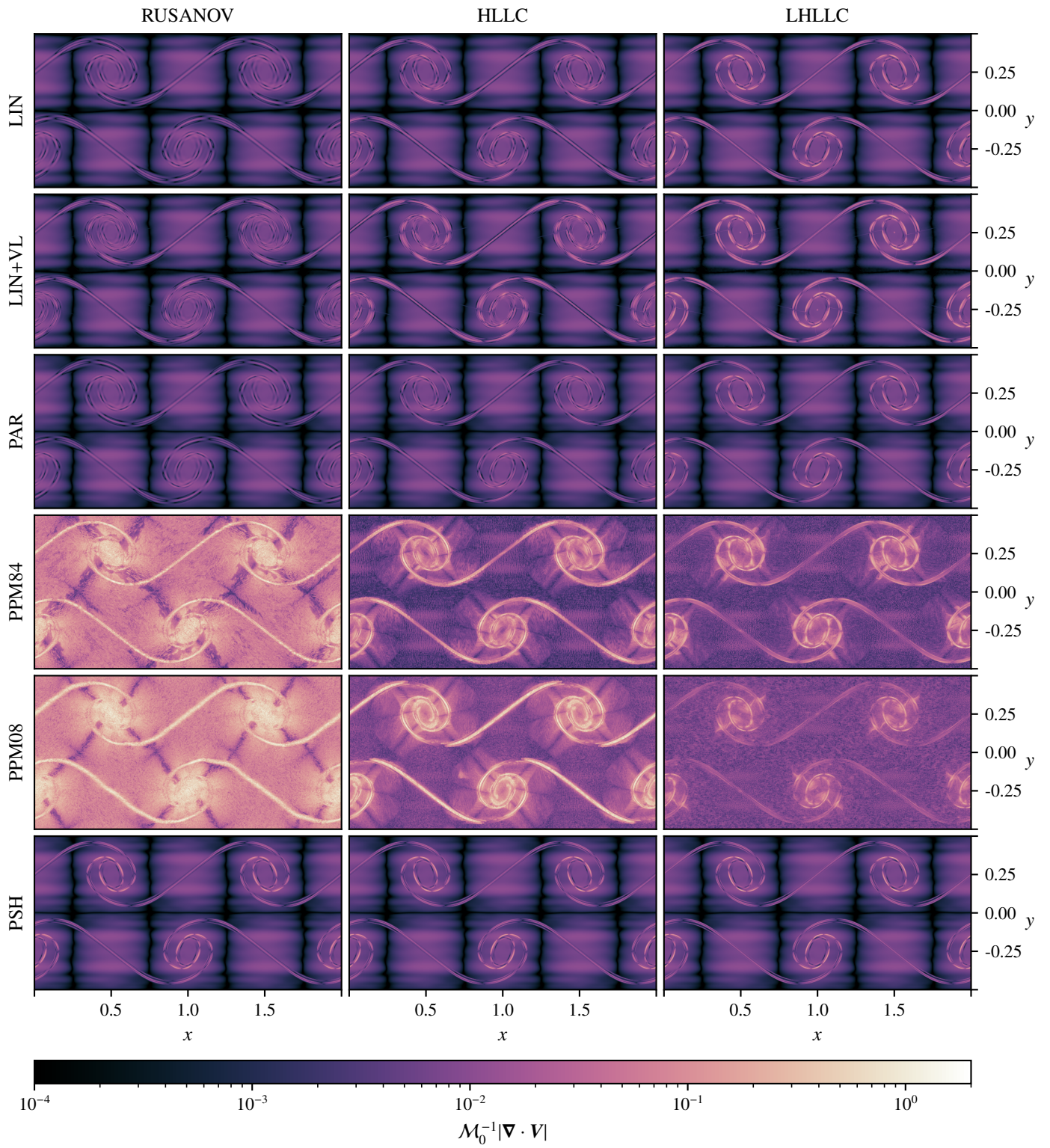


Fig. D.7. As Fig. 4 but showing simulations computed on the  $4096 \times 2048$  grid.





**Fig. D.8.** As Fig. 6 but showing simulations computed on the  $4096 \times 2048$  grid.

### 3.3 Publication III: Turbulent dynamo action in an oxygen-burning shell

In this Chapter, the new MHD capabilities of SLH are used to study an astrophysical system. In particular, this paper presents simulations of small-scale dynamo action in an idealized oxygen-burning shell of a massive star. The setup is taken from the work of [Andrassy et al. \(2022\)](#) and is idealized in that detailed nuclear burning is replaced by a time-independent heat source, the EoS is that of an ideal gas, the stratification is plane-parallel, and neutrino cooling is disregarded. These simulations do not aim to provide a realistic model of a core-collapse supernova progenitor, but rather their goal is to infer the efficacy of the small-scale dynamo in generating dynamically relevant magnetic fields at the typical dynamical conditions found in late burning shells.

Strong small-scale dynamo action could change both the topology of the velocity field and the magnitude of the density perturbations inside the convective oxygen shell. Flow asphericities and seed perturbations in the oxygen and silicon shells of the progenitor star are often found to be fundamental ingredients for shock-revival and for producing successful models of core-collapse supernova explosions (e.g., [Couch and Ott, 2013](#); [Müller et al., 2017](#); [Vartanyan et al., 2019](#)). Despite the crucial role that turbulent dynamos may play in determining the star's fate, the hydrodynamic simulations of oxygen-burning shells presented so far either did not include magnetic fields or were affected by excessive numerical dissipation (e.g., [Jones et al., 2017](#); [Müller et al., 2016](#); [Yoshida et al., 2019](#); [Varma and Müller, 2021](#)). The proposed simulations, although idealized, are a first step toward the quantification of potential MHD effects on the dynamical evolution of oxygen-burning shells.

The setup studied here involves the presence of mixing processes occurring at the upper boundary of the convective shell, so it is fundamental to avoid strong numerical overshoots that may be generated near steep entropy gradients. Based on the results shown in Sect. 3.2, the PPM method of [Colella and Woodward \(1984\)](#) is chosen to reconstruct the Riemann states at grid cell boundaries. The quality of the numerical results is judged by means of a resolution study, where the number of grid cells is varied from  $128^3$  to  $512^3$ . This is the first time that MHD processes in an oxygen-burning shell are studied with grid resolution this high.



### **Title**

Turbulent dynamo action and its effects on the mixing at the convective boundary of an idealized oxygen-burning shell

### **Authors**

G. Leidi, R. Andrassy, J. Higl, P. V. F. Edelman, F. K. Röpke

### **Publication status**

The manuscript was published in November 2023.

### **DOI**

<https://doi.org/10.1051/0004-6361/202347621>





### **Author's contribution**

GL is the principal author of this paper. The initial idea for this project developed during discussions with FKR and RA. The initial setup for the simulations was suggested by RA. GL ran the 3D MHD simulations presented in the study, analyzed the results, produced all the figures, and wrote the manuscript. All authors actively contributed by discussing the results at various stages of the project and by suggesting improvements and corrections to the manuscript.

### **Credit**

Leidi et al., A&A, 679, A132, 2023, reproduced with permission ©ESO.

# Turbulent dynamo action and its effects on the mixing at the convective boundary of an idealized oxygen-burning shell

G. Leidi<sup>1</sup>, R. Andrassy<sup>1</sup>, J. Higl<sup>1,2</sup>, P. V. F. Edelmann<sup>3</sup>, and F. K. Röpké<sup>1,4</sup>

<sup>1</sup> Heidelberger Institut für Theoretische Studien, Schloss-Wolfsbrunnenweg 35, 69118 Heidelberg, Germany  
e-mail: [giovanni.leidi@h-its.org](mailto:giovanni.leidi@h-its.org)

<sup>2</sup> High-Performance Computing Center Stuttgart, Nobelstraße 19, 70569 Stuttgart, Germany

<sup>3</sup> Computer, Computational and Statistical Sciences (CCS) Division and Center for Theoretical Astrophysics (CTA), Los Alamos National Laboratory, Los Alamos, PO Box 1663, NM 87545, USA

<sup>4</sup> Zentrum für Astronomie der Universität Heidelberg, Institut für Theoretische Astrophysik, Philosophenweg 12, 69120 Heidelberg, Germany

Received 1 August 2023 / Accepted 27 September 2023

## ABSTRACT

Convection is one of the most important mixing processes in stellar interiors. Hydrodynamic mass entrainment can bring fresh fuel from neighboring stable layers into a convection zone, modifying the structure and evolution of the star. Because flows in stellar convection zones are highly turbulent, multidimensional hydrodynamic simulations are fundamental to accurately capture the physics of mixing processes. Under some conditions, strong magnetic fields can be sustained by the action of a turbulent dynamo, adding another layer of complexity and possibly altering the dynamics in the convection zone and at its boundaries. In this study, we used our fully compressible SEVEN-LEAGUE HYDRO code to run detailed and highly resolved three-dimensional magnetohydrodynamic simulations of turbulent convection, dynamo amplification, and convective boundary mixing in a simplified setup whose stratification is similar to that of an oxygen-burning shell in a star with an initial mass of  $25 M_{\odot}$ . We find that the random stretching of magnetic field lines by fluid motions in the inertial range of the turbulent spectrum (i.e., a small-scale dynamo) naturally amplifies the seed field by several orders of magnitude in a few convective turnover timescales. During the subsequent saturated regime, the magnetic-to-kinetic energy ratio inside the convective shell reaches values as high as 0.33, and the average magnetic field strength is  $\sim 10^{10}$  G. Such strong fields efficiently suppress shear instabilities, which feed the turbulent cascade of kinetic energy, on a wide range of spatial scales. The resulting convective flows are characterized by thread-like structures that extend over a large fraction of the convective shell. The reduced flow speeds and the presence of magnetic fields with strengths up to 60% of the equipartition value at the upper convective boundary diminish the rate of mass entrainment from the stable layer by  $\approx 20\%$  as compared to the purely hydrodynamic case.

**Key words.** stars: interiors – convection – dynamo – magnetohydrodynamics (MHD) – turbulence

## 1. Introduction

Convection plays a key role in the evolution of stars. In the deep, optically thick layers, convective flows can efficiently transport energy and angular momentum outward, so they determine both the thermal structure and the rotational profile of stars (see, e.g., Maeder 2009; Kippenhahn et al. 2013). Furthermore, because the characteristic spatial scales of convection are much larger than the mean free path in the stellar plasma, stellar convection zones are highly turbulent environments, with Reynolds numbers that can be as high as  $10^{14}$  (Jermyn et al. 2022). Turbulent flows quickly mix chemical elements over the relatively short convective turnover timescale, thus profoundly affecting the nuclear energy generation in burning layers of stars and their evolution.

Despite the huge imprint of convection on stars, most one-dimensional (1D) stellar evolution codes still rely on simplified parametrizations of the convective energy transport, such as the popular mixing-length theory (MLT; Prandtl 1925; Böhm-Vitense 1958). On the one hand, these parameterized theories allow 1D models to simulate the evolution of stars over thermal and nuclear timescales, which is still unfeasible in multi-D. On the other hand, the parameters that enter these prescrip-

tions cannot be derived from first principles and need to be calibrated. Usually, their value is tuned so that 1D models can reproduce the global properties of our Sun (see, e.g., Richard et al. 1996), but the universality of this approach has been heavily questioned in the literature (Trampedach et al. 2014; Magic et al. 2015; Joyce & Chaboyer 2018; Sonoi et al. 2019). Moreover, local theories of convection such as the MLT assume that convective mixing stops at the position of the formal convective boundary. More realistically, convective plumes approach the convective boundary with nonzero velocities and give rise to hydrodynamic processes that can entrain some excess mass and entropy from the neighboring stable layer into the convection zone. Evidence of extra mixing occurring at stellar convective boundaries has been provided by a number of observations, including eclipsing binaries (Valle et al. 2016; Claret & Torres 2016), old open clusters (Aparicio et al. 1990), or asteroseismology (Bossini et al. 2015; Aerts 2021). The entrainment of fresh fuel into a burning layer can prolong its lifetime, enlarge convective cores in upper main sequence stars, and determine the structure of supernova progenitors in more massive stars (Müller 2020, and references therein). In stellar evolution codes, mixing at convective boundaries is crudely modeled by means of additional parametrizations, usually in the form of diffusive

over-mixing or convective penetration (Anders & Pedersen 2023, and references therein). The uncertainties arising from the usage of such simplistic models limit the predictive power of stellar evolution calculations and have far-reaching consequences for supernova explosions, the formation of stellar populations, and galactic chemical evolution. Although several non-local theories of convection have been presented in the literature (see, e.g., Xiong 1978; Kuhfuss 1986; Canuto 1997, 2011; Li & Yang 2007; Garaud et al. 2010), they have not been extensively used in 1D stellar calculations so far.

To overcome the limitations of stellar-evolution models, several research groups have started focusing their efforts in the past two decades on multi-D hydrodynamic modeling of turbulent convection and mixing at convective boundaries in different classes of stellar objects, including core-convective main sequence stars (Gilet et al. 2013; Horst et al. 2020; Higl et al. 2021; Baraffe et al. 2023; Herwig et al. 2023; Androssy et al. 2023), envelope-convective stars (Pratt et al. 2016; Hotta 2017; Käpylä 2019; Blouin et al. 2023), and more massive stars during late burning stages (Meakin & Arnett 2007; Jones et al. 2017; Cristini et al. 2017; Androssy et al. 2020; Rizzuti et al. 2023). In this approach, nonlinear hydrodynamic processes are captured self-consistently, which allows parameterized theories of convection and convective boundary mixing to be tested and calibrated for different stellar masses and evolutionary stages.

One more layer of complexity to the problem of stellar convection is, however, represented by the possible presence of magnetic fields, which have been observed both in low- and high-mass stars (Brun & Browning 2017; Keszthelyi 2023, and references therein). The coupling between turbulent fluid motions and magnetic fields can give rise to small-scale dynamos (SSDs; Meneguzzi et al. 1981; Brandenburg & Subramanian 2005; Schekochihin et al. 2007), which amplify magnetic fields on scales smaller than the forcing scale of turbulence. As observed in numerous simulations of solar convection (Vögler & Schüssler 2007; Pietarila Graham et al. 2010; Rempel 2014; Thaler & Spruit 2015; Hotta et al. 2016; Hotta 2017), SSDs can drastically change the morphology of the convective flows, reduce their speed, and alter the dynamics of the overshoot region at the bottom of the solar convection zone as compared to the purely hydrodynamic case.

Other than the Sun, effects of magnetohydrodynamic (MHD) processes on the properties of convective flows have also been investigated in cool (Browning 2008; Käpylä 2021; Bhatia et al. 2022) and upper-main-sequence stars (Brun et al. 2005; Featherstone et al. 2009; Augustson et al. 2016), but very few MHD simulations of late burning stages of massive stars have been run to date (Varma & Müller 2021, 2023; Canivete Cuissa & Teyssier 2022). In contrast to the main sequence phase, these late evolutionary stages are characterized by vigorous convective shells that can entrain a substantial amount of mass on relatively short timescales, possibly giving rise to shell mergers (Ritter et al. 2018; Mocák et al. 2018; Yadav et al. 2020; Androssy et al. 2020). If an efficient SSD action takes place inside these shells, it could reduce the mass entrainment rate at the convective boundaries and possibly delay or even inhibit the occurrence of the merger events. Numerical simulations of the dynamical amplification of magnetic fields in these layers then become essential for determining the stratification of the supernova progenitor and the fate of the star. Acquiring more insight into dynamo mechanisms in late burning shells of massive stars is also particularly important because magnetic fields can act as seeds to magneto-rotationally powered supernovae (Müller & Varma 2020).

In this paper, we investigated the effects of a small-scale turbulent dynamo acting in a late stellar convective shell using our fully compressible, MHD, SEVEN-LEAGUE HYDRO (SLH) code. In particular, we used an idealized setup whose stratification is close to that of an oxygen-burning shell in a massive star (Androssy et al. 2022). In this study, we did not intend to perform realistic simulations of such an evolutionary stage. Instead, we checked the efficiency of small-scale dynamo action in generating dynamically relevant magnetic fields on the typical timescales set by convective motions in the oxygen shell and quantified their impact on the evolution of the convection and on the mixing at the convective boundary.

The paper is structured as follows: in Sect. 2, we give a brief description of the numerical methods used to run the simulations needed for this study. The details of the initial stratification are provided in Sect. 3. In Sect. 4, we present the numerical results, including the evolution of the small-scale turbulent dynamo and its effects on the boundary mixing. Finally, in Sect. 5, we draw conclusions and summarize the main results.

## 2. Methods

### 2.1. Equations solved

We described the physical problem by means of the fully compressible equations of ideal MHD with time-independent gravity,

$$\frac{\partial \rho}{\partial t} + \nabla \cdot (\rho \mathbf{V}) = 0, \quad (1)$$

$$\frac{\partial(\rho \mathbf{V})}{\partial t} + \nabla \cdot [\rho \mathbf{V} \otimes \mathbf{V} + (p + p_B) \mathbb{I} - \mathbf{B} \otimes \mathbf{B}] = \rho \mathbf{g}, \quad (2)$$

$$\frac{\partial(\rho e_{\text{tot}})}{\partial t} + \nabla \cdot [(\rho e_{\text{tot}} + p + p_B) \mathbf{V} - \mathbf{B}(\mathbf{B} \cdot \mathbf{V})] = 0, \quad (3)$$

$$\frac{\partial \mathbf{B}}{\partial t} + \nabla \cdot (\mathbf{V} \otimes \mathbf{B} - \mathbf{B} \otimes \mathbf{V}) = \mathbf{0}, \quad (4)$$

$$\frac{\partial(\rho \psi)}{\partial t} + \nabla \cdot (\rho \psi \mathbf{V}) = 0, \quad (5)$$

where  $\rho$  denotes the density,  $\mathbf{V} = (V_x, V_y, V_z)$  the velocity vector,  $\mathbf{B} = (B_x, B_y, B_z)$  the magnetic field<sup>1</sup>,  $p_B = |\mathbf{B}|^2/2$  the magnetic pressure,  $\mathbf{g} = (g_x, g_y, g_z)$  the gravitational acceleration,  $e_{\text{tot}} = e_{\text{int}} + |\mathbf{V}|^2/2 + |\mathbf{B}|^2/(2\rho) + \phi$  the total energy per unit mass,  $e_{\text{int}}$  the internal energy per unit mass,  $\phi$  the gravitational potential,  $\psi$  the mass fraction of a passive tracer, and  $\mathbb{I}$  the unit tensor. The system in Eqs. (1)–(5) is closed by an Equation of State (EoS) for the gas pressure  $p$ ,

$$p = p(\rho, e_{\text{int}}). \quad (6)$$

In our simulations, we assumed an ideal gas law,

$$p(\rho, e_{\text{int}}) = (\gamma - 1)\rho e_{\text{int}}, \quad (7)$$

where  $\gamma = 5/3$  is the adiabatic index.

We stress that the absence of the viscous and resistive dissipation terms in Eqs. (2)–(4) does not mean that the simulated flows are inviscid and nonresistive. In fact, the numerical methods that we used to solve the equations of ideal MHD (see Sect. 2.2) must add a certain amount of numerical dissipation into the system in order to achieve numerical stability.

<sup>1</sup> We use the Lorentz-Heaviside units throughout the paper ( $\mathbf{B} = \mathbf{b}/\sqrt{4\pi}$ ).

## 2.2. Numerical methods

We solved Eqs. (1)–(5) with the SLH code, which is suited for simulating low-Mach-number (magneto-)convection and excitation of internal gravity waves (IGWs) in the deep interiors of stars (Miczek et al. 2015; Edelmann et al. 2017, 2021; Horst et al. 2020, 2021; Andrassy et al. 2022, 2023; Leidi et al. 2022). SLH makes use of a second-order finite-volume discretization and upwinding techniques that require an approximate solution to the Riemann problem at each cell interface. Here, the pair of Riemann states was reconstructed using the Piecewise-Parabolic-Method (PPM) of Colella & Woodward (1984). Upwind, hyperbolic fluxes were computed at cell interfaces with the low-dissipation version of the HLLD solver (LHLLD) of Minoshima & Miyoshi (2021). LHLLD modifies the stabilizing pressure-diffusion term in the original HLLD solver of Miyoshi & Kusano (2005) to ensure that the magnitude of numerical dissipation (relative to the physical central flux) is independent of the Mach number of the flow,  $\mathcal{M} = |V|/c$ , where  $c = (\gamma p/\rho)^{1/2}$  is the sound speed. This correction dramatically reduces the excessive amount of numerical diffusion introduced by shock-capturing methods in simulations of subsonic flows (Miczek et al. 2015; Leidi et al. 2022).

To suppress the development of spurious flows due to grid discretization errors in strongly stratified setups, we used a well-balancing technique (the Deviation method, Berberich et al. 2021; Edelmann et al. 2021). In this method, the vector of conserved quantities,  $\mathbf{U} = (\rho, \rho\mathbf{V}, \rho e_{\text{tot}}, \mathbf{B}, \rho\psi)$ , is split into a time-independent hydrostatic component,  $\tilde{\mathbf{U}}$ , and a fully nonlinear perturbation,  $\delta\mathbf{U}$ . Equations (1)–(5) are then solved by enforcing  $\partial\tilde{\mathbf{U}}/\partial t = \mathbf{0}$ , which is achieved in practice by subtracting the hydrostatic fluxes and source terms from the spatial residuals. Such a measure is necessary because conventional finite volume methods discretize hyperbolic fluxes and gravitational source terms at different locations on the computational grid, so hydrostatic solutions cannot be maintained for long times. If ignored, these discretization errors can dramatically affect the evolution of buoyancy-driven flows and produce grossly inaccurate numerical solutions (Edelmann et al. 2021).

To keep the strength of magnetic monopoles under control, we used a staggered constrained transport (CT) method (Evans & Hawley 1988). Different from the finite volume discretization, here the surface-averaged magnetic field components are evolved at cell interfaces by performing the line integral of the electromotive force along the cell edges. Thanks to this operation, the update on the cell-volume average of  $\nabla \cdot \mathbf{B}$  vanishes to machine precision. In SLH, the upwind electromotive force at the cell edges is computed according to the CT-Contact scheme of Gardiner & Stone (2005).

Finally, both cell-centered and staggered quantities were evolved in time with a semi-discrete scheme based on the method of lines. The resulting system of ordinary differential equations was solved using the explicit strong stability preserving (SSP) RK2 method of Shu & Osher (1988). Further details regarding the implementation of the fully unsplit MHD solver in SLH can be found in Leidi et al. (2022).

## 3. Setup

We used the setup first described in Andrassy et al. (2022), who performed a comparison of five different hydrodynamic codes (SLH, PPMSTAR, MUSIC, FLASH, and PROMPI) on a problem involving turbulent convection, convective boundary mixing, and the excitation of IGWs in an overlying stable layer.

The thermodynamic conditions of this test setup resemble those found during oxygen shell burning in a star with an initial mass of  $25 M_{\odot}$  (Jones et al. 2017). However, Andrassy et al. (2022) adopted a few simplifications to make the study easily reproducible by other research groups. In particular, the geometry of the shell was plane-parallel, the EoS was that of an ideal gas, neutrino cooling was not included, and detailed nuclear burning was replaced by a time-independent heat source term, whose amplitude was set such that convective motions were driven with root-mean-square velocities characteristic of late evolutionary stages in massive stars ( $\mathcal{M}_{\text{rms}} \approx 0.04$ ).

We mapped the initial hydrostatic stratification (see Fig. 1) on a 3D Cartesian grid with spatial domain  $(x, y, z) \in [-L_{\text{ref}}, L_{\text{ref}}] \times [L_{\text{ref}}, 3L_{\text{ref}}] \times [-L_{\text{ref}}, L_{\text{ref}}]$ , where  $L_{\text{ref}} = 4 \times 10^8$  cm. We used periodic boundaries in the horizontal  $x$ - and  $z$ -direction. At the top and bottom boundaries of the domain, instead, we adopted impermeable, stress-free boundary conditions for the velocity field,

$$\frac{\partial V_x}{\partial y} = \frac{\partial V_z}{\partial y} = V_y = 0, \quad (8)$$

we forced the magnetic field to be purely horizontal,

$$\frac{\partial B_x}{\partial y} = \frac{\partial B_z}{\partial y} = B_y = 0, \quad (9)$$

and for the scalar quantities we assumed

$$\frac{\partial \rho}{\partial y} = \frac{\partial p}{\partial y} = \frac{\partial \psi}{\partial y} = 0. \quad (10)$$

The gravitational acceleration, assumed to be time-independent, points downward in the  $y$ -direction and goes to zero at the vertical boundaries according to Eq. (1) of Andrassy et al. (2022). In that work, such a choice for the gravitational acceleration was made to allow the hydrostatic density and pressure profiles to become constant at the domain boundaries, making the problem consistent with the conditions in Eq. (10). Although unrealistic, turning off the gravity at the boundaries does not appreciably alter the stratification of the oxygen shell, which is mostly affected by the aforementioned simplifications, as can be seen in Fig. 1 of Andrassy et al. (2022). For consistency with their model, we decided not to modify the profile of the gravitational acceleration here.

The stratification is isentropic up to approximately  $y = 2L_{\text{ref}}$ , and it smoothly turns subadiabatic in the upper half of the domain. Overall, the grid covers 4.35 pressure scale heights in the vertical direction. To be able to track the time evolution of the mass entrained into the convection zone, we filled the convectively stable layer with a passive tracer at  $t = 0$  s, whose abundance progressively drops to zero across the convective boundary. Further details regarding the initial stratification and the heat source can be found in Andrassy et al. (2022).

To start the dynamo action, we planted an initially horizontal magnetic field into the grid,  $B_x = 10^5$  G. The strength of the seed field was chosen such that the Lorentz force exerted on the fluid at early times was weak enough to not affect the development of convection.

We judged the numerical convergence of the results obtained in this work by running simulations on grids with  $128^3$ ,  $256^3$ , and  $512^3$  cells. To compute meaningful time-averaged quantities and avoid introducing temporal correlations caused by the turbulent nature of the convective flows, all test cases were run until  $t_{\text{max}} = 25\tau_{\text{conv}}$ , where  $\tau_{\text{conv}} = 63.36$  s is the mean convective turnover timescale in the purely hydrodynamic case, defined



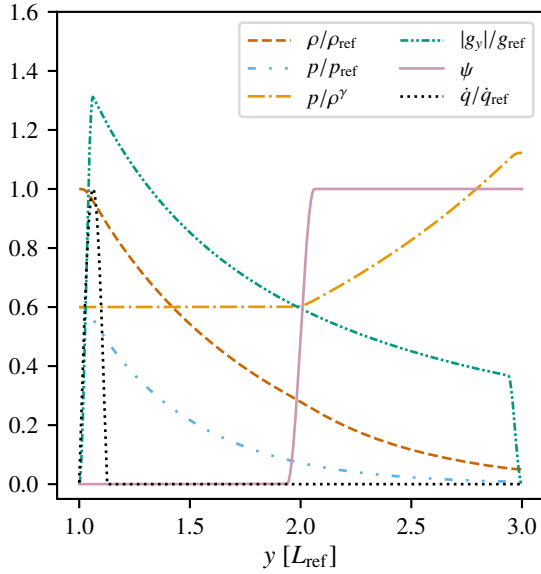


**Fig. 1.** Profiles of density, pressure, pseudo-entropy ( $p/\rho^\gamma$ ), gravity, mass fraction of a passive tracer ( $\psi$ ), and heat source term ( $\dot{q}$ ) as a function of the vertical coordinate  $y$  at  $t = 0$  s. Here,  $\rho_{\text{ref}} = 1.82 \times 10^6 \text{ g cm}^{-3}$ ,  $p_{\text{ref}} = 4.64 \times 10^{23} \text{ dyne cm}^{-2}$ ,  $g_{\text{ref}} = 6.37 \times 10^8 \text{ cm s}^{-2}$ ,  $\dot{q}_{\text{ref}} = 1.76 \times 10^{20} \text{ erg cm}^{-3} \text{ s}^{-1}$ , and  $L_{\text{ref}} = 4 \times 10^8 \text{ cm}$ .

according to Eq. (16) of [Andrassy et al. \(2022\)](#). By  $t = t_{\text{max}}$ , the growing convective layer is still sufficiently far away from the upper boundary of the spatial domain that the imposed boundary conditions do not appreciably alter the dynamics of the mixing region. Thus, we decided not to extend the simulations beyond  $t_{\text{max}}$ . Finally, in order to capture possible differences between the MHD and the purely hydrodynamic case, we ran an additional set of simulations without magnetic fields.

## 4. Results

### 4.1. Onset of convection and kinematic stage of the dynamo

To break the initial symmetry, we added a small-amplitude perturbation to the hydrostatic density stratification according to Eq. (6) of [Andrassy et al. \(2022\)](#). The energy injected by the heat source at the base of the box leads to the development of buoyant parcels of hot fluid that rise in the adiabatic layer (see Fig. 2). As soon as these flows cross the boundary of the subadiabatic layer, the buoyant acceleration changes sign (so it points downward in the  $y$ -direction) and forces the rising plumes to turn around. The large-scale buoyant fluid elements that are driven by the energy source quickly develop shear instabilities that cascade down to smaller scales, and turbulent convection fully develops by  $t \approx \tau_{\text{conv}}$ .

As shown in Fig. 3, the mean magnetic energy density inside the convective shell<sup>2</sup>,

$$\tilde{E}_B = \frac{1}{2} \langle |\mathbf{B}|^2 \rangle_{\text{conv}}, \quad (11)$$

increases exponentially in time. The growth rate of the instability is higher on finer grids, which indicates that the amplification process mostly occurs on intermediate or small spatial scales. It could be an SSD, where the magnetic field is randomly stretched at scales smaller than the forcing scale of turbulence.

<sup>2</sup>  $\langle \cdot \rangle$  is the volume-weighted spatial average operator.

However, two other processes could contribute to the amplification of small-scale magnetic fields in this setup: turbulent induction, which is the stretching of large-scale magnetic fields by a turbulent, small-scale velocity component ([Schekochihin et al. 2007](#)), and turbulent cascade of magnetic energy toward smaller scales ([Pietarila Graham et al. 2010](#)). In fact, the large-scale fields that are needed to excite the latter two processes, not only are characteristic of large-scale dynamos ([Brandenburg 2009](#); [Charbonneau 2013](#)), but they can also be supported by the large-scale velocity structures typical of turbulent convection ([Käpylä et al. 2018](#)). Moreover, the imposed boundary conditions (see Sect. 3) allow the integrated horizontal magnetic flux, and consequently the mean horizontal magnetic field, to be preserved in time inside the spatial domain. Therefore, the mean horizontal field takes the value of the chosen seed field,  $B_x = 10^5 \text{ G}$ , and represents a persistent large scale magnetic field component that could, in principle, contribute to the amplification of magnetic energy via turbulent induction.

To get a better understanding of the underlying mechanisms that amplify the magnetic energy in these simulations, we computed transfer functions  $T_{XYZ}(\mathbf{k})$  in the Fourier space between the kinetic ( $K$ ) and magnetic ( $B$ ) energy reservoirs inside the convective layer, following the approach of [Pietarila Graham et al. \(2010\)](#). In particular,  $T_{XYZ}(\mathbf{k})$  represents the energy received (or lost in case of  $T_{XYZ}(\mathbf{k}) < 0$ ) per unit time and per unit wavenumber at scale  $\mathbf{k}$  of energy type  $Y$  from all scales of energy type  $X$  via process  $Z$ . The transfer of magnetic energy to the  $k$ th component of kinetic energy is determined by the net work done on the fluid by the magnetic tension force,

$$T_{\text{BKT}}(\mathbf{k}) = \frac{1}{2} \hat{\mathbf{V}}(\mathbf{k}) \cdot [\widehat{\mathbf{B} \cdot \nabla \mathbf{B}}]^*(\mathbf{k}) + \frac{1}{2} (\widehat{\rho \mathbf{V}})(\mathbf{k}) \cdot \left[ \frac{1}{\rho} \widehat{\mathbf{B} \cdot \nabla \mathbf{B}} \right]^*(\mathbf{k}) + \text{c.c.}, \quad (12)$$

and the magnetic pressure force,

$$T_{\text{BKP}}(\mathbf{k}) = -\frac{1}{4} \hat{\mathbf{V}}(\mathbf{k}) \cdot [\widehat{|\mathbf{B}|^2}]^*(\mathbf{k}) - \frac{1}{4} (\widehat{\rho \mathbf{V}})(\mathbf{k}) \cdot \left[ \frac{1}{\rho} \widehat{|\mathbf{B}|^2} \right]^*(\mathbf{k}) + \text{c.c.}, \quad (13)$$

where  $*$  is the complex conjugate, c.c. is the complex conjugate of the whole expression on the right-hand side, and  $\widehat{\cdot}$  represents the Fourier projection<sup>3</sup>. Magnetic energy on scale  $\mathbf{k}$  is produced or removed via stretching of the magnetic field lines,

$$T_{\text{KBS}}(\mathbf{k}) = \hat{\mathbf{B}}(\mathbf{k}) \cdot [\widehat{\mathbf{B} \cdot \nabla \mathbf{V}}]^*(\mathbf{k}) + \text{c.c.}, \quad (14)$$

and through compression and advection of the magnetic field,

$$T_{\text{KBCA}}(\mathbf{k}) = -\hat{\mathbf{B}}(\mathbf{k}) \cdot [\widehat{\mathbf{B} \nabla \cdot \mathbf{V}}]^*(\mathbf{k}) - \hat{\mathbf{B}}(\mathbf{k}) \cdot [\widehat{\mathbf{V} \cdot \nabla \mathbf{B}}]^*(\mathbf{k}) + \text{c.c.} \quad (15)$$

Because here we solved the fully compressible MHD equations,  $T_{\text{KBCA}}(\mathbf{k})$  includes both the transport of energy within the magnetic energy reservoir and the generation of magnetic energy through fluid compression. These two processes, however, cannot be decoupled ([Rempel 2014](#)), which can be seen by expanding the advective flux of magnetic energy as

$$-\nabla \cdot \left( \mathbf{V} \frac{|\mathbf{B}|^2}{2} \right)(\mathbf{k}) = -\hat{\mathbf{B}}(\mathbf{k}) \cdot \left[ (\mathbf{V} \cdot \nabla) \mathbf{B} + \frac{\mathbf{B}}{2} \nabla \cdot \mathbf{V} \right]^*(\mathbf{k}) + \text{c.c.} \quad (16)$$

<sup>3</sup> A thorough derivation of the transfer functions computed here can be found in Appendix A.1 of [Pietarila Graham et al. \(2010\)](#).



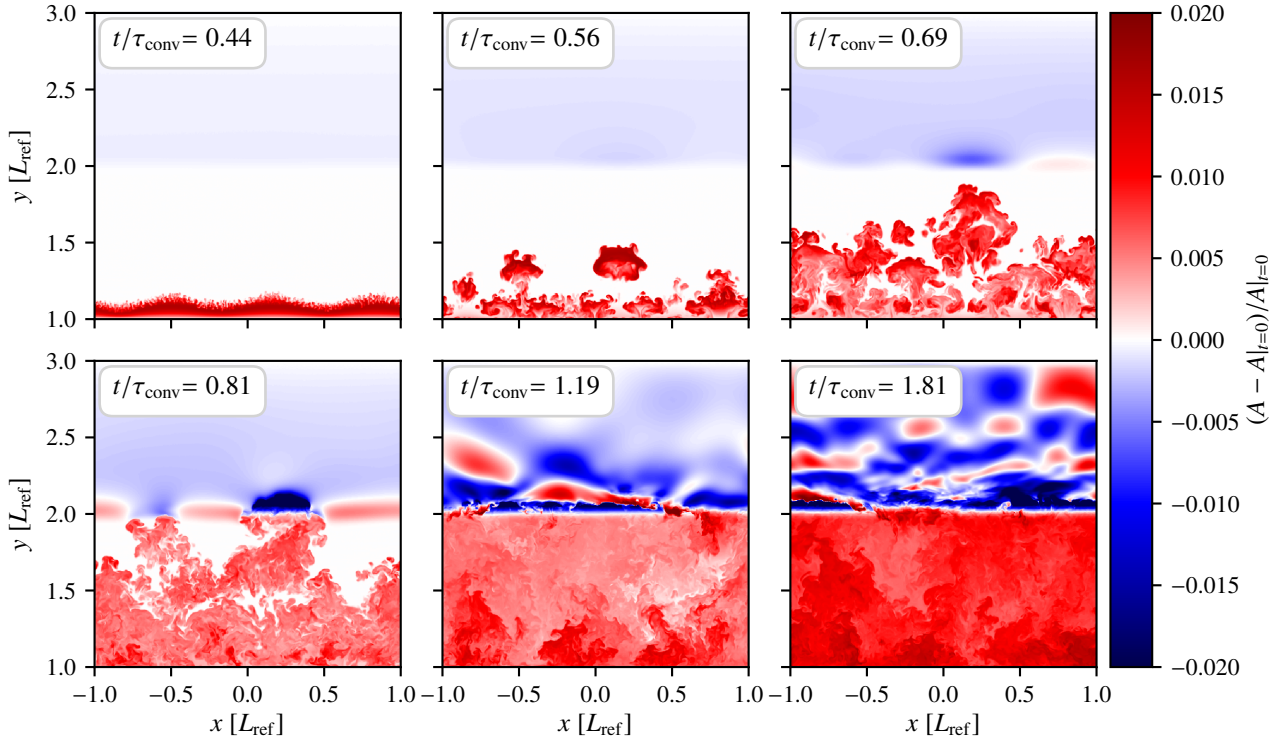


**Fig. 2.** Development of convection in the MHD simulation of the idealized oxygen shell run on a  $512^3$  grid. The panels show fluctuations in pseudo-entropy ( $A = p/\rho^\gamma$ ) in the  $z = 0$  plane at different times, as indicated by the insets. The entropy generated by the heat source at the base of the box (see Fig. 1) is mixed throughout the initially adiabatic layer by turbulent convection. This process slowly increases the entropy content of the convection zone in time. The broad stripe of negative entropy fluctuation visible in the upper half of the domain at early times is due to the thermal expansion of the convective layer. The turbulent flows also excite IGWs at the upper convective boundary (lower center panel) which then propagate in the subadiabatic layer.

To simplify the calculations, instead of computing 3D Fourier projections in Eqs. (12)–(15), we averaged transfer functions  $T_{XYZ}(k_h, y_j)$  obtained at each horizontal plane  $y_j$  inside the convection zone,

$$T_{XYZ}(k_h) = \langle T_{XYZ}(k_h, y_j) \rangle_{y_j \in (L_{\text{ref}}, 2L_{\text{ref}})}. \quad (17)$$

Here,  $k_h$  is the horizontal wavenumber  $k_h = \sqrt{k_x^2 + k_z^2}$ , where

$$k_x = \begin{cases} m, & 0 \leq m \leq \lfloor \frac{N_x-1}{2} \rfloor, \\ -N_x + m, & \lfloor \frac{N_x-1}{2} \rfloor < m < N_x, \end{cases} \quad (18)$$

$$k_z = \begin{cases} n, & 0 \leq n \leq \lfloor \frac{N_z-1}{2} \rfloor, \\ -N_z + n, & \lfloor \frac{N_z-1}{2} \rfloor < n < N_z, \end{cases} \quad (19)$$

$\lfloor \cdot \rfloor$  is the floor function, and  $N_x$  and  $N_z$  are the number of cells in the  $x$ - and  $z$ - direction, respectively.

Figure 4 shows results from the transfer analysis performed on the grid with  $512^3$  cells. Stretching of the magnetic field lines contributes most of the magnetic energy generation at spatial wavenumbers close to  $k_h = 50$ . In these simulations, the typical velocities in the convection zone are considerably subsonic ( $\mathcal{M}_{\text{rms}} \approx 0.04$ ), so fluid compression due to the ram pressure of the convective flows ( $p_{\text{ram}} \sim \mathcal{M}^2$ ) has a negligible contribution to the generation of magnetic energy (see  $T_{\text{KBC}}(k_h) = -\hat{\mathbf{B}}(k_h) \cdot [\mathbf{B}\nabla \cdot \mathbf{V}]^*(k_h) + \text{c.c.}$  in Fig. 4). Therefore,  $T_{\text{KBCA}}(k_h)$  measures mostly the advective transport of magnetic energy to scale  $k_h$  from all scales of the magnetic field, similar to the case of incompressible MHD,

$$T_{\text{KBCA}}(k_h) \approx -\hat{\mathbf{B}}(k_h) \cdot [\mathbf{V}\nabla \cdot \mathbf{B}]^*(k_h) + \text{c.c.} \quad (20)$$

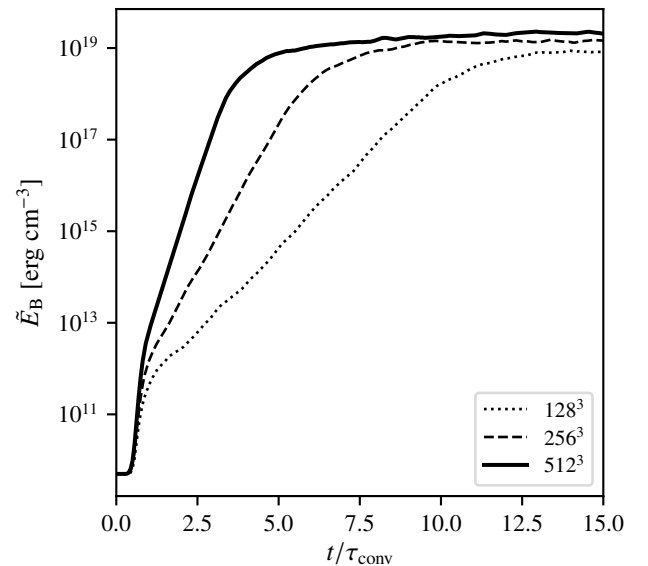


**Fig. 3.** Time evolution of the mean magnetic energy density inside the convection zone for the indicated grid resolutions.

We observe that the magnetic cascade mainly removes magnetic energy from large scales, where  $T_{\text{KBCA}} < 0$ , and redistributes it at scales with  $k_h > 75$ , where  $T_{\text{KBCA}} > 0$ . This process dominates the generation of magnetic energy over stretching only at  $k_h > 130$ , which corresponds to a spatial scale of 3.9 times the width of the grid cells,  $\Delta x$ . Work done by

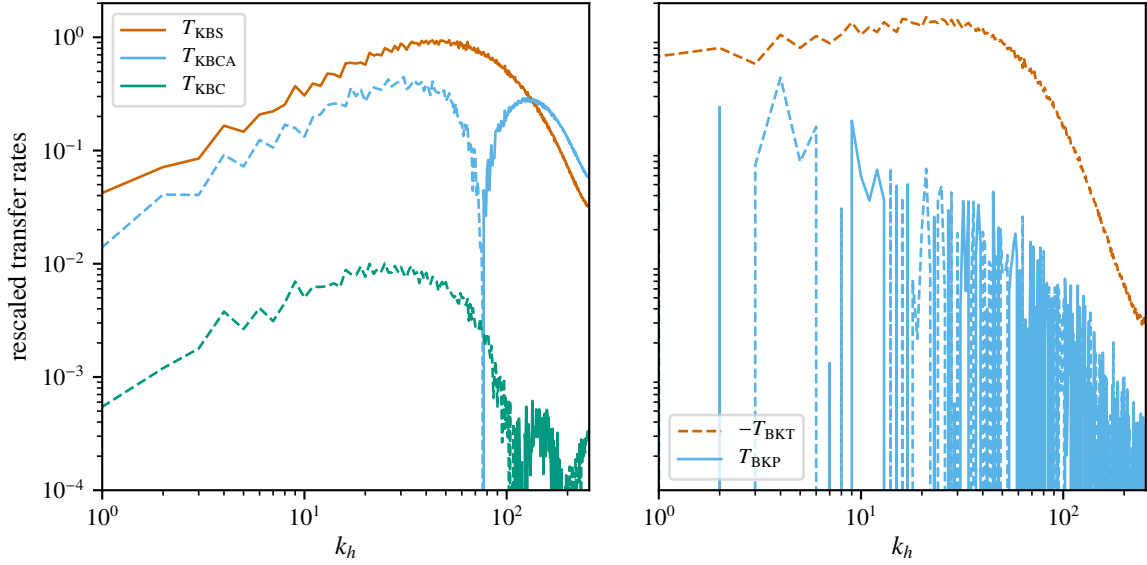


**Fig. 4.** Transfer functions extracted from the convection zone on the  $512^3$  grid and averaged over the kinematic stage of the dynamo. The panel on the left shows the transfer rates from the kinetic ( $K$ ) to the magnetic ( $B$ ) energy reservoir, whereas the panel on the right shows magnetic-to-kinetic energy transfer rates. The time averaging was performed such that, at each time  $t$ , all the transfer curves were rescaled by the maximum value of  $T_{KBS}(k_h)$ . The resulting curves were then averaged over the time interval  $t \in (1.5\tau_{\text{conv}}, 3\tau_{\text{conv}})$ . Dashed lines represent negative transfer rates, while solid lines are used for positive rates.

fluid motions against the magnetic tension force ( $-T_{\text{BKT}}$ ) most efficiently transforms kinetic energy at  $k_h \approx 30$  into magnetic energy. Work done by the magnetic pressure force on the fluid is negligible everywhere except on very large scales. These results allow us to find the range of wavenumbers where the magnetic field is most efficiently stretched by fluid motions. As pointed out by Pietarila Graham et al. (2010), the spatial wavenumber at which magnetic field is generated ( $\mathbf{q}$ ), the one at which it is stretched ( $\mathbf{k}$ ), and the one at which the flow works against magnetic tension ( $\mathbf{p}$ ) form a triadic relation,

$$\mathbf{k} = \mathbf{q} - \mathbf{p}. \quad (21)$$

By considering the most extreme cases in which  $\mathbf{q}$  and  $\mathbf{p}$  have the same or the opposite orientation, we estimate that the magnetic field lines are most efficiently stretched at  $20 \lesssim k_h \lesssim 80$ . As we show in Sect. 4.2, this interval lies at the bottom of the inertial range of the turbulent kinetic energy spectrum. Thus, the amplification of magnetic energy is mostly caused by the action of a small-scale turbulent dynamo, with a minor contribution from the turbulent cascade close to the grid scale.

Further evidence of small-scale turbulent dynamo action can be provided by checking the scaling of the growth rate of the magnetic energy,  $\gamma = \partial \ln \bar{E}_B / \partial t$ , with the grid resolution. Because in this work we used the Implicit Large Eddy Simulation (ILES) method, the magnetic Prandtl number ( $\text{Pr}_m = \nu/\eta$ ) is likely to be close to or larger than unity (Vögler & Schüssler 2007; Rempel 2014). In this regime of Prandtl numbers, an SSD can only be started if the fluid Reynolds number,  $\text{Re} = V_{\text{rms}} L_{\text{ref}}/\nu$ , is larger than a critical threshold. The growth rate of the magnetic energy in an unstable SSD should then scale as  $\text{Re}^{1/2}$  (Kazantsev 1968; Schekochihin et al. 2004). Although the effective value of the kinematic viscosity ( $\nu$ ) and resistivity ( $\eta$ ) coefficients are determined by the underlying numerical methods used to solve the MHD equations, in the ILES approach the fluid Reynolds number should depend on the spatial resolution as  $\Delta x^{-4/3}$  (Cristini et al. 2017), which leads to  $\gamma \propto \text{Re}^{1/2} \propto \Delta x^{-2/3}$ . Our study indicates that the growth rate  $\gamma$  follows the predicted

theoretical scaling (see Fig. 5). These results can only be confirmed by using an explicit kinematic viscosity coefficient so that  $\text{Re}$  can be measured directly, which, however, is beyond the scope of this work.

At early times, the magnetic energy is still subdominant with respect to the kinetic energy content of the flow. Therefore, the Lorentz force does not affect the evolution of the convection, and we do not observe any systematic difference in the velocity field between the MHD and the hydrodynamic simulations. This is the kinematic stage of the dynamo, which lasts for several convective turnover timescales, depending on the resolution of the grid.

#### 4.2. Nonlinear phase of the dynamo

The amplification of the magnetic field due to the action of the small-scale turbulent dynamo proceeds until the Lorentz force becomes strong enough to start having a feedback effect on the flow. Such a change in the evolution of the dynamo happens when the magnetic energy approaches equipartition with the kinetic energy content of the eddies on the small scales of turbulence. Strong, small-scale magnetic fields inhibit the development of shear instabilities that feed the turbulent cascade and drive the dynamo amplification. The stretching of the magnetic field lines happens now on larger scales, where turbulence has not been quenched. Work done against the magnetic tension force by the turbulent convective flows sustains the magnetic field against numerical (resistive) dissipation, and the dynamo reaches saturation. By  $t/\tau_{\text{conv}} \approx 15$ , all of the MHD simulations presented here have entered this phase. This stage of the dynamo, however, does not represent a statistical steady state solution of the simulated setup. In fact, the continuous injection of entropy into the system by the heat source and the mixing processes that take place at the convective boundary (see Sect. 4.3) both contribute to the entrainment of material from the overlying stable layer. Therefore, the size, mass, and entropy content of the convective layer keep increasing over time.

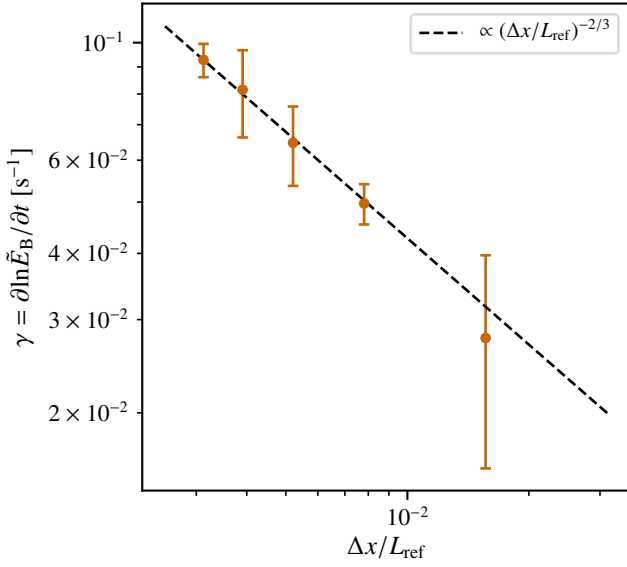


**Fig. 5.** Growth rate of the mean magnetic energy inside the convection zone (averaged over the kinematic phase of the dynamo) as a function of the grid spacing,  $\Delta x$ . For this analysis, we also simulated the kinematic phase of the dynamo on grids with  $384^3$  and  $640^3$  cells ( $\Delta x/L_{ref} = 5.2 \times 10^{-3}$ , and  $\Delta x/L_{ref} = 3.1 \times 10^{-3}$ , respectively). Error bars represent three standard deviations, computed over the time series. The expected theoretical scaling for SSD amplification ( $\gamma \propto \text{Re}^{1/2} \propto \Delta x^{-2/3}$ ) is represented by the black dashed line.

The magnetic-to-kinetic energy ratio, shown in Fig. 6, reaches saturation with a mean value of  $\approx 0.22$  on the finest grid, with sporadic, intermittent episodes in which it reaches values as high as 0.33. During the nonlinear phase of the dynamo, the mean kinetic energy density inside the convective shell in the MHD simulations,

$$\tilde{E}_K = \frac{1}{2} \langle \rho |\mathbf{V}|^2 \rangle_{\text{conv}}, \quad (22)$$

is on average 25% lower than that in the hydrodynamic case on the  $512^3$  grid (see Fig. 7). We obtained this result by first computing the time average  $\langle \cdot \rangle$  of  $\tilde{E}_K$  over  $t \in (15\tau_{\text{conv}}, 25\tau_{\text{conv}})$ , and then by calculating

$$\epsilon = \{\tilde{E}_{K,\text{MHD}}\} / \{\tilde{E}_{K,\text{HYDRO}}\} - 1. \quad (23)$$

However, the large temporal fluctuations that characterize  $\tilde{E}_K$  made it necessary to provide an error estimate on  $\epsilon$  in order to prove the statistical significance of this result. The error on  $\epsilon$  is a combination of the statistical uncertainties on  $\{\tilde{E}_{K,\text{HYDRO}}\}$  and  $\{\tilde{E}_{K,\text{MHD}}\}$ , which we computed as follows. First we obtained the standard deviation  $\sigma_K$  of  $\tilde{E}_K$  over the selected time series for both the hydrodynamic and MHD setups. Second, we estimated the statistical uncertainty on the mean quantity  $\{\tilde{E}_K\}$  by taking into account possible temporal correlations introduced by the turbulent nature of the convective flows. According to Fig. 4 of [Andrassy et al. \(2022\)](#), the autocorrelation function of the convective velocity drops to zero after a time shift  $\Delta t \approx \tau_{\text{conv}}$ , which suggests that there is approximately one independent realization of the convective flows per convective turnover. Thus, we approximated the uncertainty associated to  $\{\tilde{E}_K\}$ ,  $\tilde{\sigma}_K$ , as

$$\tilde{\sigma}_K = \frac{\sigma_K}{\sqrt{N_{\text{to}}}}, \quad (24)$$

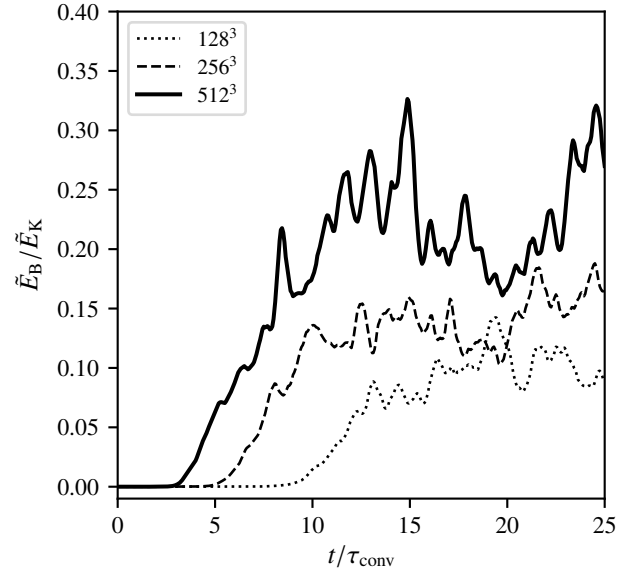


**Fig. 6.** Time evolution of the mean magnetic-to-kinetic energy ratio inside the convective shell.

where  $N_{\text{to}} = 10$  is the number of convective turnovers (see also Table 1). Finally, we computed the variance of  $\epsilon$ ,

$$\sigma_\epsilon^2 = \left( \frac{\partial \epsilon}{\partial \{\tilde{E}_{K,\text{HYDRO}}\}} \right)^2 \tilde{\sigma}_{K,\text{HYDRO}}^2 + \left( \frac{\partial \epsilon}{\partial \{\tilde{E}_{K,\text{MHD}}\}} \right)^2 \tilde{\sigma}_{K,\text{MHD}}^2. \quad (25)$$

We find  $\sigma_\epsilon \approx 3\%$ , making a mean relative deviation of 25% statistically significant (i.e., different from zero) by more than  $8\sigma_\epsilon$ .

In the ILES approach, increasing the grid resolution reduces the amount of numerical resistivity introduced into the system, making the turbulent dynamo progressively more efficient. Consequently, the mean magnetic energy density in our simulations increases by a factor of two from the  $128^3$  to the  $512^3$  grid, where the typical strength of the magnetic field is  $\approx 5 \times 10^9$  G (see Table 2). On the other hand,  $\tilde{E}_K$  does not seem to show a significant resolution dependence when averaged over the saturated phase of the dynamo,  $t \in (15\tau_{\text{conv}}, 25\tau_{\text{conv}})$ , as can be noted from the values provided in Table 1. Averaging over a wider time window could potentially reveal a statistically significant trend in  $\{\tilde{E}_K\}$  with increasing spatial resolution. However, this is not possible with our current setup, in which the convective boundary approaches the upper domain boundary at late times, potentially altering the dynamics of the mixing region and producing unreliable results (see also Sect. 3). We also note that a fixed time-averaging window, in principle, samples different evolutionary times of the dynamo depending on grid resolution. In fact, the oxygen shell does not have a statistical steady state solution, and the time at which the dynamo enters its nonlinear regime is resolution dependent. However, as visible in Fig. 7, neither  $\tilde{E}_K$  nor  $\tilde{E}_B$  show clear, long-term trends in the saturated phase of the dynamo. This result suggests that the secular evolution of the mean stratification can be neglected for this analysis since it does not seem to affect basic properties of the flows and of the dynamo.

The suppression of small-scale shear instabilities in the convective flows caused by the generated strong magnetic fields can be noted in Fig. 8, where we compare snapshots of the Mach number taken from an MHD and a purely hydrodynamic simulation in the nonlinear phase of the dynamo. In contrast to the hydrodynamic case, where turbulence is essentially isotropic

**Table 1.** Mean kinetic energy density (in units of  $\text{erg cm}^{-3}$ ) inside the convection zone, averaged over  $t \in (15\tau_{\text{conv}}, 25\tau_{\text{conv}})$  for the indicated grid resolutions in the hydrodynamic and MHD cases.

$N$	$\tilde{E}_K/10^{20}$ (HYDRO)	$\tilde{E}_K/10^{20}$ (MHD)
128	$1.25 \pm 0.03$	$0.97 \pm 0.03$
256	$1.26 \pm 0.02$	$1.00 \pm 0.03$
512	$1.22 \pm 0.03$	$0.91 \pm 0.03$

**Notes.** The errors represent one standard deviation over the time series divided by  $\sqrt{N_{\text{to}}}$ , where  $N_{\text{to}} = 10$  is the estimated number of independent data points (one per convective turnover).

**Table 2.** Mean magnetic field strength inside the convection zone, averaged over  $t \in (15\tau_{\text{conv}}, 25\tau_{\text{conv}})$  for the indicated grid resolutions.

$N$	$\langle  b  / \sqrt{4\pi} \rangle_{\text{conv}}$ [ $10^9$ G]
128	$3.49 \pm 0.06$
256	$4.24 \pm 0.06$
512	$5.06 \pm 0.08$

**Notes.** The errors represent one standard deviation over the time series divided by  $\sqrt{N_{\text{to}}}$ , where  $N_{\text{to}} = 10$  is the estimated number of independent data points (one per convective turnover).

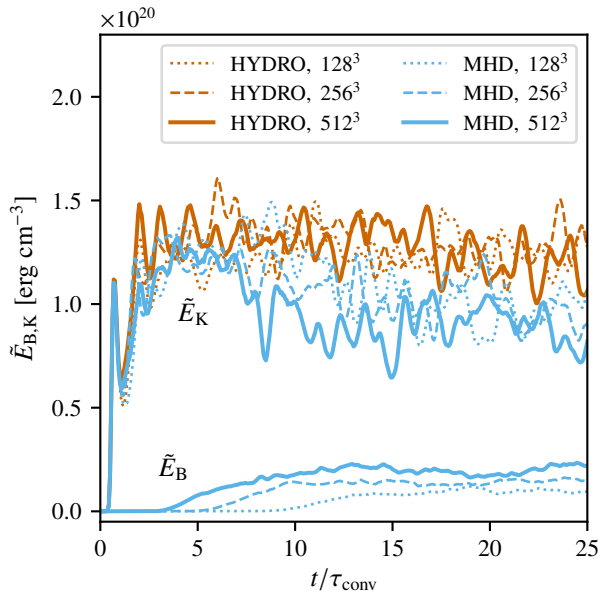


**Fig. 7.** Time evolution of the mean kinetic energy density inside the convection zone,  $\tilde{E}_K$ , for the purely hydrodynamic (vermilion) and MHD (light blue) simulations. The time evolution of the mean magnetic energy density in the MHD simulations,  $\tilde{E}_B$ , is also shown.

on spatial scales smaller than  $L_{\text{ref}}$ , the velocity field in the MHD simulation is characterized by the presence of anisotropic, thread-like structures that extend over a large part of the convective shell.

A comparison of horizontally averaged velocity profiles (see Fig. 9) shows that horizontal velocities in the MHD case are reduced by as much as 30% in the convective layer, as compared to the simulations without magnetic fields. Vertical velocities, instead, are diminished on average only by 10%. As visible in Fig. 10, the partial suppression of the horizontal mixing in

the MHD runs increases the magnitude of the root-mean-square entropy fluctuation inside the convection zone with respect to the hydrodynamic simulations. A larger contrast in the thermal content between up- and downflows in turn increases the efficiency of the convective energy transport. For this reason, despite the mild suppression of vertical velocities in the convection zone caused by the action of the dynamo, we do not observe any significant difference in the vertical enthalpy fluxes,

$$\mathcal{F}_H = \langle (e_{\text{int}} + p)V_y \rangle_{x,z}, \quad (26)$$

between the MHD and the hydrodynamic setups (see Fig. 11). Only in the overshoot layer, where  $\mathcal{F}_H < 0$ , the MHD simulations are characterized by a smaller unsigned enthalpy flux than their hydrodynamic counterpart. This result may be due to the combined effects of reduced flow speeds and entropy fluctuations at the upper convective boundary in the MHD case, as visible in Figs. 9 and 10, respectively.

In Fig. 12, we show the kinetic and magnetic energy spectra computed in the  $y = 1.5 L_{\text{ref}}$  plane, averaged over the saturated phase of the dynamo. The kinetic energy spectra resulting from the hydrodynamic simulations converge to the Kolmogorov scaling ( $k_h^{-5/3}$ , Kolmogorov 1941) in the inertial range. The scale at which the power spectrum deviates from the Kolmogorov law due to the action of numerical dissipation becomes smaller as the resolution is progressively increased, as expected in the ILES approach. The kinetic energy spectra in the MHD simulations, instead, deviate from the hydrodynamic curves already at wavenumbers of  $k_h \approx 10$ , where the dynamo is most efficient at converting kinetic energy into magnetic energy (i.e., it achieves maximum  $|T_{\text{BKT}}|/\tilde{E}_K$ ). The observed drop of kinetic energy in the MHD case corresponds to an increase of magnetic power in the inertial range, and the sum of the two energy contributions approximately resembles the kinetic energy spectrum in the hydrodynamic simulations. The wavenumber at which the magnetic-to-kinetic energy ratio becomes greater than unity decreases on finer grids<sup>4</sup>. On the grid with  $512^3$  cells, the break-even point is at  $k_h = 10$ , which corresponds to approximately half of the pressure scale height at  $y = 1.5 L_{\text{ref}}$ . Unlike the case of forced, isotropic MHD turbulence (Haugen et al. 2004; Schekochihin et al. 2004; Isakov et al. 2007; Brandenburg 2011), our simulations of stratified convection also show a substantial amount (up to 30%) of magnetic power stored at wavenumbers  $k_h < 10$ . This field component is generated by coherent structures in the form of large-scale up- and downflows that stretch the magnetic field lines over a large fraction of the size of the convection zone. The presence of a large-scale field component can be observed in Fig. 13, where we show vertical and horizontal cuts in  $B_y$  for all our three grids. A small-scale component with mixed polarity also becomes more noticeable on progressively finer grids with reduced numerical dissipation.

Both the horizontal and the vertical component of the magnetic field become stronger as the grid is refined (see Fig. 14). The magnetic field smoothly turns horizontal across the upper convective boundary, where the convective flows overturn due to the negative buoyant acceleration. At the bottom of the shell, the magnetic field is forced to be horizontal in order to retain its solenoidal property given the imposed boundary conditions. We note that the reflecting boundary forces the convective flows to abruptly change direction over a few computational cells, which artificially enhances the stretching and the compression

<sup>4</sup> Energy spectra extracted from different planes in the convective shell show qualitatively similar results.



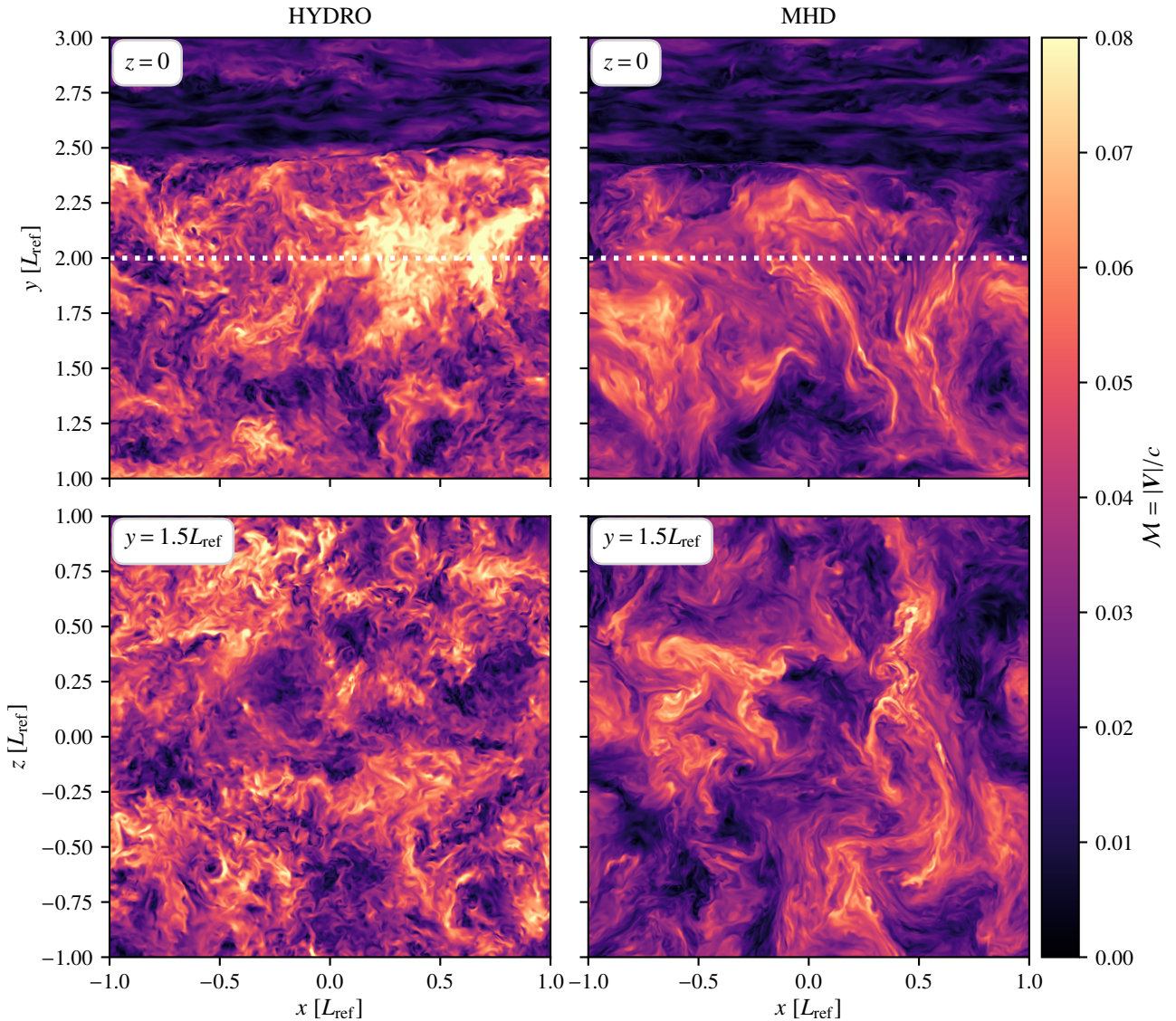


**Fig. 8.** Snapshots of the Mach number on the  $512^3$  grid at  $t/\tau_{\text{conv}} = 22$ . The panels on the left show results from the purely hydrodynamic simulation, while the panels on the right show the MHD simulation. The upper row shows vertical cuts taken in the  $z = 0$  plane, while the lower row shows a horizontal cut through the  $y = 1.5 L_{\text{ref}}$  plane. The white-dotted line indicates the initial position of the convective boundary.

of the magnetic field lines. This process, however, only affects the generation of magnetic energy in a narrow region close to the bottom boundary of the convective shell. In simulations of SSD action in the solar convection zone, [Hotta \(2017\)](#) finds that including part of the underlying stable layer does not appreciably alter the generation of the magnetic field as compared to simulations with closed boundary conditions. This author shows that an imposed steep, positive entropy gradient across the solar overshoot region prevents convective plumes from penetrating into the stable layer deeper than a small fraction of the pressure scale height, at least on the characteristic timescales set by convection. Thus, in those simulations, the bottom boundary of the solar convective region acts like a reflecting wall for the turbulent flows and the magnetic fields. Oxygen-burning shells of massive stars are also characterized by steep, stabilizing entropy gradients at their bottom boundary ([Meakin & Arnett 2007](#); [Jones et al. 2017](#); [Varma & Müller 2021](#)). In the model of [Jones et al. \(2017\)](#), which this setup is based on, the square of the Brunt–Väisälä frequency at the silicon-oxygen boundary is

several times larger than that at the upper boundary of the oxygen shell (see Fig. 4 of [Jones et al. 2017](#)). Because this quantity is directly related to the buoyancy jump, entrainment of material from the underlying stable layer into the convection zone can easily be neglected over the timescales simulated here. All these considerations give us confidence that the chosen boundary conditions are well suited for the simulations presented in this study.

The strength of the magnetic field is not uniform across the convective shell. As previously discussed, the magnetic energy approaches equipartition with the kinetic energy content of the turbulent eddies in the inertial range. Because the mean flow speed does not vary considerably across the convective shell, the spatial dependence of the magnetic field strength is mostly set by the density stratification. Indeed, the vertical profile of the root-mean-square magnetic field rescaled by its local equipartition value ( $B_{\text{eq}} = \sqrt{\rho} V_{\text{rms}}$ ) shows much less dependence on  $y$  as compared with the results shown in Fig. 15. The height-dependence of the dynamo action can also be seen in Fig. 16,



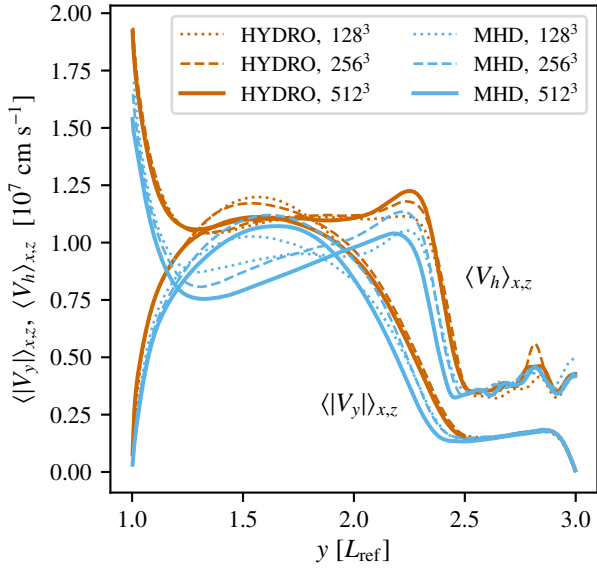


**Fig. 9.** Vertical profiles of the horizontal ( $V_h = \sqrt{V_x^2 + V_z^2}$ ) and vertical ( $V_y$ ) velocity components averaged over  $t \in (15\tau_{\text{conv}}, 25\tau_{\text{conv}})$ . Here, light blue is used to indicate the quantities extracted from the MHD simulations, whereas vermilion is used for the hydrodynamic simulations. An estimate of the statistical uncertainty associated to the averaged profiles can be inferred by looking at the typical dispersion among the hydrodynamic simulations, which represent a set of three independent (and numerically converged) realizations of the oxygen shell.

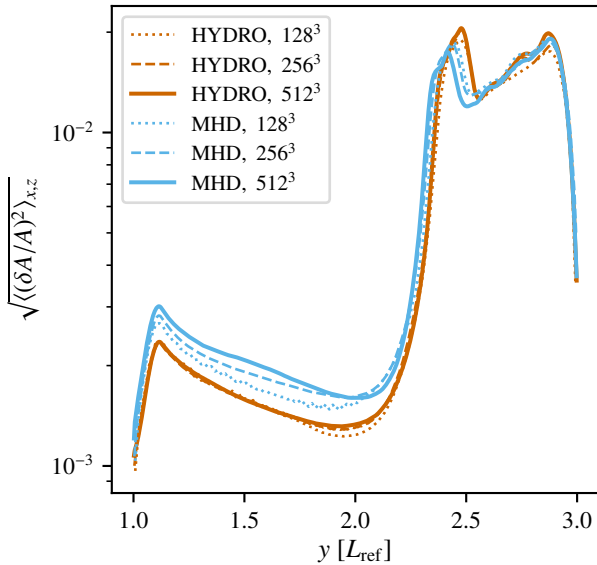


**Fig. 10.** Vertical profiles of the root-mean-square relative pseudo-entropy fluctuation in the MHD (light blue) and purely hydrodynamic simulations (vermilion), averaged over  $t \in (15\tau_{\text{conv}}, 25\tau_{\text{conv}})$ . The upper convective boundary is, on average, at the position of the peaks visible at  $y = (2.3\text{--}2.4) L_{\text{ref}}$ .

where we show horizontal averages of the Lorentz work,

$$W_L = \langle \mathbf{V} \cdot [(\nabla \times \mathbf{B}) \times \mathbf{B}] \rangle_{x,z}. \quad (27)$$

As a reference, we also show the buoyancy work,

$$W_b = \langle V_y g_y \delta \rho \rangle_{x,z}, \quad (28)$$

where  $\delta \rho$  is the density fluctuation. Buoyancy generates kinetic energy in the whole convective shell except in the overshoot

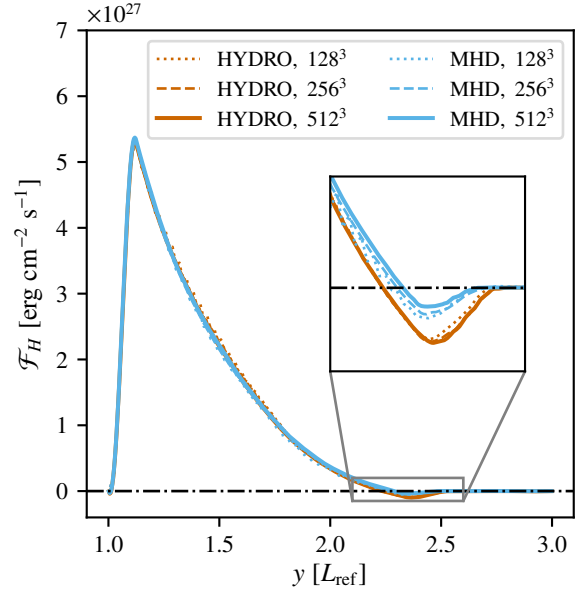


**Fig. 11.** Vertical profiles of the vertical enthalpy flux ( $\mathcal{F}_H$ ) averaged over  $t \in (15\tau_{\text{conv}}, 25\tau_{\text{conv}})$ . Here, light blue is used to indicate the quantities extracted from the MHD simulations, whereas vermilion is used for the hydrodynamic simulations.

layer, where it is responsible for the deceleration of the convective flows. On all grids, the magnitude of the Lorentz work is maximum at the bottom of the convective shell and progressively drops to zero toward the upper convective boundary.  $W_L$  is negative throughout the whole convective layer, meaning that, on average, kinetic energy is everywhere converted into magnetic energy. Moreover, profiles of the Lorentz work approach convergence on the finest grids. This result confirms that most of the conversion of kinetic energy into magnetic energy happens on relatively large spatial scales, which are well resolved even with moderate grid resolutions.

We note that the dynamo does not operate in the subadiabatic layer, although a seed field is present there as well. The turbulent structures created by the nonlinear breaking of IGWs (visible in Fig. 8), which is one of the mechanisms that can excite an SSD in stable stratifications (Skoutnev et al. 2021), are not efficient enough to build a significant magnetic field in these simulations. The magnetic field in the stable layer reaches saturation with average strengths of only two to ten times that of the initial seed field.

#### 4.3. Impact of magnetic fields on the growth of the convective shell

The turbulent convective flows generated in this setup give rise to a rich variety of hydrodynamic processes at the upper convective boundary, including shear instabilities, breaking of surface gravity waves, and convective overshooting. These processes contribute to the entrainment of high-entropy material from the overlying stable layer into the convection zone, which causes the convective shell to grow in time (see also Fig. 8). We computed the mass entrained per unit surface area inside the convection zone by using horizontal averages of the density and the passive tracer  $\psi$  as in Andrassy et al. (2022),

$$M_e(t) = \int_{L_{\text{ref}}}^{y_{\text{cb}}(t)} \bar{\rho}(y, t) \bar{\psi}(y, t) dy. \quad (29)$$

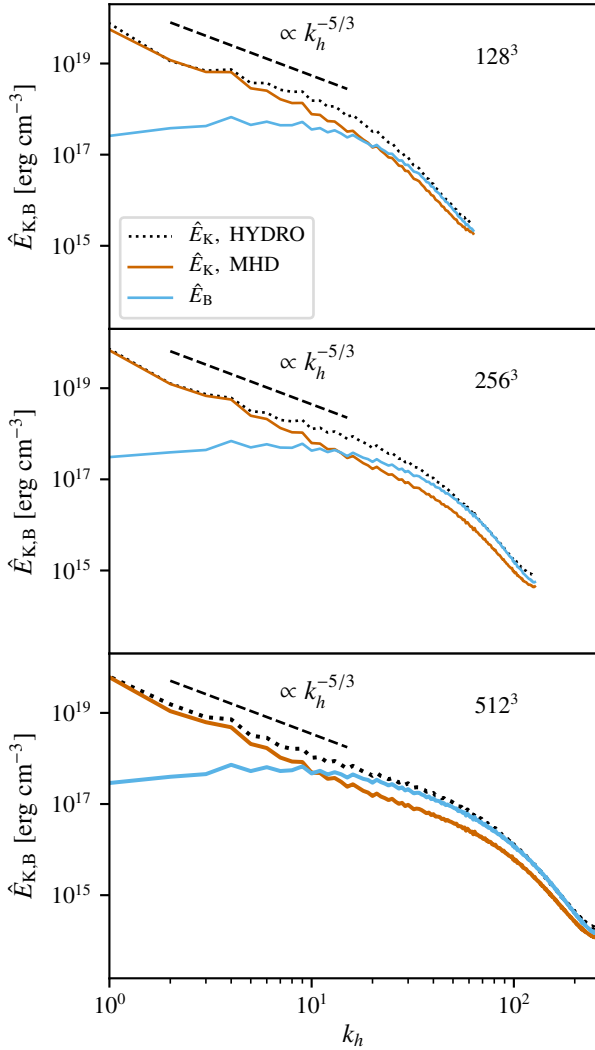


**Fig. 12.** Magnetic (light blue) and kinetic (black-dotted for the hydrodynamic simulations, and vermilion for the MHD simulations) energy spectra computed in the  $y = 1.5 L_{\text{ref}}$  plane and averaged over the time interval  $t \in (15\tau_{\text{conv}}, 25\tau_{\text{conv}})$ . Each panel shows the curves extracted from a different grid. The black-dashed lines indicate the Kolmogorov scaling law,  $k_h^{-5/3}$ .

At each time, we assumed that the vertical coordinate of the upper convective boundary,  $y_{\text{cb}}$ , was the position of the steepest gradient in  $\bar{\psi}$ . In Fig. 17 we show the time evolution of the entrained mass for all the simulations run in this study. In the hydrodynamic case, numerical convergence is reached already on the lowest-resolved grid (with  $128^3$  cells) within a maximum relative statistical uncertainty of 5%, which is consistent with the results obtained by [Andrassy et al. \(2022\)](#). Instead, the mass entrained in the MHD runs slightly decreases with increasing the grid resolution. A significant deviation between the MHD and the hydrodynamic simulations is visible only after  $15\tau_{\text{conv}}$ , when the dynamo has fully entered its nonlinear phase. By the time the simulations have finished, the best resolved MHD setup has entrained 12% less mass than the hydrodynamic runs, and the mass entrainment rate  $\dot{M}_e$  has been reduced by  $\approx 20\%$ .

Because MHD effects do not dramatically reduce the mass entrainment rate at the upper convective boundary, finding the mechanisms responsible for the observed discrepancy in  $\dot{M}_e$  between the MHD and the hydrodynamic results is challeng-

ing. One possible explanation is that convective flows in the MHD simulations have some of their kinetic energy converted into magnetic energy by the action of the SSD (see the discussion in Sect. 4.2), which reduces the amount of energy available to overcome the buoyancy of the entrained high-entropy material as compared to the hydrodynamic case ([Spruit 2015](#)). Furthermore, strong horizontal magnetic fields (see Fig. 14) could considerably reduce the growth rate of the shear instabilities that take place at the convective boundary, which are in part responsible for the mixing. Magnetic fields aligned with the shear flows, in fact, have a stabilizing effect against the growth of Kelvin–Helmholtz instabilities, especially if the Alfvénic Mach number  $\mathcal{M}_{\text{Alf}} = \sqrt{\rho}|V|/|B|$  is close to unity ([Chandrasekhar 1961](#); [Frank et al. 1996](#)). As shown in Fig. 15, the mean magnetic field at the upper convective boundary reaches values as high as 60% of the equipartition field ( $\mathcal{M}_{\text{Alf}} \gtrsim 1.5$ ), so short-wavelength Kelvin–Helmholtz instabilities are likely to be partly suppressed.

As pointed out by a number of authors ([Meakin & Arnett 2007](#); [Andrassy et al. 2020, 2023](#); [Horst et al. 2020](#)), some degree of mixing at stellar convective boundaries can be induced by nonadiabatic effects. In this setup, the mean entropy inside the convection zone increases by the action of the heat source, and eventually overcomes the entropy level of a narrow subadiabatic layer right above the upper convective boundary. This layer becomes negatively buoyant, so it sinks and gets mixed into the convection zone. This process enlarges the size of the convective shell over time as long as the source of entropy generation is active. In the work of [Andrassy et al. \(2022\)](#), it was estimated that by the end of the simulations,  $\approx 60\%$  of  $M_e$  in this setup was due to the heating. This process is expected to operate regardless of the properties of the convective flows, so MHD processes would only be able to affect the remaining 40% of the entrainment rate. In the absence of heating-induced mixing, magnetic fields would then suppress as much as 50% of the mass entrainment.

## 5. Summary and discussion

We have run 3D simulations of turbulent convection, dynamo amplification and convective boundary mixing in an idealized oxygen-burning shell of a  $25 M_{\odot}$  star. In particular, we have searched for possible MHD effects on the boundary mixing and the properties of the convective flows by performing a comparison between an MHD and a purely hydrodynamic setup. The numerical results have been carefully analyzed by means of a convergence study, in which the grid resolution was progressively increased from  $128^3$  to  $512^3$  cells.

Random stretching of the magnetic field lines due to the turbulent motions in the convective shell excites small-scale dynamo (SSD) action on all of the considered grids. The dynamo instability amplifies the seed field by  $\approx 4$  orders of magnitude in a few convective turnover timescales. The kinematic phase of the dynamo ends when the magnetic field becomes strong enough to affect the evolution of the flows on the small scales of turbulence. During the saturated stage, the work done by fluid motions against magnetic tension forces sustains the magnetic field against numerical resistive dissipation. The saturated mean magnetic-to-kinetic energy ratio reaches values in the 20–30% range. The magnetic field strength in the oxygen shell moderately increases with the grid resolution, and it has characteristic values of  $\sim 10^{10}$  G in the  $512^3$  simulation. Such strong fields partly suppress the small-scale isotropic features in the velocity field typical of turbulent convection in hydrodynamic simulations. The resulting flows present anisotropic,

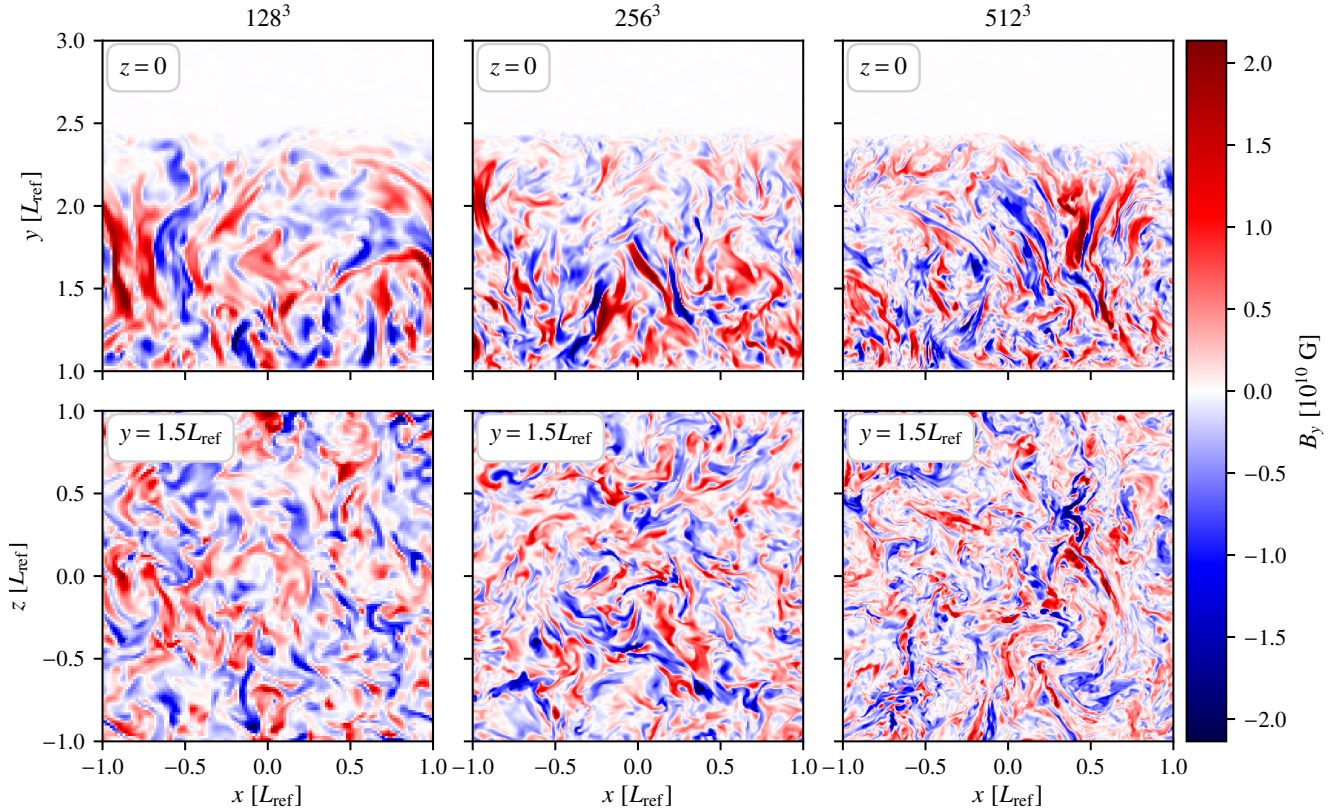


**Fig. 13.** Distribution of  $B_y$  on the  $z = 0$  plane (upper row) and the  $y = 1.5 L_{\text{ref}}$  plane (lower row) at  $t/\tau_{\text{conv}} = 22$  for the indicated grid resolutions.

thread-like structures that extend over a large fraction of the convective shell. The magnetic fields generated during the oxygen burning stage can be further amplified if parts of the oxygen shell end up collapsing onto a neutron star. By assuming a simple flux-freezing model, we estimate that the magnetic field strength at the surface of the neutron star would be on the order of  $10^{15}$ – $10^{16}$  G, which is in agreement with values inferred from observations of magnetars (Kouveliotou et al. 1998; Woods & Thompson 2006; Olausen & Kaspi 2014).

Vertical and horizontal fluid velocities in the bulk of the convective layer in the MHD simulations are reduced, as compared to the hydrodynamic runs, on average by 10% and 20%, respectively. The fact that the dynamo does not have the same impact on the different fluid velocity components could be related to the transport of thermal energy inside the convection zone. In fact, in order for convection to transport the excess heat deposited by the energy source outward with partly suppressed vertical velocities, the thermal content of the buoyant flows must be enhanced. Because the heat source is unchanged in the MHD simulations, this can only be achieved by reducing the horizontal mixing of entropy between the up- and the downflows. Indeed, we observe that root-mean-square entropy fluctuations are systematically enhanced in the MHD simulations, which in turn increases the thermal contrast between the convective plumes. Consequently, we do not observe a significant impact of magnetic fields on the vertical enthalpy fluxes.

Power spectra computed in the bulk of the convective shell reveal that 30% of the total magnetic energy is stored at spatial wavenumbers  $k_h < 10$ . Such a large-scale field component is generated by large-scale convective cells, which can efficiently stretch the magnetic field lines on length scales comparable to the size of the convection zone. The kinetic energy spectra in the MHD sim-

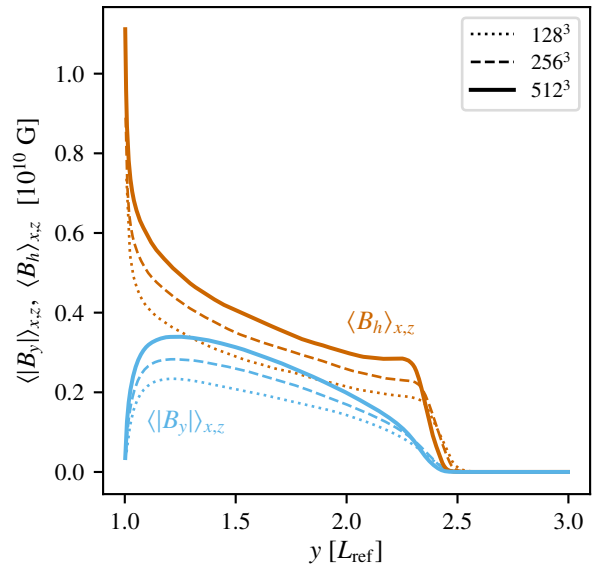


**Fig. 14.** Vertical profiles of the horizontal ( $B_h = \sqrt{B_x^2 + B_z^2}$ ) and vertical ( $B_y$ ) magnetic field, averaged over the time interval  $t \in (15\tau_{\text{conv}}, 25\tau_{\text{conv}})$ .

ulations deviate from the Kolmogorov law ( $k_h^{-5/3}$ ) in the inertial range, where the efficiency of the dynamo is maximum. On the finest grid, the magnetic energy becomes greater than the kinetic energy at a spatial wavenumber of  $k_h \approx 10$ , corresponding to half of a pressure scale height in the convection zone.

The mass entrained into the convection zone in the MHD case is smaller by 12% than that in the hydrodynamic setup.

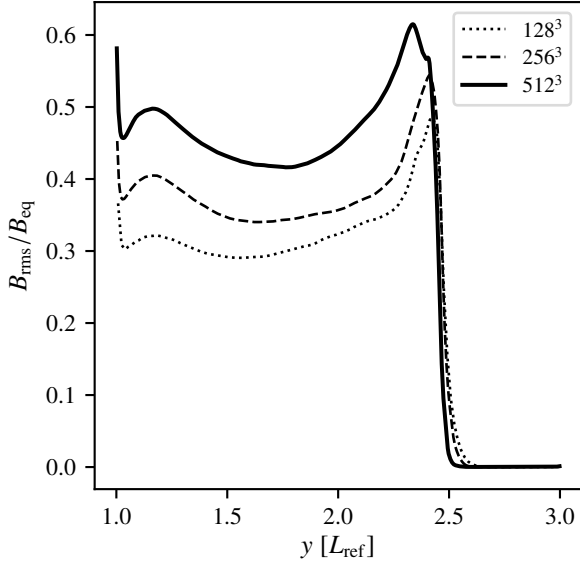


**Fig. 15.** Vertical profiles of the root-mean-square magnetic field divided by the equipartition field, averaged over the time interval  $t \in (15\tau_{\text{conv}}, 25\tau_{\text{conv}})$ .

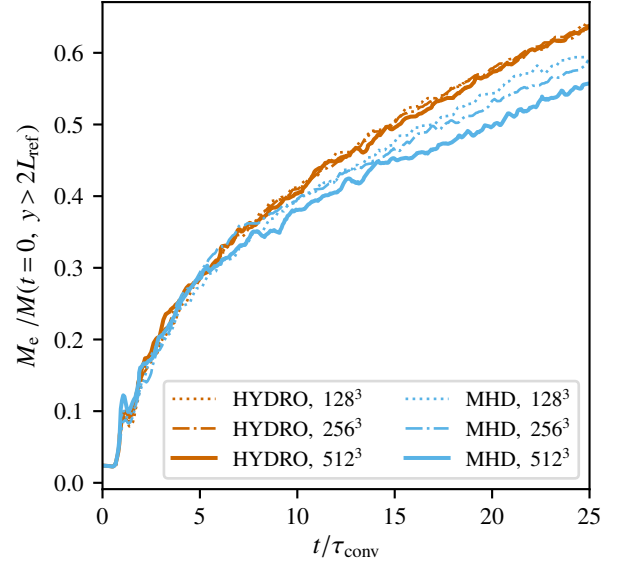


**Fig. 17.** Time evolution of the mass entrained from the stable layer into the convection zone, rescaled by the total mass contained in the stable layer at  $t = 0$  s. Light blue is used for the MHD simulations, whereas vermilion is used for the purely hydrodynamic runs.

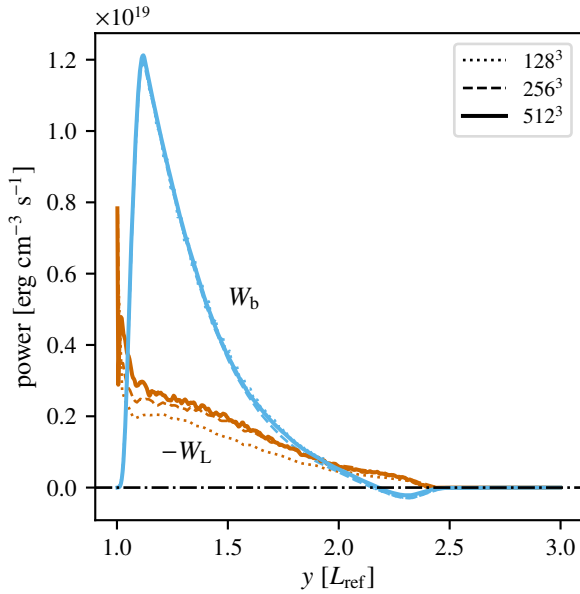


**Fig. 16.** Vertical profiles of the buoyancy (light blue) and Lorentz work (vermilion) averaged over  $t \in (15\tau_{\text{conv}}, 25\tau_{\text{conv}})$  for the indicated grid resolutions.

The partial suppression of the mixing at the convective boundary correlates with the average strength of the magnetic field in the convection zone. It is possible that the reduction of the kinetic energy of the convective flows caused by the action of the small-scale turbulent dynamo and the presence of magnetic fields with strengths up to 60% of the equipartition value at the convective boundary contribute to the partial suppression of the mixing. By the end of the simulations, the mass entrainment rate is reduced by 20% with respect to the hydrodynamic simulations.

In our simulations, SSDs seem to have only a mild effect on the growth of the convective oxygen shell. This is consistent with the findings of Varma & Müller (2021), who ran global MHD simulations of an oxygen shell in an  $18 M_{\odot}$  star. Overall, these authors do not observe any significant impact of the small-

scale turbulent dynamo on the properties of the convective flows as compared to a non-MHD simulation. Those results, however, may have been affected by low effective Reynolds numbers, which are typical for global simulations of turbulent convection at moderate grid resolutions. Our “box-in-a-star” approach, used in combination with special numerical solvers optimized for tackling stratified, subsonic magnetoconvection, allows us to achieve much higher effective resolution than that obtained by Varma & Müller (2021). We find that the small-scale turbulent dynamo reduces the kinetic energy content of the convective shell by 25% on average and significantly changes the topology of the velocity field with respect to the purely hydrodynamic problem. These results are particularly important in the context of the “perturbation-aided” explosion mechanism, whose efficiency is set by both the magnitude of the convective velocities and the typical spatial scales of convection in the burning shells of the supernova progenitor (Müller et al. 2017; Couch et al. 2020).

One point of concern is related to the usage of the Implicit Large Eddy Simulation (ILES) approach in this study, which gives rise to effective magnetic Prandtl numbers  $\text{Pr}_m = \nu/\eta$  close to or even larger than unity. Such large values of  $\text{Pr}_m$  are an overestimation of the actual conditions found in oxygen-burning shells. Based on the analytic expressions of the viscous and resistive coefficients provided in Augustson et al. (2019), we estimate that realistic magnetic Prandtl numbers in the oxygen shell considered here range from  $\text{Pr}_m = 0.001$  to  $\text{Pr}_m = 0.1$ . It is well known that certain properties of the small-scale turbulent dynamo are sensitive to the value of  $\text{Pr}_m$ . In particular, the strength of the saturated magnetic field is often found to be an increasing function of  $\text{Pr}_m$  (Schekochihin et al. 2004; Brandenburg 2011; Käpylä et al. 2018). Unfortunately, no general consensus has been reached so far as to the behavior of SSDs at low  $\text{Pr}_m$ , which is likely setup dependent. More MHD simulations of the oxygen-burning phase with realistic Prandtl numbers are therefore required in order to properly establish the impact of magnetic fields on the dynamics of the convective shell. Finally, we did not include a nuclear-burning network in



our simplified setup, so further investigation on possible indirect effects of magnetic fields on the nuclear energy generation and nucleosynthesis is certainly needed.

*Acknowledgements.* The work of G.L. and F.K.R. was supported by the German Research Foundation (DFG) through the grant RO 3676/3-1. P.V.F.E. was supported by the US Department of Energy through the Los Alamos National Laboratory (LANL). LANL is operated by Triad National Security, LLC, for the National Nuclear Security Administration of the US Department of Energy (Contract No. 89233218CNA000001). This work has been assigned a document release number LA-23-27290. G.L., R.A., J.H., and F.K.R. acknowledge support by the Klaus Tschira Foundation. The authors would like to thank Hirschi R., Rizzuti F., and Varma V. (Keele University) for fruitful discussions and hosting a visit to Keele University.

## References

- Aerts, C. 2021, *Rev. Mod. Phys.*, **93**, 015001
- Anders, E. H., & Pedersen, M. G. 2023, *Galaxies*, **11**, 56
- Andrassy, R., Herwig, F., Woodward, P., & Ritter, C. 2020, *MNRAS*, **491**, 972
- Andrassy, R., Higl, J., Mao, H., et al. 2022, *A&A*, **659**, A193
- Andrassy, R., Leidi, G., Higl, J., et al. 2023, *A&A*, submitted [arXiv:2307.04068]
- Aparicio, A., Bertelli, G., Chiosi, C., & Garcia-Pelayo, J. M. 1990, *A&A*, **240**, 262
- Augustson, K. C., Brun, A. S., & Toomre, J. 2016, *ApJ*, **829**, 92
- Augustson, K. C., Brun, A. S., & Toomre, J. 2019, *ApJ*, **876**, 83
- Baraffe, I., Clarke, J., Morison, A., et al. 2023, *MNRAS*, **519**, 5333
- Berberich, J. P., Chandrasekhar, P., & Klingenberg, C. 2021, *Comput. Fluids*, **219**, 104858
- Bhatia, T. S., Cameron, R. H., Solanki, S. K., et al. 2022, *A&A*, **663**, A166
- Blouin, S., Mao, H., Herwig, F., et al. 2023, *MNRAS*, **522**, 1706
- Böhm-Vitense, E. 1958, *Z. Astrophys.*, **46**, 108
- Bossini, D., Miglio, A., Salaris, M., et al. 2015, *MNRAS*, **453**, 2290
- Brandenburg, A. 2009, in *Advances in Theory and Simulations of Large-Scale Dynamos*, eds. M. J. Thompson, A. Balogh, J. L. Culhane, et al. (New York: Springer), 87
- Brandenburg, A. 2011, *ApJ*, **741**, 92
- Brandenburg, A., & Subramanian, K. 2005, *Phys. Rep.*, **417**, 1
- Browning, M. K. 2008, *ApJ*, **676**, 1262
- Brun, A., & Browning, M. 2017, *Liv. Rev. Sol. Phys.*, **14**, 4
- Brun, A. S., Browning, M. K., & Toomre, J. 2005, *ApJ*, **629**, 461
- Canivete Cuissa, J. R., & Teyssier, R. 2022, *A&A*, **664**, A24
- Canuto, V. M. 1997, *ApJ*, **482**, 827
- Canuto, V. M. 2011, *A&A*, **528**, A78
- Chandrasekhar, S. 1961, *Hydrodynamic and Hydromagnetic Stability* (Oxford: Clarendon Press)
- Charbonneau, P. 2013, *Solar and Stellar Dynamos: Saas-Fee Advanced Course 39 Swiss Society for Astrophysics and Astronomy* (Berlin, Heidelberg: Springer-Verlag)
- Claret, A., & Torres, G. 2016, *A&A*, **592**, A15
- Colella, P., & Woodward, P. R. 1984, *J. Comput. Phys.*, **54**, 174
- Couch, S. M., Warren, M. L., & O'Connor, E. P. 2020, *ApJ*, **890**, 127
- Cristini, A., Meakin, C., Hirschi, R., et al. 2017, *MNRAS*, **471**, 279
- Edelmann, P. V. F., Röpke, F. K., Hirschi, R., Georgy, C., & Jones, S. 2017, *A&A*, **604**, A25
- Edelmann, P. V. F., Horst, L., Berberich, J. P., et al. 2021, *A&A*, **652**, A53
- Evans, C. R., & Hawley, J. F. 1988, *ApJ*, **332**, 659
- Featherstone, N. A., Browning, M. K., Brun, A. S., & Toomre, J. 2009, *ApJ*, **705**, 1000
- Frank, A., Jones, T. W., Ryu, D., & Gaalaas, J. B. 1996, *ApJ*, **460**, 777
- Garaud, P., Ogilvie, G. I., Miller, N., & Stellmach, S. 2010, *MNRAS*, **407**, 2451
- Gardiner, T. A., & Stone, J. M. 2005, *J. Comput. Phys.*, **205**, 509
- Gilet, C., Almgren, A. S., Bell, J. B., et al. 2013, *ApJ*, **773**, 137
- Haugen, N. E. L., Brandenburg, A., & Dobler, W. 2004, *Phys. Rev. E*, **70**, 016308
- Herwig, F., Woodward, P. R., Mao, H., et al. 2023, *MNRAS*, **525**, 1601
- Higl, J., Müller, E., & Weiss, A. 2021, *A&A*, **646**, A133
- Horst, L., Edelmann, P. V. F., Andrassy, R., et al. 2020, *A&A*, **641**, A18
- Horst, L., Hirschi, R., Edelmann, P. V. F., Andrassy, R., & Röpke, F. K. 2021, *A&A*, **653**, A55
- Hotta, H. 2017, *ApJ*, **843**, 52
- Hotta, H., Rempel, M., & Yokoyama, T. 2016, *Science*, **351**, 1427
- Iskakov, A. B., Schekochihin, A. A., Cowley, S. C., McWilliams, J. C., & Proctor, M. R. E. 2007, *Phys. Rev. Lett.*, **98**, 208501
- Jermyn, A. S., Anders, E. H., Lecoanet, D., & Cantiello, M. 2022, *ApJS*, **262**, 19
- Jones, S., Andrassy, R., Sandalski, S., et al. 2017, *MNRAS*, **465**, 2991
- Joyce, M., & Chaboyer, B. 2018, *ApJ*, **856**, 10
- Käpylä, P. J. 2019, *A&A*, **631**, A122
- Käpylä, P. J. 2021, *A&A*, **651**, A66
- Käpylä, P. J., Käpylä, M. J., & Brandenburg, A. 2018, *Astron. Nachr.*, **339**, 127
- Kazantsev, A. P. 1968, *Sov. J. Exp. Theor. Phys.*, **26**, 1031
- Keszthelyi, Z. 2023, *Galaxies*, **11**, 40
- Kippenhahn, R., Weigert, A., & Weiss, A. 2013, *Stellar Structure and Evolution* (Berlin, Heidelberg: Springer)
- Kolmogorov, A. 1941, *Akademiia Nauk SSSR Doklady*, **30**, 301
- Kouveliotou, C., Dieters, S., Strohmayer, T., et al. 1998, *Nature*, **393**, 235
- Kuhfuss, R. 1986, *A&A*, **160**, 116
- Leidi, G., Birke, C., Andrassy, R., et al. 2022, *A&A*, **668**, A143
- Li, Y., & Yang, J. Y. 2007, *MNRAS*, **375**, 388
- Maeder, A. 2009, *Physics, Formation and Evolution of Rotating Stars* (Berlin, Heidelberg: Springer)
- Magic, Z., Weiss, A., & Asplund, M. 2015, *A&A*, **573**, A89
- Meakin, C. A., & Arnett, D. 2007, *ApJ*, **667**, 448
- Meneguzzi, M., Frisch, U., & Pouquet, A. 1981, *Phys. Rev. Lett.*, **47**, 1060
- Miczek, F., Röpke, F. K., & Edelmann, P. V. F. 2015, *A&A*, **576**, A50
- Minoshima, T., & Miyoshi, T. 2021, *J. Comput. Phys.*, **446**, 110639
- Miyoshi, T., & Kusano, K. 2005, *J. Comput. Phys.*, **208**, 315
- Mocák, M., Meakin, C., Campbell, S. W., & Arnett, W. D. 2018, *MNRAS*, **481**, 2918
- Müller, B. 2020, *Liv. Rev. Comput. Astrophys.*, **6**, 3
- Müller, B., & Varma, V. 2020, *MNRAS*, **498**, L109
- Müller, B., Melson, T., Heger, A., & Janka, H.-T. 2017, *MNRAS*, **472**, 491
- Olausen, S. A., & Kaspi, V. M. 2014, *ApJS*, **212**, 6
- Pietarila Graham, J., Cameron, R., & Schüssler, M. 2010, *ApJ*, **714**, 1606
- Prandtl, L. 1925, *Zeitschrift Angewandte Mathematik und Mechanik*, **5**, 136
- Pratt, J., Baraffe, I., Goffrey, T., et al. 2016, *A&A*, **593**, A121
- Rempel, M. 2014, *ApJ*, **789**, 132
- Richard, O., Vauclair, S., Charbonnel, C., & Dziembowski, W. A. 1996, *A&A*, **312**, 1000
- Ritter, C., Andrassy, R., Côté, B., et al. 2018, *MNRAS*, **474**, L1
- Rizzuti, F., Hirschi, R., Arnett, W. D., et al. 2023, *MNRAS*, **523**, 2317
- Schekochihin, A. A., Cowley, S. C., Taylor, S. F., Maron, J. L., & McWilliams, J. C. 2004, *ApJ*, **612**, 276
- Schekochihin, A. A., Iskakov, A. B., Cowley, S. C., et al. 2007, *New J. Phys.*, **9**, 300
- Shu, C.-W., & Osher, S. 1988, *J. Comput. Phys.*, **77**, 439
- Skoutnev, V., Squire, J., & Bhattacharjee, A. 2021, *ApJ*, **906**, 61
- Sonoi, T., Ludwig, H. G., Dupret, M. A., et al. 2019, *A&A*, **621**, A84
- Spruit, H. C. 2015, *A&A*, **582**, L2
- Thaler, I., & Spruit, H. C. 2015, *A&A*, **578**, A54
- Trampedach, R., Stein, R. F., Christensen-Dalsgaard, J., Nordlund, Å., & Asplund, M. 2014, *MNRAS*, **442**, 805
- Valle, G., Dell'Omodarme, M., Prada Moroni, P. G., & Degl'Innocenti, S. 2016, *A&A*, **587**, A16
- Varma, V., & Müller, B. 2021, *MNRAS*, **504**, 636
- Varma, V., & Müller, B. 2023, *MNRAS*, **526**, 5249
- Vögler, A., & Schüssler, M. 2007, *A&A*, **465**, L43
- Woods, P. M., & Thompson, C. 2006, *Compact Stellar X-ray Sources* (Cambridge: Cambridge University Press)
- Xiong, D.-R. 1978, *Chin. Astron.*, **2**, 118
- Yadav, N., Müller, B., Janka, H. T., Melson, T., & Heger, A. 2020, *ApJ*, **890**, 94



# CHAPTER 4

---

## Conclusions

---

This thesis focused on the development and application of a numerical scheme optimized for modeling MHD flows in stellar interiors. This kind of simulations is crucial to improve current theories of stellar evolution and to gain insight into the explosion mechanism of core-collapse supernovae. As discussed in Chapter 1, the dynamical conditions found in the interior of stars pose various challenges to the widely popular high-resolution shock-capturing (HRSC) methods for MHD, which are mostly suited for supersonic flows. The low Mach MHD scheme proposed in this work overcomes the numerical difficulties faced by HRSC methods, thus enabling the exploration of magnetized flow regimes that were previously inaccessible.

An implementation of this scheme is now available in the finite-volume SLH code. In Sect. 3.3, the newly developed MHD method saw a first astrophysical application in production-quality simulations of turbulent dynamo action in an oxygen-burning shell of a massive star. These simulations allow us to study the impact of strong magnetic fields on the dynamical evolution of the convective flows in the oxygen shell and are a first step toward building accurate models of core-collapse supernova progenitors.

Section 4.1 gives a short summary of the publications presented in Chapter 3. The main results of this thesis are then discussed in the context of stellar evolution modeling in Sect. 4.2, along with an outlook on potential future applications of the new MHD capabilities of SLH.

### 4.1 Summary of the individual publications

#### 4.1.1 Implementation of a low-Mach scheme optimized for stellar MHD flows [Section 3.1]

Conservative, finite-volume methods for ideal MHD are routinely used in simulations of highly magnetized and supersonic flows, but they are inadequate for low-Mach-number flow regimes. Three major shortcomings limit their use when modeling MHD flows in stellar interiors, namely the overly strict CFL condition on the time step, the large numerical dissipation introduced by standard approximate Riemann solvers, and discretization errors that destroy the hydrostatic equilibrium of the background stratification.

The main deficiencies of HRSC schemes have been corrected in the work presented in Sect. 3.1. First, the strict condition on the time step is overcome using a semi-implicit time discretization technique, in which the induction equation is solved explicitly while the rest of the system is advanced with an implicit time stepper. These two integration substeps are then coupled via Strang splitting. The resulting implicit-explicit Strang splitting (IESS) method maintains numerical stability even over the relatively long Alfvén and advective time steps, thus significantly increasing the overall efficiency of the code. Second, the flawed Mach number scaling of the numerical

dissipation is adjusted by means of a low-dissipation Riemann solver, which retrieves the correct asymptotic limit of the MHD equations as  $\mathcal{M} \rightarrow 0$ . Third, a well-balancing method is used to preserve hydrostatic solutions on the finite grid.

Five verification benchmarks have been designed to put the newly implemented scheme to the test and to infer its numerical properties. These tests include a linear wave analysis, a stable magnetized vortex, a smooth Kelvin–Helmholtz instability, a buoyant bubble rising in a strongly stratified medium, and a small-scale turbulent dynamo in a setup whose thermodynamic conditions are close to that of an oxygen-burning shell of a massive star.

The low Mach MHD method successfully passed the benchmarks. These numerical experiments also allowed the main numerical properties of IESS to be quantified. In particular, this study showed that i) the IESS method is second-order accurate in both space and time; ii) SLH can model magnetized flows even at Mach numbers of  $10^{-5} - 10^{-4}$ , which correspond to the lowest values expected for stellar convection; iii) thanks to the use of a semi-implicit time discretization technique, the proposed MHD method is  $\approx 100$  faster than a scheme based on explicit time steppers when modeling flows at  $\mathcal{M} = 10^{-4}$ ; iv) although IESS is not optimized for strongly magnetized plasmas, it performs relatively well even at a plasma- $\beta$  of 0.01; v) the low-dissipation solver allows stratified, small-scale dynamos to be excited even on coarse grids spanning only 16 cells per pressure scale height.

#### **4.1.2 Comparison of higher-order Godunov-type methods in simulations of astrophysical subsonic flows [Section 3.2]**

In the second publication (see Sect. 3.2), all combinations of 6 spatial reconstruction schemes and 3 Riemann solvers were compared using two test problems involving subsonic flows only. These included a convergable Kelvin–Helmholtz instability and a setup involving turbulent convection, convective boundary mixing, and excitation of internal waves. The goal of this study was to assess the computational cost of each combination of methods required to achieve a desired accuracy in the numerical solution.

It was found that higher than second order, unlimited reconstruction methods generate strong undershoots and overshoots in regions where the conservative quantities are characterized by large gradients. These numerical artifacts do not appear (or are significantly reduced) in simulations using TVD methods. On the other hand, TVD methods introduce artificial acoustic noise that dominates the spectrum of physical, high-frequency waves, whereas unlimited reconstructions produce much cleaner spectra. By extracting the dissipation length scale from the kinetic energy spectrum of turbulent flows, it was possible to measure the computational effort required by each combination of methods to resolve a given spatial scale in the turbulent flow field. In particular, the least efficient method (i.e., van Leer reconstruction with the Rusanov solver) is  $\approx 10000$  less efficient than a low-dissipation solver combined with a 7<sup>th</sup>-order reconstruction method. Moreover, the low-dissipation scheme always outmatches the HLLC solver when the spatial reconstruction is fixed.

This study also showed that no single reconstruction method is ideal for all problems of stellar hydrodynamics. If artificial overshoots are largely to be avoided in the simulation, as it may be necessary in studies of convective boundary mixing, the PPM method of [Colella and Woodward \(1984\)](#) or the modification to PPM of [Colella and](#)

[Sekora \(2008\)](#) are the most suitable choices. If internal waves need to be modeled accurately without generating excessive overshoots near steep thermal stratifications, an unlimited parabolic method is preferable instead.

### 4.1.3 Simulations of turbulent dynamo action in an oxygen-burning shell [Section 3.3]

The new numerical MHD scheme optimized for stellar MHD flows presented in Sect. 3.1 was used to simulate the excitation of a small-scale turbulent dynamo in a convective oxygen shell of a  $25 M_{\odot}$  star (see Sect. 3.3). This problem involves convective boundary mixing processes occurring at the upper boundary of the shell, which enlarge the size of the convective region over time. In light of the results obtained in the comparison study shown in Sect. 3.2, the PPM method of [Colella and Woodward \(1984\)](#) was chosen to perform the spatial reconstruction of the Riemann states at the grid cell boundaries. The initial stratification of the shell was taken from [Andrassy et al. \(2022\)](#), to which a weak seed field was added to trigger dynamo amplification.

A small-scale dynamo is successfully excited on all of the grids considered in this study. The weak initial seed field ( $B_x = 10^5$  G) is amplified exponentially to values on the order of  $10^{10}$  G. The instability proceeds until the magnetic field becomes strong enough to back-react on the flow, suppressing the small scale features in the velocity field. In the subsequent saturated phase of the dynamo, the total magnetic energy inside the convection zone stabilizes around values close to 30% of the kinetic energy content of the convection. Such strong fields reduce the average speed of the convective flows and suppress shear instabilities at the convective boundary of the oxygen shell. Consequently, the rate of convective boundary mixing in the MHD simulations is reduced by 20% as compared to simulations run without magnetic fields.

These simulations proved that turbulent dynamo action is strong enough to change the typical spatial scales of convection and the magnitude of fluctuations of thermodynamic quantities around the hydrostatic state. Therefore, magnetic fields cannot be ignored in the context of the perturbation-aided supernova explosion scenario. Furthermore, less efficient mixing at convective boundaries may have implications for shell mergers.

## 4.2 Discussion and outlook

### 4.2.1 Low-Mach-number modeling of stellar MHD flows

The novel MHD method developed in this thesis has proven to be a powerful tool for modeling fully compressible, magnetized flows at the dynamical conditions found in the interior of stars. In Sect. 3.1, the IESS method implemented in SLH was used to simulate small-scale turbulent dynamo action at mean Mach numbers of  $\approx 10^{-4}$ , but in principle flows with even lower Mach numbers can be modeled. Only at Mach numbers of  $10^{-8} - 10^{-7}$  do rounding errors due to the finite precision of floating-point arithmetic significantly affect the quality of the numerical solution<sup>1</sup> (e.g., [Edelmann](#)

---

<sup>1</sup>In low-Mach flows, the amplitude of the fluctuations of the thermodynamic quantities relative to their mean state is approximately  $\mathcal{M}^2$ . Therefore, at  $\mathcal{M} \approx 10^{-8}$ , the relative physical fluctuations produced by the flow are comparable to the machine epsilon of double-precision numbers ( $\epsilon \approx 2.22 \times 10^{-16}$ ). However, rounding errors can build up to significant values at even higher Mach numbers if the number

et al., 2021). Since the Mach number of convection in stars is usually higher than  $10^{-5}$  (e.g., Jermyn et al., 2022), SLH is suited to model all stages of stellar evolution, from the main sequence of low-mass, fully convective stars to the last moments before the collapse of the iron core in massive stars.

To date, no conservative scheme other than that implemented in SLH has been presented in the literature that is capable of simulating highly subsonic stellar MHD flows without modifying the original set of ideal MHD equations. A few pressure-based methods have recently been developed for low Mach MHD, but they do not include gravitational sources (Dumbser et al., 2019; Fambri, 2021). Other conservative, time-implicit codes optimized for fully compressible, low Mach stellar flows, such as MUSIC (e.g., Viallet et al., 2011) or ANTARES (e.g., Muthsam et al., 2010), do not have MHD capabilities. Thus, SLH is so far the only code that can efficiently model fully compressible MHD flows in the regions deep inside stars, which are beyond the reach of other methods developed for stellar MHD as discussed in Sect. 1. In fact, thanks to the use of semi-implicit time discretization techniques, SLH is about 10 or 100 times faster than state-of-the-art stellar MHD codes when the Mach number of the flow is  $10^{-3}$  or  $10^{-4}$ , respectively. Specialized Riemann solvers and well-balancing methods allow SLH to achieve high effective Reynolds numbers in simulations of turbulent flows and drive turbulent dynamos even on relatively coarse grids. When modeling flows at  $\mathcal{M} \approx 10^{-3}$ , conventional methods typically need to use grids that are 4 times finer than those used by SLH to achieve the same accuracy in the numerical solution, making the simulation 256 times more expensive in 3D (see Sect. 3.1 and 3.2).

#### 4.2.1.1 How to choose the optimal combination of numerical methods in simulations of stellar MHD flows

The study presented in Sect. 3.2 has shown that the choice of Riemann solver and spatial reconstruction scheme has profound consequences on the quality of the numerical solution in simulations of subsonic astrophysical flows. The low-dissipation solver proposed by Minoshima and Miyoshi (2021) is easy to implement in any Godunov-like code and has a negligible impact on the number of floating point operations per second. When the Mach number of the flow is  $\approx 10^{-2}$ , the use of a low-dissipation Riemann solver reduces the computational cost of the simulation per fixed accuracy by a factor of 2 to 10 compared to shock-capturing methods, depending on the spatial reconstruction method used. At even lower Mach numbers, such as those found in the convective cores of massive main-sequence stars, the difference in performance between asymptotic-preserving methods and HRSC schemes is even more dramatic. The choice of spatial reconstruction depends mainly on the astrophysical setup. In general, the use of higher-order methods sensibly reduces the amount of numerical dissipation introduced into the system compared to second-order reconstruction schemes. Higher-order TVD methods should be preferred to unlimited reconstructions in simulations where preserving the boundness of the solution is crucial for the correct treatment of the physical processes of interest. For example, mass fractional abundances should always be bounded between 0 and 1 to avoid any need to clip unphysical abundances, which would lead to mass conservation errors. In addition, strong overshoots in the state quantities at steep stellar convective boundaries might lead to incorrect conclusions about convective boundary mixing processes. On the

---

of integration steps is particularly large.

other hand, it has been shown in Sect. 3.2 that TVD methods generate spurious excess power in the frequency regime of pressure waves. Therefore, for asteroseismic studies, unlimited polynomials should be used to reconstruct the Riemann states, thus drastically reducing the numerical “noise” introduced in the high-frequency part of the spectrum.

Still uncertain are the implications of the treatment of the  $\nabla \cdot \mathbf{B} = 0$  constraint in Godunov-type schemes for the dynamics of low-Mach-number MHD flows. As discussed in Sect. 1, several methods have been proposed in the literature to mitigate the effects of numerical magnetic monopoles in HRSC schemes. In SLH, the Contact constrained transport method of Gardiner and Stone (2005) is used to keep the update on the magnetic flux across the boundaries of each cell within rounding errors. However, this discretization method does not guarantee that magnetic monopoles are generally absent during the evolution of the flow or that the numerical scheme remains stable under all circumstances. Furthermore, the need for a staggered representation of the magnetic field makes constrained transport methods difficult to use on arbitrarily curvilinear grids, which are often required in simulations of stellar MHD. Other cell-centered methods, such as Powell’s 8-wave model or hyperbolic divergence cleaning, which are easy to use on any grid, may provide reasonably accurate results even if they are not formally divergence-free. The properties of each of these methods can only be inferred with numerical experiments. A few works tried to compare the performance of different  $\nabla \cdot \mathbf{B}$  solver for MHD in simulations of magnetized blasts (Tóth, 2000), accretion disks (Flock et al., 2010), or the solar corona (Zhang and Feng, 2016). None of these studies focused on subsonic flow regimes. To establish the best method to be used in simulations of MHD flows in stellar interiors, future works should focus on comparing  $\nabla \cdot \mathbf{B}$  solvers using setups that closely resemble the dynamical conditions found in production-quality simulations of low-Mach-number stellar MHD.

#### 4.2.1.2 Magnetic field generation mechanisms

Thanks to the special properties of the MHD scheme implemented in SLH, the implications of strong magnetic fields for stellar evolution can be studied for the first time in a self-consistent way. This represents a major breakthrough in stellar evolution modeling, where so far the effects of magnetic fields on the stellar structure have only been considered using simplified prescriptions. For example, a diffusive model is often used in 1D codes to represent the mixing and the transport of angular momentum induced by the Spruit–Tayler dynamo in differentially rotating stable layers of stars (e.g., Spruit, 2002; Heger et al., 2005; Petrovic et al., 2005). Not only do such simplified theories crudely approximate the inherently multidimensional MHD processes associated with the Spruit–Tayler dynamo, but they also rely on tunable parameters that limit the predictive power of the stellar models. Multidimensional MHD simulations are therefore fundamental to overcome the limitations of 1D codes and to quantitatively interpret the interplay between magnetic fields and dynamical shear instabilities in radiative layers of stars.

Fully compressible MHD simulations are also crucial in gaining insight into the generation mechanism of magnetic fields in convective regions of stars. Due to the high Reynolds numbers that characterize stellar interiors, a turbulent, small-scale dynamo (e.g., Schekochihin et al., 2004; Brandenburg and Subramanian, 2005) is likely to be excited in every convection zone that arises during stellar evolution, even in the absence



of rotation. Rotation adds another layer of complexity to the problem, organizing the convective flows and leading to large-scale dynamos, as it occurs in the convective envelope of our Sun (e.g., [Ghizaru et al., 2010](#); [Augustson et al., 2015](#); [Brun and Browning, 2017](#); [Käpylä et al., 2023](#)). Indeed, dynamo action has been identified in numerous MHD simulations of stellar convection, predominantly in upper-main-sequence (e.g. [Brun et al., 2005](#); [Augustson et al., 2016](#)) and low-mass stars (e.g., [Dobler et al., 2006](#); [Käpylä, 2021](#)). Recently, turbulent dynamos have been explored also in late burning shells of massive stars (e.g., [Varma and Müller, 2021](#); [Canivete Cuissa and Teyssier, 2022](#)). However, the implications of efficient dynamo action for convective boundary mixing and the transport of angular momentum remain largely unknown. Moreover, the results presented in most of the aforementioned studies were obtained either by solving a modified set of partial differential equations, or by increasing the luminosity of the star to drive faster convection. With the exception of the work presented by [Varma and Müller \(2021\)](#), who simulated an oxygen-burning shell in a core-collapse supernova progenitor, no fully compressible MHD simulation of stellar interiors has ever been run at the nominal stellar luminosity. Such simulations are highly desirable for the even more challenging cases of upper-main-sequence and red-giant stars, for which it is now possible to estimate the magnetic field strength near or inside the core with asteroseismic techniques (e.g., [Fuller et al., 2015](#); [Lecoanet et al., 2022](#); [Li et al., 2022](#); [Deheuvels et al., 2023](#)). A comparison between the results of realistic MHD simulations of stellar convection run with the SLH code and asteroseismic observations would allow us to determine whether the magnetic field in a given star has been generated dynamically or if it is the remnant of earlier stages of star formation, as discussed in the next section.

#### 4.2.1.3 MHD effects on internal waves

Another interesting application of the new capabilities of SLH is the study of potential MHD effects on the properties of internal waves in stars. Waves in stellar interiors can be divided into two main groups: pressure waves, where the restoring force for small fluid displacements from hydrostatic equilibrium is provided by pressure gradients, and gravity waves, where the restoring force is provided by the buoyancy of the fluid. The frequencies of the resonant  $p$ - and  $g$ -modes of oscillation are sensitive to the stellar structure, so their study serves to probe the interior properties of a star (e.g., [Aerts, 2021](#)). [Cantiello et al. \(2016\)](#) showed that magnetic fields stronger than  $10^5$  G can affect the properties of  $g$ -modes in slowly pulsating B (SPB) stars. Such magnetic field strengths are not implausible for SPB stars. In fact, [Lecoanet et al. \(2022\)](#) inferred a magnetic field strength of  $\approx 5 \times 10^5$  G near the convective core of the SPB star HD 43317. Strong magnetic fields in the core of red giant stars are also thought to suppress mixed dipole modes (i.e., modes that behave as pressure waves in the convective envelope and as gravity waves in the radiative core) by trapping mode energy inside the core (e.g., [Stello et al., 2016](#); [Cantiello et al., 2016](#)). However, the exact mechanism of mode trapping in the core of these objects is not fully understood yet. Furthermore, the origin of the magnetic field in the interior of red giants is unknown. Magnetic field strengths inferred in the core by asteroseismic techniques are on the order of  $10^5$  G ([Li et al., 2022](#); [Deheuvels et al., 2023](#)), which is consistent with dynamo action in the convective core during the main sequence (e.g., [Augustson et al., 2016](#)), but a fossil origin cannot be excluded ([Bugnet et al., 2021](#)). Since the flows in the core of red-giant stars

are low Mach, SLH is the perfect tool to constraint the topology, strength, and origin of the magnetic field in the stellar core by comparing the spectrum of the observed mixed modes to simulation results. This is one of the main advantages of using a fully compressible code such as SLH over anelastic methods, which do not retain pressure modes of oscillation in the numerical solution and therefore cannot be used to infer the properties of the magnetic field in red giants from asteroseismic data.

#### 4.2.2 MHD simulations of late burning shells of massive stars

The simulations shown in Sect. 3.3 demonstrated that small-scale, turbulent dynamos can have a significant impact on the dynamical evolution of oxygen-burning shells of massive stars. In this thesis, it was found that efficient dynamo action reduces the kinetic energy content of the convective flows by up to 30% compared to the purely hydrodynamic case. This in turn reduces the amount of energy available to overcome the buoyancy of the entrained material and slows down the mixing occurring at the upper convective boundary of the shell. Although the magnetic fields amplified by the turbulent dynamo are not strong enough to completely suppress convective boundary mixing, a lower mass entrainment rate can delay or even prevent shell mergers in later evolutionary stages. Shell mergers have been found in a number of numerical studies which did not consider magnetic fields (e.g., Ritter et al., 2018; Andrassy et al., 2020; Yadav et al., 2020), and their occurrence profoundly changes the structure of core-collapse supernova progenitors.

The turbulent dynamo operating in the oxygen shell generates superequipartition magnetic fields ( $\sim 10^{10}$  G) on spatial scales corresponding to the local pressure scale height. The Lorentz force exerted by such strong magnetic fields suppresses shear instabilities in the inertial range of the turbulent spectrum and changes the topology of the convective flows. In particular, during the nonlinear phase of the dynamo, convection proceeds in the form of large-scale, thread-like structures, where strong magnetic tension forces partly suppress the horizontal mixing between up- and downflows. This allows the convective plumes to better retain their heat content compared to the purely hydrodynamic case, resulting in larger entropy fluctuations around the background, hydrostatic state.

Both the reduced convective velocities and the altered topology of the turbulent convective flows affect the efficacy of the perturbation aided supernova explosion mechanism (e.g., Couch et al., 2020; Müller, 2024). In particular, it is expected that the turbulent dynamo amplification in the convective shells of the supernova progenitor ultimately results in a reduced ram pressure in the gain region behind the stalled shock. However, if the magnetic field generated by the turbulent dynamo is “frozen” in the plasma, it can be further amplified to strengths on the order of  $10^{15} - 10^{16}$  G when the convective oxygen shell reaches the gain region. These magnetic field strengths are in the range of observations for magnetars (e.g., Kouveliotou et al., 1998; Woods and Thompson, 2006; Olausen and Kaspi, 2014) and could potentially trigger shock revival (e.g., Bugli et al., 2020; Powell et al., 2023). Despite the unique insight provided by the simulations performed with the SLH code in this thesis, MHD simulation of supernova progenitors in the last moments prior to core-collapse are needed to provide realistic initial conditions for core-collapse supernova explosions and better judge the role of magnetic fields in reviving the stalled shock.

Finally, it should be noted that the main properties of the small-scale turbulent dy-

namo depend on the magnetic Prandtl number, which is defined as the ratio of the kinematic viscosity to the magnetic diffusivity,

$$\text{Pr}_m = \frac{\nu}{\eta}. \quad (4.1)$$

Because SLH does not add explicit viscosity and magnetic diffusivity to the set of stellar MHD equations (see Sect. 2), the value of  $\text{Pr}_m$  achieved in simulations of MHD turbulence is not fixed, but rather it is determined by the underlying properties of the numerical scheme and the local flow conditions. In this so-called “implicit large eddy simulation” approach (e.g., [Grinstein et al., 2007](#)),  $\text{Pr}_m$  is typically close to unity (e.g., [Riva and Steiner, 2022](#)). In reality, the plasma in the late burning shells of massive stars has typical magnetic Prandtl numbers in the range from  $10^{-3}$  to 0.1 (e.g., [Varma and Müller, 2021](#)). Whether small-scale dynamos can be successfully excited even at such low values of  $\text{Pr}_m$  is still open question. Recently, ([Warnecke et al., 2023](#)) demonstrated that turbulent dynamo action is possible even at  $\text{Pr}_m \approx 10^{-3}$ , but that work only covered the kinematic stage of the dynamo instability. The strength of the magnetic field in the saturated phase of the dynamo is usually found to be an increasing function of  $\text{Pr}_m$ , although the dependence is very mild (e.g., [Schekochihin et al., 2004](#); [Brandenburg, 2011](#)). Low magnetic Prandtl number flows are particularly difficult to simulate because of the large separation between the viscous and resistive scales. In fact, in order to excite a small-scale dynamo, magnetic Reynolds numbers on the order of 100 must usually be achieved in the flow, which requires very fine grids with thousands of grid cells per axis when  $\text{Pr}_m \ll 1$ . In the future, numerical simulations of oxygen burning shells run at more realistic values of  $\text{Pr}_m$  will be needed to better establish the effects of turbulent dynamo action on the dynamics of the convective flows and the convective boundary mixing.

---

## List of abbreviations

---

<b>1D</b>	one-dimensional
<b>3D</b>	three-dimensional
<b>CBM</b>	convective boundary mixing
<b>CFL</b>	Courant-Friedrichs-Lewy
<b>CT</b>	constrained transport
<b>CTU</b>	corner transport upwind
<b>ENO</b>	essentially non-oscillatory
<b>EoS</b>	equation of state
<b>HLL</b>	Harten-Lax-van Leer
<b>HLLC</b>	Harten-Lax-van Leer-Contact
<b>HLLD</b>	Harten-Lax-van Leer-Discontinuities
<b>HRSC</b>	high-resolution shock-capturing
<b>IESS</b>	implicit explicit Strang splitting
<b>MHD</b>	magnetohydrodynamics
<b>MLT</b>	mixing-length theory
<b>MPI</b>	message passing interface
<b>MUSCL</b>	monotonic upstream-centered scheme for conservation laws
<b>ODE</b>	ordinary differential equation
<b>PPM</b>	piecewise parabolic method
<b>RSST</b>	reduced speed of sound technique
<b>SLH</b>	Seven-League Hydro
<b>SSD</b>	small-scale dynamo
<b>TVD</b>	total variation diminishing
<b>UCT</b>	upwind constrained transport
<b>WENO</b>	weighted essentially non-oscillatory





---

## List of publications by Giovanni Leidi

---

P. V. F. Edelmann, L. Horst, J.P. Berberich, R. Andrassy, J. Higl, **G. Leidi**, C. Klingenberg, and F. K. Röpke.

*Well-balanced treatment of gravity in astrophysical fluid dynamics simulations at low Mach numbers.*

A&A, 652:A53, August 2021.

**(Not used in this thesis)**

R. Andrassy, J. Higl, H. Mao, M. Mocák, D. G. Vlaykov, W. D. Arnett, I. Baraffe, S. W. Campbell, T. Constantino, P. V. F. Edelmann, T. Goffrey, T. Guillet, F. Herwig, R. Hirschi, L. Horst, **G. Leidi**, C. Meakin, J. Pratt, F. Rizzuti, F. K. Röpke, and P. Woodward.

*Dynamics in a stellar convective layer and at its boundary: Comparison of five 3D hydrodynamics codes.*

A&A, 659:A193, March 2022.

**(Not used in this thesis)**

**G. Leidi**, C. Birke, R. Andrassy, J. Higl, P. V. F. Edelmann, G. Wiest, C. Klingenberg, and F. K. Röpke.

*A finite-volume scheme for modeling compressible magnetohydrodynamic flows at low Mach numbers in stellar interiors.*

A&A, 668:A143, December 2022.

**(Used in Section 3.1)**

**G. Leidi**, R. Andrassy, W. Barsukow, J. Higl, P. V. F. Edelmann, and F. K. Röpke.

*Turbulent dynamo action and its effects on the mixing at the convective boundary of an idealized oxygen-burning shell.*

A&A, 679:A132, November 2023.

**(Used in Section 3.3)**

R. Andrassy, **G. Leidi**, J. Higl, P. V. F. Edelmann, F. R. N. Schneider, and F. K. Röpke.

*Towards a self-consistent model of the convective core boundary in upper main sequence stars. Part I: 2.5D and 3D simulations.*

A&A, 683:A97, March 2024.

**(Not used in this thesis)**

**G. Leidi**, R. Andrassy, W. Barsukow, J. Higl, P. V. F. Edelmann, and F. K. Röpke.

*Performance of high-order Godunov-type methods in simulations of astrophysical low Mach number flows.*

Accepted for publication in A&A in February 2024.

**(Used in Section 3.2)**



---

## Bibliography

---

- Aerts, C. (2021). Probing the interior physics of stars through asteroseismology. *Rev. Mod. Phys.*, 93:015001.
- Anders, E. H. and Pedersen, M. G. (2023). Convective boundary mixing in main-sequence stars: Theory and empirical constraints. *Galaxies*, 11(2).
- Andrassy, R., Herwig, F., Woodward, P., and Ritter, C. (2020). 3D hydrodynamic simulations of C ingestion into a convective O shell. *Mon. Not. Roy. Astron. Soc.*, 491(1):972–992.
- Andrassy, R., Higl, J., Mao, H., Mocák, M., Vlaykov, D. G., Arnett, W. D., Baraffe, I., Campbell, S. W., Constantino, T., Edelmann, P. V. F., Goffrey, T., Guillet, T., Herwig, F., Hirschi, R., Horst, L., Leidi, G., Meakin, C., Pratt, J., Rizzuti, F., Röpkke, F. K., and Woodward, P. (2022). Dynamics in a stellar convective layer and at its boundary: Comparison of five 3D hydrodynamics codes. *Astron. Astrophys.*, 659:A193.
- Andrassy, R., Leidi, G., Higl, J., Edelmann, P. V. F., Schneider, F. R. N., and Roepke, F. K. (2023). Towards a self-consistent model of the convective core boundary in upper-main-sequence stars. *arXiv e-prints*, page arXiv:2307.04068.
- Augustson, K., Brun, A. S., Miesch, M., and Toomre, J. (2015). Grand Minima and Equatorward Propagation in a Cycling Stellar Convective Dynamo. *Astrophys. J.*, 809(2):149.
- Augustson, K. C., Brun, A. S., and Toomre, J. (2011). Convection and dynamo action in B stars. In Brummell, N. H., Brun, A. S., Miesch, M. S., and Ponty, Y., editors, *Astrophysical Dynamics: From Stars to Galaxies*, volume 271, pages 361–362.
- Augustson, K. C., Brun, A. S., and Toomre, J. (2016). The Magnetic Furnace: Intense Core Dynamos in B Stars. *Astrophys. J.*, 829(2):92.
- Aydemir, A. Y. and Barnes, D. C. (1985). An Implicit Algorithm for Compressible Three-Dimensional Magnetohydrodynamic Calculations. *Journal of Computational Physics*, 59(1):108–119.
- Balsara, D. S. (2004). Second-Order-accurate Schemes for Magnetohydrodynamics with Divergence-free Reconstruction. *Astrophys. J. Supp. Ser.*, 151(1):149–184.
- Balsara, D. S., Montecinos, G. I., and Toro, E. F. (2016). Exploring various flux vector splittings for the magnetohydrodynamic system. *Journal of Computational Physics*, 311:1–21.
- Balsara, D. S. and Spicer, D. S. (1999). A Staggered Mesh Algorithm Using High Order Godunov Fluxes to Ensure Solenoidal Magnetic Fields in Magnetohydrodynamic Simulations. *Journal of Computational Physics*, 149(2):270–292.
- Baraffe, I., Clarke, J., Morison, A., Vlaykov, D. G., Constantino, T., Goffrey, T., Guillet,

- T., Le Saux, A., and Pratt, J. (2023). A study of convective core overshooting as a function of stellar mass based on two-dimensional hydrodynamical simulations. *Monthly Notices of the Royal Astronomical Society*, 519(4):5333–5344.
- Berberich, J. P., Chandrashekar, P., and Klingenberg, C. (2021). High order well-balanced finite volume methods for multi-dimensional systems of hyperbolic balance laws. *Computers & Fluids*, 219:104858.
- Bhatia, T. S., Cameron, R. H., Solanki, S. K., Peter, H., Przybylski, D., Witzke, V., and Shapiro, A. (2022). Small-scale dynamo in cool stars. I. Changes in stratification and near-surface convection for main-sequence spectral types. *Astron. Astrophys.*, 663:A166.
- Blouin, S., Mao, H., Herwig, F., Denissenkov, P., Woodward, P. R., and Thompson, W. R. (2023). 3D hydrodynamics simulations of internal gravity waves in red giant branch stars. *Monthly Notices of the Royal Astronomical Society*, 522(2):1706–1725.
- Böhm-Vitense, E. (1958). Über die Wasserstoffkonvektionszone in Sternen verschiedener Effektivtemperaturen und Leuchtkräfte. Mit 5 Textabbildungen. *Zeitschrift für Astrophysik*, 46:108.
- Boyd, T. J. M. and Sanderson, J. J. (2003). *The Physics of Plasmas*. Cambridge University Press.
- Brackbill, J. U. and Barnes, D. C. (1980). The Effect of Nonzero  $\nabla \cdot \mathbf{B}$  on the numerical solution of the magnetohydrodynamic equations. *Journal of Computational Physics*, 35(3):426–430.
- Brandenburg, A. (2011). Nonlinear Small-scale Dynamos at Low Magnetic Prandtl Numbers. *Astrophys. J.*, 741(2):92.
- Brandenburg, A. and Subramanian, K. (2005). Astrophysical magnetic fields and nonlinear dynamo theory. *Phys. Rep.*, 417(1-4):1–209.
- Brio, M. and Wu, C. C. (1988). An Upwind Differencing Scheme for the Equations of Ideal Magnetohydrodynamics. *Journal of Computational Physics*, 75(2):400–422.
- Browning, M. K. (2008). Simulations of Dynamo Action in Fully Convective Stars. *Astrophys. J.*, 676(2):1262–1280.
- Brun, A. and Browning, M. (2017). Magnetism, dynamo action and the solar-stellar connection. *Living Reviews in Solar Physics*, 14:4.
- Brun, A. S., Browning, M. K., and Toomre, J. (2005). Simulations of Core Convection in Rotating A-Type Stars: Magnetic Dynamo Action. *Astrophys. J.*, 629(1):461–481.
- Brun, A. S., Miesch, M. S., and Toomre, J. (2004). Global-Scale Turbulent Convection and Magnetic Dynamo Action in the Solar Envelope. *Astrophys. J.*, 614(2):1073–1098.
- Bugli, M., Guilet, J., Obergaulinger, M., Cerdá-Durán, P., and Aloy, M. A. (2020). The impact of non-dipolar magnetic fields in core-collapse supernovae. *Mon. Not. Roy. Astron. Soc.*, 492(1):58–71.

- Bugnet, L., Prat, V., Mathis, S., Astoul, A., Augustson, K., García, R. A., Mathur, S., Amard, L., and Neiner, C. (2021). Magnetic signatures on mixed-mode frequencies. I. An axisymmetric fossil field inside the core of red giants. *Astron. Astrophys.*, 650:A53.
- Cameron, R. H., Dikpati, M., and Brandenburg, A. (2017). The Global Solar Dynamo. *Space Science Reviews*, 210(1-4):367–395.
- Canivete Cuissa, J. R. and Teyssier, R. (2022). Toward fully compressible numerical simulations of stellar magneto-convection with the RAMSES code. *Astron. Astrophys.*, 664:A24.
- Cantiello, M., Fuller, J., and Bildsten, L. (2016). Asteroseismic Signatures of Evolving Internal Stellar Magnetic Fields. *Astrophys. J.*, 824(1):14.
- Canuto, V. M. (1997). Compressible turbulence. *Astrophys. J.*, 482:827–851.
- Cargo, P. and Gallice, G. (1997). Roe Matrices for Ideal MHD and Systematic Construction of Roe Matrices for Systems of Conservation Laws. *Journal of Computational Physics*, 136(2):446–466.
- Castro, N., Fossati, L., Langer, N., Simón-Díaz, S., Schneider, F. R. N., and Izzard, R. G. (2014). The spectroscopic Hertzsprung-Russell diagram of Galactic massive stars. *Astron. Astrophys.*, 570:L13.
- Chacón, L. (2008). An optimal, parallel, fully implicit Newton-Krylov solver for three-dimensional viscoresistive magnetohydrodynamics. *Physics of Plasmas*, 15(5):056103.
- Charbonneau, P. (2020). Dynamo models of the solar cycle. *Living Reviews in Solar Physics*, 17(1):4.
- Claret, A. and Torres, G. (2016). The dependence of convective core overshooting on stellar mass. *Astron. Astrophys.*, 592:A15.
- Colella, P. (1990). Multidimensional upwind methods for hyperbolic conservation laws. *Journal of Computational Physics*, 87(1):171–200.
- Colella, P. and Sekora, M. D. (2008). A limiter for PPM that preserves accuracy at smooth extrema. *Journal of Computational Physics*, 227(15):7069–7076.
- Colella, P. and Woodward, P. R. (1984). The Piecewise Parabolic Method (PPM) for Gas-Dynamical Simulations. *Journal of Computational Physics*, 54:174–201.
- Couch, S. M. and Ott, C. D. (2013). Revival of the Stalled Core-collapse Supernova Shock Triggered by Precollapse Asphericity in the Progenitor Star. *Astrophys. J. Lett.*, 778(1):L7.
- Couch, S. M., Warren, M. L., and O’Connor, E. P. (2020). Simulating turbulence-aided neutrino-driven core-collapse supernova explosions in one dimension. *The Astrophysical Journal*, 890(2):127.



- Courant, R., Friedrichs, K., and Lewy, H. (1928). Über die partiellen Differenzengleichungen der mathematischen Physik. *Mathematische Annalen*, 100:32–74.
- Crank, J., Nicolson, P., and Hartree, D. R. (1947). A practical method for numerical evaluation of solutions of partial differential equations of the heat-conduction type. *Proceedings of the Cambridge Philosophical Society*, 43(1):50.
- Cristini, A., Hirschi, R., Meakin, C., Arnett, D., Georgy, C., and Walkington, I. (2019). Dependence of convective boundary mixing on boundary properties and turbulence strength. *Mon. Not. Roy. Astron. Soc.*, 484(4):4645–4664.
- Cristini, A., Meakin, C., Hirschi, R., Arnett, D., Georgy, C., Viallet, M., and Walkington, I. (2017). 3D hydrodynamic simulations of carbon burning in massive stars. *Monthly Notices of the Royal Astronomical Society*, 471(1):279–300.
- Crosley, M. K. and Osten, R. A. (2018). Constraining stellar coronal mass ejections through multi-wavelength analysis of the active m dwarf eq peg. *The Astrophysical Journal*, 856(1):39.
- Dai, W. and Woodward, P. R. (1998). On the Divergence-free Condition and Conservation Laws in Numerical Simulations for Supersonic Magnetohydrodynamical Flows. *Astrophys. J.*, 494(1):317–335.
- Davis, A., Jones, S., and Herwig, F. (2019). Convective boundary mixing in a post-He core burning massive star model. *Mon. Not. Roy. Astron. Soc.*, 484(3):3921–3934.
- Dedner, A., Kemm, F., Kröner, D., Munz, C. D., Schnitzer, T., and Wesenberg, M. (2002). Hyperbolic Divergence Cleaning for the MHD Equations. *Journal of Computational Physics*, 175(2):645–673.
- Deheuvels, S., Li, G., Ballot, J., and Lignières, F. (2023). Strong magnetic fields detected in the cores of 11 red giant stars using gravity-mode period spacings. *Astron. Astrophys.*, 670:L16.
- Dobler, W., Stix, M., and Brandenburg, A. (2006). Magnetic Field Generation in Fully Convective Rotating Spheres. *Astrophys. J.*, 638(1):336–347.
- Dumbser, M., Balsara, D. S., Tavelli, M., and Fambri, F. (2019). A divergence-free semi-implicit finite volume scheme for ideal, viscous, and resistive magnetohydrodynamics. *International Journal for Numerical Methods in Fluids*, 89(1-2):16–42.
- Edelmann, P. V. F. (2014). *Coupling of Nuclear Reaction Networks and Hydrodynamics for Application in Stellar Astrophysics*. Dissertation, Technische Universität München.
- Edelmann, P. V. F., Horst, L., Berberich, J. P., Andrassy, R., Higl, J., Leidi, G., Klingenberg, C., and Röpke, F. K. (2021). Well-balanced treatment of gravity in astrophysical fluid dynamics simulations at low Mach numbers. *Astron. Astrophys.*, 652:A53.
- Edelmann, P. V. F. and Röpke, F. K. (2016). SLH Seven-League Hydro code. In Brömmel, D., Frings, W., and Wylie, B. J. N., editors, *JUQUEEN Extreme Scaling Workshop 2016*, number FZJ-JSC-IB-2016-01 in JSC Internal Report, pages 63–67.

- Edelmann, P. V. F., Röpke, F. K., Hirschi, R., Georgy, C., and Jones, S. (2017). Testing a one-dimensional prescription of dynamical shear mixing with a two-dimensional hydrodynamic simulation. *Astron. Astrophys.*, 604:A25.
- Einfeldt, B., Roe, P. L., Munz, C. D., and Sjogreen, B. (1991). On Godunov-Type Methods near Low Densities. *Journal of Computational Physics*, 92(2):273–295.
- Evans, C. R. and Hawley, J. F. (1988). Simulation of Magnetohydrodynamic Flows: A Constrained Transport Model. *Astrophys. J.*, 332:659.
- Fambri, F. (2021). A novel structure preserving semi-implicit finite volume method for viscous and resistive magnetohydrodynamics. *International Journal for Numerical Methods in Fluids*, 93(12):3447–3489.
- Fan, Y. and Fang, F. (2014). A Simulation of Convective Dynamo in the Solar Convective Envelope: Maintenance of the Solar-like Differential Rotation and Emerging Flux. *Astrophys. J.*, 789(1):35.
- Federrath, C. and Klessen, R. S. (2012). The Star Formation Rate of Turbulent Magnetized Clouds: Comparing Theory, Simulations, and Observations. *Astrophys. J.*, 761(2):156.
- Feng, X., Wang, H., Xiang, C., Liu, X., Zhang, M., Zhao, J., and Shen, F. (2021). Magnetohydrodynamic Modeling of the Solar Corona with an Effective Implicit Strategy. *Astrophys. J. Supp. Ser.*, 257(2):34.
- Ferziger, J. H. and Perić, M. (2002). *Computational Methods for Fluid Dynamics*. Springer, Berlin, third edition.
- Flock, M., Dzyurkevich, N., Klahr, H., and Mignone, A. (2010). High-order Godunov schemes for global 3D MHD simulations of accretion disks. I. Testing the linear growth of the magneto-rotational instability. *Astron. Astrophys.*, 516:A26.
- Freytag, B., Steffen, M., Ludwig, H. G., Wedemeyer-Böhm, S., Schaffenberger, W., and Steiner, O. (2012). Simulations of stellar convection with CO5BOLD. *Journal of Computational Physics*, 231(3):919–959.
- Fromang, S., Hennebelle, P., and Teyssier, R. (2006). A high order Godunov scheme with constrained transport and adaptive mesh refinement for astrophysical magnetohydrodynamics. *Astron. Astrophys.*, 457(2):371–384.
- Fuchs, F. G., McMurry, A. D., Mishra, S., Risebro, N. H., and Waagan, K. (2011). Approximate Riemann Solvers and Robust High-Order Finite Volume Schemes for Multi-Dimensional Ideal MHD Equations. *Communications in Computational Physics*, 9(2):324–362.
- Fuller, J., Cantiello, M., Stello, D., Garcia, R. A., and Bildsten, L. (2015). Asteroseismology can reveal strong internal magnetic fields in red giant stars. *Science*, 350(6259):423–426.
- Garaud, P., Ogilvie, G. I., Miller, N., and Stellmach, S. (2010). A model of the entropy flux and Reynolds stress in turbulent convection. *Monthly Notices of the Royal Astro-*

- nomical Society*, 407(4):2451–2467.
- Gardiner, T. A. and Stone, J. M. (2005). An unsplit Godunov method for ideal MHD via constrained transport. *Journal of Computational Physics*, 205(2):509–539.
- Ghizaru, M., Charbonneau, P., and Smolarkiewicz, P. K. (2010). Magnetic Cycles in Global Large-eddy Simulations of Solar Convection. *Astrophys. J. Lett.*, 715(2):L133–L137.
- Gilet, C., Almgren, A. S., Bell, J. B., Nonaka, A., Woosley, S. E., and Zingale, M. (2013). Low Mach Number Modeling of Core Convection in Massive Stars. *Astrophys. J.*, 773(2):137.
- Glatzmaier, G. A. (1984). Numerical simulations of stellar convective dynamos. I. The model and method. *Journal of Computational Physics*, 55:461–484.
- Godunov, S. K. (1959). A difference method for numerical calculation of discontinuous solutions of the equations of hydrodynamics. *Matematicheskii Sbornik*, 89(3):271–306.
- Godunov, S. K. (1972). Symmetric form of the magnetohydrodynamic equation. *Chislennye Metody Mekh. Sploshnoi Sredy*, v. 3, no. 1, pp. 26–34, 3(1).
- Greenough, J. A. and Rider, W. J. (2003). A quantitative comparison of numerical methods for the compressible euler equations: Fifth-order weno and piecewise-linear godunov. *Journal of Computational Physics*, 196(1).
- Grinstein, F., Margolin, L., and Rider, W. (2007). *Implicit Large Eddy Simulation: Computing Turbulent Fluid Dynamics*. Cambridge University Press.
- Guenther, D. B., Demarque, P., and Gruberbauer, M. (2014). Modeling Convective Core Overshoot and Diffusion in Procyon Constrained by Asteroseismic Data. *Astrophys. J.*, 787(2):164.
- Heger, A., Woosley, S. E., and Spruit, H. C. (2005). Presupernova Evolution of Differentially Rotating Massive Stars Including Magnetic Fields. *Astrophys. J.*, 626(1):350–363.
- Higl, J., Müller, E., and Weiss, A. (2021). Calibrating core overshooting parameters with two-dimensional hydrodynamical simulations. *Astron. Astrophys.*, 646:A133.
- Horst, L., Edelmann, P. V. F., Andrásy, R., Röpke, F. K., Bowman, D. M., Aerts, C., and Ratnasingam, R. P. (2020). Fully compressible simulations of waves and core convection in main-sequence stars. *Astron. Astrophys.*, 641:A18.
- Horst, L., Hirschi, R., Edelmann, P. V. F., Andrassy, R., and Roepke, F. K. (2021). Multi-dimensional low-Mach number time-implicit hydrodynamic simulations of convective helium shell burning in a massive star. *Astron. Astrophys.*, 653:A55.
- Hosea, M. E. and Shampine, L. F. (1996). Analysis and implementation of tr-bdf2. *Applied Numerical Mathematics*, 20:21–37.
- Hotta, H. (2017). Solar Overshoot Region and Small-scale Dynamo with Realistic En-

- ergy Flux. *Astrophys. J.*, 843(1):52.
- Hotta, H., Rempel, M., and Yokoyama, T. (2015). Efficient Small-scale Dynamo in the Solar Convection Zone. *Astrophys. J.*, 803(1):42.
- Hotta, H., Rempel, M., Yokoyama, T., Iida, Y., and Fan, Y. (2012). Numerical calculation of convection with reduced speed of sound technique. *Astron. Astrophys.*, 539:A30.
- Iijima, H., Hotta, H., and Imada, S. (2019). Semiconservative reduced speed of sound technique for low Mach number flows with large density variations. *Astron. Astrophys.*, 622:A157.
- Iliadis, C. (2007). *Nuclear Physics of Stars*. Weinheim: Wiley-VCH.
- Jermyn, A. S., Anders, E. H., Lecoanet, D., and Cantiello, M. (2022). An Atlas of Convection in Main-sequence Stars. *Astrophys. J. Supp. Ser.*, 262(1):19.
- Jiang, G.-S. and Shu, C.-W. (1996). Efficient implementation of weighted eno schemes. *Journal of Computational Physics*, 126(1):202–228.
- Jones, S., Andrassy, R., Sandalski, S., Davis, A., Woodward, P., and Herwig, F. (2017). Idealized hydrodynamic simulations of turbulent oxygen-burning shell convection in  $4\pi$  geometry. *Monthly Notices of the Royal Astronomical Society*, 465(3):2991–3010.
- Joyce, M. and Tayar, J. (2023). A Review of the Mixing Length Theory of Convection in 1D Stellar Modeling. *Galaxies*, 11(3):75.
- Käppeli, R. (2022). Well-balanced methods for computational astrophysics. *Living Reviews in Computational Astrophysics*, 8(1):2.
- Käpylä, P. J. (2019). Overshooting in simulations of compressible convection. *Astron. Astrophys.*, 631:A122.
- Käpylä, P. J. (2021). Star-in-a-box simulations of fully convective stars. *Astron. Astrophys.*, 651:A66.
- Käpylä, P. J., Browning, M. K., Brun, A. S., Guerrero, G., and Warnecke, J. (2023). Simulations of Solar and Stellar Dynamos and Their Theoretical Interpretation. *Space Science Reviews*, 219(7):58.
- Käpylä, P. J., Mantere, M. J., Cole, E., Warnecke, J., and Brandenburg, A. (2013). Effects of Enhanced Stratification on Equatorward Dynamo Wave Propagation. *Astrophys. J.*, 778(1):41.
- Keszthelyi, Z. (2023). Magnetism in high-mass stars. *Galaxies*, 11(2).
- Kippenhahn, R., Weigert, A., and Weiss, A. (2012). *Stellar Structure and Evolution*. Astronomy and Astrophysics Library. Springer Berlin Heidelberg.
- Klingenberg, C. and Waagan, K. (2010). Relaxation solvers for ideal mhd equations - a review. *Acta Mathematica Scientia*, 30(2):621–632. Mathematics Dedicated to professor James Glimm on the occasion of his 75th birthday.

- Kouveliotou, C., Dieters, S., Strohmayer, T., van Paradijs, J., Fishman, G. J., Meegan, C. A., Hurley, K., Kommers, J., Smith, I., Frail, D., and Murakami, T. (1998). An X-ray pulsar with a superstrong magnetic field in the soft  $\gamma$ -ray repeater SGR1806 - 20. *Nature*, 393(6682):235–237.
- Kuhfuss, R. (1986). A model for time-dependent turbulent convection. *Astron. Astrophys.*, 160(1):116–120.
- Kupka, F. and Muthsam, H. J. (2017). Modelling of stellar convection. *Living Reviews in Computational Astrophysics*, 3(1):1.
- Lamb, H. (1932). *Hydrodynamics*. The University Press.
- Landau, L. D., Lifshitz, E. M., Sykes, J. B., and Reid, W. H. (1959). *Fluid Mechanics*. Pergamon Press Oxford, England.
- Lantz, S. R. and Fan, Y. (1999). Anelastic Magnetohydrodynamic Equations for Modeling Solar and Stellar Convection Zones. *Astrophys. J. Supp. Ser.*, 121(1):247–264.
- Lax, P. D. and Wendroff, B. (1960). Systems of conservation laws. *Communications on Pure and Applied Mathematics*, 13:217–237.
- Lecoanet, D., Bowman, D. M., and Van Reeth, T. (2022). Asteroseismic inference of the near-core magnetic field strength in the main-sequence B star HD 43317. *Mon. Not. Roy. Astron. Soc.*, 512(1):L16–L20.
- Lecoanet, D. and Edelman, P. V. F. (2023). Multidimensional Simulations of Core Convection. *Galaxies*, 11(4):89.
- Leidi, G., Andrassy, R., Higl, J., Edelman, P. V. F., and Röpke, F. K. (2023). Turbulent dynamo action and its effects on the mixing at the convective boundary of an idealized oxygen-burning shell. *Astron. Astrophys.*, 679:A132.
- LeVeque, R. (1990). *Numerical Methods for Conservation Laws*. Lectures in Mathematics ETH Zürich. Birkhäuser Verlag.
- LeVeque, R. J. (2002). *Finite Volume Methods for Hyperbolic Problems*. Cambridge Texts in Applied Mathematics. Cambridge University Press.
- LeVeque, R. J. (2007). *Finite Difference Methods for Ordinary and Partial Differential Equations*. Society for Industrial and Applied Mathematics.
- Li, G., Deheuvels, S., Ballot, J., and Lignières, F. (2022). Magnetic fields of 30 to 100 kG in the cores of red giant stars. *Nature*, 610(7930):43–46.
- Li, S. (2005). An HLLC Riemann solver for magneto-hydrodynamics. *Journal of Computational Physics*, 203(1):344–357.
- Lighthill, M. J. (1952). On Sound Generated Aerodynamically. I. General Theory. *Proceedings of the Royal Society of London Series A*, 211(1107):564–587.
- Liu, X.-D., Osher, S., and Chan, T. (1994). Weighted essentially non-oscillatory



- schemes. *Journal of Computational Physics*, 115(1):200–212.
- Londrillo, P. and del Zanna, L. (2004). On the divergence-free condition in Godunov-type schemes for ideal magnetohydrodynamics: the upwind constrained transport method. *Journal of Computational Physics*, 195(1):17–48.
- Lütjens, H. and Luciani, J.-F. (2010). XTOR-2F: A fully implicit Newton-Krylov solver applied to nonlinear 3D extended MHD in tokamaks. *Journal of Computational Physics*, 229(21):8130–8143.
- Maeder, A. (2008). *Physics, Formation and Evolution of Rotating Stars*. Astronomy and Astrophysics Library. Springer Berlin Heidelberg.
- Martí, J. M. and Müller, E. (2015). Grid-based Methods in Relativistic Hydrodynamics and Magnetohydrodynamics. *Living Reviews in Computational Astrophysics*, 1(1):3.
- Mathis, S., Bugnet, L., Prat, V., Augustson, K., Mathur, S., and Garcia, R. A. (2021). Probing the internal magnetism of stars using asymptotic magneto-asteroseismology. *Astron. Astrophys.*, 647:A122.
- Matthaeus, W. H. and Brown, M. R. (1988). Nearly incompressible magnetohydrodynamics at low Mach number. *Physics of Fluids*, 31(12):3634–3644.
- Meakin, C. A. and Arnett, D. (2007). Turbulent Convection in Stellar Interiors. I. Hydrodynamic Simulation. *Astrophys. J.*, 667(1):448–475.
- Meneguzzi, M., Frisch, U., and Pouquet, A. (1981). Helical and nonhelical turbulent dynamos. *Phys. Rev. Lett.*, 47(15):1060–1064.
- Mestel, L. (1999). Stellar magnetism. *Int. Ser. Monogr. Phys*, 99.
- Michielsen, M., Pedersen, M. G., Augustson, K. C., Mathis, S., and Aerts, C. (2019). Probing the shape of the mixing profile and of the thermal structure at the convective core boundary through asteroseismology. *Astron. Astrophys.*, 628:A76.
- Miczek, F. (2013). *Simulation of low Mach number astrophysical flows*. Dissertation, Technische Universität München.
- Miczek, F., Röpke, F. K., and Edelmann, P. V. F. (2015). New numerical solver for flows at various Mach numbers. *Astron. Astrophys.*, 576:A50.
- Mignone, A. and Del Zanna, L. (2021). Systematic construction of upwind constrained transport schemes for MHD. *Journal of Computational Physics*, 424:109748.
- Miller, C. L., Neilson, H. R., Evans, N. R., Engle, S. G., and Guinan, E. (2020). Rotation, Convective Core Overshooting, and Period Changes in Classical Cepheid Stellar Evolution Models. *Astrophys. J.*, 896(2):128.
- Minoshima, T. and Miyoshi, T. (2021). A low-dissipation hlld approximate riemann solver for a very wide range of mach numbers. *Journal of Computational Physics*, 446:110639.

- Miyoshi, T. and Kusano, K. (2005). A multi-state HLL approximate Riemann solver for ideal magnetohydrodynamics. *Journal of Computational Physics*, 208(1):315–344.
- Mocák, M., Meakin, C., Campbell, S. W., and Arnett, W. D. (2018). Turbulent mixing and nuclear burning in stellar interiors. *Monthly Notices of the Royal Astronomical Society*, 481(3):2918–2932.
- Morán-Fraile, J., Holas, A., Röpke, F. K., Pakmor, R., and Schneider, F. R. N. (2024). Faint calcium-rich transient from a double detonation of a 0.6  $M_{\odot}$  carbon-oxygen white dwarf star. *Astron. Astrophys.*, 683:A44.
- Mösta, P., Richers, S., Ott, C. D., Haas, R., Piro, A. L., Boydston, K., Abdikamalov, E., Reisswig, C., and Schnetter, E. (2014). Magnetorotational Core-collapse Supernovae in Three Dimensions. *Astrophys. J. Lett.*, 785(2):L29.
- Müller, B. (2020). Hydrodynamics of core-collapse supernovae and their progenitors. *Living Reviews in Computational Astrophysics*, 6(1):3.
- Müller, B. (2024). Supernova Simulations. *arXiv e-prints*, page arXiv:2403.18952.
- Müller, B., Melson, T., Heger, A., and Janka, H.-T. (2017). Supernova simulations from a 3D progenitor model - Impact of perturbations and evolution of explosion properties. *Mon. Not. Roy. Astron. Soc.*, 472(1):491–513.
- Müller, B., Viallet, M., Heger, A., and Janka, H.-T. (2016). The Last Minutes of Oxygen Shell Burning in a Massive Star. *Astrophys. J.*, 833(1):124.
- Muthsam, H. J., Kupka, F., Löw-Baselli, B., Obertscheider, C., Langer, M., and Lenz, P. (2010). ANTARES - A Numerical Tool for Astrophysical RESearch with applications to solar granulation. *New Astronomy*, 15(5):460–475.
- Olausen, S. A. and Kaspi, V. M. (2014). The McGill Magnetar Catalog. *Astrophys. J. Supp. Ser.*, 212(1):6.
- Passos, D. and Charbonneau, P. (2014). Characteristics of magnetic solar-like cycles in a 3D MHD simulation of solar convection. *Astron. Astrophys.*, 568:A113.
- Petrovic, J., Langer, N., Yoon, S. C., and Heger, A. (2005). Which massive stars are gamma-ray burst progenitors? *Astron. Astrophys.*, 435(1):247–259.
- Powell, J. and Müller, B. (2020). Three-dimensional core-collapse supernova simulations of massive and rotating progenitors. *Mon. Not. Roy. Astron. Soc.*, 494(4):4665–4675.
- Powell, J., Müller, B., Aguilera-Dena, D. R., and Langer, N. (2023). Three dimensional magnetorotational core-collapse supernova explosions of a 39 solar mass progenitor star. *Mon. Not. Roy. Astron. Soc.*, 522(4):6070–6086.
- Powell, K. G. (1994). Approximate Riemann solver for magnetohydrodynamics (that works in more than one dimension).
- Powell, K. G., Roe, P. L., Linde, T. J., Gombosi, T. I., and De Zeeuw, D. L. (1999). A

- Solution-Adaptive Upwind Scheme for Ideal Magnetohydrodynamics. *Journal of Computational Physics*, 154(2):284–309.
- Prandtl, L. (1925). 7. Bericht über Untersuchungen zur ausgebildeten Turbulenz. *Zeitschrift Angewandte Mathematik und Mechanik*, 5(2):136–139.
- Pratt, J., Baraffe, I., Goffrey, T., Geroux, C., Viallet, M., Folini, D., Constantino, T., Popov, M., and Walder, R. (2016). Spherical-shell boundaries for two-dimensional compressible convection in a star. *Astron. Astrophys.*, 593:A121.
- Prialnik, D. (2000). *An Introduction to the Theory of Stellar Structure and Evolution*. Cambridge University Press.
- Pudritz, R. E. and Ray, T. P. (2019). The Role of Magnetic Fields in Protostellar Outflows and Star Formation. *Frontiers in Astronomy and Space Sciences*, 6:54.
- Reiners, A. (2012). Observations of Cool-Star Magnetic Fields. *Living Reviews in Solar Physics*, 9(1):1.
- Rempel, M. (2005). Solar Differential Rotation and Meridional Flow: The Role of a Subadiabatic Tachocline for the Taylor-Proudman Balance. *Astrophys. J.*, 622(2):1320–1332.
- Ritter, C., Andrassy, R., Côté, B., Herwig, F., Woodward, P. R., Pignatari, M., and Jones, S. (2018). Convective-reactive nucleosynthesis of K, Sc, Cl and p-process isotopes in O-C shell mergers. *Mon. Not. Roy. Astron. Soc.*, 474(1):L1–L6.
- Riva, F. and Steiner, O. (2022). Methodology for estimating the magnetic Prandtl number and application to solar surface small-scale dynamo simulations. *Astron. Astrophys.*, 660:A115.
- Rizzuti, F., Hirschi, R., Arnett, W. D., Georgy, C., Meakin, C., Murphy, A. S., Rauscher, T., and Varma, V. (2023). 3D stellar evolution: hydrodynamic simulations of a complete burning phase in a massive star. *Mon. Not. Roy. Astron. Soc.*, 523(2):2317–2328.
- Romano, D., Karakas, A. I., Tosi, M., and Matteucci, F. (2010). Quantifying the uncertainties of chemical evolution studies. II. Stellar yields. *Astron. Astrophys.*, 522:A32.
- Röpke, F. K. and De Marco, O. (2023). Simulations of common-envelope evolution in binary stellar systems: physical models and numerical techniques. *Living Reviews in Computational Astrophysics*, 9(1):2.
- Rusanov, V. (1962). The calculation of the interaction of non-stationary shock waves and obstacles. *USSR Computational Mathematics and Mathematical Physics*, 1(2):304–320.
- Salaris, M. and Cassisi, S. (2005). *Evolution of Stars and Stellar Populations*. Wiley.
- Schekochihin, A. A., Cowley, S. C., Taylor, S. F., Maron, J. L., and McWilliams, J. C. (2004). Simulations of the Small-Scale Turbulent Dynamo. *Astrophys. J.*, 612(1):276–307.

- Schneider, F. R. N., Ohlmann, S. T., Podsiadlowski, P., Röpke, F. K., Balbus, S. A., Pakmor, R., and Springel, V. (2019). Stellar mergers as the origin of magnetic massive stars. *Nature*, 574(7777):211–214.
- Schober, J., Schleicher, D., Bovino, S., and Klessen, R. S. (2012). Small-scale dynamo at low magnetic Prandtl numbers. *Physical Review E*, 86(6):066412.
- Shu, C.-W. (2009). High order weighted essentially nonoscillatory schemes for convection dominated problems. *SIAM Review*, 51(1):82–126.
- Shu, C.-W. and Osher, S. (1988). Efficient implementation of essentially non-oscillatory shock-capturing schemes. *Journal of Computational Physics*, 77(2):439–471.
- Sonoi, T., Ludwig, H. G., Dupret, M. A., Montalbán, J., Samadi, R., Belkacem, K., Caffau, E., and Goupil, M. J. (2019). Calibration of mixing-length parameter  $\alpha$  for MLT and FST models by matching with CO<sup>5</sup>BOLD models. *Astron. Astrophys.*, 621:A84.
- Spruit, H. C. (2002). Dynamo action by differential rotation in a stably stratified stellar interior. *Astron. Astrophys.*, 381:923–932.
- Spruit, H. C. (2013). Essential Magnetohydrodynamics for Astrophysics. *arXiv e-prints*, page arXiv:1301.5572.
- Stancliffe, R. J., Fossati, L., Passy, J. C., and Schneider, F. R. N. (2015). Confronting uncertainties in stellar physics: calibrating convective overshooting with eclipsing binaries. *Astron. Astrophys.*, 575:A117.
- Stello, D., Cantiello, M., Fuller, J., Huber, D., Garcia, R. A., Bedding, T. R., Bildsten, L., and Silva Aguirre, V. (2016). A prevalence of dynamo-generated magnetic fields in the cores of intermediate-mass stars. *Nature*, 529(7586):364–367.
- Stone, J. M. and Gardiner, T. (2009). A simple unsplit Godunov method for multidimensional MHD. *New Astronomy*, 14(2):139–148.
- Strang, G. (1968). On the construction and comparison of difference schemes. *SIAM Journal on Numerical Analysis*, 5(3):506–517.
- Takahashi, K., Yamada, S., and Yamada (2014). Exact Riemann solver for ideal magnetohydrodynamics that can handle all types of intermediate shocks and switch-on/off waves. *Journal of Plasma Physics*, 80(2):255–287.
- Temaj, D., Schneider, F. R. N., Laplace, E., Wei, D., and Podsiadlowski, P. (2024). Convective-core overshooting and the final fate of massive stars. *Astron. Astrophys.*, 682:A123.
- Teyssier, R. and Commerçon, B. (2019). Numerical Methods for Simulating Star Formation. *Frontiers in Astronomy and Space Sciences*, 6:51.
- Toro, E. F. (2009). *Riemann Solvers and Numerical Methods for Fluid Dynamics: A Practical Introduction*. Springer, Berlin Heidelberg.
- Torrilhon, M. and Balsara, D. S. (2004). High order WENO schemes: investigations

- on non-uniform convergence for MHD Riemann problems. *Journal of Computational Physics*, 201(2):586–600.
- Tóth, G. (2000). The  $\nabla \cdot \mathbf{B}=0$  Constraint in Shock-Capturing Magnetohydrodynamics Codes. *Journal of Computational Physics*, 161(2):605–652.
- Trampedach, R., Stein, R. F., Christensen-Dalsgaard, J., Nordlund, Å., and Asplund, M. (2014). Improvements to stellar structure models, based on a grid of 3D convection simulations - I.  $T(\tau)$  relations. *Mon. Not. Roy. Astron. Soc.*, 442(1):805–820.
- Valle, G., Dell’Omodarme, M., Prada Moroni, P. G., and Degl’Innocenti, S. (2016). Calibrating convective-core overshooting with eclipsing binary systems. The case of low-mass main-sequence stars. *Astron. Astrophys.*, 587:A16.
- Van Dyk, S. D. (2017). The direct identification of core-collapse supernova progenitors. *Philosophical Transactions of the Royal Society of London Series A*, 375(2105):20160277.
- van Leer, B. (1974). Towards the Ultimate Conservation Difference Scheme. II. Monotonicity and Conservation Combined in a Second-Order Scheme. *Journal of Computational Physics*, 14:361–+.
- VandenBerg, D. A., Bergbusch, P. A., and Dowler, P. D. (2006). The Victoria-Regina Stellar Models: Evolutionary Tracks and Isochrones for a Wide Range in Mass and Metallicity that Allow for Empirically Constrained Amounts of Convective Core Overshooting. *Astrophys. J. Supp. Ser.*, 162(2):375–387.
- Varma, V. and Müller, B. (2021). 3D simulations of oxygen shell burning with and without magnetic fields. *Monthly Notices of the Royal Astronomical Society*, 504(1):636–647.
- Vartanyan, D., Burrows, A., Radice, D., Skinner, M. A., and Dolence, J. (2019). A successful 3D core-collapse supernova explosion model. *Mon. Not. Roy. Astron. Soc.*, 482(1):351–369.
- Viallet, M., Baraffe, I., and Walder, R. (2011). Towards a new generation of multi-dimensional stellar evolution models: development of an implicit hydrodynamic code. *Astron. Astrophys.*, 531:A86.
- Waagan, K., Federrath, C., and Klingenberg, C. (2011). A robust numerical scheme for highly compressible magnetohydrodynamics: Nonlinear stability, implementation and tests. *Journal of Computational Physics*, 230(9):3331–3351.
- Warnecke, J., Käpylä, P. J., Käpylä, M. J., and Brandenburg, A. (2016). Influence of a coronal envelope as a free boundary to global convective dynamo simulations. *Astron. Astrophys.*, 596:A115.
- Warnecke, J., Korpi-Lagg, M. J., Gent, F. A., and Rheinhardt, M. (2023). Numerical evidence for a small-scale dynamo approaching solar magnetic Prandtl numbers. *Nature Astronomy*, 7:662–668.
- Willson, L. A. (2000). Mass Loss From Cool Stars: Impact on the Evolution of Stars and Stellar Populations. *Ann. Rev. Astron. Astrophys.*, 38:573–611.



- Woods, P. M. and Thompson, C. (2006). Soft gamma repeaters and anomalous X-ray pulsars: magnetar candidates. In *Compact stellar X-ray sources*, volume 39, pages 547–586.
- Yadav, N., Müller, B., Janka, H. T., Melson, T., and Heger, A. (2020). Large-scale Mixing in a Violent Oxygen-Neon Shell Merger Prior to a Core-collapse Supernova. *Astrophys. J.*, 890(2):94.
- Yoshida, T., Takiwaki, T., Kotake, K., Takahashi, K., Nakamura, K., and Umeda, H. (2019). One-, Two-, and Three-dimensional Simulations of Oxygen-shell Burning Just before the Core Collapse of Massive Stars. *Astrophys. J.*, 881(1):16.
- Zanni, C., Ferrari, A., Rosner, R., Bodo, G., and Massaglia, S. (2007). MHD simulations of jet acceleration from Keplerian accretion disks. The effects of disk resistivity. *Astron. Astrophys.*, 469(3):811–828.
- Zhang, M. and Feng, X. (2016). A comparative study of divergence cleaning methods of magnetic field in the solar coronal numerical simulation. *Frontiers in Astronomy and Space Sciences*, 3:6.